Molecular mechanisms of YAP signalling in the context of cancer

Xie, Bailu

Award date:
2019

Awarding institution:
University of Bath

Molecular mechanisms of YAP signalling in the context of cancer

Bailu Xie

A thesis submitted for the degree of Doctor of Philosophy

University of Bath

Department of Pharmacy and Pharmacology

September 2018

Signed:……..…

Date:……

Acknowledgements

First and foremost, my gratitude goes to my parents, who love me and support me unconditionally for the path I choose. Their courage, integrity, strong will and wisdom when they were struggling in chaotic eras have always inspired me.

Secondly, I am profoundly grateful to have Randy Mrsny as my supervisor, without whom my dream to pursue a PhD in the UK would not have come true. He is truly a caring, fair and intelligent scholar who always sees the goodness in people and does everything he can to raise people up. He is a natural born expert in public engagement, capable of transforming complicated jargons and concepts into entertaining fun facts, like easily chewable tablets for anyone to swallow comfortably. Moreover, his extraordinary optimism and energy always cast away the doubts and negative aura during difficult times. He has provided freedom for me to explore in all aspects of science and will catch me when I falls. Therefore, I grow strong with a positive attitude and mature into a confident and independent scientist, believing I can do anything owing to his continuous encouragement and faith in my capabilities.

Thirdly, I appreciate my supervisory team for their guidance. I am indebted to Paul De Bank, who has immense sense of duty and useful suggestions, rescuing me in numerous occasions promptly. And Makoto Furutani-Seiki, Steve Ward and Amanda Mackenzie have kindly provided their professional opinions on my project.

I feel fortunate to work with fabulous labmates and have fun outside the lab as well: Emma Harvey, Khaled Almansour, Ana Cravo, Theresa Ikem, Flo Laurent, Ruiying (Molly) Li, Julia Mackay, Alistair Taverner, Magdalena Pérez, Tiago Fortunato and Kim Luetchford.

I am extremely thankful for the generosities of Kim Moorwood and Silvia Muñoz Descalzo at the Dept. of Biology to offer me the valuable biological techniques that are critical to my project.

During my PhD study, I got the opportunities to observe and practice isolating hepatic and pancreatic stellate cells with Mert Erkan's group members at KOÇ University hospital, Turkey. I benefit from Mert's clinical expertise, excellent medical teaching, scientific research and sharing of the valuable patient-derived stellate cells. Meanwhile, I worked with a talented medical student İbrahim Büdeyri who has the same enthusiasm in cancer research as me. I will always remember the hospitality of the Turkish people whenever I needed help. The friendly smiles and conversations with Buket Yiğit, Tayfun Barlas, Seher Emreoglu, Gökçe Yeter, Yağmur Kılıç, Belitsu Salgin, Şimal Laçin and Kenan Bilmez have enriched my two-week exchange study at KOÇ University hospital.

I am very fortunate to be part of a cancer research team with Vanessa Mundorf, Janina Betz, Julia Sperlich, and Nicole Teusch from Technische Hochschule (TH) Köln, University of Technology, Arts and Sciences in Germany. They represent German characteristics such as efficiency, quality, professionalism and reliability that I look up to. During our wonderful time together in the lab, Vanessa and Janina have offered tremendous help for me to establish the cancer models and screen anti-cancer agents.

I would also like to express my deeply gratitude to the technical specialists in Microscopy and Analysis Suit (MAS) and Chemical Characterisation and Analysis Facility (CCAF): Anne Gesell, Ursula Potter, Diana Lednitzky, Arian Rogers, Shaun Reeksting and Mervyn Lewis. They are indispensable for the progress of my project. Also, their patience and sense of humour always make my day, especially Anne Gesell who has cheered me up in hard times and mentored me in life and professional microscopic skills.

Special thanks to Reiss Mcguinness who was an incredible companion when I first came to the UK.

I would also like to thank the funding from University Graduate School Scholarship, Funds for Women Graduates (FFWG), EACR Travel Fellowship, and Great Britain-China Educational Trust to relieve my financial burden during my PhD studies.

Last but not the least, I would like to thank my own curiosity, passion for science and perseverance that pull me through ordeals of my life.

Abstract

Over the last 40 years, little progress has been made in improving the treatment outcomes of pancreatic ductal adenocarcinoma (PDAC). The desmoplastic and hypo-vascular microenvironment of this cancer limits access to therapeutic strategies. Stellate cells, comprising the majority of stroma and secreting large amount of extracellular matrix (ECM), have been suggested to provide a supportive environment for pancreatic cancer whilst playing a suppressive role in cancer growth. In order to identify strategies capable of modulating pancreatic cancer stroma without promoting cancer growth, it is imperative to establish an *in vitro* human cancer model resembling the human cancer microenvironment.

Conventional models of PDAC using 2D culture of human PDAC cells and mouse models have previously been useful to study PDAC biology. Unfortunately, the usage of such systems to screen potential therapeutic agents has not delivered significant improvements in the overall survival of patients with PDAC. 3D co-culture models of human PDAC cells, patient-derived stellate cells and ECM have been used to better recapitulate the human tumour microenvironment. Since mouse models and commercial matrices used in cancer models are expensive and variable between batches, it would be beneficial to explore other alternatives to reduce the cost and the variability of PDAC models. An inexpensive de-cellularized preparation termed Myogel can be produced in large quantities, providing a potential scaffold to recreate ECM in the human PDAC microenvironment. There are little data on using unmodified hyaluronic acid (HA), which is abundant in pancreatic cancer, to build the 3D co-culture PDAC models.

Yes-associated protein (YAP) is a transcriptional coactivator that can translocate between the cytoplasm and the nucleus. The expression and localisation of YAP is the key to YAP signalling, which functions to sense signals from external and internal changes in cells. Complex signalling networks have been elucidated that involve mechanisms of YAP signalling in the context of cancer. Cell junction/cell polarity, metabolic status, mechanical cues and G-protein-coupled receptors are regarded to affect YAP subcellular localisation, and thus its function. YAP signalling exerts significant impact on tumour initiation, progression, metastasis, malignancy and drug resistance in a number of cancers. YAP has been shown to position itself as an integral part in the crosstalk between various cell signalling pathways to promote cancer growth in solid tumour. Due to effects of the mechanical cues on YAP signalling, a realistic human PDAC model is required to recapitulate YAP signalling in the spatial manner.

In the current study, an *in vitro* 3D fibrotic cancer model with human pancreatic cancer cells, ECM, and patient-derived stellate cells to recreate the human pancreatic cancer microenvironment in the liver and pancreas was established, suitable for high-throughput assay and examining YAP signalling.

After identified that unmodified hyaluronic acid was biocompatible with cancer cells and could promote nuclear accumulation of YAP, mixing PDAC cells and stellate cells in a collagen I matrix with or without HA was performed, resulting in the formation of multiple cancer cells cores inside the 3D co-culture models that resemble the fibrotic cancer microenvironment in patients with advanced and metastatic PDAC. Dynamic YAP subcellular localisation is found in these 3D co-culture models of PDAC cells and stellate cells. Reduction of p53 expression correlates with YAP cytoplasmic localisation in

these 3D co-culture models of PDAC cells and stellate cells. Potential anti-cancer compounds Pseudopterosin A-D and Tylophorinine, derived from natural products, can reduce p53, Ki67 and YAP expression in these 3D co-culture models of PDAC cells and stellate cells.

Future work could easily be built on choosing the high stellate cells to cancer cells ratio such as 5:1 or 10:1 with HA and reduced collagen I to carry on refining the PDAC models. Imaging methods combining optical clearing with ethanol and BABB, Z-stack and Airyscan using the Zeiss LSM880 with a 10x objective lens are validated to be robust for future phenotypic analysis in thick cancer models with approximately 500 µm diameter without disturbing the samples, leading to higher efficiency comparing with the traditional histology methods such as tissue processing using paraffin.

Abbreviations

ACE	Automatic Component Extraction
AJ	Adherens junction
AMPK	AMP-activated protein kinase
APS	Ammonium persulfate
BABB	Benzyl alcohol: benzyl benzoate, 1:2
BSA	Bovine serum albumin
CAFs	Cancer-associated fibroblasts
Cat. #	Catalogue number
CDK	Cyclin-dependent kinase
CLSM	Confocal laser scanning microscopy
COL	Collagen
CTLA-4	Cytotoxic T lymphocyte-associated antigen - 4
DAPI	4’,6-diamidino-2-phenylindole dihydrochloride
DIC	Differential interference contrast
DMSO	Dimethyl Sulfoxide
EACA	6-aminocaproic acid
ECM	Extracellular matrix
EDTA	Ethylenediaminetetraacetic acid
EGFR	Epithelial growth factor receptor
EMT	Epithelial to mesenchymal transition
FAP	Fibroblast activation protein
FBS	Fetal bovine serum

GEMMs	Genetically engineered mouse models
GPCRs	G-protein-coupled receptors
HA	Hyaluronic acid
HSCs	Hepatic stellate cells
KRAS	*Kirsten rat sarcoma oncogene homologue*
LATS1/2	Large Tumour Suppressor 1 and 2 kinases
MDSCs	Myeloid-derived suppressor cells
MET	Mesenchymal to epithelial transition
MHCII	Major histocompatibility class II
miR	MicroRNA
MP	Multiphoton
MS/MS	Tandem mass spectroscopy
MST1/2	Mammalian Sterile 20-like 1 and 2 kinases
Ocln	Occludin
P/S	Penicillin and streptomycin
PanIN	Pancreatic intraepithelial neoplasia
PBS	Phosphate buffered saline
PD-1	Programmed cell death protein - 1
PDAC	Pancreatic ductal adenocarcinoma
PFA	Paraformaldehyde
PMSF	Phenylmethylsulfonyl fluoride
polyHEMA	Poly(2-hydroxyethyl methacrylate)
PSM	Porcine skeletal muscle
PsA-D	Pseudopterosin A-D

PSCs	Pancreatic stellate cells
PSM	Porcine skeletal muscle
PVP	Polyvinylpyrrolidone
RIPA	Radio-Immune Precipitation Assay
SC	Stellate cells
SD	standard deviation
SDS	Sodium dodecyl sulfate
SDS-PAGE	Sodium dodecyl sulfate-polyacrylamide gel electrophoresis
SH3	Src homology domain 3
SHH	Sonic hedgehog (SHH)
TAMs	Tumour-associated macrophages
TBS	Tris Buffered Saline
TBS-T	Tris Buffered Saline and Tween® 20
TEAD	Transcription enhancer activator domain
TEMED	Tetramethylethylenediamine
TGF-β	Transforming growth factor- β
TJ	Tight junction
TYLO	Tylophorinine
YAP	Yes-associated protein
αSMA	Alpha-smooth muscle actin

Table of contents

List of Figures

List of Tables

Chapter 1. Introduction

Cancer is a disease caused by abnormal cells growing in an uncontrollable way affecting all parts of human body, leading to multiple organ failures and ultimate death of the patients. Cancer cases are estimated to be over 14 million globally [Torre *et al*, 2015], posing a heavy burden on human society. Cancer is responsible for millions of deaths every year worldwide. As illustrated in Figure 1, the leading cause of cancer deaths are those involving cells of the lung, large intestine (colorectal), liver, breast, stomach (gastric), pancreas, oesophagus, prostate, uterus [Torre *et al*, 2015], most of which originate in epithelial cells and result in structures known as solid tumours. Research on these various epithelial-derived cancers have facilitated a variety of preventative approaches and therapeutic treatments. With improvements in cancer care and a greater understanding of cancer biology, cancer death rates have been decreasing for many of these epithelial-derived cancers. In England and Wales, the 5-year survival rates for colorectal cancers have doubled since 1970, reaching nearly 60% in 2011. The 5-year survival rates for breast cancer, prostate cancer and melanoma have risen from 47.9-52.7%, 36.6-36.9%, 51.1-52.3% in 1971-72 to 86.7%, 84.8-87.1%, 89-90.4% in 2010-11 [Quaresma *et al*, 2015]. Opposingly, improvements in these cancer management approaches have not had significant impact on improving the outcomes for patients with pancreatic cancer. This issue will be the main research theme in the current project.

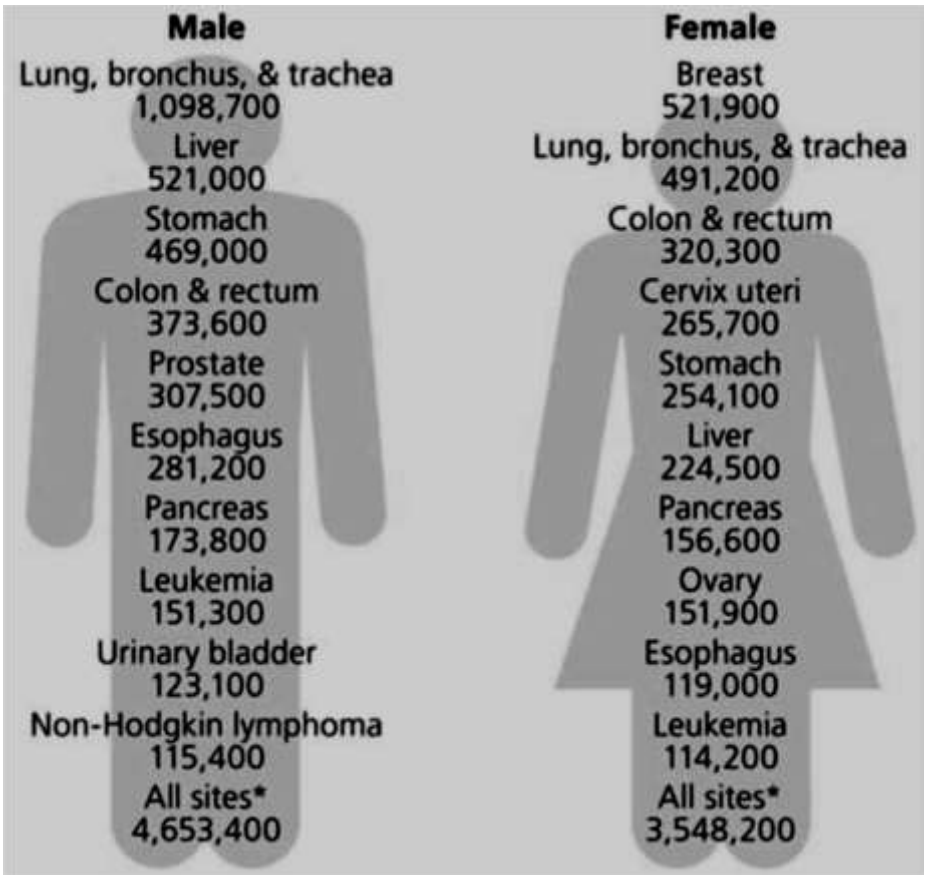

Figure 1. Global estimated cancer mortality by gender in 2012.

The figure is adapted from Torre *et al* [Torre *et al*, 2015] with copyright permission from John Wiley and Sons. * Excluding non-melanoma skin cancers.

1.1 Background of pancreatic ductal adenocarcinoma (PDAC)

Over 90% of pancreatic cancer are pancreatic ductal adenocarcinoma (PDAC). By 2020, the number of patients with PDAC is projected to exceed 420,000 worldwide with around 410,000 annual deaths [Neoptolemos *et al*, 2018]. PDAC is currently the fourth most common cause of death from cancer in Europe, estimating 128,000 deaths in 2018 [Ferlay *et al*, 2018]. The 5-year survival rate of patients diagnosed with PDAC has remained stable and is predicted to stay below 5 % for a long time [Siegel *et al*, 2015]. The median overall survival rate for patients with PDAC is currently 1–10 months worldwide [Hariharan *et al*, 2008]. The progression of ductal cells in the pancreas into aggressively proliferating PDAC and the dysregulation of cell signalling pathways associated with that conversion, especially those connecting yes-associated protein (YAP) signalling, will be reviewed. Studies to unravel the characteristics of this deadly disease and potential therapeutic strategies targeting YAP signalling are proposed in this chapter.

1.1.1 Development of PDAC

Due to a lack of reliable detection methods at early stage, about 80% of patients diagnosed with PDAC present locally advanced and metastatic disease [GM *et al*, 2018; Lau *et al*, 2017; Neoptolemos *et al*, 2018; Salgado *et al*, 2018; Uccello *et al*, 2018]. Cellular and molecular changes in the pathogenesis of PDAC present a unique pancreatic cancer microenvironment, which are depicted in Figure 2 [Khan *et al*, 2017]. At the onset of pancreatic intraepithelial neoplasia (PanIN), pancreatic ductal cells become enlarged and the stroma begins to become modified in its composition of cells and collagen. As PanIN progresses, the size and the number of neoplastic cells increase while more stromal cells are recruited to the environment. Over time this environment loses its ability to suppress the growth of the hypertrophied epithelial cells and a transition to PDAC occurs. When PDAC develops, the pancreatic ductal cell transforms into a highly proliferative and invasive cell, gaining the ability to evade the immune-surveillance and tuning the stromal cells to be in favour of promoting tumour growth.

Pancreatic cancer cells are the centre of a PDAC tumour. This not only means they are the origin of sins in the microenvironment but also the way they become surrounded by other components that position them at the central core in the tumour microenvironment (or multiple cores in the cancer tissue). Genetic and metabolic alterations occur in pancreatic cancer cells that enable them to evolve and survive in human body without limitations to their ability to divide. Pancreatic cancer cells are often positively stained with cell protein markers such as carcinoembryonic antigen (CEA), carbohydrate antigen (CA) 19-9, cancer antigen (CA) 125, SMAD4, cytokeratins, mucins and p53 [Ansari *et al*, 2016; Boj *et al*, 2015; Pang *et al*, 2015; Wormann *et al*, 2016]. Interestingly, only 10% of cells within pancreatic cancer tumour are pancreatic cancer cells [Neesse *et al*, 2011], indicating the immense detrimental impact of a few pancreatic cancer cells on human body. Compared to primary tumours in the pancreas site, more cancer cells are detected at metastatic site in the liver of patients with PDAC [Whatcott *et al*, 2015]; however, the exact percentage of cancer cell regions in the liver has not yet been confirmed in large cohort of patients with metastatic PDAC.

In the PDAC microenvironment where cancer cells grow and evolve, pancreatic stellate cells (PSCs), a group of prominent stromal cells expression αSMA, are found to comprise as much as 80-90% of the pancreatic tumour, secreting large amount of extracellular matrix (ECM) such as collagen I, collagen IV,

fibronectin and laminins, as well as cytokines and chemokines to provide a supportive environment for pancreatic cancer progression [Erkan *et al*, 2008]. Moreover, the dense cell-cell and cell-matrix environments resulting from interactions between cancer cells and stellate cells create a barrier surrounding cancer cells to protect cancer cells from anti-cancer treatments and immune response [Diwakarla *et al*, 2017; Djurec *et al*, 2018]. Nonetheless, a contradictory role of PSCs and the fibrotic environment in pancreatic cancer microenvironment have been proposed, indicating that PSCs and fibrosis can serve to suppress tumour progression [Erkan, 2013; Ozdemir *et al*, 2014; Rhim *et al*, 2014]. This hypothesis is derived from the data that elimination of stromal components causes unexpected acceleration of pancreatic cancer growth [Ohuchida *et al*, 2004; Ozdemir *et al*, 2014; Rhim *et al*, 2014]. Early evidence could be traced back to a study where enhanced invasion of pancreatic cancer cells was observed after they were co-cultured with irradiated PSCs from a patient *in vitro* [Ohuchida *et al,* 2004], which raised the question about the undesired tumour-promoting effect that could potentially offset the beneficial outcomes of destroying the tumour stroma using radiotherapy. Recent evidences have indicated that a shorter survival due to an accelerated cancer progression in genetic modified mice with pancreatic cancer was observed after destroying the tumour stroma in two independent research groups [Ozdemir *et al*, 2014; Rhim *et al*, 2014]. Also, PDAC patients with low expression of stromal cell marker (αSMA) correlated with poorer overall survival compared to the ones with high expression of αSMA [Ozdemir *et al*, 2014] and high collagen deposition in clinical specimen was associated with longer survival [Erkan *et al*, 2008]. Hence, more prudent experimental designs to distinguish tumour-promoting PSCs from tumour-suppressive PSCs and understand the role of fibrosis in the development of PDAC are required.

Significantly, the immune cells that infiltrate PDAC tumours express immunosuppressive genotypes and phenotypes [Bailey *et al*, 2016; Seo *et al*, 2017]. Expression of genes related to regulatory T cells, overexpression of cytotoxic T lymphocyte-associated antigen (CTLA)-4, programmed cell death protein (PD)-1, and mutations of Toll-like receptors have been identified in PDAC tumours through genomic analysis [Bailey *et al*, 2016]. The number of T cells is markedly increased in tumours compared to those in the blood of patients with PDAC, with a great portion of cells expressing immune inhibitory markers [Seo *et al*, 2017]. Therefore, immune cells that might otherwise maintain a check on nascent cancerous pancreatic cells can fail to prevent cancer progression because of these potent suppression mechanisms.

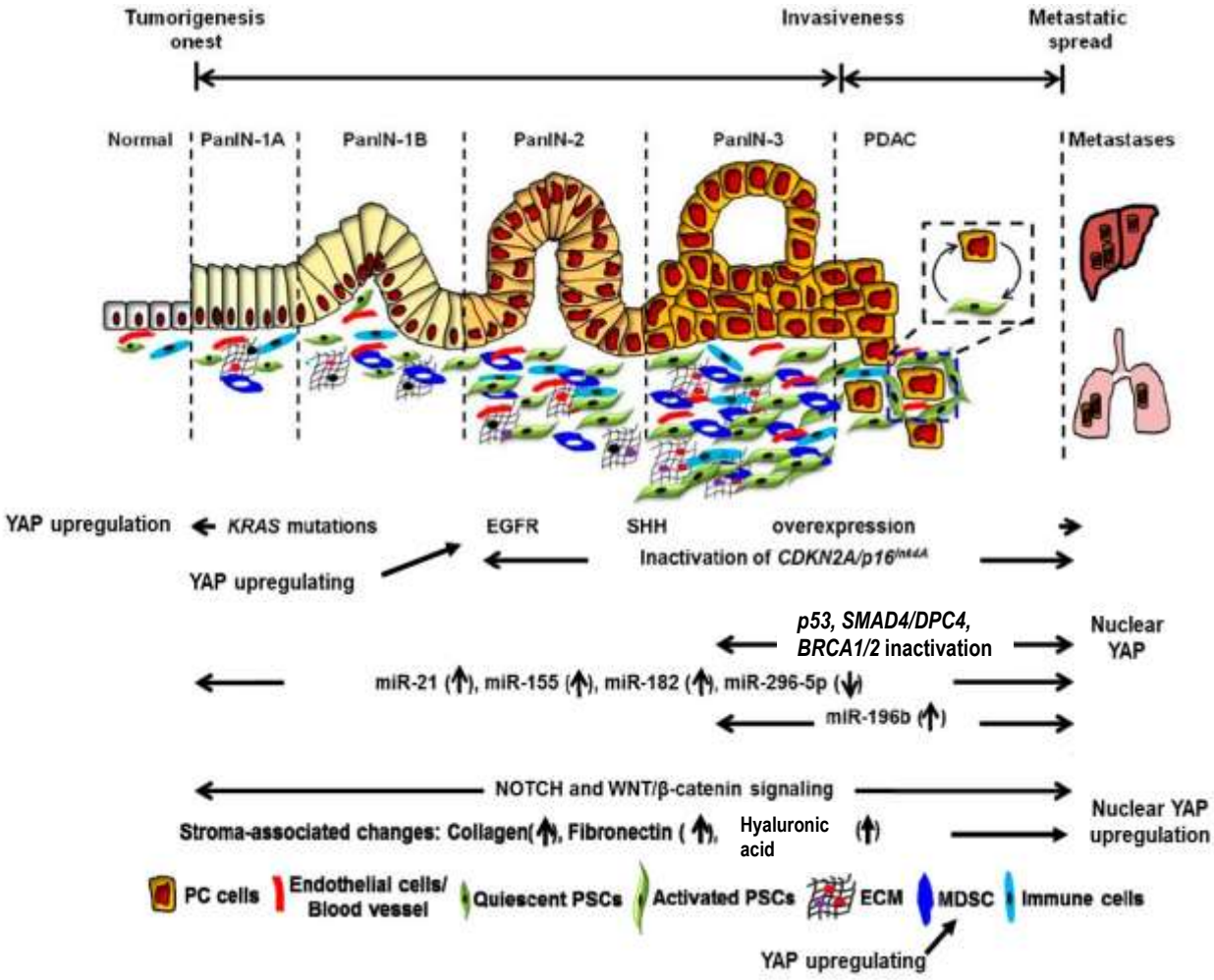

Figure 2. Histopathological and molecular changes in the pathogenesis of PDAC.

The figure is adapted from Khan *et al* [Khan *et al*, 2017], which is distributed under the terms and conditions of the Creative Commons Attribution (CC BY) license (http://creativecommons.org/licenses/by/4.0/). At the onset of pancreatic intraepithelial neoplasia (PanIN), pancreatic ductal cells become enlarged and the stroma begins to become modified in its composition of cells and extracellular matrix (ECM). As PanIN progresses, the size and the number of neoplastic cells increase while more stromal cells such as pancreatic stellate cells (PSCs) are recruited to the environment. When PDAC develops, the pancreatic ductal cell transforms into a highly proliferative and invasive cell, pancreatic cancer (PC) cell. *Kirsten rat sarcoma oncogene homologue (KRAS)* mutation, NOTCH and WNT/β-catenin signalling pathway dysregulation, epithelial growth factor receptor (EGFR), sonic hedgehog (SHH) protein overexpression, and upregulation of microRNA-21 (miR-21), miR-155, miR-182, miR-296-5p, miR-196b have all been associated with driving the oncogenic conversion associated with PanIN-1A to metastatic PDAC phenotype changes. During these transitions there are changes such as increased collagen, fibronectin, and hyaluronic acid present in the local environment and mutations in the *p16/cyclin-dependent kinase (CDK)N2A gene, p53, SMAD4/DPC4, and BRCA1/2*. Myeloid-derived suppressor cells (MDSCs) are also found in the PDAC environment to promote cancer immune tolerance. YAP (yes-associated protein) signalling has been linked to dysregulated pathways involving EGFR, RAS, WNT/β-catenin, TGF- β/SMAD4, HH, and DNA damage response.

1.1.2 Dysregulation of cell signalling pathways in PDAC

There are numerous abnormal alterations that can occur at the molecular level during the development of the PDAC. *Kirsten rat sarcoma oncogene homologue (KRAS)* mutation, NOTCH and WNT/β-catenin signalling pathway dysregulation, epithelial growth factor receptor (EGFR), sonic hedgehog (SHH) protein overexpression, and upregulation of microRNA-21 (miR-21), miR-155, miR-182, miR-296-5p, miR-196b have all been associated with driving the oncogenic conversion associated with PanIN-1A to metastatic PDAC phenotype changes [Khan *et al*, 2017]. During these transitions there are changes such as increased collagen, fibronectin, and hyaluronic acid present in the local environment and mutations in the *p16/cyclin-dependent kinase (CDK)N2A gene, p53, SMAD4/DPC4, and BRCA1/2* (Figure2) [Khan *et al*, 2017].

KRAS mutation, transforming growth factor- β (TGF-β)/SMAD4 pathway inactivation, NOTCH and WNT/β-catenin signalling pathway dysregulation and EGFR overexpression send continue growth-promoting signals in cancer cells [Garrido-Laguna *et al*, 2015; Ruess *et al*, 2017]. Inactivation of *CDKN2A/p16* causes cancer cells to lose the ability to suppress the cell cycle, resulting in enhanced proliferation in cancer cells [Ruess *et al*, 2017; Weinberg *et al*, 2015]. *BRCA1/2* inactivation causes defective DNA damage repair responses in cancer cells, leading to an inability to correct gene malfunction [Garrido-Laguna *et al*, 2015; Greer *et al*, 2007]. Pancreatic cancer cells can produce excessive levels of SHH that activate pancreatic stellate cells, which in turn support the malignancy of cancer cells [Li *et al*, 2014].

ECM constituents can have potent effects on cell signalling events within PDAC cells, which in turn regulate their proliferation capacity and susceptibility to chemotherapeutics. Collagens activate SMAD and the focal adhesion kinase pathway to disrupt E-cadherin/ β-catenin complexes, leading to EMT and tumour proliferation [Veenstra *et al*, 2018]. Fibronectin interacts with integrins to promote cell survival [Topalovski *et al*, 2016]. Fibronectin and laminins are reported to protect cancer against apoptotic death [Topalovski *et al*, 2016; Veenstra *et al*, 2018]. Abundant hyaluronic acid, a glycosaminoglycan, are present in the pancreatic cancer microenvironment and thus increase tumour interstitial fluid pressure to impair local drug delivery. Also, HA binds to the surface receptor EGRF and CD44, which are overexpressed in pancreatic cancer cells and contributes to cell proliferation and motility [Chen *et al*, 2018a; Kultti *et al*, 2012].

In recent years, yes-associated protein (YAP) signalling has drawn attention due to its potential crosstalk between various cell signalling pathways [Rozengurt *et al*, 2018; Zhang *et al*, 2015]. YAP signalling will be elaborated in the following sections.

1.2 Laboratory/Biological Models for pancreatic cancer research

Over the last 40 years, little progress has been made in improving PDAC outcomes. The desmoplastic and hypo-vascular microenvironment of this cancer limits access to therapeutic strategies. Stellate cells, comprising the majority of stroma and secreting large amount of extracellular matrix (ECM), have been suggested to provide a supportive environment for pancreatic cancer cells whilst certain subtypes of them can play a suppressive role in cancer growth. 2D culture models and animal models have been useful to study pancreatic cancer biology; however, they do not recapitulate the highly fibrotic properties in human pancreatic cancer microenvironment in late-stage of PDAC development. In order to identify strategies capable of modulating pancreatic cancer stroma without promoting cancer growth, it is imperative to establish an *in vitro* cancer model resembling the human PDAC microenvironment. The following sections will discuss the conventional and novel models in cancer research, focusing on pancreatic cancer.

1.2.1 2D culture (mono-culture and co-culture)

AsPC-1, BxPC-3, Capan-1, Capan-2, CFPAC-1, HPAC, HPAF-II, Hs 766T, MIA PaCa-2, PANC-1, SU.86.86, SUIT-2, SW 1990, and T3M4 are well-characterized human pancreatic cancer cell lines that have been used in a wide range of studies testing anti-cancer reagents in a 2D format [Deer *et al*, 2010; Iwamura *et al*, 1987; Missiaglia *et al*, 2004]. The majority of these research studies have examined abnormal cellular signalling events and explored the reduction or overexpression of certain proteins associated with uncontrolled proliferation [Deer *et al*, 2010; Missiaglia *et al*, 2004]. While 2D culture can be easily applied to high-throughput assay in a 96-well or 384-well plate, cancer cells are not grown in a 3D architecture as they are in patients with PDAC. Moreover, the cell-cell contact and cell-matrix contact that cancer cells are exposed to cannot be readily recreated in a 2D culture model, which might alter the gene expression and cell signalling compared to the cells inside patients. More importantly, in terms of mimicking how therapeutic strategies reach cancer cells, 2D culture fails to recapitulate multiple barriers in a tumour and thereby produce limited data on the effectiveness and efficiency of the penetration of treatments in a 3D environment with drug delivery obstacles.

Alterations after cancer cells are grown in 3D culture compared to 2D culture have been excellently reviewed by Hoarau-Vechot *et al* and Yamada *et al* [Hoarau-Vechot *et al*, 2018; Yamada *et al*, 2007]. Cell proliferation and growth, cell polarity and tumour progression, migration and response to therapies are the main focus in those reviews. There are three key issues related to the improvement of pancreatic cancer treatment we would like to highlight using the literatures in pancreatic cancer research.

Firstly, targeting cancer stem cells is crucial for long-term survival of patients because cancer stem cells are the leading cause of resistance to therapy and relapse in patients. Therefore, only models that recapitulate this phenomenon will facilitate the improvement in therapeutic strategies to eliminate cancer stem cells in the tumour microenvironment. 3D cultures are regarded to promote the stemness of cancer cell lines to a greater extent than 2D cultures [Hoarau-Vechot *et al*, 2018]. For instance, the ratio of cells in the whole cell populations expressing the stem cell marker CD44 was markedly increased from 40.8% in a 2D pancreatic cancer model to 72.4% in a 3D pancreatic cancer model [Yeon

et al, 2013]. Meanwhile, the ratio of cells with triple positive stem cell markers CD44, CD24 and epithelial specific antigen (ESA) in 3D pancreatic cancer models was twice as many as the one in 2D pancreatic cancer models [Yeon *et al*, 2013].

Secondly, there are marked difference in metabolism-associated genes, apoptosis-related genes, chemoresistance-related genes, ECM genes, and miRNA profiles between 2D and 3D culture models [Yamada *et al*, 2007]. Lactate accumulation in the culture medium, expression of glucose transporter 1 (GLUT1) and lactate dehydrogenase (LDHA) were higher in 3D than 2D [Longati *et al*, 2013]. Expression of miRNAs miR-21 and miR-335 that cause chemoresistance was elevated in 3D culture persistently compared to a decrease trend in 2D after cultured for 4 days [Longati *et al*, 2013]. Another miRNAs related to gemcitabine resistance in pancreatic cancer, miR-34 family and miR-221, were also upregulated in 3D culture compared with 2D culture [Yeon *et al*, 2013]. mRNA expression of relevant genes such as COL1A1 (collagen I), COL6A1 (collagen VI), FN1 (fibronectin I), and LUM (lumican) was increased in 3D compared to 2D [Longati *et al*, 2013]. Elevation of genes contributing to anti-apoptosis in cancel cells, such as Bcl-2, Bcl-x, c-IAP-1, and c-IAP-2, were detected in 3D pancreatic cancel models but not in 2D models [Tai *et al*, 2014].

Thirdly, numerous studies have provided extensive evidences that higher concentration of anti-cancer agents are required to inhibit the proliferation and growth of cancer cells in 3D culture than 2D culture [Hoarau-Vechot *et al*, 2018]. For instance, the IC50 of gemcitabine and paclitaxel were significantly increased at 32-fold and 14-fold respectively for 3D pancreatic cancer models compared to 2D pancreatic cancer models [Tai *et al*, 2014]. Cell viability after treatment with a number of anti-cancer agents has been compared in 2D and 3D culture, as listed in Table 1 [Longati *et al*, 2013].

Co-culture of pancreatic cancer cell lines with fibroblasts directly in 2D illustrated changes in signalling and proliferation in these pancreatic cancer cells [Fujita *et al*, 2009]. Pancreatic cancer cells were co-cultured with pancreatic stellate cells (PSCs) directly and indirectly, exhibiting increased proliferative activity and activation of Notch signalling pathway in presence of PSCs [Fujita *et al*, 2009]. Of note, the PSCs are tumour stromal cells considered to be subjected to contact inhibitory effect in 2D culture; however, cancer cells can overcome contact inhibition in 2D culture [Hoarau-Vechot *et al*, 2018]. Whether growth rates of distinct cell types in the co-culture models in 2D are realistic to the ones in 3D warrants further investigation.

Table 1. Differential effects of anti-cancer agents on cell viability in 2D and 3D cultures.

The table is adapted from Longati *et al* [Longati *et al*, 2013], which is distributed under the terms and conditions of the Creative Commons Attribution (CC BY) license (http://creativecommons.org/licenses/by/4.0/).

Name	Class	Concentration	Viability after treatment,%	
			2D	3D
Gemcitabine	nucleoside analogue	1 μM	63	83
H107	microtubulin inhibitor	10 μM	10	97
CB5	microtubulin inhibitor	10 μM	58	93
CB7	microtubulin inhibitor	10 μM	55	100
CB13	microtubulin inhibitor	10 μM	70	95
AXP-107-11	genistein derivative	100 μM	40	65
6-MP	mercaptopurine	200 μM	53	97
6-MPR	mercaptopurine	200 μM	52	95
MT100	allicin derivative	200 μM	19	37
Allicin	diallyl thiosulfinate	200 μM	19	46
act16412	sHH inhibitor	20 μM	72	100
GANT61	sHH inhibitor	20 μM	85	100

1.2.2 Animal models of PDAC

Animal models are frequently used to establish a 3D cancer model that can recreate certain aspects of the microenvironment in solid tumours observed in patients. Commonly used animal models for PDAC research can be divided into three categories: cell-line xenografts, patient-derived xenografts, and genetically engineered mouse models.

Cell line xenograft models typically allow human pancreatic cancer cells to be propagated within immunocompromised (nude) mice. This model format provides an environment for cancer cells to grow in 3D organization, but the other cells within the tumours that are generated are of mouse, and not human, origin. For ease of xenograft generation and accessibility to growing tumours for analysis, human PDAC cells are injected in a subcutaneous site, commonly into the flank region of the mouse [Jiang *et al*, 2018]. In the case of PDAC, such a xenograft model does not represent the local environment of the pancreas where this cancer arises nor does it represent liver tissue that is the one of the primary sites of metastasis. Even after implanting various PDAC cell lines into the head of the pancreas in nude mice, the highly desmoplastic environment and metastatic sites are rarely seen [Logsdon *et al*, 2015], demonstrating that creating a xenograft PDAC model in nude mice is not readily possible. In order to induce a stroma that is characteristic of PDAC tumours, human pancreatic stellate cells can be injected together with cancer cell lines, resulting in a slight improvement in creating a more realistic tumour environment [Jiang *et al*, 2018]. However, species differences and a lack of tissue density in the subcutaneous space limit the ability of these models to create a realistic PDAC microenvironment, limiting this approach as a useful model to predict clinical benefit of therapeutic agents and methods.

Patient-derived xenograft mouse models can also be established with fractions of cancer tissue in the subcutaneous space, using the same nude mice approach as cell line xenografts. Although the exact distance from the head of the pancreas is unknown, tumours retain similar gene patterns and stromal features as the original ones in patients after growth in nude mice as explants [Logsdon *et al*, 2015]. Introduction of human immune cells into these patient-derived xenograft models has also been attempted to restore, in part, the complex set of immunological events occurring within PDAC tumours [Logsdon *et al*, 2015]. However, the high cost for maintenance of such mouse models and the genetic differences in the cancer microenvironment still restrict the application of patient-derived xenograft mouse models as a tool to predict successful clinical translation of therapeutic agents and methods.

Genetically engineered mouse models (GEMMs) are useful to precisely mimic gene alterations that occur in human PDAC cells, providing a tool to explore targeted therapies *in vivo*. GEMMs with KRAS mutation have been successfully generated in PDAC mice, which result in similar metastatic and histological patterns as patients with PDAC [Logsdon *et al*, 2015]. However, some gene changes, such as *TP53*, in GEMMs do not always match the situation in patients and the development of PDAC tumours is relatively faster in GEMMs than that observed in patients [Feigin *et al*, 2016; Gopinathan *et al*, 2015]. Again genetic discrepancies between species and high cost of such complex and labour-intensive mouse models urge the need to establish other PDAC models.

As noted above, there are substantial limitations for current mice models to adequately examine the effect of potential therapeutic agents and to predict outcomes in patients. While some of these models are lengthy and costly in their efforts to align with PDAC tumours, there remain still striking genetic

differences from human. Nevertheless, some of these models continue to play an important role in the evaluation of novel therapies in pre-clinical studies.

1.2.3 3D culture (mono-culture and co-culture)

There are numerous review articles summarizing how to establish 3D culture of cancer models [Friedrich *et al*, 2007; Hoarau-Vechot *et al*, 2018; Kapalczynska *et al*, 2018; LaBarbera *et al*, 2012]. The eight practical methods below are derived from those reviews, highlighting the past, the presence and the emerging trend of 3D culture establishments and potential use in high-throughput screening.

1) 3D culture in spinner flasks/bioreactors

The earliest report on 3D culture of cancer models was published in 1970 by Sutherland *et al*, who grew spheroids in matrix-free medium to mimic lung tumour and colorectal tumour in spinner flasks [Inch *et al*, 1970]. Since then, numerous studies have conducted in spinner flasks, roller tubes, rotating vessels (bioreactors) where cells are subjected to a swirling force, so as to prevent cells attaching to the surface of the culture vessels and promote cell-cell aggregates in suspension as shown in Figure 3 [Friedrich *et al*, 2007]. One of the major drawbacks that render this approach less suitable for high-throughput assay is the transferring steps where extra efforts are needed to transfer the spheroids from the flasks or bioreactors into the 96-well or 384-well plates, limiting the efficiency. In recent year, a novel bioreactor has been developed by Cellesce Ltd, aiming to achieve scalable high-throughput assay [Storm *et al*, 2016].

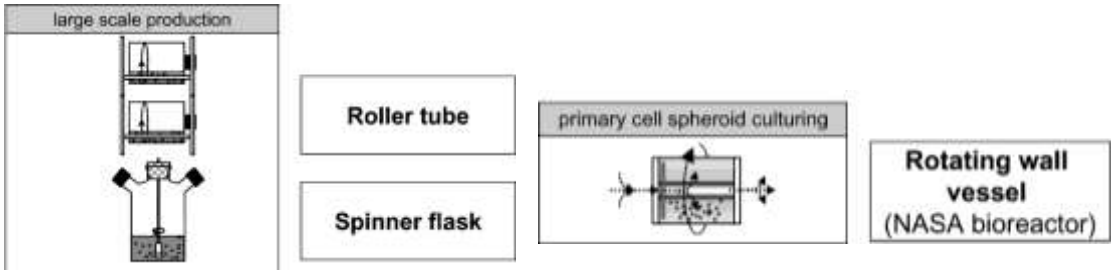

Figure 3. 3D culture in spinner flasks and bioreactors.

The figure is adapted from Friedrich *et al* [Friedrich *et al*, 2007] with copyright permission from Taylor & Francis. Cells are subjected to a swirling force to prevent cells settle to the bottom and promote cell-cell aggregates in suspension in spinner flasks, roller tubes, rotating vessels (bioreactors).

2) 3D culture with gel-like substances/scaffold: agarose, Matrigel®, collagen, silk, alginate, hyaluronic acid, methylcellulose

In essence, the goal of 3D culture is to reduce odds of cell-surface attachment to zero because cells grown *in vitro* with a low density culture medium have the tendency to settle to the bottom surface of the culture vessels due to gravity. Another approach to counteract gravity was introduced by Yuhas JM *et al* in 1977 [Yuhas *et al*, 1977]. The method simply involved gel-like substances, agarose, to create

either a viscous environment or a layer between cells and the bottom surface of the culture vessels, preventing cells adhering to the surface. Nowadays, commonly used gel-like substances include naturally derived hydrogels such as Matrigel®, collagen, alginate, and fibrin, synthetic and some semi-synthetic hydrogels with a combination of synthetic and natural polymers such as hyaluronic acid and methylcellulose [Caliari *et al*, 2016; Highley *et al*, 2016; Maritan *et al*, 2017]. Most of methods to build 3D cancer models with cancer cells, fibroblasts and immune cells could be summarized as either embedding cells in gel-like substances or seeding cells on top of the solidified gel (Figure 4) [Hoarau-Vechot *et al*, 2018]. Most of the gel-like substances are also naturally-occurring components in tumour microenvironment in patients, such as collagen, fibronectin, hyaluronic acid and laminins, contributing to tumorigenicity. Some of the gel-like substances such as agarose, alginate, silk and methylcellulose are not present in the tumour microenvironment but could increase the viscosity of the culture environment and serve as scaffolds for a 3D architecture [Gopinathan *et al*, 2018]. Naturally-occurring gel-like substances that present in human tumour environment, the biomaterials derived from non-mammal species, and the synthetic hydrogels have advantages and limitations. For instance, naturally-occurring gel-like substances including collagen, fibronectin, and laminins are the best materials to mimic the cell-matrix interactions that determine the genotypes and phenotypes of the cancer cells. However, they are usually extracted from animals, leading to batch-to-batch difference and relative high cost that hamper the standardization of the methods across different labs. The biomaterials derived from non-mammal species and the synthetic hydrogels are more consistent between batches than naturally-occurring gel-like substances, making them ideal for standardization. However, it is uncertain that whether they could pose changes to the genotypes and phenotypes of cancer cells that could result in variation from the ones inside cancer patients, which warrants further investigation.

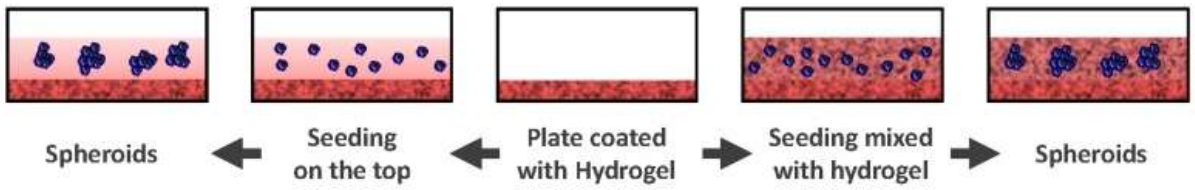

Figure 4. Building 3D culture with gel-like substances/hydrogels.

The figure is adapted from Hoarau-Vechot *et al* [Hoarau-Vechot *et al*, 2018], which is distributed under the terms and conditions of the Creative Commons Attribution (CC BY) license (http://creativecommons.org/licenses/by/4.0/). Most of 3D culture methods to grow cancer cells, fibroblasts and immune cells could be summarized as either embedding cells in gel-like substances or seeding the cells on top of the solidified gel.

3) 3D culture in a hanging drop format

The pioneers of 3D culture using a hanging drop format are Harrison and Carrel, who reported culturing the 3D neutron cells in 1910-1911 [Carrel *et al*, 1911; Millet *et al*, 2012]. As shown in Figure 5A, the idea of a hanging drop format is to utilize surface tension to hang microliters of cell suspension (20-40 µL) onto the lid of culture dishes or special device inside cell culture vessels so that aggregation of cells

occurs at the tip of a droplet to form 3D spheroids. Traditional hanging drop method involves transferring the spheroids on the lid to each well of 96-well plates, which is labour-intensive to the operator (Figure 5B). Commercially Hanging Drop plates markedly increase the efficiency but also the cost of establishment of the models for high-throughput assay. In our lab, we have cultured 3D pancreatic cancer spheroids in a hanging drop format using droplets on the lid of a dish (Figure 5B) and commercialized GravityPLUS™ HangingDrop Plates (Figure 5C), with the latter resulting in shorter experimental time.

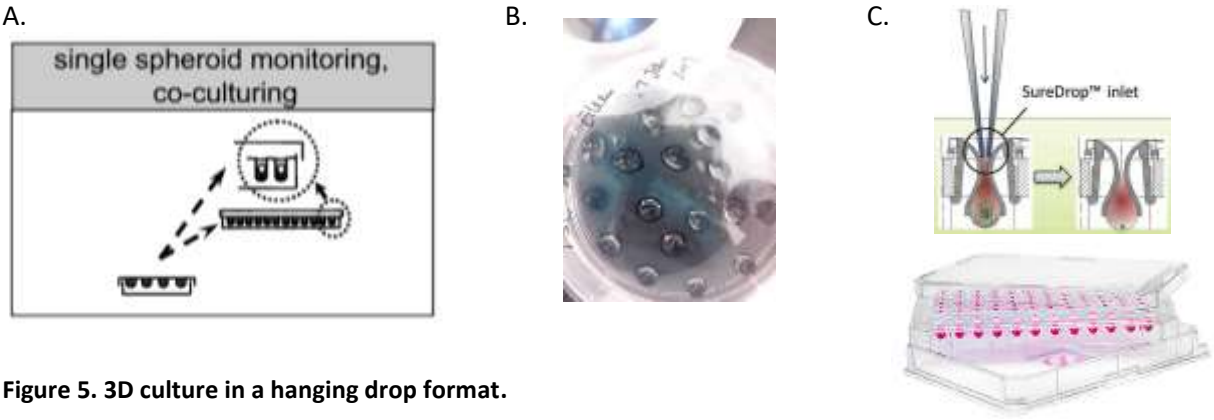

Figure 5. 3D culture in a hanging drop format.

Aggregation of cells to form 3D spheroids occurs at the tip of a droplet after hanging microliters of cell suspension (20-40 µL) onto the lid of culture dishes or special device inside cell culture vessels. A. The figure is adapted from Friedrich *et al* [Friedrich *et al*, 2007] with permission from Taylor & Francis. B. Hanging drops in a culture dish. C. Diagram and figure of the GravityPLUS™ HangingDrop Plates from www.perkinelmer.co.uk.

4) 3D culture in low-attachment plates with centrifugation

Low-attachment 96-well plates with centrifugation are another commonly used approach to establish 3D culture models. There are a number of ways to make the low-attachment plates. Gel-like substances such as agarose, collagen I and Matrigel® or poly(2-hydroxyethyl methacrylate) (polyHEMA) can be used to coat the growth surface of the microplates. Commercial low-attachment plates are also available. The centrifugation step facilitates cell aggregation to form spheroids with or without mixing with gel-like substances. This method has been widely used in various labs. For example, single spheroid in each well of 96-well plates using mixture of cancer cells with Matrigel® after centrifugation has been generated to analyse cell proliferation, invasion and test toxicity of agents [Ivascu *et al*, 2006; Li *et al*, 2011; Sperlich *et al*, 2018]. Agarose-coated microtiter plates were used to perform spheroid-based drug screen on the basis of the NCI-DTP 60-cell line screen [Friedrich *et al*, 2009]. Most of the studies required 3-4 days for the cells to form an acceptable spheroid structure. Recently, pancreatic cancer spheroids were reported to be established 24 hours after centrifugation, which could speed up the drug screening process in the future [Kota *et al*, 2018].

5) 3D culture in micropatterning

As seen in Figure 6, without using 96-well low-attachment microplates or the gel-like matrix, large-scale uniform 3D cancer spheroids, ranging from 150 µm in diameter [Hirschhaeuser *et al*, 2010] to 700 µm [Yeon *et al*, 2013], can be formed in identical microwells printed by micropatterning. Micropatterning is a technology involving the poly(dimethylsiloxane) thin film printing to develop an alternative material surface for cells suspended in normal cell culture medium to adhere to each other without adhering to the surface. The material can be printed as a new microplate [Yeon *et al*, 2013] or as a membrane that can be inserted into 6-well plates [Hirschhaeuser *et al*, 2010]. Using the new microplates printed by micropatterning, doxorubicin and gemcitabine have been tested in 3D pancreatic cancer spheroids [Yeon *et al*, 2013]. The next step for the development of this technology is to determine whether it will be adapted to a large number of labs and commercialized into new plates to serve as an alternative culture device accepted by all researchers around the world.

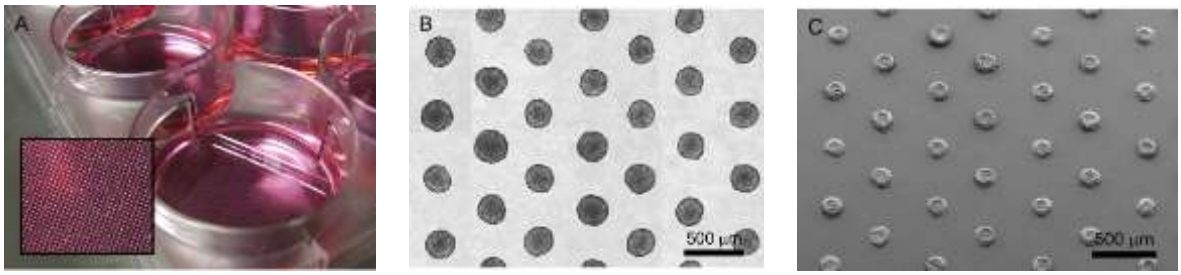

Figure 6. 3D culture in micropatterning.

The figure is adapted from Hirschhaeuser et al [Hirschhaeuser *et al*, 2010] with permission from Elsevier. Micropatterning is a technology involving poly(dimethylsiloxane) thin film printing to develop an alternative material surface for cells suspended in normal cell culture medium to adhere to each other without adhering to the surface.

6) 3D culture using magnetic levitation

Another growing trend to establish 3D culture is using magnetic levitation, which has been developed into products to market. This technology requires incubation of cancer cells with standardized gold and iron oxide nanoparticles and cell-adhesive peptide prior to assembling the spheroids [Souza *et al*, 2010]. After cells are magnetized, aggregation of cells to form spheroids is aided by magnetic attraction as presented in Figure 7 [Leonard *et al*, 2016]. The materials have been validated to be biocompatible with cancer cells and fibroblasts; several types of cancer spheroids, e.g., glioblastoma, breast cancer, lung cancer, and colorectal cancer, are formed and used to perform anticancer drug testing after magnetic levitation [Bumpers *et al*, 2015; Haisler *et al*, 2013; Jaganathan *et al*, 2014; Leonard *et al*, 2016; Souza *et al*, 2010; Turker *et al*, 2018]. 3D culture established by magnetic levitation could be used for high-throughput screening because of the availability of matching commercialized 96-well plates; however, the total cost of anti-cancer drug screening will be increased [Haisler *et al*, 2013]. Co-culture models with cancer cells and fibroblasts by magnetic levitation have illustrated the layers of cancer cells formed at the periphery of the co-culture spheroids, opposite to the situation where layers of

fibroblasts are formed outside the cancer cells core in human tumour microenvironment [Leonard *et al*, 2016]. Further refinement of the approach is needed.

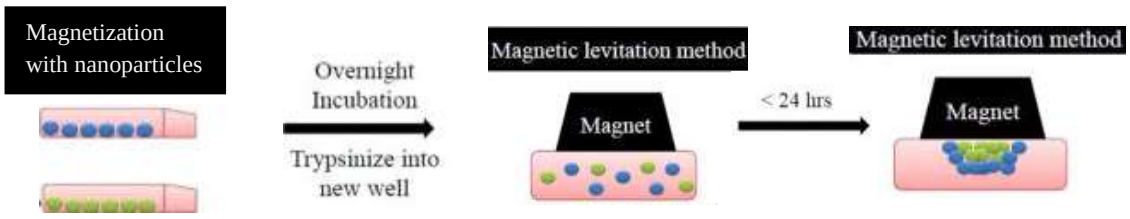

Figure 7. 3D culture using magnetic levitation.

Schematic presentation is adapted from Leonard *et al* [Leonard *et al*, 2016] with permission from Springer Nature. After cells are magnetized, aggregation of cells to form spheroids is aided by magnetic attraction.

7) 3D culture using bio-printing

In recent years, efforts are undertaken to develop bio-printing, a technique based on machinery and computer programming, to build 3D culture models in an accurate, defined, consistent, fast and precise manner. Similar to embedding cells in gel-like material, cancer cells, fibroblasts, immune cells and ECM, the major components in the cancer microenvironment, are mixed with various approaches and spatially dispensed in a microscale within seconds, aided by state-of-art equipment [Zhang *et al*, 2016]. Another fascinating aspect of bio-printing is the capability to construct the vascularity in tumours. A 3D glioblastoma model with vascular niche [Knowlton *et al*, 2015], a 3D breast cancer co-culture model with cancer cells and macrophage [Knowlton *et al*, 2015], a 3D ovarian cancer co-culture model with cancer cells and fibroblasts [Xu *et al*, 2011] have been successfully established, opening brand new door for optimising 3D culture of human cancer models. Although there is limited data reporting building 3D culture models by bio-printing in 96-well plates to perform high-throughput anti-cancer agents testing, we are positive that it will be soon achievable. Nevertheless, as the issue accompany the development of almost every new technology, the cost of bio-printing has been relatively too high so far, restricting its use in high-throughput drug screening at the moment.

8) 3D culture using microfluidics

Microfluidic methods contain a sophisticate chip device with micro-chambers or micro-channels where the cells are seeded by control pressure with injection or dielectrophoretic forces [Beer *et al*, 2017]. Dielectrophoresis is a phenomenon where forces in a non-uniform electric field can be exerted on particles including living cells [Beer *et al*, 2017]. This technology allows improved mixing with solutes and drugs in a 3D format and a more accurate way to mimic diffusion of drugs in 3D. Some research groups have developed self-made chips [Lee *et al*, 2018a; Patra *et al*, 2016]. The HepaChip®, the size of which is similar to the microscope slide (25 mm x 76mm x 1mm), is well-established and available on the market [Beer *et al*, 2017; Hagmeyer *et al*, 2014]. A self-made micro-channel chip has been used to establish 3D pancreatic cancer models separating pancreatic cancer cells with collagen I in one channel from stellate cells with collagen I in another channel, which lacked the direct cell-cell contact and interaction of the receptors on cancer cells with stellate cells [Lee *et al*, 2018a]. HepaChip® has been used to build a viable 3D pancreatic cancer mono-culture model with only pancreatic cancer cell lines and test the sensitivity of cisplatin in the models [Beer *et al*, 2017]. The microfluidic method has not been standardized across different labs so the future application in high-throughput screening needs further investigation, especially in the context of large-scale formation of hundreds of spheroids within a short time.

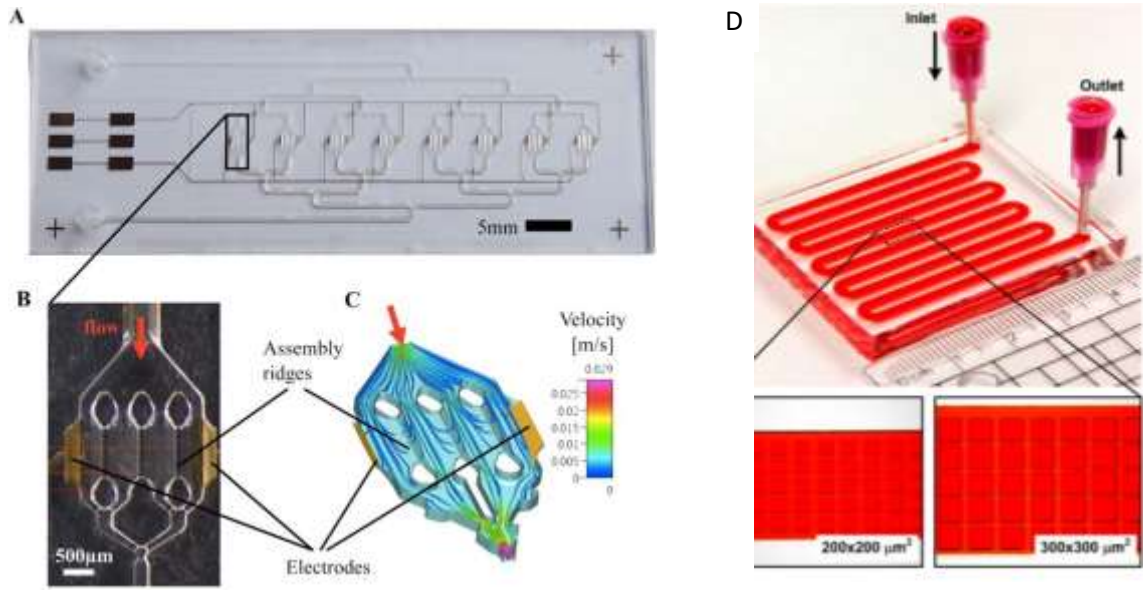

Figure 8. 3D culture using microfluidics.

A-C. The figure is adapted from Beer *et al* [Beer *et al*, 2017], illustrating the commercialized microfluidics, HepaChip®. D. The figure is adapted from Patra *et al* [Patra *et al*, 2016], illustrating the self-made microfluidics. Both articles are distributed under the terms and conditions of the Creative Commons Attribution (CC BY) license (http://creativecommons.org/licenses/by/4.0/).

In summary, growing pancreatic cancer cell lines in 3D cultures has been described in a number of studies. These approaches have used a variety of strategies that have included using centrifugation in low-attachment plates coated with polyHEMA [Phung *et al*, 2011], hydrogels [Tibbitt *et al*, 2009], or agarose-containing scaffold-free medium without ECM [Diep *et al*, 2012], hanging-drop plates containing scaffold-free medium without ECM [Tung *et al*, 2011], mixing cells with methylcellulose [Ware *et al*, 2016], and growing cells on top of animal-derived ECM containing collagen or Matrigel or both [Baker *et al*, 2016; Coleman *et al*, 2014b]. Co-cultures of pancreatic cancer cell lines with stellate cells by direct mixing has also been employed in similar 3D cultures [Coleman *et al*, 2014b]. Methylcellulose facilitates formation of 3D co-culture models with mixture of PANC-1, AsPc-1, BxPC-3, Capan-1 and MIA PaCa-2 cells with patient-derived pancreatic stellate cells [Ware *et al*, 2016]. In spite of the abundancy of HA in pancreatic cancer, only a few studies have included HA in a 3D model, mostly where there is an unnatural chemical cross-linked form of HA such as thiol-modified hyaluronic acid [Sherman *et al*, 2017]. An approach using unmodified HA would add value to a 3D pancreatic cancer models by optimising HA conditions *in vitro*.

1.2.4 Patient-derived organoids

A model using patient-derived cancer cells and stromal cells, termed organoids, has become common-place in pancreatic cancer research as more and more papers published since 2014 have used this approach. Compared to animal models, organoids can potentially provide a more realistic model to recreate cellular composition and ECM components that are particularly relevant to the unique features of pancreatic cancer and the microenvironment of PDAC tumours observed in patients, with patient-derived tissue and rodent-derived ECM components being used by many research groups [Boj *et al*, 2015; Koikawa *et al*, 2018; Seino *et al*, 2018]. Immune cells can also incorporated into these models [Tsai *et al*, 2018]. Most studies still involved transplantation of organoids into mice to study the properties of cancer cells [Boj *et al*, 2015; Seino *et al*, 2018]. Moreover, patient-derived organoids have been utilized to test therapeutic anti-cancer agents. For example, drug response of gemcitabine and JAK inhibitors such as AZD1480 has been assessed by optical metabolic imaging in human PDAC organoids [Walsh *et al*, 2016]. Therapeutic profiling of 5-fluorouracil, oxaliplatin, nab-paclitaxel and irinotecan has also been analysed on 66 organoids and revealed interpatient variability in drug response [Tiriac *et al*, 2018].

Compared with animal models, patient-derived organoids can markedly reduce the cost of PDAC models and thus accelerate screening potential anti-cancer drugs using high-throughput assays, when evidence-based data showing that transplanting organoids in mice is unnecessary could be obtained. Thus, organoids provide a promising new tool to supplement traditional animal models. Heterogeneity between individual tumours, however, would need to be carefully stratified to identify effective treatments for distinct patient subgroups. Another issue is that animal-derived ECM factors provide additional variabilities between batches [Baker *et al*, 2016]. Reducing variations of these ECM factors by consistent, low-cost and standardized biomaterials would not only reduce the cost of these models but also make the PDAC models more realistic to human tumours.

Since mouse models and commercial matrices used in 3D cultures and organoids can be expensive, it would be beneficial to explore other alternatives to reduce their cost, especially in the context of

screening large databases of potential novel therapeutics in conditions that represent the PDAC tumour environment [Baker *et al*, 2016]. In 3D culture models and organoids of PDAC, rat tail collagen I and Matrigel® (mouse sarcoma-derived products) are used to recreate an ECM environment containing collagen I, collagen IV, fibronectin, and laminins that are present in the pancreatic cancer tumour microenvironment [Laklai *et al*, 2016; Ohlund *et al*, 2009]. A decellularized ECM preparation obtained from skeletal muscle, termed Myogel, can be prepared in large quantities in an inexpensive manner from a wide variety of animal sources. Myogel contains collagen I, collagen IV, laminins, and fibronectin, making it a promising scaffold element for tissue engineering [Abberton *et al*, 2008; Wolf *et al*, 2012] and supports the growth of many cell types, such as C2C12 myoblasts, human perivascular stem cells, NIH 3T3 fibroblasts, NIH 3T3-L1 cells, HMEC endothelial cells, primary muscle progenitor cells, primary aortic smooth muscle cells, and corneal epithelial cells [Abberton *et al*, 2008; DeQuach *et al*, 2012; Francis *et al*, 2009; Stern *et al*, 2009; Wolf *et al*, 2012]. Importantly, the biomechanical properties of ECM from skeletal muscle can mimic the tissue tension properties present in some tumour microenvironments [Abberton *et al*, 2008; Francis *et al*, 2009; Gillies *et al*, 2011a; Gillies *et al*, 2011b; Lin *et al*, 2014; Wolf *et al*, 2012].

Collagens in Myogel were reported to be between 27-72% of the total ECM extract [Abberton *et al*, 2008; Stern *et al*, 2009], allowing it to be compressed and manipulated to create different levels of external pressures. In particular, the content of collagens was 486.7 ± 133 μg per mg of the porcine skeletal muscle extract [Abberton *et al*, 2008], higher than the one (0.029 μg per mg) reported in porcine pancreas [Mirmalek-Sani *et al*, 2013]. The investigation of cell proliferation and cell migration using Myogel [Cheema *et al*, 2013; Nyga *et al*, 2013] could provide novel insights into using Myogel as a potential alternative matrix to culture pancreatic cancer cells and pancreatic stellate cells to mimic the PDAC tumour microenvironment.

1.3 Background of YAP signalling in cancer

Yes-associated protein (YAP, UniProt P46937) is a transcriptional coactivator that can translocate between the cytoplasm and the nucleus. YAP protein domains consist of several sites that interact with other proteins. As seen in Figure 9, the N-terminal region of YAP, the transcription enhancer activator domain (TEAD) binding domain, can bind to TEADs once YAP enters the nucleus to enhance cell proliferation. This translocation is dependent upon phosphorylation at specific serine residues. Phosphorylation of serine at position 61 (S61), S109, and S127 inhibits the binding to TEAD whilst promotes binding to 14-3-3 in the cytoplasm to cause cell growth arrest [Abylkassov *et al*, 2016]. WW domains in YAP interact with serine-threonine kinases known as LATS1/2 and MST1/2 (discussed below), which are an integral part of Hippo pathway and can phosphorylate YAP under dense cell-cell contact conditions [Abylkassov *et al*, 2016; Harvey *et al*, 2013]. The Src homology domain 3 (SH3) binding domain can interact with p53-binding protein-2, a member of the apoptosis stimulating proteins of p53 family regulating apoptosis [Espanel *et al*, 2001; Sullivan *et al*, 2007]. Near the C-terminal of YAP, there is a transactivation domain where S381, S384, tyrosine 391 (Y391), and Y407 can be phosphorylated. Phosphorylation at S397 is considered to induce YAP degradation by ubiquitin proteasome in the cytoplasm [Abylkassov *et al*, 2016]. The PDZ binding motif present in the YAP protein is also essential for transcription.

The expression and localisation of YAP is the key to YAP signalling, which functions to sense signals from external and internal changes in cells. These changes affect cell fate with regard to proliferation and functional properties related to mechanistic cues [Harvey *et al*, 2013].

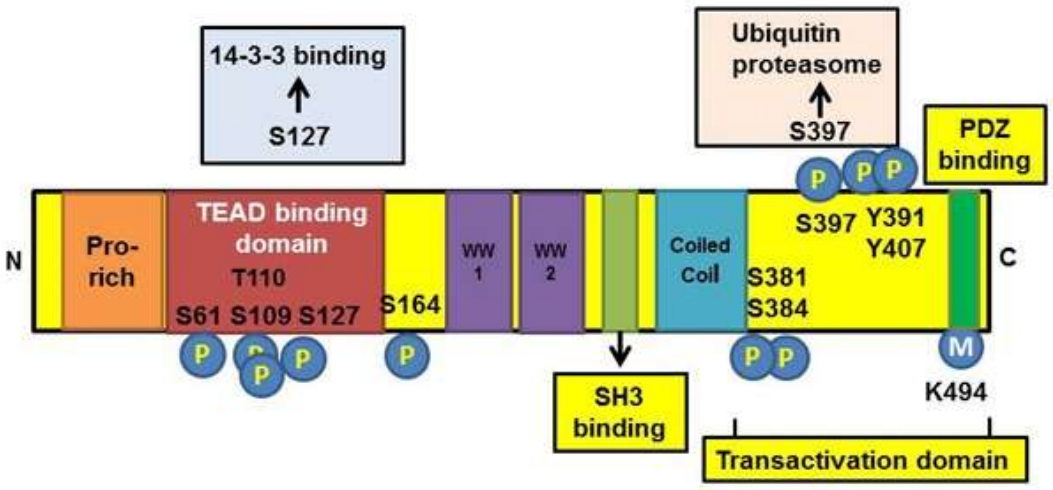

Figure 9. YAP protein domains.

The figure is from Abylkassov *et al* [Abylkassov *et al*, 2016], which is distributed under the terms and conditions of the Creative Commons Attribution (CC BY) license (http://creativecommons.org/licenses/by/4.0/). TEAD binding domain and transactivation domain can be phosphorylated, thus promoting binding to 14-3-3 and preventing YAP binding to TEAD. WW domains interact with serine-threonine kinases in Hippo pathways. The SH3 binding domain can interact with p53-binding protein-2.

As illustrated in Figure 10, YAP signalling exerts significant impact on tumour initiation, progression, metastasis, malignancy and drug resistance in a number of cancers. For instance, increased expression and nuclear accumulation of YAP in patients with lung cancer, breast cancer, colorectal cancer and liver cancer associate with cancer metastasis and poor prognosis [Zanconato *et al*, 2016b]. Reduced expression of YAP impairs cancer growth in mice transplanted with human cancer cell lines derived from lung cancer, colorectal cancer, liver cancer, prostate cancer, cervical cancer, melanoma, head and neck cancer, as well as osteosarcoma, suggesting that intervention of YAP signalling can control cancer progression [Zanconato *et al*, 2016b]. High level of YAP expression in the nucleus is correlated with treatment resistance in patients with colorectal cancer, esophageal cancer, and head and neck cancer [Zanconato *et al*, 2016b]. Studies of YAP in pancreatic cancer will be elaborated in the following sections.

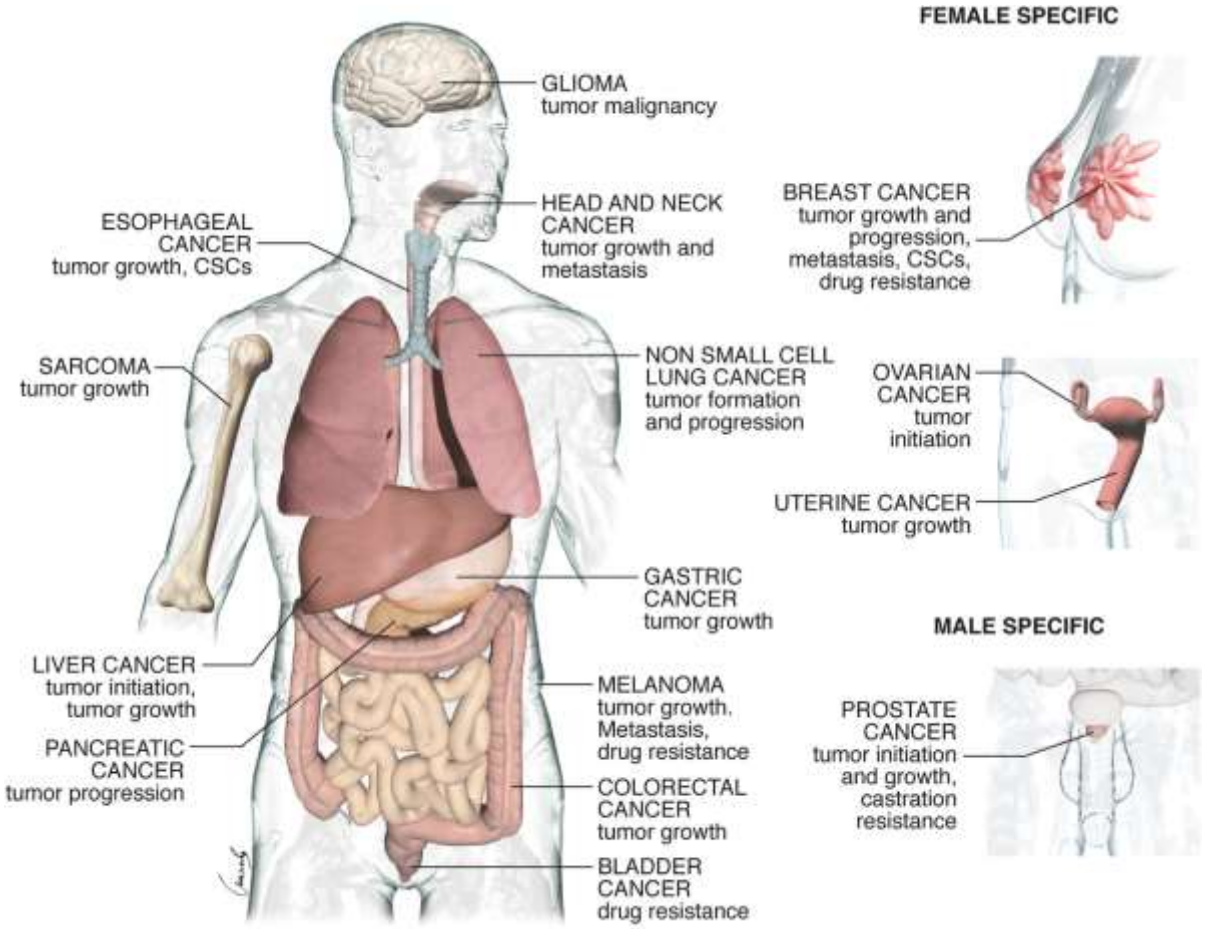

Figure 10. Role of YAP in different types of cancers.

The figure is adapted from Zanconato *et al* [Zanconato *et al*, 2016b] with copyright permission from Elsevier. Increased expression and nuclear accumulation of YAP in patients with lung cancer, breast cancer, colorectal cancer and liver cancer associate with cancer metastasis and poor prognosis. Reduced expression of YAP impairs cancer growth in lung cancer, colorectal cancer, liver cancer, prostate cancer, cervical cancer, melanoma, head and neck cancer, and osteosarcoma. High level of YAP expression in the nucleus is correlated with treatment resistance in patients with colorectal cancer, esophageal cancer, and head and neck cancer. CSCs: cancer stem cells.

1.3.1 Upstream regulation of YAP signalling

Complex signalling networks have been elucidated that involve mechanisms of YAP signalling in the context of cancer. As shown in Figure 11, cell junction/cell polarity, metabolic status, mechanical cues and G-protein-coupled receptors (GPCRs) are regarded to affect YAP subcellular localisation, and thus its function; their actions being capable of resulting phosphorylation or de-phosphorylation YAP to control the translocation of YAP between the cytoplasm and the nucleus. Phosphorylated YAP is sequestrated in the cytoplasm and is therefore unable to bind to TEADs in the nucleus to promote cell growth. Phosphorylation of YAP by the key kinases, Mammalian Sterile 20-like 1 and 2 kinases (MST1/2) and Large Tumour Suppressor 1 and 2 kinases (LATS1/2) in Hippo pathway, is regarded as an important mechanism to inhibit YAP nuclear entry [Yu *et al*, 2015]. However, researchers have proposed possible regulation of YAP by non-Hippo pathway in cancer because of two reasons: 1) mutations in LATS1/2 are not common in all types of cancers while nuclear accumulation of YAP are often detected in cancer tissue [Zanconato *et al*, 2016b] and 2) tense mechanical cues such as a stiff matrix for cells to grow on or stressed metabolic status do not always cause changes in YAP phosphorylation by LATS1/2 because YAP is still found to be in the cytoplasm despite effective depletion of LATS1/2 [Aragona *et al*, 2013; Dupont *et al*, 2011; Mo *et al*, 2015; Wang *et al*, 2015]. Since cell junction/cell polarity, metabolic status, mechanical cues and GPCRs are all also upstream regulators of LAST1/2 and MST1/2, focusing on how those pathways regulate YAP signalling can provide insights in dynamic localisation of YAP in cancer.

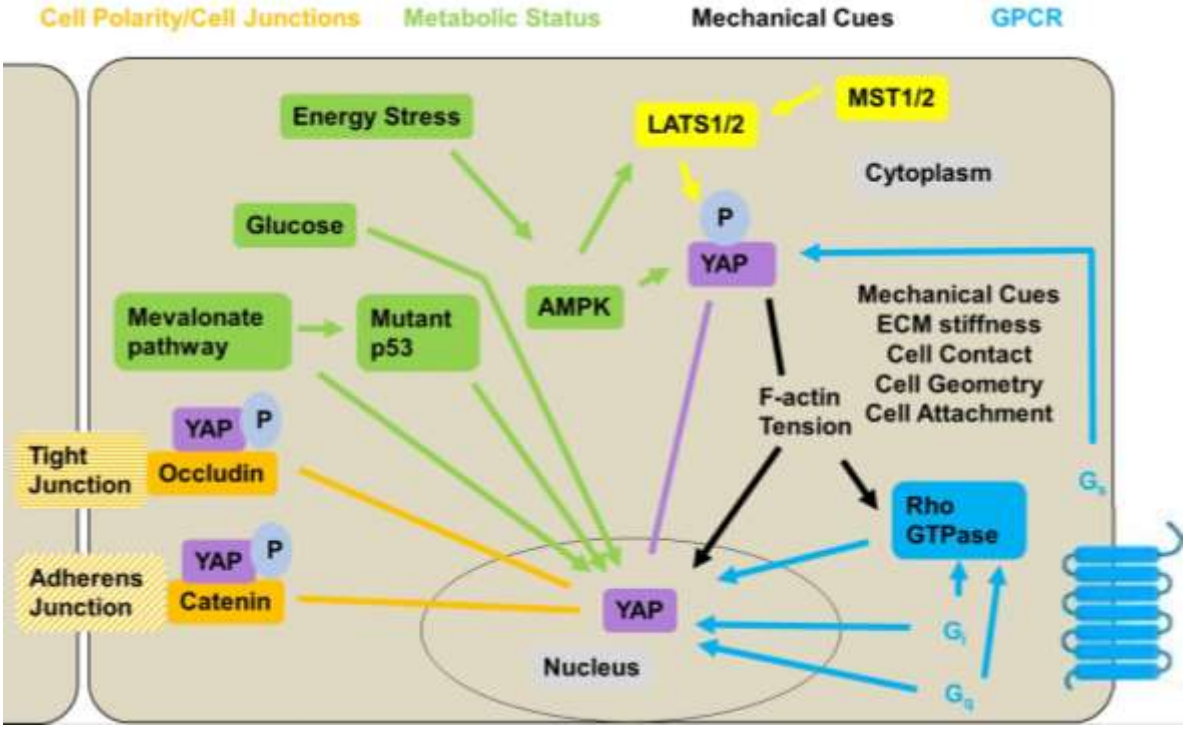

Figure 11. Upstream regulation of YAP signalling.

The figure is adapted from Yu *et al* [Yu *et al*, 2015] with copyright permission from Elsevier. The binding of catenin proteins at AJs and Ocln at TJs to YAP, activation of AMPK, LATS1/2 and G_s-coupled receptors can promote phosphorylation of YAP and retain YAP in the cytoplasm. Tension in the cytoplasm, activation of mevalonate pathway and Rho GTPase can induce nuclear accumulation of YAP. Line: inhibiting; arrow: promoting.

Cell junction/cell polarity involving adherens junction (AJ) and tight junction (TJ) structures plays a critical role in YAP signalling regulated by the Hippo pathway; events that can regulate cell growth [Gumbiner *et al*, 2014]. Recent studies have suggested localisation of YAP interactions may involve α-catenin proteins at AJs and occludin (Ocln) at TJs [Cravo *et al*, 2015; Schlegelmilch *et al*, 2011]. These interactions at AJs and TJs may function as sensors for external cell-cell and cell-matrix interactions that signal to the cell as a way to maintain a stable, differentiated format despite adjacent cell jostling and transient changes to its environment. At times when AJs and TJs are dismantled, such as during the process of wound repair, YAP no longer has these stabilized cell-cell and cell-matrix signalling complexes within the cell to bind and is now more accessible to de-phosphorylation that will lead to its increased movement to the nucleus as part of the epithelial to mesenchymal transition (EMT) mechanism to stimulate proliferation. Under normal conditions, once these cell-cell and cell-matrix interactions are re-established as the drive for proliferation subsides, YAP returns to competent AJ and TJ structures to once again position itself in a non-proliferative organization within the cell as it undergoes a mesenchymal to epithelial (MET) transformation. In the context of solid tumours, the EMT that occurs as part of this repair process does not reverse, i.e. there is no ensuing MET event.

Emerging evidence has suggested that the metabolic status in cells regulates YAP signalling by phosphorylating YAP and preventing nuclear translocation of YAP when cells are under energy stress. Indeed, reduced glucose levels in normal cells activates LATS1/2 in the Hippo pathway and the AMP-activated protein kinase (AMPK) independently from the Hippo pathway to cause cytoplasmic retention of YAP by phosphorylation [Mo *et al*, 2015; Wang *et al*, 2015]. Active glucose uptake and glycolysis is one of the key features of cancer cells. By analysing clinical biopsies, tumours with a high glycolytic gene expression signature have been shown to have high YAP nuclear expression [Enzo *et al*, 2015]. Blockage of glucose metabolism by small molecule glucose-mimics or 2-deoxy-glucose reverses YAP nuclear translocation in breast cancer cell lines [Enzo *et al*, 2015]. Moreover, activation of AMPK by anti-diabetic metformin induces YAP phosphorylation *in vitro* [Mo *et al*, 2015]. Another bit of interesting evidence is that statin molecules capable of inhibiting the mevalonate pathway that drives cholesterol biosynthesis can promote YAP cytoplasmic localization in cell lines derived from different solid cancer types [Sorrentino *et al*, 2014]. Such a finding correlates well with data showing that blunting the cholesterol synthetic pathway in gastric cancer cells can lead to induction of apoptosis [Goulitquer *et al*, 2018]. Notably, mutant p53, a prominent mutation in many epithelial-derived cancers, is found to be actively involved in the regulation of YAP by mevalonate pathway [Sorrentino *et al*, 2014]. In breast cancer cell lines grown in 2D, mutant p53 binds to YAP in the nucleus to enhance proliferation [Di Agostino *et al*, 2016] and depletion of mutant p53 reduces the production of enzymes critical to mevalonate pathway in cancer cells and the nuclear accumulation of YAP [Sorrentino *et al*, 2014].

Ligands that activate GPCRs have been widely studied to explore their effect on YAP signalling [Yu *et al*, 2015]. These results have suggested that stimulation of different subtypes of GPCRs can lead to either nuclear or cytoplasmic translocation of YAP. For instance, stimulation of $G_{12/13}$-coupled receptors by lysophosphatidic acid and sphingosine 1-phosphophate activates the Rho GTPase pathway to de-phosphorylate YAP and induce nuclear accumulation of YAP [Yu *et al*, 2012]. Also, activation of G_q-coupled receptors increases inositol triphosphate and activation of G_i-coupled receptors that inhibit adenylyl cyclase, both of which promoting nuclear localisation of YAP [Yu *et al*, 2012]. However, activation of G_s-coupled receptors by glucagon or epinephrine activates protein kinase A, causing phosphorylation and sequestration of YAP in the cytoplasm [Yu *et al*, 2012]. Dobutamine, a ligand to

G_q-, G_i- and G_s-coupled receptors, has been shown to inhibit YAP nuclear translocation in some but not all pancreatic cancer cell lines [Cravo *et al*, 2015]. The dominant effects regulating the YAP signalling after activation of different subtypes of GPCRs need further investigation.

Mechanical cues can modulate YAP signalling by re-organizing the F-actin/actomyosin that is associated with the cytoskeleton via the Hippo pathway and the Rho GTPase pathway. Using soft mechanical conditions as a cue where the Rho pathway is inhibited or F-actin is destroyed or the adhesive island area is reduced, YAP is still found to be in the cytoplasm despite the absence of LATS1/2 [Aragona *et al*, 2013; Dupont *et al*, 2011]. A stiff extracellular matrix (ECM) creates high tension, activates the integrin-focal adhesion-kinase-Src pathway and the Rho GTPase pathway, leading to the inhibition of YAP phosphorylation with or without the presence of LATS1/2 and subsequent nuclear YAP translocation [Aragona *et al*, 2013; Dupont *et al*, 2011]. Flattening the shape of a cell also increases stress fibre tension, F-actin contractility, and the opening of nuclear pores for YAP entry into the nucleus [Dobrokhotov *et al*, 2018]. Increased tension resulting from cell accumulation due to excessive proliferation rates is common in cancer and is associated with tumour progression [Butcher *et al*, 2009]. Interestingly, extracellular tension by high cell-cell contact frequency also acts on junction proteins such as catenins, resulting in the retention of YAP in the cytoplasm [Gumbiner *et al*, 2014]. Most of the studies on how mechanotransduction regulates YAP signalling, however, mainly focus on cells grown in 2D, which is unlike the native tumour architecture and microenvironment in patients where various cell types and factors are involved. The evolution of the cancer cell genotype and phenotype over time and the dynamic and complex nature of the tumour microenvironment would lead to various degrees of mechanical forces, possibly leading to a dynamic exchange of YAP nuclear and cytoplasmic accumulation over time.

1.3.2 Dual downstream effect of YAP signalling

Although YAP signalling is believed to induce cancer cell growth in solid tumours, it is considered to have tumour restraining function in haematological cancers [Cacemiro *et al*, 2017; Cottini *et al*, 2014]. For example, induction of YAP expression in leukaemia and myeloma cell lines reduced cell proliferation and promoted apoptosis [Cottini *et al*, 2014], as opposed to the suppression of cell growth resulting from the inhibition of YAP expression in solid tumours [Cravo *et al*, 2015; Diep *et al*, 2012]. In a transgenic mouse model with induced YAP expression in the haematopoietic system, YAP had no effect on the function of haematopoietic stem cells [Jansson *et al*, 2012]; however, up-regulation of YAP expression has been associated with tumorigenesis in many human solid tumours [Harvey *et al*, 2013]. One potential mechanism underlying the tumour-inhibitory effect of YAP in haematological cancers involves the binding of YAP to p73 [Cottini *et al*, 2014]. As a result, some researchers have suggested introduction of YAP expression in haematological cancer cells as a possible strategy for managing haematological cancers, contrary to what one might consider for a strategy to treat solid tumours [Cottini *et al*, 2014; Luk *et al*, 2014]. To our knowledge, there is no comprehensive report on the expression of TEADs in haematological cancers; if TEADs are expressed in haematological cancers, it would be necessary to investigate the effect of the interactions between YAP and transcription factors such as TEADs and p73 on the cell fate in haematological cancer cells. Therefore, efforts are required to fully understand the YAP signalling in human haematological cancers, such as the selective

binding of YAP to TEADs or p73, so as to prevent the undesired tumour-promoting activity in the strategies involving the upregulation of YAP expression in patients with haematological cancers.

Early studies identified the connective tissue growth factor (*CTGF*) gene as a target gene regulated by the binding of YAP to TEADs [Fan *et al*, 2013; Zhao *et al*, 2008]. Recently, YAP-upregulated gene signature in pancreatic cancer has been summarized as illustrated in Figure 12, including a gene encoding mitotic kinases (*AURKA*), a gene encoding cyclins (*CCND1*), a gene related to cell growth and division (*NOTCH2*) [Rozengurt *et al*, 2018]. Regulating the complex networks of gene expression by YAP can contribute to the tumour growth and tumour relapse in $Kras^{G12D}$-driven pancreatic cancer mouse models after oncogenic Kras extinction [Kapoor *et al*, 2014].

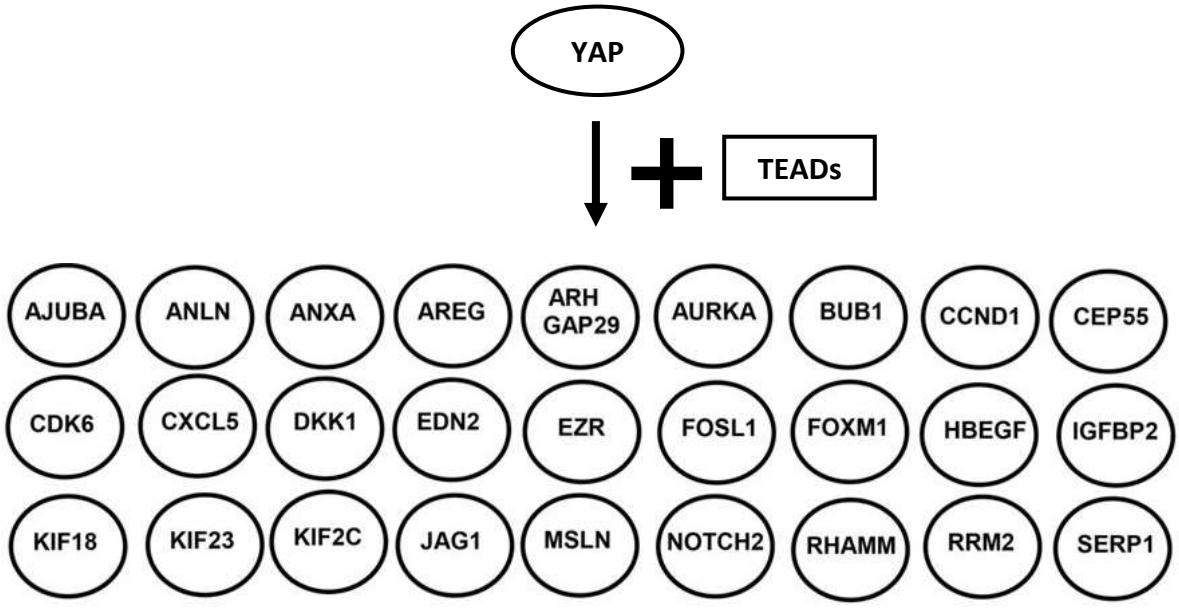

Figure 12. YAP-upregulated gene signature in pancreatic cancer.

The figure is adapted from Rozengurt *et al* [Rozengurt *et al*, 2018], which is distributed under the terms and conditions of the Creative Commons Attribution (CC BY) license (http://creativecommons.org/licenses/by/4.0/). The downstream effects of YAP signalling include activation of a gene encoding mitotic kinases (*AURKA*), a gene encoding cyclins (*CCND1*), a gene related to cell growth and division (*NOTCH2*) [Rozengurt *et al*, 2018].

1.3.3 Pharmacological intervention of YAP signalling in treating epithelial cancer

Intervention of YAP signalling to control solid cancer involves therapeutic approaches to regulate metabolic status, mechanical cues, GPCRs and YAP-TEADs binding. The current therapeutic methods are summarized in Figure 13 [Zanconato *et al*, 2016a]. Statins inhibit mevalonate pathway, Rho inhibitors reverse the stiff mechanical cue and block GPCR signalling, and verteporfin inhibits YAP-TEADs binding, preventing the YAP functioning as a proliferative driving force in cancer cells [Zanconato *et al*, 2016a]. In recent years, the capabilities of natural products to inhibit tumour growth by facilitating degradation of YAP are promising [Chen *et al*, 2018b]. The expression and localisation of YAP could potentially be a biomarker to evaluate the therapeutic outcomes. If a novel reagent decreases YAP expression or promotes YAP cytoplasmic localisation with high potency and low toxicity, it might

become a candidate in translational medicine. YAP is essential to survival in normal cells but there may be other mechanisms to compensate the loss of YAP function.

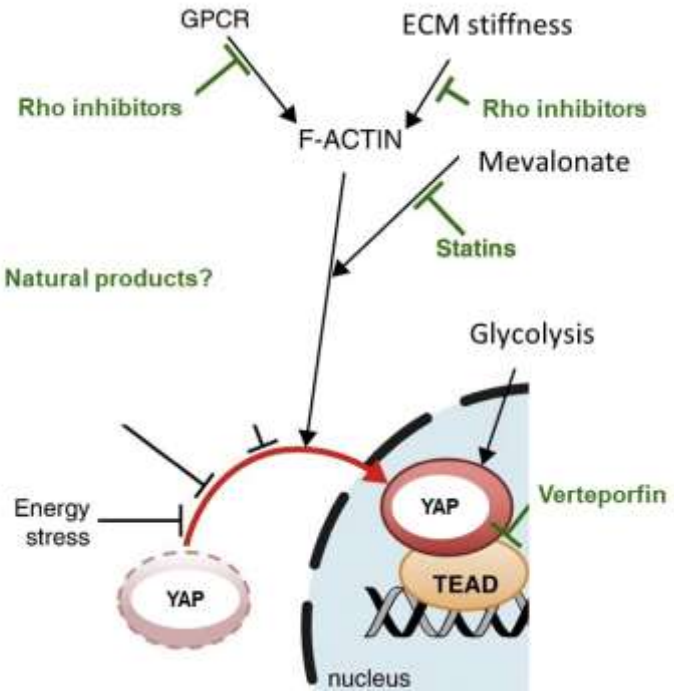

Figure 13. Agents of potential therapeutic usage affecting YAP signalling.

The figure is adapted from Zanconato *et al* [Zanconato *et al*, 2016a], indicating the strategies to inhibit nuclear accumulation of YAP and YAP-TEADs binding: Rho inhibitors reverse the stiff mechanical cue and block GPCR signalling [Zanconato *et al*, 2016a]. Statins inhibit mevalonate pathway [Zanconato *et al*, 2016a]. The natural products may facilitate degradation of YAP [Chen *et al*, 2018b]. Verteporfin inhibits YAP-TEADs binding [Zanconato *et al*, 2016a]. The article is distributed under the terms and conditions of the Creative Commons Attribution (CC BY) license (http://creativecommons.org/licenses/by/4.0/).

1.3.4 Crosstalk between dysfunctional cell signalling pathways and YAP signalling

As depicted in Figure 2, YAP signalling has been linked to dysregulated pathways involving EGFR, RAS, WNT/β-catenin, TGF- β/SMAD4, HH, and DNA damage response in various experimental models.

Overexpression of YAP is able to increase mRNA and protein level of EGFR in ovarian cancer cell lines and human ovarian cancer xenografts [He *et al*, 2015]. Although activation of mutant HRAS increases YAP levels and nuclear localization of YAP in U87MG glia cell lines transfected with mutant HRAS [Reddy *et al*, 2013], suppressing mutant KRAS is not able to reduce YAP expression in a fraction of cancer cells in $KRAS^{G12D}$-driven GEMMs of pancreatic cancer, leading to relapse by amplification of *YAP* gene in cancer cells [Kapoor *et al*, 2014]. By reducing *CTNNB1* (a gene encoding β-catenin) with RNA knockdown technique, decreased YAP mRNA levels is detected in colorectal cancer cells [Konsavage *et al*, 2012]. Meanwhile, the proliferation and survival of colorectal cancer cell lines transfected with β-catenin reported genes and harbouring mutations in Wnt/β-catenin pathway are dependent on YAP and the formation of β-catenin-YAP complex [Rosenbluh *et al*, 2012]. In a live cancer GEMMs, nuclear translocation of YAP is induced by TGF-β in tumorigenic liver cells, leading to increased SMAD2/3 activity which interacts with SMAD4 [Nishio *et al*, 2016]. Meanwhile, transfection of a mesothelioma cell line NCI-H290 with vectors carrying Smad2/3/4 and YAP is able to increase the transcription activity of *CTGF*, which is essential for cell proliferation and ECM production in mesothelioma [Fujii *et al*, 2012]. In osteosarcoma, high level of YAP is detected in tumour tissues from GEMMs with enhanced HH signalling and inhibiting HH signalling decreases YAP expression [Chan *et al*, 2014]. YAP signalling can also activate HH signalling when YAP translocate into the nucleus in a GEMM of skin cancer [Akladios

et al, 2017]. Amplification of *YAP* gene is found in mammary tumours from a breast cancer GEMM with deletion of *BRCA1* by knocking out the *BRCA1* gene [Overholtzer *et al*, 2006]. Our group has reported the YAP expression and localisation using AsPC-1 and HPAF-II cell lines cultured in 2D, where the tight junction protein Ocln induces YAP cytoplasmic localization to inhibit cell growth [Cravo *et al*, 2015]. Because PDAC cells are in an EMT state, loss of Ocln leads to the dissociation of a binding partner of YAP that can sequestered YAP in the cytoplasm, thus promoting nuclear translocation of YAP [Cravo *et al*, 2015].

Recently, YAP expression has shown to be correlated with myeloid-derived suppressor cells (MDSCs) and tumour-associated macrophages (TAMs) in *Kras:Trp53* mutant (KPC) mice and in patients with PDAC [Murakami *et al*, 2017]. Depletion of YAP in the pancreas of the mice resulted in less MDSCs and more major histocompatibility class II (MHCII) positive macrophages in the pancreas following pancreatitis, indicating that the YAP signalling plays a role in the immunosuppression in pancreatic cancer [Murakami *et al*, 2017]. The stiffness of matrix manipulated by collagen contraction affects the nuclear translocation of YAP in pancreatic cancer cell lines [Rice *et al*, 2017]. Fibronectin is considered to be more effective to induce nuclear accumulation of YAP in genetic modified non-tumorigenic epithelial cell line [Miroshnikova *et al*, 2017]. HA stimulates focal adhesion kinase (FAK), Ras GTPases, and modulates actin cytoskeleton as events that are associated with YAP signalling [Kultti *et al*, 2012]. However, there are only limited direct data on how laminins and HA affect YAP signalling in PDAC.

1.3.5 Treatments for PDAC by targeting YAP signalling

Surgery and chemoradiation are effective only in a small number of patients diagnosed with PDAC [Neoptolemos *et al*, 2018]. The treatment algorithm for patients with all stages of pancreatic cancer mostly consists of 5-fluorouracil and gemcitabine [Neoptolemos *et al*, 2018]. However, relapse and drug resistance are still common and the overall survival remains low. The pivotal reason for this low level of long-term survival rate is the desmoplastic and hypo-vascular microenvironment of pancreatic cancer, which limits access to the tumour by diagnostic methods and therapeutic strategies.

Destroying the stroma in PDAC is one approach to overcome the obstacle(s) established by this acellular components for therapeutic strategies to reach and eradicate the PDAC cells. Although targeting hyaluronic acid using hyaluronidase combined with gemcitabine and nab-paclitaxel has elicited high response rate in phase I/II trials and has moved into phase III testing [Doherty *et al*, 2018], efforts to destroy the pancreatic stroma with therapeutic agents such as matrix metalloproteinases inhibitor Marimastat [Bramhall *et al*, 2001; Bramhall *et al*, 2002; Moore *et al*, 2003] and SHH pathway inhibitor Vismodegib [Kim *et al*, 2014] have failed to improve the survival rates in other clinical trials. Furthermore, efforts to induce stromal depletion by genetic modification in mouse models lead to acceleration of pancreatic cancer tumour growth [Ozdemir *et al*, 2014; Rhim *et al*, 2014] and patients with reduced numbers of PSCs suffered worse survival [Ozdemir *et al*, 2014], raising the possibility that at least some of the PSCs around pancreatic cancer cells may suppress cancer cell growth. Cautions in targeting tumour stroma in PDAC have been raised and more prudent experimental designs to eradicate tumour-promoting PSCs from tumour-suppressive PSCs in PDAC are required. It has been postulated that a subset of pancreatic cancer cells can regulate tissue tension to activate tumour-promoting genes after the loss of pancreatic stellate cells [Laklai *et al*, 2016], linking to YAP signalling.

As summarized in Table 1, outcomes of regulating YAP signalling in PDAC have been reported *in vitro* and *in vivo*. YAP expression has been shown to be responsible for chemo-resistance of gemcitabine in pancreatic cancer cells [Yuan *et al*, 2016], raising the possibility of combining gemcitabine with targeted therapy that can reduce YAP expression to augment therapeutic efficacy. Inhibition of YAP signalling using verteporfin and RAF signalling blockage reduces cell proliferation in 2D models [Zhao *et al*, 2017]. Effects of targeting YAP signalling have been assessed in mice models [Jiang *et al*, 2018]. Reduced YAP expression by YAP knockdown and verteporfin treatment in xenografts and GEMMs can inhibit tumour growth [Jiang *et al*, 2018; Wei *et al*, 2017; Zhao *et al*, 2017]. Depletion of YAP in the pancreas of mice has resulted in less MDSCs and more MHCII positive macrophages in the pancreas following pancreatitis, indicating the YAP signalling plays a role in the immunosuppression of pancreatic cancer [Murakami *et al*, 2017]. Combining YAP-depleting strategies or inhibiting YAP-TEADs interaction with verteporfin can sensitize the treatments against RAF kinases, one of the downstream pathway effectors of *KRAS* mutation, in pancreatic cancer cells and xenografts [Wei *et al*, 2017; Zhao *et al*, 2017]. Targeting GPCRs using dobutamine [Cravo *et al*, 2015], a widely used medicine in the clinic to assess cardiac function, can also considered as an approach to target YAP signalling if a pharmacological profile could be established for sustaining its actions on nuclear exclusion of YAP. Inhibiting the mevalonate pathway using statins and activating AMPK using metformin has shown to reduce YAP nuclear localization *in vivo* and *in vitro* [Mo *et al*, 2015] . Due to the extensive use of metformin in diabetic patient populations, epidemiological studies to examine favourable outcomes in PDAC might be warranted. Although around 74% of pancreatic cancer cells harbour a *TP53* mutation [Waddell *et al*, 2015], it is currently unclear if targeting *TP53* mutations that affect YAP function would be a feasible

therapeutic approach. Natural products have shown anti-tumour activity in epidemiological studies of PDAC [Boreddy *et al*, 2013]. Irinotecan and paclitaxel have been used in as parts of combinatory treatments for PDAC [Neoptolemos *et al*, 2018]. Tylophorinine and tylophorine are two interesting natural products that have drawn medicinal chemists' attention on biosynthesis and extraction [Gantait *et al*, 2017; Govindachari *et al*, 1965]. A tylophorine analogue, DCB-3503, can inhibit pancreatic cancer cell growth by targeting the abnormal cell-cycle signalling in PANC-1 and HPAC pancreatic cancer cell lines, providing a promising new compound to be tested in PDAC [Shiah *et al*, 2006]. The effects of tylophorinine on YAP signalling and PDAC growth remain to be determined.

Table 2. Outcomes of regulating YAP signalling in PDAC.

Genetic deletion and/or pharmacological inhibition of YAP	PDAC Model	Major outcomes	Ref
Deletion of YAP	2D BxPC-3 and PANC-1	Inhibition of cell proliferation	[Diep *et al*, 2012]
	KPC and KPYC GEMMs*	Tissue regeneration	[Murakami *et al*, 2017]
		Reactivation of T cells	
		Promotion of apoptosis in neoplastic ducts	
		Increased infiltration of MHCII+ macrophages	
		Reduction of MDSCs and MDSC-polarizing cytokines	
Deletion of YAP with pan-RAF inhibitor	2D AsPC1 and PANC-1	Suppression of PDAC cell proliferation and clonogenic ability	[Zhao *et al*, 2017]
		Sensitisation to the pan-RAF inhibitor	
Deletion of YAP and gemcitabine	2D PANC-1	Sensitisation to gemcitabine	[Yuan *et al*, 2016]
Verteporfin	2D PANC-1 and SW1990 cells	Inhibition of migration, cell proliferation and cell cycle progression	[Wei *et al*, 2017]
		Induction of cell apoptosis	
	SW1990 xenografts	Suppression of tumour growth	[Wei *et al*, 2017]
		Reduction of angiogenesis markers	
Verteporfin with pan-RAF inhibitor	2D AsPC1 and AsPC1 xenografts	Sensitisation to the pan-RAF inhibitor	[Zhao *et al*, 2017]
Dobutamine	2D HPAFII and AsPc1	Inhibition of cell proliferation	[Cravo *et al*, 2015]

*: *p48-Cre (*Cre*), Yap$^{flox/flox}$;p48-Cre* (Yap^{KO}), *LSL-Kras^{G12V};LSL-p53^{R172H};p48-Cre* (KPC) and *LSL-Kras^{G12V};LSL-p53^{R172H};Yap$^{flox/flox}$;p48-Cre* (KPYC) mice.

1.4 Aims and objectives

Little progress has been made in improving the overall survival of pancreatic cancer because the desmoplastic and hypo-vascular microenvironment of this cancer limits access to therapeutic strategies. Stellate cells, comprising the majority of stroma and secreting large amount of extracellular matrix (ECM), have been suggested to provide a supportive environment for pancreatic cancer whilst playing a suppressive role in cancer growth. 2D culture models and animal models have been useful to study pancreatic cancer biology; however, they fail to represent the highly fibrotic properties in human pancreatic cancer microenvironment in late-stage of PDAC development. In order to identify strategies capable of modulating pancreatic cancer stroma without promoting cancer growth, it is imperative to establish an *in vitro* 3D cancer model resembling the human cancer microenvironment. YAP has been shown to position itself as an integral part in the crosstalk between various cell signalling pathways to promote cancer growth in solid tumour [Rozengurt *et al*, 2018; Zhang *et al*, 2015]. Due to effects of the mechanical cues on YAP signalling, a realistic human PDAC model is required to recapitulate YAP signalling in the spatial manner.

The aim of the project is to establish an *in vitro* 3D human cancer model with human pancreatic cancer cell lines, ECM-like materials, and human stellate cells to recreate the highly fibrotic human PDAC microenvironment in the liver and pancreas suitable for high-throughput assay and delineating YAP signalling in pancreatic cancer.

The objectives are:

1. To optimise the protocol for 3D co-cultures of human pancreatic cancer cell lines, ECM-like materials, and human stellate cells.

2. To evaluate Myogel and unmodified hyaluronic acid as culture matrix elements for modelling pancreatic cancer.

3. To study expression and subcellular localisation of endogenous YAP and the interactions of YAP, TEADs, and Ocln in 3D human pancreatic cancer models.

4. To investigate the effects of natural products, Pseudopterosin A-D and Tylophorinine, on 3D human pancreatic cancer models to test their potential for treating pancreatic cancer.

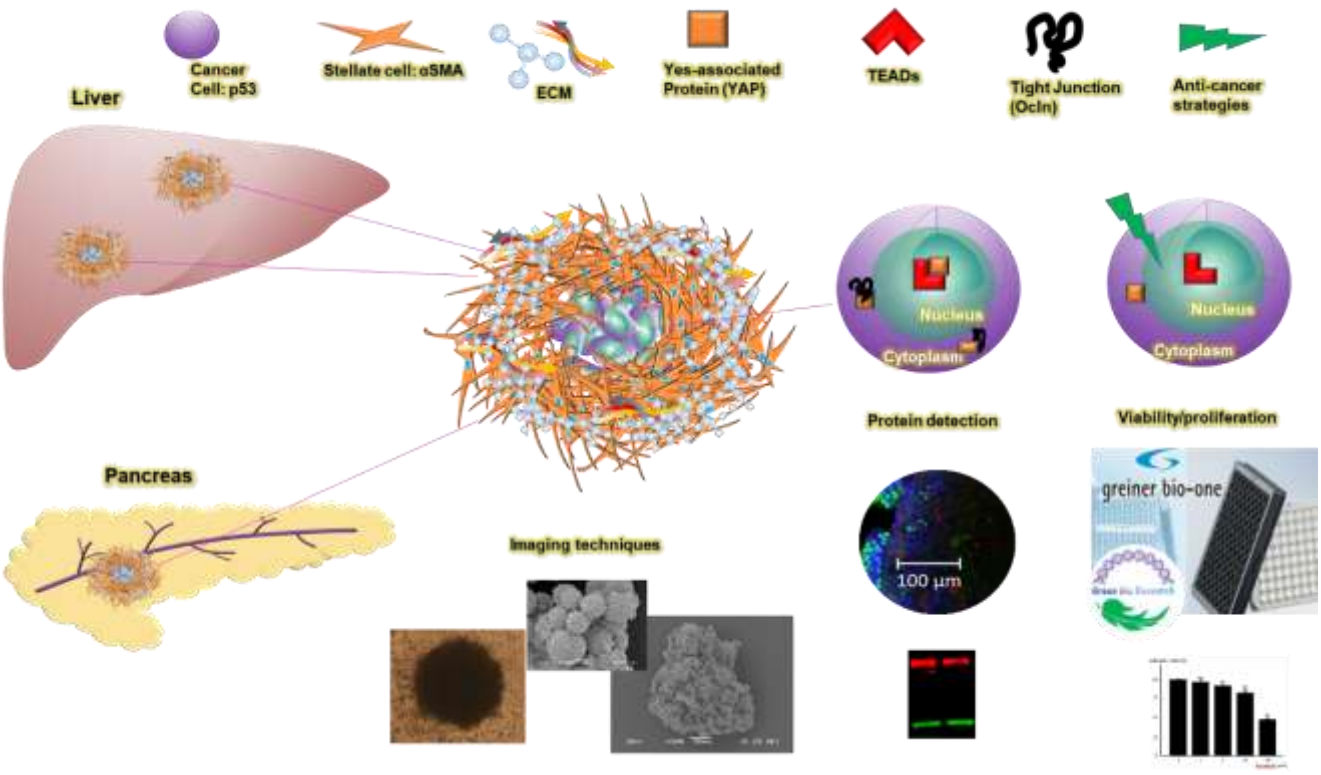

Figure 14. Diagram of aims and objectives.

In order to recreate human PDAC microenvironment to study YAP signalling and screen anti-cancer agents, an *in vitro* 3D human pancreatic cancer model with human pancreatic cancer cell lines, ECM-like materials, and human stellate cells will be established to mimic the human PDAC microenvironment in the liver and pancreas suitable for high-throughput assay.

Chapter 2. Materials and Methods

2.1 2D cell culture

Human pancreatic cancer cell lines Capan-2 and PANC-1 were obtained from the American Type Culture Collection (Manassas, VA). Cells were maintained in DMEM cell culture medium with high-glucose (4 g/L) (Gibco™, Cat. # 41965-039) supplemented with 10% foetal bovine serum (FBS, Gibco™, Cat. # 10500064), and 100 U/mL penicillin combined with 100 mg/mL streptomycin (P/S, Sigma-Aldrich Chemical Co., Cat. # P4333).

Patient-derived hepatic and pancreatic stellate cells were generous gifts from Dr Erkan at KOÇ University hospital, Turkey. Ethical approval was obtained from Ethics Committee for Biomedical Sciences of KOÇ University. Stellate cells were maintained in DMEM/F12 cell culture medium containing DMEM with low-glucose (1 g/L) (Gibco™, Cat. # 22320022) and Ham's F-12 Nutrient Mix (Gibco™, Cat. # 21765029) at 1:1 (volume/volume) supplemented with 20% FBS and P/S as described [Jiang *et al*, 2009; Zhang *et al*, 2007] .

All cells were routinely cultivated in a humidified incubator with 5% CO_2 at 37 °C.

2.2 3D cell culture

2.2.1 Preparation of polyHEMA low-attachment plates

PolyHEMA low-attachment plates were prepared as described previously [Phung *et al*, 2011]. A 120 mg/mL stock solution of poly-HEMA (Sigma-Aldrich Chemical Co., Cat. # P3932) was prepared in 95% ethanol (VWR, Cat. # 20821.330) and incubated while stirring with a magnetic bar at room temperature (15-20°C) overnight. To make a working solution of poly-HEMA, 1 mL of poly-HEMA stock solution was pipetted into 23 mL of 95% ethanol to obtain a final concentration of 5 mg/mL. The fresh working solution was prepared every time new plates were made. 50-60 µL of poly-HEMA working solution was pipetted into each well of a 96-well U-bottomed plate (Nunc™, Cat. # 163320). The ethanol was evaporated at 37 °C for 72-96 hours under humid-free conditions. Before use, plates were sterilized in the hood with lids off using UV light for 40-60 minutes. Sterilised plates were sealed with Parafilm and stored at room temperature.

2.2.2 Co-culture of cancer cells and stellate cells in scaffold-free conditions

Stellate cells and cancer cells were grown to reach 60-90% confluence, trypsinized using 0.25% trypsin (Gibco™, Cat. # 15090046, volume/volume) with 0.02% ethylenediaminetetraacetic acid (EDTA, Sigma, Cat. # E9884, weight/volume) diluted in phosphate buffered saline (PBS, Oxoid, Cat. # BR0014G) at 37 °C, 1 minute for PANC-1 cells and 5 minutes for stellate cells and Capan-2 cells. Cells were isolated into single cell suspensions and were then mixed to achieve the final cell mixtures in each hanging drop composed of 0, 5,000, 10,000, 20,000 or 40,000 stellate cells with either 0 or 500 cancer cells, respectively. Cell suspensions were centrifuged and resulting pellets were suspended in DMEM/F12

with 10% FBS and P/S in final volumes of 20 µL or 40 µL in each drop at the stellate cells to cancer cells ratios of 0, 10:1, 20:1, 40:1 or 80:1. 20 µL of each cell mixture was pipetted manually as single droplets on the upside-down lid of the 100 mm cell culture dish (Falcon™, Cat. # 353003) and the lid with 20-40 droplets was handled carefully to cover the dish containing 6 mL PBS or DMEM/F12 with P/S. In some experiments, 40 µL were pipetted into GravityPLUS™ HangingDrop plates (InSphero, Cat. # ISP-06-001). Suspended cell mixtures were cultivated in a humidified incubator with 5% CO_2 at 37 °C.

After 4 days in hanging drop culture, the spheroids that formed were transferred individually one-by one spheroid using large bore (cut) pipette tips to a polyHEMA plate well containing 100 µL fresh medium each well. In some experiments, ~200 µL of air was added through the inlet of the GravityPLUS™ Plate wells to push the spheroid to the polyHEMA plates. Spheroids were cultured in polyHEMA plates for 3 days without changing the medium.

2.2.3 Preparation of Myogel

Porcine skeletal muscle (PSM) was decellularized as previously described [Abberton *et al*, 2008]. The quadriceps and hamstring PSM was purchased from Waitrose without trace the strain of the pigs. Samples of PSM were weighed, aliquoted and stored in -20°C as ~30g per bag. PSM (~30g) was defrosted at room temperature and homogenised with 90 mL ice-cold 3.4 M sodium chloride (Sigma, Cat. # S9625), containing 0.5 mM phenylmethylsulfonyl fluoride (PMSF, Sigma, Cat. # P7626), 2 mM EDTA, 0.1 M 6-aminocaproic acid (EACA, Sigma, Cat. # a2504), and 2 mM N-ethylmaleimide (Sigma, Cat. # e3876), using a Kenwood Hand Blender HB722A. After homogenisation, samples were centrifuged at 1780 x g for 5 minutes, and the supernatant was discarded. Pellets were then homogenised again with fresh 90 mL ice-cold 3.4 M sodium chloride buffer containing 0.5 mM PMSF, 2 mM EDTA, 0.1 M EACA, and 2 mM N-ethylmaleimide and then centrifuged to collect the pellets. After the third homogenisation and centrifugation, the pellets were treated with 30 mL 2 M urea (Sigma, Cat. # u1250) in Tris Buffered Saline (TBS) with 0.05 M Tris base (Sigma, Cat. # T6066) with 0.15 M sodium chloride, overnight at 4 °C. The extraction in urea was centrifuged at 10,000 x g for 30 minutes and the supernatant was stored at 4 °C. Pellets were suspended in 30 mL 2 M urea/TBS and left overnight at 4 °C. The second urea extraction was centrifuged at 10,000 x g for 30 minutes and the supernatant was stored at 4 °C. The combined supernatants (~90 mL) were dialysed in SnakeSkin™ Dialysis Tubing 3.5K MWCO (Thermo Scientific™, Cat. # 68035) or 10K MWCO (Thermo Scientific™, Cat. # 68100) against 0.5% v/v chloroform (Sigma, Cat. # 288306) in 1.5 L TBS at 4 °C for approximately 20 hours. After dialysis in 0.5% chloroform, the dialysate was changed to fresh 1.8 L TBS approximately every 12 hour for two days. After dialysis in TBS, the dialysate was changed to DMEM/F12 with P/S. After overnight dialysis, the resulting solution, Myogel, was stored at 4 °C and -20°C.

The BCA Protein Assay (Thermo Scientific™ Pierce™, Cat. # 23227) was used to determine the total protein concentration of Myogel preparations. Bovine serum albumin (BSA) standards (125-2,000 µg/mL) were prepared from BSA ampoule provided with the protein assay kits. The working detection reagent was prepared by mixing 50 parts of BCA Reagent A with 1 part of BCA Reagent B. 20 µL of a Myogel preparation (1:10 or 1:20 dilution in DMEM/F12) and standards, run as duplicates, were pipetted into a 96-well flat-bottom plate (Thermo Scientific™ Nunc™, Cat. # 167008) and then 200 µL working reagent was added to each well. Plates were incubated at 37°C for 30 minutes and measured for absorbance at 562nm using FLUOstar Omega spectrometer. The average of 562 nm absorbance

measurement for blank replicates (DMEM/F12) was subtracted from the 562 nm measurements of all BSA standard and unknown sample replicates. A standard curve for the BSA standards was prepared by plotting the average blank-corrected 562nm measurement vs. its concentration in µg/mL. This standard curve was used to determine the Myogel protein concentrations.

2.2.4 Mono-culture of cancer cells or cancer spheroids in Myogel

Initially, Myogel was mixed with 5 M NaOH (Fisher Chemical, Cat. # S/4920/53) to result in a pH of the preparation of 8 which was higher than the isoelectric points of collagen I, collagen IV, laminin, and fibronectin to reduce viscosity [Uquillas *et al*, 2012] and the chance of contamination. 30 µL of the resulting mixture was pipetted per well into polyHEMA plates. After the plates were incubated at 37 °C overnight, 70 µL of PANC-1 cells suspensions containing 2,000 cells in DMEM/F12 with 10% FBS and P/S was pipetted into each well and the plates were incubated for 10 days arbitrarily at 37 °C under standard cell culture conditions.

In order to test the feasibility of using Myogel directly after dialysis without increasing the pH, Capan-2 and PANC-1 grown in flasks as 2D was trypsinized. After centrifugation, cell pellets were suspended in FBS. 1 volume of FBS with cells were mixed with 9 volumes of Myogel and seeded at 100 µL per well into 96-well F-bottom µCLEAR® black plates (Greiner, Cat. # 655986) and cultured for 4 days. Myogel without cells was used as a control to test the contamination.

Capan-2 and PANC-1 spheroids were formed from 500 cells per 40 µL DMEM/F12 with 10% FBS and P/S using hanging-drop method. On day 4 of incubation, spheroids were transferred into 96-well F-bottom µCLEAR® black plates coated with 70 µL Myogel in 10% FBS per well, with one spheroid per well, and incubated at 37 °C for 4 days.

2.2.5 Preparation of hyaluronic acid

As previously reported in the product specification [Madihally *et al*, 1999], 200 mg hyaluronic acid (HA) sodium salt from *Streptococcus equi* (SIGMA, Cat. # 53747) was weighed and 20 mL PBS was added to make the 10 mg/mL HA stock solution. HA stock solution were autoclaved according to the reference [Madihally *et al*, 1999] stated on the manufacturer's website and stored at 4°C until use.

2.2.6 Mono-culture of cancer spheroids in hyaluronic acid

On day 0, 500 cells per 40 µL DMEM/F12 with 10% FBS and P/S of Capan-2 and PANC-1 cell suspension was delivered into each well of GravityPLUS™ HangingDrop plates as 3D culture.

On day 4, 10 mg/mL HA stocking solution was diluted using DMEM/F12 with P/S. 70 µL of 0, 1, 3, 5 µg/µL HA in DMEM/F12 with P/S was pipetted into each well of the polyHEMA plate. FBS was adjusted to achieve the final concentration of 10% FBS in each well. ~200 µL of air was added to the 3D culture through the inlet of the GravityPLUS™ Plate wells to let one cancer spheroid drop into one well of low-

attachment polyHEMA plates containing HA. Wells with the same volume of PBS (the solvent used to dissolve hyaluronic acid) as the ones in the highest concentration of hyaluronic acid (5 mg/mL) served as controls to observe spheroids grown in an environment with less nutrients than the ones grown in standard culture medium.

2.2.7 Co-culture of cancer spheroids and stellate cells in hyaluronic acid

On day 0, 500 cells per 40 µL DMEM/F12 with 10% FBS and P/S of Capan-2 and PANC-1 cell suspension was delivered into each well of GravityPLUS™ HangingDrop Plate as 3D culture.

On day 4, 10 mg/mL HA stock solution was diluted using DMEM/F12 with P/S. 70 µL of 0 or 20,000 stellate cells in DMEM/F12 with P/S and 0, 1, 3, 5 mg/mL HA was pipetted into each well of the polyHEMA plate. FBS was adjusted to achieve the final concentration of 10% FBS in each well. ~200 µL of air was added to the 3D culture through the inlet of the GravityPLUS™ Plate wells to let one cancer spheroid drop into one well of low-attachment polyHEMA plates containing HA with or without stellate cell suspension. Wells with HA and stellate cell suspension were used as control. The plates were incubated for 3-8 days.

2.2.8 Co-culture of cancer spheroids and stellate cells in hyaluronic acid and collagen I

On day 0, 500 cells per 40 µL DMEM/F12 with 10% FBS and P/S of Capan-2 and PANC-1 cell suspension was delivered into each well of GravityPLUS™ HangingDrop Plate as 3D culture.

On day 4, 10 mg/mL HA stock solution was diluted using DMEM/F12 with P/S. 70 µL of 0 or 20,000 stellate cells in DMEM/F12 with P/S, 5 mg/mL HA and 0.3 mg/mL rat tail collagen I (Gibco™, Cat. # A1048301) was pipetted into each well of the polyHEMA plate. FBS was adjusted to achieve the final concentration of 10% FBS in each well. ~200 µL of air was added to the 3D culture through the inlet of the GravityPLUS™ HangingDrop Plate wells to let one cancer spheroid drop into one well of low-attachment polyHEMA plates containing HA and collagen I. The plates were incubated for 3 days.

2.2.9 Co-culture of cancer cells and stellate cells in collagen I

Stellate cells and cancer cells were grown to reach 60-90% confluence. Cells were trypsinized and lifted using 0.25% trypsin with 0.02% EDTA at 37 °C, with the process being halted by the addition medium composed of DMEM/F12 + 10% FBS + P/S. Cell count in the collected cell preparations was determined using a glass haemocytometer. Mixtures of stellate cells and cancer cells were prepared at a 2:1 ratio to produce a final cell suspension of 1,000 stellate cells and 500 cancer cells per 50 µL (20,000 cells/mL stellate cells and 10,000 cells/mL cancer cells), in each well of a 96-well plate. Tubes with stellate cells and cancer cells mixture were centrifuged at 125 g for 5 minutes and the supernatant was aspirated to discard trypsin. Cell pellets were suspended in medium DMEM/F12 + 10% FBS + P/S with the volume matching the cell suspension of 20,000 cells/mL stellate cells and 10,000 cells/mL cancer cells. Collagen

I was added to reach the final concentration of 0.1 mg/mL and mixed well. 50 µL cell-collagen mixture was pipetted into each well of 96-well polyHEMA plates. 50 µL fresh medium DMEM/F12 + 10% FBS + P/S was added next day.

2.2.10 Co-culture of cancer cells and stellate cells in collagen I and hyaluronic acid

10 mg/mL HA in PBS was sterilized by autoclaving and stored at 4°C until use. 7 mg/mL HA was diluted using DMEM/F12 + P/S. Stellate cells and cancer cells were grown to reach 60-90% confluence. Cells were trypsinized and lifted using 0.25% trypsin with 0.02% EDTA at 37 °C, with the process being halted by the addition of medium composed of DMEM/F12 + 10% FBS + P/S. Cell count in the collected cell preparations was determined using a glass haemocytometer. Mixtures of stellate cells and cancer cells were prepared at a 2:1 ratio to produce a final cell suspension of 1,000 stellate cells and 500 cancer cells per 50 µL (20,000 cells/mL stellate cells and 10,000 cells/mL cancer cells), in each well of a 96-well plate. Tubes with stellate cells and cancer cells mixture were centrifuged at 125 g for 5 minutes and the supernatant was aspirated to discard trypsin. Cell pellets were suspended in medium DMEM/F12 + 10% FBS + P/S with half of the final total volume matching the cell suspension of 20,000 cells/mL stellate cells and 10,000 cells/mL cancer cells. The same volume as half of the final total volume of 7 mg/mL HA in previous step was added to reach the final concentration of 3.5 mg/mL HA with gentle mixing. Collagen I was added to reach the final concentration of 0.3, 0.1, 0.05, 0.03 mg/mL with gentle mixing. 50 µL cell/collagen/HA mixture was pipetted into each well of 96-well polyHEMA plates. 50 µL fresh medium DMEM/F12 + 10% FBS + P/S was added next day.

2.3 Spheroid size measurement

Phase-contrast images were acquired using Leica DMI4000 B (50x magnification) and 4-18 spheroids per group were captured on day 4, day 5, day 6 and day 7 after initiation of cell culture. Spheroid size was determined by CellProfiler software (version 3.0.0). The workflow for spheroid size measurement was as follows:

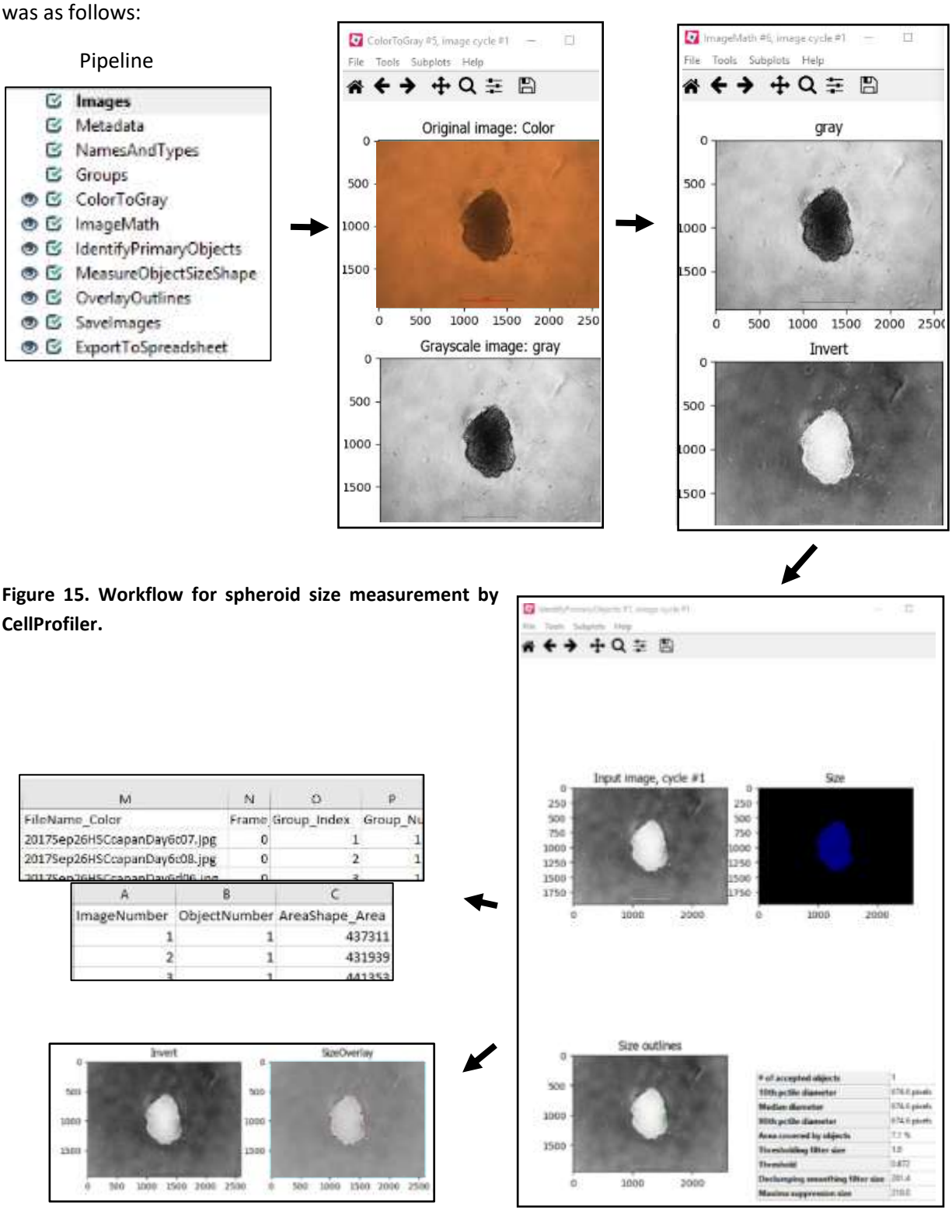

Figure 15. Workflow for spheroid size measurement by CellProfiler.

Coloured images were imported and converted to greyscale images by the module 'ColorToGray'. Black colour in greyscale images resulting from the conversion were inverted to white colour by 'ImageMath' so that the black region where one spheroid located could become white in order to be recognized and measured by the image processing software. The white region indicating the whole spheroid was identified as the object by the module 'IdentifyPrimaryObjects', setting mostly 300–1700 pixels as the diameter to be identified so that the pipeline was versatile for measuring small spheroids (diameters of 350 pixels in average) containing stellate cells and large spheroids (diameters of 1400 pixels in average) containing PANC-1 cells. Objects outside the diameter range and touching the border of the image were discarded in order to reduce the false measurement of the background noise which led to long processing time and inaccurate identification of spheroids. Threshholding strategies were optimized to identify the objects, balancing the accuracy and efficiency. 'Global', 'Otsu' and 'Three classes' options were selected as the thresholding. The pixels in the middle intensity class were assigned to the background. The threshold smoothing scale was 1.3488 and the correction factor was 1.0, with threshold range from 0.0 as lower bound and 1.0 as upper bound. 'Intensity' was selected as the method to distinguish clumped objects and draw dividing lines between clumped objects. The size of the smoothing filter for declumping and minimum allowed distance between local maxima were automatically calculated.

The pipeline in counting large spheroids in HA and collagen I touching the borders of the images in the section 5.5.1 was modified because the areas where the spheroids were present exceed the limit of the field of view that the microscope could capture. In the module 'IdentifyPrimaryObjects', 300–3000 pixels were set as the diameter to be identified. Objects outside the diameter range and touching the border of the image were retained. The pixels in the middle intensity class were assigned to the foreground due to a light appearance of the spheroids.

The number of pixels in the region indicating the area of the spheroid in each image was extracted by the module 'MeasureObjectSizeShape' while the area of the spheroid was outlined by the module 'OverlayOutlines'. A new image was generated by the module 'SaveImages' for manual verification. All the images imported to the pipeline and exported as new images with overlay spheroids were inspected by one operator to ensure the correct area of spheroids on each image. Images showing false identification of areas of spheroids such as including excess background to the identified area of the actual spheroid were deleted from the final calculation. Areas of spheroids that were segmented into different objects were added together to count the final area.

The measurements in pixel were exported by the module 'ExportToSpreadsheet'. The mean of the values in the column 'AreaShape_Area' in each experiment group was calculated by Excel to be used as Area in the following formula. Normalisation of spheroid size was calculated by the following formula:

$$\text{Percentage of spheroid size} = \frac{100\% \times \text{Area (Day X)}}{\text{Area (Day 4 or Day 5)}}$$

The area in micrometre^2 of spheroid size was calculated by the area in pixel multiply the ratio of the micrometre of the scale bar to the distance of the scale bar in pixel measured by CellProfiler in the image.

2.4 Cell viability in Myogel

Cell viability of cancer cells in 2D and 3D with Myogel was examined using AlamarBlue® assay. 10 µL of freshly-made 5 µg/µL resazurin (Sigma, Cat. # R7017) in PBS was added to the wells (100 µL) with or without cells at the final concentration of 0.5 µg/µL after 2 and 4 days. After an 18-hour incubation at 37°C in a humidified, 5% CO_2 atmosphere, fluorescence intensities were measured using FLUOstar Omega spectrometer set at excitation of 540 nm and emission detection of 590 nm. Fluorescence of five-six wells containing cells or spheroids with or without Myogel were measured. Medium and Myogel only wells were measured as contamination control.

2.5 MassSpec analysis of Myogel

In order to validate the presence of collagen I, collagen IV, fibronectin and laminin in the Myogel as previously reported, tandem mass spectroscopy (MS/MS) was performed to identify those proteins. Before analysis by MS, in-solution digestion using trypsin or in-gel digestion was performed according to the protocol from the website: http://www.chem.ox.ac.uk/spectroscopy/mass-spec/MS%20service/Proteomics%20protocols/Protocol%20In%20solution%20digestion_nov2016.pdf. 180 µg Myogel (20 µL) was mixed with 100 µL 6 M urea in Tris buffer (0.4 M, pH 7.8) and vortexed for 2 minutes. 40 µg of BSA (Sigma, Cat. # A7906) and 60 µg of collagen I were used as controls. 5 µL of the DTT (Fermentas, Cat. # R0862) reducing reagent was added and vortexed. The mixture was incubated for 60 minutes at room temperature or 37 °C. 20 µL of the iodoacetamide (Sigma, Cat. # I1149) alkylating reagent was added and vortexed. The mixture was incubated for 60 minutes at room temperature or 37 °C. 20 µL of the DTT reducing reagent was added and vortexed. The mixture was incubated for 60 min at room temperature or 37 °C. 775 µL MilliQ-H_20 was added and the solution was vortexed. 20 µL of 0.2 µg/µL trypsin (Sigma, Cat. # T1426) was added and the digestion was carried out overnight at room temperature or at 37 °C. 10 µL of acetic acid (Sigma, Cat. # 27225) was added and the solution was purified by phenomenex™ Strata™ C18-E column. After the proteins was dried completely in a speed-vac, the pellets was resuspended in 50 µL 98% MilliQ-H_20 with 2% HPLC-grade acetonitrile (VWR, Cat. # 83639.320) and 0.1% formic acid (Sigma, Cat. # 27001-M).

For in-gel digestion, the protein mixtures in Myogel were separated in a single dimension by sodium dodecyl sulfate-polyacrylamide gel electrophoresis (SDS-PAGE) with 6% of acrylamide gel. Rat tail collagen I was used as a positive control for collagen I and BSA was used as a methodological control. The gel was stained with fresh Coomassie blue R-250 (Fisher Bioreagents™, Cat. # BP101-25) at room temperature for 1 hour and destained in boiling water until the blue bands were visible and the background was transparent. The protein bands ranging from 100 kDa to 300 kDa in the lanes containing Myogel and collagen I while the single band near 70 kDa in the lane containing BSA were cut into smaller pieces (1-2 mm^3). The gel pieces were placed in a 1.5 mL tube and sent to the Department of Biology to perform the in-gel digestion.

MS instruments were operated by technical specialists, Shaun Reeksting and Mervyn Lewis, in Chemical Characterisation and Analysis Facility (CCAF). The Chip-based analysis was conducted using an HPLC-Chip Cube system coupled to a 6520 quadrupole time-of-flight (QTOF) mass spectrometer (Agilent

Technologies, Santa Clara, CA) operated in ESI positive-ion mode. Liquid chromatography was performed using a Large-Capacity Chip (II) with a 160 nL enrichment column and analytical column of 150 mm x 75 µM with Zorbax 300SB-C18 packing material at 5 µm (G4240-62010, Agilent, Santa Clara, CA, USA). The ChipCube source was operated at 300 °C with 5 L/min N_2 drying gas, the capillary voltage set to 1900 V and fragmentor at 170 V. The TOF MS scan range was from 300 – 1700 mass-to-charge ratio (*m/z*) at an acquisition rate of 4 spectra per second. For MS/MS 5 multiply charged precursor ions per spectrum, having between 2 – 5 charges, were selected for MS/MS and thereafter excluded after collecting 2 spectra, then released after 0.1 minute. The MS/MS mode mass range was from 50 – 1700 *m/z* at 3 spectra per second with the collision energy set relative to the ion mass with the formula 3.6*m/z* / 100 - 4.8. The source was interfaced with an Agilent 1260/1200 series HPLC system consisting of a 1260 Cap pump, 1200 Nano pump, 1200 Micro WPS and 1290 Infinity Thermostat (Agilent, Santa Clara, CA, USA). Between 0.2 and 1 µL sample was loaded on the enrichment column using the capillary pump flow with H_2O + 0.1% formic acid (FA) at a flow rate of 4 µL/min. The sample was eluted onto the analytical column using the nano pump at a flow rate of 0.3 µL/min. Solvent A and B consisted of H_2O + 0.1% formic acid (FA) and ACN:H_2O 90:10 with 0.1% FA. Gradient step were as follows: 0-28 minutes from 3% B to 50%B, 28-30 min to from 50% B to 100% B, 30-31 minutes 100%B, 31-32 minutes from 100% to 3% B. Internal lock mass calibration was active during the run using one calibrant reference mass at 1221.9906 *m/z*. Data processing and file exporting was performed using the Masshunter Workstation software version B.50.00 (Agilent, Santa Clara, CA, USA). Automated MS/MS database searching was performed using Mascot v2.4.1 (Matrix Science, MA, USA) with the SwissProt database using the following search parameters: allowed 2 max trypsin cleavages, fixed carbamidomethyl and variable oxidation of methionine modifications with a peptide mass tolerance of 20 ppm and a fragment mass tolerance of 0.1 Da.

2.6 Immunoblotting

Twenty spheroids were collected in 1.5 mL Eppendorf tube on ice and the cell culture medium was discarded as much as possible. 100 µL of Radio-Immune Precipitation Assay (RIPA, Thermo Scientific™, Cat. # 89900) lysis buffer containing Halt Protease Inhibitor Cocktail (Thermo Scientific™, Cat. # 78430) and Phosphatase Inhibitors Cocktail IV (Fisher Bioreagents™, Cat. # 12851650) was added to each tube, homogenised with Axygen™ Tissue Grinder for 1.5 And 2.0 mL tubes (Axygen™, Cat. # Axygen PES-15-B-SI) and vortexed about 10 second and the tubes were left on ice for 10 minutes. The homogenisation and vortex was repeated twice. The total time for cell lysis was 1 hour. After the cell lysis on ice, the tubes were centrifuged at 4 °C, 16,000 g for 10 minutes. The supernatants were stored in - 80°C until further analysis.

10x SDS-PAGE stock running buffer was made by dissolving 30.3 g Tris base, 144 g glycine (Fisher Bioreagents™, Cat. # BP381-1), and 10 g sodium dodecyl sulfate (SDS, Fisher, Cat. # S/5200/53) in 1 L Milli-Q water. 100 mL of the stock running buffer was diluted to 1 L using Milli-Q water to make 1x SDS-PAGE running buffer. Running buffer was stored at room temperature.

10x stock transfer buffer was made by dissolving 30.3 g Tris base, and 144 g glycine in 1 L Milli-Q water. 100 mL of the stock transfer buffer was diluted to 800 mL using Milli-Q water and 200 mL methanol

(VWR, Cat. # 20864.320) was added to make 1x transfer buffer, which was put in 4 °C at least 1 hour before transfer steps. The 1x transfer buffer was freshly made every time.

10x stock TBS was made by dissolving 24.2 g Tris base, and 80 g sodium chloride in 800 mL Milli-Q water. After the pH was adjusted to 7.5 using HCl (VWR, Cat. # 20254.401), Milli-Q water was added to make the final volume of 1 L stock TBS. 100 mL of the stock TBS was diluted to 1 L using Milli-Q water to make 1x TBS. 1 mL TWEEN® 20 (Sigma, Cat. # P1379) was added to 1 L TBS to make 1x TBS-T.

The blocking buffer contained 5% (w/v) BSA in 1x TBS or 1x TBS-T.

Preparation of the SDS-PAGE gel was as follows: 8% resolving gel solution was made of 53% Milli-Q water, 20% Acrylamide/Bis-acrylamide (40% solution, Mix ratio 29:1, Sigma, Cat. # A7802), 25% Tris/HCl (1.5 M, pH 8.8), 1% SDS (10% solution), 1% ammonium persulfate (APS, 10% solution, w/v, Fisher, Cat. # A/P470/46), and 0.1% tetramethylethylenediamine (TEMED, Fisher Chemical, Cat. # T/P190/04). The solution was pipetted into the cassettes and overlaid with butanol (Fisher, Cat. # B/4800/08). After 30 minutes, the butanol was washed off with tap water and the excess water was wiped with tissue. 4% stacking gel solution was made of 58% Milli-Q water, 15% Acrylamide/Bis-acrylamide (40% solution), 25% Tris/HCl (0.5 M, pH 6.8), 1% SDS (10% solution), 1% APS (10% solution), and 0.1% TEMED. The solution was pipetted into the cassettes to overlay the resolving gel and the sample lane combs were inserted. After 30 minutes, gels were ready and stored at 4°C for no more than 1 week.

Reduced samples were prepared with loading buffers by mixing 52 µL protein sample (cell lysate or Myogel preparation) with 20 µL NuPAGE® LDS sample buffer (4x, Invitrogen™, Cat. # NP0007) and 8 µL NuPAGE® Reducing Agent (10x, Invitrogen™, Cat. # NP0009). Samples with loading buffers were heated for denaturing electrophoresis at 95 °C for 3-5 minutes and then stored in -80 °C until further analysis. 10 µL of cell lysates with loading buffers or 20 µL of Myogel with loading buffers were loaded at each well and 1-3 µL PageRuler™ Prestained 10-180 kDa Protein Ladder (Thermo Scientific™, Cat. # 26616) or Spectra™ Multicolor High Range Protein Ladder (Thermo Scientific™, Cat. # 26625) were used. Rat tail collagen I, Matrigel® Basement Membrane Matrix (Matrigel, Corning, Cat. # 734-0269P) and fibronectin bovine plasma (Sigma, Cat. # F1141) were used as controls in characterisation of Myogel. Two gels were run at 100 V for about 2 hour until the 40 kDa band in the protein ladders was at 20% above the bottom of the gel.

Prior to the transfer step, two Immobilon® FL PVDF transfer membranes (EMD Millipore, Cat. # IPFL00010) were cut and soaked in 100% methanol for 15 seconds and then placed in the transfer buffer. The blotting pads were soaked in transfer buffer and air bubbles were removed by squeezing the blotting pads while they were submerged in buffer.

At the end of the running step, the gels were removed from the cassettes and the stacking gels were trimmed away. The remaining gels were placed in transfer buffer until use. Filter papers were soaked briefly in transfer buffer immediately before use. One blotting pad was placed into the cathode (-) core of the blot module (Invitrogen™, Cat. # EI9051) and one filter paper was placed onto the blotting pad, followed by strict order of one gel, one membrane, one filter paper, one blotting pad and then one filter paper. The other gel was placed on top of the last filter paper with the membrane on top of the gel and then one filter paper followed by the blotting pad. The blot module containing the gel/membrane sandwich was secured in the lower buffer chamber. The blot module and the outer buffer chamber were filled with cold transfer buffer. The transfer conditions were 30 V constantly for 1.5 hours.

After the transfer step, the membranes were briefly placed in TBS and then blocked with 5% (w/v) BSA in TBS or TBS-T at room temperature for 1 hour. Each membrane was then probed with one antibody against one target protein and one housekeeper protein antibody from different species at 4°C overnight. The dilution of antibodies were summarized in Table 2. The membranes were washed thrice for 5 minutes each time in TBS-T. Fluorescent secondary antibodies in blocking buffer were added to the membranes and the membranes were incubated in dark boxes prevented from light at room temperature for 1-1.5 hours. The membranes were washed thrice for 3-5 minutes each time in TBS-T and scanned by Odyssey® CLx Infrared Imaging System LI-COR Bioscences.

Table 3. List of antibodies in immunoblotting.

Antibody	Species Clonality	Manufacturer	Cat. #	Dilution
HDAC1(10E2)	Monoclonal Mouse IgG1	Santa Cruz biotechnology	sc-81598	1:5,000
αSMA	Goat polyclonal	Abcam	ab21027	1:1,000
αSMA	Rabbit polyclonal	Abcam	ab5694	1:1,000
GAPDH Antibody (FL-335)	Rabbit polyclonal	Santa Cruz biotechnology	sc-25778	1:10,000
p53 (DO-1)	Monoclonal Mouse IgG2a	Santa Cruz biotechnology	sc-126	1:1,000
YAP(63.7)	Monoclonal Mouse IgG2a	Santa Cruz biotechnology	sc-101199	1:1,000
COL1A1(3G3)	Mouse monoclonal IgG3	Santa Cruz biotechnology	sc-293182	1:100
Laminin β-2 (C4)	Monoclonal Mouse IgG1	Santa Cruz biotechnology	sc-59980	1:500
Fibronectin (EP5)	Monoclonal Mouse IgG1	Santa Cruz biotechnology	sc-8422	1:500
COL4A6 (G-2)	Monoclonal Mouse IgG1	Santa Cruz biotechnology	sc-398655	1:500
IRDye 680RD Donkey anti-Mouse IgG	Donkey	LI-COR	926-68072	1:10,000
IRDye 800CW Donkey anti-Goat IgG	Donkey	LI-COR	926-32214	1:10,000
IRDye 680RD Donkey anti-Rabbit IgG	Donkey	LI-COR	926-68073	1:10,000
IRDye 800CW Donkey anti-Mouse IgG	Donkey	LI-COR	925-32212	1:10,000

2.7 Treatments of anti-cancer agents on the co-culture models in collagen I

3D co-culture was done as in the section 2.2.8. 50 mM gemcitabine hydrochloride (Santa Cruz Biotechnology, Cat. # sc-204763), 10 mM Pseudopterosin A-D (PsA-D) from Prof. Dr. Russell Kerr, Veterinary College, University of Prince Edward Island and 10 mM Tylophorinine from Prof. Dr. Proksch, Institute of Pharmacological Biology and Biotechnology, Heinrich-Heine University Düsseldorf, all of which were dissolved in Dimethyl Sulfoxide (DMSO, Sigma, Cat.# D2650), were added to the spheroids on day 4 to reach the final concentration of 100 µM gemcitabine, 70 µM PsA-D and 0.1 µM Tylophorinine respectively. The concentration of 100 µM gemcitabine was chosen according to the IC50 previously reported in 3D mono-culture of MIAPaCa-2 and PANC-1 cells [Wen *et al*, 2013]. The concentrations of 70 µM PsA-D and 0.1 µM Tylophorinine were chosen based on the IC50 results provided by our collaborators, Janina Betz, Julia Sperlich, and Nicole Teusch. 0.7% DMSO was used as the solvent control and 10% fresh medium was used as untreated control. After the addition of agents, the spheroids were further cultured for 3 days.

2.8 Immunofluorescence

The following protocol was kindly provided by Silvia Muñoz Descalzo from Department of Biology [Nichols *et al*, 2009] and was modified slightly. 3-6 spheroids were fixed in 4% paraformaldehyde (PFA, Sigma, Cat. # P6148) in PBS using Eppendorf tubes for 0.5-1 hour at room temperature. After fixing, the spheroids were rinsed 4 times in 3 mg/mL polyvinylpyrrolidone (PVP, Sigma, Cat. # P0930) in PBS (PBS/PVP) and then stored in 4 °C for no more than 1 week until immunofluorescence studies.

Before antibodies staining, the spheroids were permeabilised in 0.25% Triton™ X-100 (Sigma, Cat. # X100) in PBS/PVP for 0.5-1 hour. After permeabilisation, the spheroids were placed in blocking solution (0.1% BSA and 0.01% Tween 20 in PBS) for 0.5 hour. The spheroids were incubated in primary antibody solution (1:100 in blocking solution) for 19-24 hours with gentle shaking in the 4 °C. Antibodies were summarized in Table 3. Before incubation with secondary antibodies, the spheroids were rinsed thrice for 15 minutes each time in blocking solution with vigorous shaking at room temperature. The spheroids were incubated in secondary antibody solution (1:200 in blocking solution) and 4',6-diamidino-2-phenylindole dihydrochloride (DAPI, Sigma, Cat. # D9542) with gentle shaking in the 4 °C, protected from light. After an overnight incubation, the spheroids were rinsed 4 times for 15 minutes in blocking solution with vigorous shaking at room temperature, protected from light.

Extra cautions were taken for processing PANC-1 mono-culture spheroids due to their loose nature. Quick centrifugation was performed to collect fragments of PANC-1 mono-culture spheroids before aspiration of solution.

After the ending of the final shaking, the blocking solution was aspirated as much as possible and the spheroids were incubated with at least 500 µL of increasing ethanol concentration mixed with MiliQ water for 30 minute at room temperature in the following sequence: 1) 30% ethanol; 2) 50% ethanol; 3) 70% ethanol; 4) 90% ethanol; 5) 96% ethanol; 6) 100% ethanol; 7) 100% ethanol. At the end of the ethanol incubation, the ethanol was aspirated as much as possible and the spheroids were incubated in benzyl alcohol (Alfa Aesar, Cat. # L03258) and benzyl benzoate (Alfa Aesar, Cat. # L03292) at 1:2 (v/v,

BABB) for at least 1 hour at room temperature. At the end of the BABB incubation, spheroids were transferred to the wells of an ibidi µ-Plate 96 well black (ibidi, Cat. # 89626) with as little BABB as possible to prevent the movement of spheroids in BABB so that the spheroids stayed stationary in the wells. The plates could be stored at 4 °C until analysis.

Table 4. List of antibodies used in immunofluorescence.

Antibody	Species Clonality	Manufacturer	Cat. #	Dilution
p53	Polyclonal Goat IgG	R&D systems	AF1355	1:100
p53 (DO-1)	Monoclonal Mouse IgG2a	Santa Cruz biotechnology	sc-126	1:100
YAP(63.7)	Monoclonal Mouse IgG2a	Santa Cruz biotechnology	sc-101199	1:100
YAP(H-125)	Rabbit polyclonal	Santa Cruz biotechnology	sc-15407	1:100
Occludin (H-279)	Rabbit polyclonal	Santa Cruz biotechnology	sc-5562	1:100
Pan-TEAD(D3F7L)	Rabbit monoclonal	Cell Signaling Technology	#13295	1:100
αSMA	Goat polyclonal	Abcam	ab21027	1:100
αSMA	Rabbit polyclonal	Abcam	ab5694	1:100
FAP	Rabbit polyclonal	Abcam	ab53066	1:100
Ki67(H-300)	Rabbit polyclonal	Santa Cruz biotechnology	SC-15402	1:100
Donkey anti-Goat IgG secondary antibody, Alexa Fluo 488	Donkey polyclonal	Invitrogen/ThermoFisher	A-11055	1:200
Donkey anti-Rabbit IgG secondary antibody, Alexa Fluo 546	Donkey polyclonal	Invitrogen/ThermoFisher	A10040	1:200
Chicken anti-Mouse IgG secondary antibody, Alexa Fluor 647	Donkey polyclonal	Invitrogen/ThermoFisher	A-21463	1:200
Rabbit IgG Isotype Control (3 mg/mL)	Rabbit	Invitrogen	10500C	1:1000
Goat IgG (5 mg/mL)	Goat	Invitrogen	02-6202	1:500
Mouse IgG (0.4 mg/mL)	Mouse	Santa Cruz biotechnology	sc-2025	1:200

2.9 Confocal laser scanning microscopy (CLSM)

Images were acquired on a Zeiss 880 confocal laser scanning microscope with Airyscan (Carl Zeiss) using a Plan-Apochromat 5x/0.16 M27 (12.1 mm working distance), a Plan-Apochromat 10×/0.45 NA objective lens (2 mm working distance), a Plan-Apochromat 20×/0.8 NA objective lens (0.55 mm working distance) or a Plan-Apochromat (oil) 40×/1.3 NA objective lens (0.21 mm working distance) below 20 °C. Fluorophores were excited simultaneously using at least two different laser wavelengths as specified below, 488/561/633 main beam splitter and -405 main beam splitter_InVis with the non-descanned detector to acquire the differential interference contrast (DIC) images.

The lasers and filter settings were as follows: 405nm (Argon) excitation and 410–497 nm filters for DAPI as DAPI channel; 488 nm (Argon) excitation and 500–553 nm filters for Alexa Fluor 488 as Alexa488 channel; 561 nm (Argon) and 562–624 nm filters for Alexa Fluor 546 as Alexa546 channel; 633 nm (HeNe) and 624-735 nm filters for Alexa Fluor 647 as Alexa647 channel.

Unless specified otherwise, most of the images in chapter 3 were recorded using two tracks with DAPI channel and Alexa546 channel in one track while Alexa488 channel and Alexa647 channel in the other. Images in chapters 4 and 5 were recorded in multitracking mode separating each channel into one track individually.

Spectral unmixing was done in Zen 2.5 (blue edition) or Zen 2.3 (blue edition) using Automatic Component Extraction (ACE) or spheroid controls. ACE was done in the software by detecting the individual spectrum of three or four dyes in the images automatically to unmix the image. Alternatively, individual spectrum of different dyes was obtained by staining the spheroids with only one dye as spheroid controls and using the same acquisition settings as the spheroids stained with three dyes. The spectrum of each dye was saved and used as a reference spectrum to unmix the images acquired with three dyes in the software.

When acquiring the single image (one optical section) near the core of spheroids in chapter 3 and 4 stained with the following combination: DAPI, rabbit anti-YAP antibodies, mouse anti-p53 antibodies, or the following combination: DAPI, goat anti-p53 antibodies, and rabbit anti-YAP antibodies, DAPI, Alexa Fluor 488, Alexa Fluor 546 and Alexa Fluor 647 were excited simultaneously using 405 nm at 2% laser power, 488 nm at 2% laser power 561 nm at 2% laser power and 633 nm at 10% laser power. Either 10x or 20x objective lens was selected to capture the whole spheroid area/region in one 1x1 image tile. When using a 40x objective lens, tile scanning was performed using 2x2 image tiles. 512x512 pixels image size in unidirectional and line sequential mode with 2 frame averaging and 8-bit depth were used. > 30% laser power setting was also used in non-cleared samples.

When acquiring a single image (one optical section) near the core of spheroids cultured in hyaluronic acid stained with DAPI and goat anti-p53 antibodies, DAPI and Alexa Fluor 488 were excited simultaneously using 405 nm at 2% laser power (master gain 570) and 488 nm at 5% laser power (master gain 605). Either 10x or 20x objective lens was selected to capture the whole spheroid area/region in one 1x1 image tile. 1024x1024 pixels image size or 512x512 pixels image size in unidirectional and line sequential mode with 2 frame averaging and 8-bit depth were used.

When acquiring a single image (one optical section) near the core of spheroids cultured in HA and collagen I stained with DAPI and goat anti-p53 antibodies, DAPI and Alexa Fluor 488 were excited simultaneously using 405 nm at 2% laser power and 488 nm at 5% laser power. Master gains were adjusted to minimise pixel saturation. A 10x objective lens was selected to capture the one optical section in one 1x1 image tile. 1024x1024 pixels image size or 512x512 pixels image size in unidirectional and line sequential mode with 2 frame averaging and 8-bit depth were used.

When imaging an entire spheroid in collagen I with or without HA on day 4 stained with DAPI and goat anti-p53 antibodies, DAPI and Alexa Fluor 488 were excited simultaneously using 405 nm at the 2% laser power and 488 nm at the 2% or 5% laser power. When imaging the entire spheroids on Day 4 stained with DAPI and mouse anti-p53 antibodies, DAPI and Alexa Fluor 647 were excited simultaneously using 405 nm at 2% laser power and 633 nm at 2% or 3% laser power. Master gains were adjusted to minimise pixel saturation. 5x, 10x or 20x objective lens was used in order to capture the whole spheroid in one 1x1 image tile. Z-stack acquisition was performed at the optimal slice interval determined by the Zen 2.3 SP1 FP1 (black edition). 1024x1024 pixels image size or 512x512 pixels image size in unidirectional and line sequential mode with 2 frame averaging and 8-bit depth were used.

When acquiring a single image (one optical section) of spheroids (collected on day 4 after initial culture) that were stained with DAPI, goat anti-p53 antibodies, rabbit anti-pan-TEAD antibodies or rabbit anti-Ocln antibodies, and mouse anti-YAP antibodies in Chapter 5, fluorescent dyes were simultaneously excited using 405 nm, 488 nm, 561 nm and 633nm lasers. The laser powers at 10% maximum and master gains were adjusted to minimise pixel saturation. A 20x objective lens, 1024x1024 pixels image size in unidirectional and line sequential mode with 2 frame averaging and 8-bit depth were used.

When imaging an entire spheroid (collected on day 4 after initial culture) stained with DAPI, rabbit anti-αSMA antibodies and mouse anti-p53 antibodies in Chapter 5, DAPI, Alexa Fluor 561 and Alexa Fluor 647 were excited simultaneously using 405 nm at 2% laser power, 561 nm at 2% laser power laser and 633nm laser at 5% laser power. Master gains were adjusted to minimise pixel saturation. Z-stack acquisition was performed at 2.683 µm slice interval using a 10x objective lens and 1024x1024 pixels image size in unidirectional and line sequential mode with 2 frame averaging and 8-bit depth.

When imaging entire spheroids treated with or without anti-cancer agents, DAPI, Alexa Fluor 488 and Alexa Fluor 561 were excited simultaneously using 405 nm (master gain 500) at 2% laser power, 488 nm (master gain 700 if using a 20x objective lens or 650 if using a 10x objective lens) at 2% laser power and 561 nm lasers (master gain 700 if using a 20x objective lens or 650 if using a 10x objective lens) at 1% laser power were used. Z-stack acquisition was performed in a defined X/Y/Z (2.768/2.768/2.683 µm) volume and 512x512 pixels image size with 1.54 µs pixel dwelling time if using a 10x objective lens or X/Y/Z (0.692/0.692/0.748 µm) volume and 1024x1024 pixels image size with 0.77 µs pixel dwelling time if using a 20x objective lens. All the Z-stack imaging was done in unidirectional and line sequential mode with 1 frame averaging and 8-bit depth.

When acquiring a single image (one optical section) near the core of spheroids treated with or without anti-cancer agents in Airyscan mode, all 4 fluorophores were excited simultaneously using 405 nm at 0.2% laser power, 488 nm at 1% laser power, 561 nm at 1% laser power, and 633 nm at 2 % laser power. A 10x objective lens, 4096x4096 pixels image size and 750 master gain in unidirectional and line sequential mode with 1 frame averaging and 8-bit depth were used. Airyscan processing was done in Zen 2.5 (blue edition).

2.10 Multiphoton microscopy (MP)

Multiphoton (MP) imaging was acquired using Zeiss 880 with Spectra Physics multiphoton lasers. 20x objective lens, 2048x2048 pixels image size in unidirectional and line sequential mode with 8 frame averaging and 8-bit depth were used.

MP wavelength optimisation was performed by Anne Gesell in Microscopy and Analysis Suit (MAS). MP excitation wavelengths ranging from 690 – 980 nm was performed on spheroids stained with 3 dyes and CLSM images at the same position were used as reference. The SP filter of 485 nm for DAPI coloured blue was considered as DAPI channel; the BP filter of 500-550 nm for Alexa Fluor 488 coloured green as Alexa488 channel; the BP filter of 570-610 nm for Alexa Fluor 546 coloured red as Alexa546 channel. After optimising the excitation wavelength, DAPI was excited with 690nm and the SP filter of 485 nm was used to collect the photons; Alexa Fluor 488 was excited with 950nm and the BP filter of 500-550 nm was used to collect the photons; Alexa Fluor 546 was excited with 850nm and the BP filter of 570-610 nm was used to collect the photons.

2.11 Image analysis for immunofluorescence

Workflow for p53 expression measurement by CellProfiler in fluorescent images was as follows:

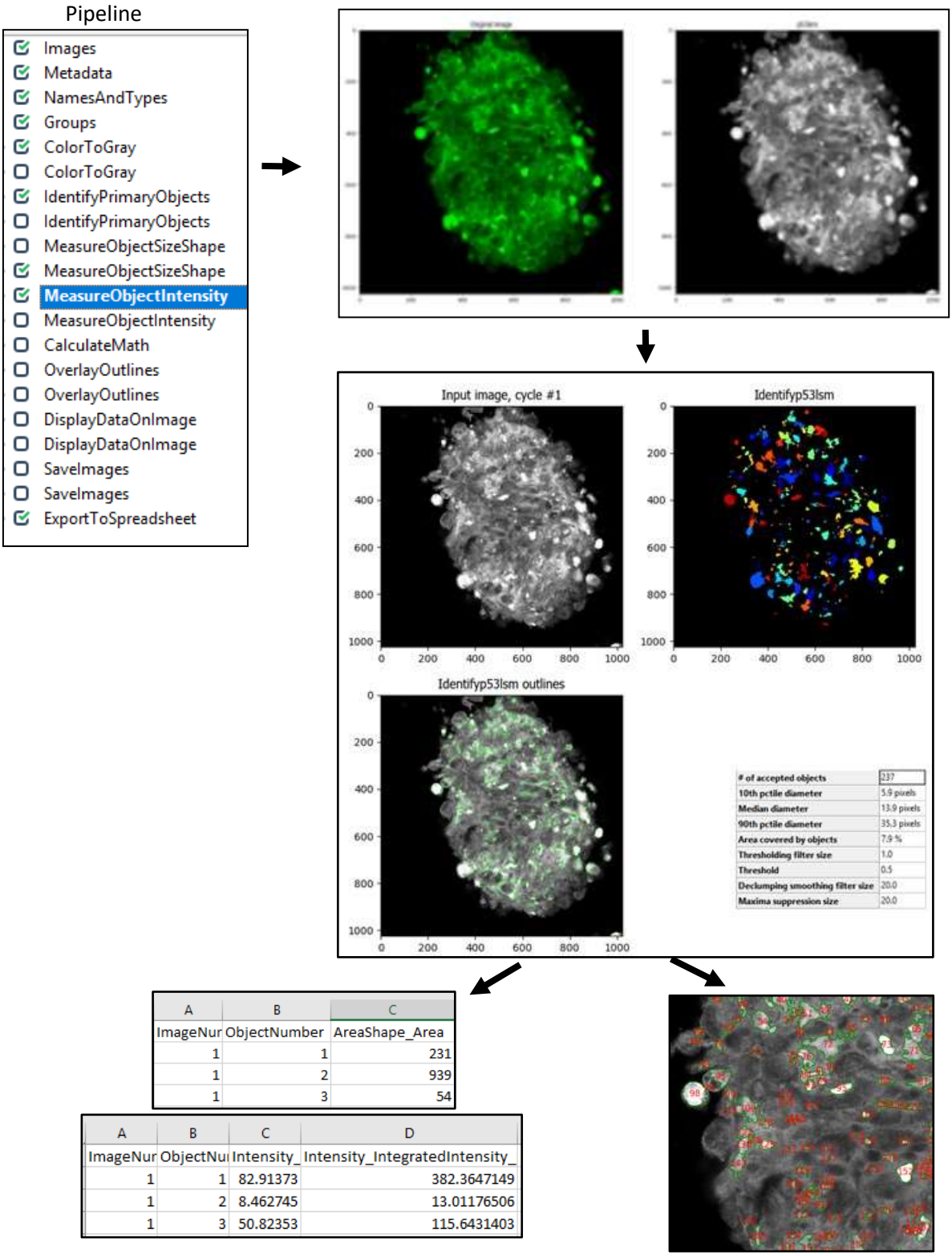

Figure 16. Workflow for p53 expression measurement by CellProfiler.

The images acquired in the p53 channel were exported individually and coloured green. Green images were imported and converted to greyscale images by the module 'ColorToGray' in order to measure the intensities. The regions indicating the positive p53 staining of nuclei were identified as objects by the module 'IdentifyPrimaryObjects', setting 5–200 pixels as the typical diameter of objects for the image acquired by MP while 5-80 for CLSM. Objects outside the diameter range and touching the border of the image were discarded. Threshholding strategies were optimized to identify the objects, balancing the accuracy and efficiency. 'Adaptive', 'Otsu' and 'Three classes' options were selected as the thresholding. The pixels in the middle intensity class were assigned to the background. The threshold smoothing scale was 1.3488 and the correction factor was 1.0, with threshold range from 0.5 as lower bound and 1.0 as upper bound. The size of adaptive window was 50. 'Shape' was selected as the method to distinguish clumped objects and draw dividing lines between clumped objects. The size of the smoothing filter was 20. After a few testing on the number of minimum allowed distance to use as a parameter to separate objects (local maxima), local maxima that were over 20 minimum allowed distance can result in under-segmentation, leading to merging too many objects together and false identification of individual p53 positive nucleus. Therefore, local maxima that were closer than 20 minimum allowed distance was suppressed in order to separate individual p53 positive object.

The regions indicating the areas of the p53 positive nuclei in each image were extracted by the module 'MeasureObjectSizeShape'. The intensities of the areas of the p53 positive nuclei were extracted by the module 'MeasureObjectIntensity'. The areas of the p53 positive nuclei were outlined by the module 'OverlayOutlines'. A new image was generated by the module 'SaveImages' for manually verification of the correctness of region measured to eliminate the incorrect identification of the p53 positive nuclei due to background noise. Objects identified as p53 positive were numbered on top of p53 positive objects in the image by 'DisplayDataOnImage' to aid matching the nuclei in the image acquired by CLSM and by MP. The resulting p53 intensities and the corresponding area were exported by the module 'ExportToSpreadsheet'. The value of p53 intensities in the column 'Intensity_IntegratedIntensity' divided by the area used to extract p53 intensities in the column 'AreaShape_Area' was used to compare the p53 relative expression between cells in the core region and near the edge of the spheroid in one optical slide.

Workflow for YAP expression measurement by CellProfiler in fluorescent images was as follows:

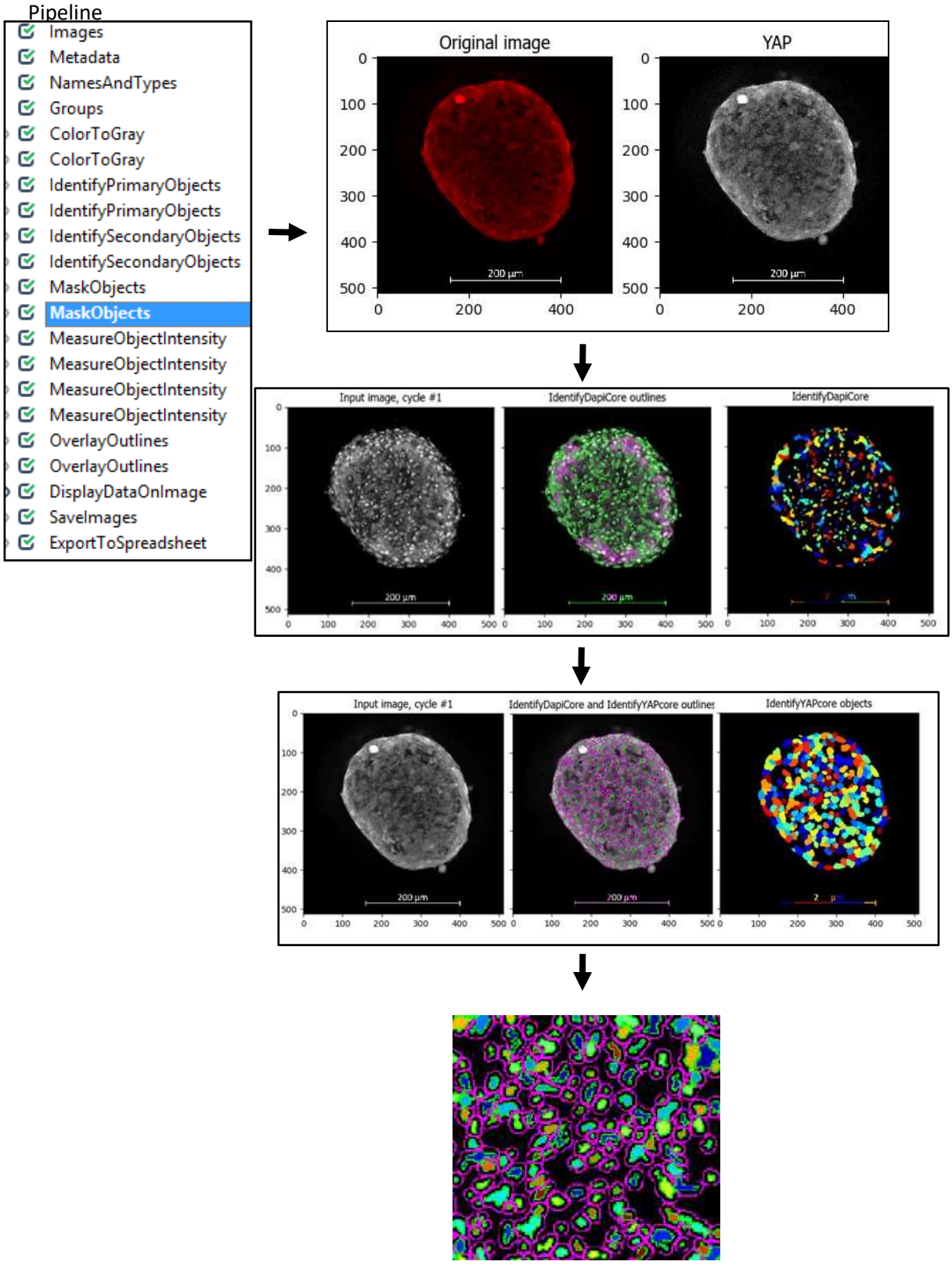

Figure 17. Workflow for YAP expression measurement by CellProfiler.

The images acquired in DAPI channel coloured blue and YAP channel coloured red were exported individually. Coloured images were imported and converted to greyscale images by the module 'ColorToGray' in order to measure the intensities. The regions indicating the DAPI staining of nuclei were identified as primary objects by the module 'IdentifyPrimaryObjects', setting 3–20 pixels as the typical diameter of objects for the image. Objects outside the diameter range and touching the border of the image were discarded. Threshholding strategies were optimized to identify the objects, balancing the accuracy and efficiency. 'Adaptive', 'Otsu' and 'Three classes' options were selected as the thresholding. The pixels in the middle intensity class were assigned to the background. The threshold smoothing scale was 1.3488 and the correction factor was 1.0, with threshold range from 0.2 as lower bound and 1.0 as upper bound. 'Intensity' was selected as the method to distinguish clumped objects and draw dividing lines between clumped objects. The size of adaptive window, the size of the smoothing filter, local maxima and minimum allowed distance were modified in different images in order to optimise the outcomes of separating individual objects identified as nuclei.

The regions indicating the YAP staining were identified as secondary objects by the module 'IdentifySecondaryObjects', using DAPI staining nuclei identified by the module 'IdentifyPrimaryObjects' as referenced input objects. 'Distance – B' was selected to identify the secondary objects. 'Global', 'Otsu' and 'Three classes' options were selected as the thresholding. The pixels in the middle intensity class were assigned to the background. The threshold smoothing scale was 0.0 and the correction factor was 1.0, with threshold range from 0.0 as lower bound and 1.0 as upper bound. The pixels to expand the primary object were adjusted in different images in order to optimise the outcomes of identifying the edge of each individual cell according to the cytoplasmic localisation of YAP. Secondary objects touching the border of the image were discarded.

The regions indicating the areas of YAP expression in nuclei were selected in the module 'MaskObjects' where the objects identified by YAP staining were masked by the objects identified by DAPI staining. The intensity of YAP expression in the nucleus of each individual cell and in the whole cell of each individual cell were extracted by the module 'MeasureObjectIntensity' separately. The areas of YAP expression in nuclei and the YAP expression in the whole cells were outlined by the module 'OverlayOutlines'. A new image was generated by the module 'SaveImages' for manually verification of the correctness of region measured to eliminate the incorrect identification of the YAP expression due to background noise. The resulting YAP intensities were exported by the module 'ExportToSpreadsheet' as a file with YAP expression in the nucleus of each individual cell generated by the module 'MaskObjects' and a file with YAP expression in the whole cell of each individual cell generated by the module 'IdentifySecondaryObjects'. The value in the column 'Intensity_IntegratedIntensity' was used to compare the YAP intensities between cells in the core region and near the edge of the spheroid or between YAP localisation in the nucleus and the cytoplasm in one optical slide. The YAP intensity in the cytoplasm of each individual cell was calculated by subtracting the YAP intensity in the nucleus from the one in the whole cell.

2.12 Statistical analysis

Data were presented as mean value ± standard deviation (SD) except in Figure 23-25 where the value in each group was presented. Graphs were generated in Microsoft Excel 2016. Normality of data was analysed by Shapiro-Wilk test in IBM® SPSS® Statistics version 25.

Non-parametric Kruskal-Wallis H test in IBM® SPSS® Statistics version 25 was used to compare the percentages of spheroid size and p53 expression. Error bars indicated SD of two-three independent experiments in spheroid size measurement or 9-17 cells in analysis of p53 expression in one independent experiment. Error bars and Graph were made by Microsoft Excel 2016. *P*-values were calculated by IBM® SPSS® Statistics version 25. $P<0.05$ (*) was considered as significant difference.

Whisker box graphs generated in Microsoft Excel 2016 were made from all the values of total YAP intensity in the whole cell of each individual cell or the intensity ratios of nuclear YAP intensity to total YAP intensity in the whole cell or cytoplasmic YAP intensity to total YAP intensity in the whole cell from around 3-150 cells near the core of the spheroid and the edge of the spheroid. Mean markers were shown. Median was exclusive from quartile calculation. Dots indicated the values in cells automatically generated by Microsoft Excel 2016. Non-parametric Mann Whitney U test in IBM® SPSS® Statistics version 25 was used to compare intensities and ratios. *P*-values were calculated by IBM® SPSS® Statistics version 25. $P<0.05$ (*) was considered as significant difference.

Two-tailed t-Test in Microsoft Excel 2016 was used to compare the fluorescence intensities in cell viability assay. Error bars indicated standard deviation of five or six wells in one independent experiment. *P*-value was calculated by Microsoft Excel 2016 using two-tailed two-sample equal variance t-Test if the sample sizes between two groups were the same or unequal variance t-Test if the sample sizes between two groups were not the same. $P<0.05$ (*) was considered as significant difference.

The R^2 used to measure linearity was calculated in Microsoft Excel 2016.

Chapter 3. YAP signalling in the 3D scaffold-free co-culture models with high ratios of stellate cells to cancer cells

Graphical Abstract

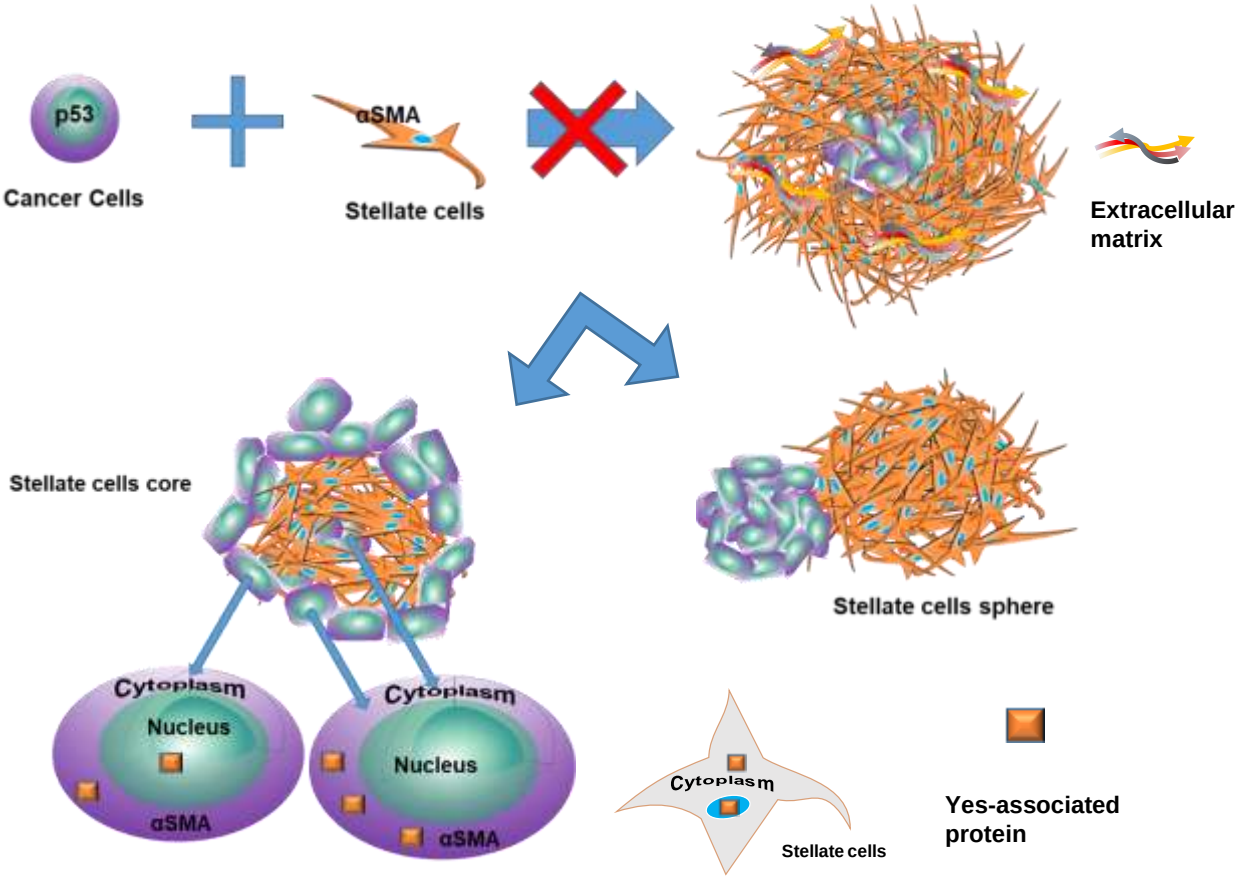

Figure 18. Diagram of YAP signalling in the 3D scaffold-free co-culture models with high ratios of stellate cells to cancer cells.

In Brief

Direct mixture of cancer cells and stellate cells co-cultured in a scaffold-free environment created a model where cancer cells became wrapped around a sphere of stellate cells. Thus, this format failed to create a model that emulated the organization observed in pancreatic tumours where clusters of cancer cells are surrounded by and intermingle with multiple layers of stellate cells. In the current models, higher level of endogenous YAP was found in the cytoplasm than in the nucleus in the majority of cancer cells, indicating a small amount of YAP localised in the nucleus might be sufficient to drive PDAC growth.

Highlights

Validation of immunofluorescence-based microscopic assessment of intact 3D co-culture spheroids with stellate cells and cancer cells using an optical clearing method with ethanol, benzyl alcohol and benzyl benzoate to characterize the expression of selected proteins in thick specimens (500 µm).

3.1 Background

YAP signalling has been studied in pancreatic cancer cell lines transfected with YAP expression lentivirus [Yuan *et al*, 2016] or retroviral phosphorylation-deficient YAP [Yang *et al*, 2015] , cell-line xenografts and genetically engineered mouse models (GEMMs) [Murakami *et al*, 2017; Wei *et al*, 2017; Yang *et al*, 2015; Zhao *et al*, 2017]. Genetic knock-out or knock-down of YAP has been shown to suppress pancreatic cancer growth while genetic inhibition of YAP phosphorylation, a method to facilitate YAP entering the nucleus, promotes cancer cell growth. Nuclear YAP expression is higher than its cytoplasmic expression in 2D culture of pancreatic cancer cells [Cravo *et al*, 2015; Diep *et al*, 2012]. Immunohistochemistry and immunofluorescence studies of pancreatic ductal adenocarcinoma (PDAC) tissues, however, can show that this bias of cellular localization may not occur consistently in these tumours [Diep *et al*, 2012; Morvaridi *et al*, 2015; Yang *et al*, 2015]. Whether a small amount of YAP in the nucleus or a higher ratio of YAP localised in the nucleus than the one in the cytoplasm is essential to induce proliferation in PDAC needs further investigation. To date, there are limited data on endogenous YAP expression in 3D co-culture models with pancreatic cancer cells and stellate cells derived from PDAC patients.

One hallmark of PDAC tumours is their highly fibrotic nature with the large number of stellate cells present in the tumour, secreting extracellular matrix (ECM) components and growth factors that can interact with and influence the cancer cells. PDAC co-culture models composed of stellate cells and cancer cells can thus provide a more realistic representation of these tumours. Previously in *in vitro* studies, stellate cells are grown in one compartment of Transwell® plates, separating from cancer cells in the other compartment [Fujita *et al*, 2009]. This method lacks 3D architecture and cell-cell contact as cancer cells experienced in patients. Alternatively, stellate cells are seeded on top of animal-derived matrix in 24-well plates and then the cancer cells are plated on the matrix layer with stellate cells [Coleman *et al*, 2014b]. This protocol does not provide a complete barrier surrounding the cancer cells and is less ideal for high-throughput assays testing hundreds of anti-cancer agents. To our understanding, the use of 3D co-culture models as a robust tool to screen potential therapeutic agents is not yet optimal. It is our opinion that the lack of a simplified protocol to prepare consistently a 3D co-culture model has limited acceptance of this approach as a screening tool.

In the PDAC microenvironment, a number of cancer-associated fibroblasts (CAFs) are originated from stellate cells, some of which are quiescent and play a role in repairing pancreatic injury [Erkan *et al*, 2012]. Normal stellate cells are present in a variety of tissues in human body, including liver and pancreas [Erkan *et al*, 2012]. During PDAC development, stellate cells are activated by neoplastic cells to become CAFs, secreting large amount of ECM and promoting tumorigenicity [Bolm *et al*, 2017; Erkan *et al*, 2012; Hwang *et al*, 2008]. The terms CAFs and stellate cells are often interchangeable in PDAC research. However, hepatic stellate cells and pancreatic stellate cells have distinct features, separating them from the subtypes of fibroblasts such as skin fibroblasts. The transcriptional phenotypes of skin fibroblasts, hepatic stellate cells and pancreatic stellate cells were compared [Buchholz *et al*, 2005]. In the same study, the morphological and functional features of HSCs and PSCs were also compared by micro-array technology and expression profiling analyses [Buchholz *et al*, 2005]. The results indicated skin fibroblasts were drastically different from hepatic stellate cells and pancreatic stellate cells in extracellular and cell surface genes, signalling molecules and transcription factors [Buchholz *et al*, 2005]. HSCs and PSCs, however, have shown to share high degree of similarities, indicating the

properties of HSCs could potentially be found in PSCs [Buchholz *et al*, 2005]. Of note, mesenchymal stem cells and myofibroblasts are regarded as the source of CAFs in PDAC [von Ahrens *et al*, 2017]. In the present study, patient-derived stellate cells are considered as CAFs. However, further studies are needed to identify the tumour-promoting stellate cells or mesenchymal stem cells or myofibroblasts as CAFs from the tumour-suppressing stellate cells in the patient-derived stellate cells we used.

AsPC-1, BxPC-3, Capan-1, Capan-2, CFPAC-1, HPAC, HPAF-II, Hs 766T, MIA PaCa-2, PANC-1, SU.86.86, SUIT-2, SW 1990, and T3M4 are well-characterized human PDAC cell lines that can proliferate almost indefinitely outside the patients and grow into substantial number of cells to accommodate high-throughput assays [Deer *et al*, 2010; Iwamura *et al*, 1987; Missiaglia *et al*, 2004]. Capan-2 and PANC-1 cell lines possess distinct features representing the heterogeneity of PDAC. For instance, Capan-2 cells are well differentiated while PANC-1 cells are poor differentiated [Deer *et al*, 2010]. *TP53* mutation is detected in PANC-1 cells while Capan-2 cells have wild-type p53 [Deer *et al*, 2010]. They serve as a tool to assess the sensitivity of anti-cancer agents in subgroups of PDAC patients.

Establishing and optimising the 3D co-culture models using human PDAC cell lines with patient-derived stellate cells can overcome the scarcities of primary PDAC cells while maintain the same species' characteristics between the *in vitro* PDAC models and the patients with PDAC. Because stellate cells comprise the majority of the PDAC tissue and acquire the proliferative ability by interacting with PDAC cells [Erkan *et al*, 2012; Ohlund *et al*, 2017], patient-derived stellate cells could be produced in large amount for high-throughput assays with relatively low variation in the laboratory.

Thus, our goal is to improve the co-culture models by simplifying the current protocols, reducing animal-derived matrix and increasing the ratios of stellate cells to cancer cells in a scaffold-free condition. A series of studies have been performed to develop an easy-to-use 3D co-culture model that could be consistent, efficient and economical. One of the criteria was to make sure that a single spheroid with multilayers of stellate cells surrounding the cancer cells could be formed in each well of 96-well plates. Another criterion was to evaluate if 10-20% cell composition in the 3D co-culture models were cancer cells so that the models could mimic the pancreatic cancer environment in the patients diagnosed with late-stage PDAC. Meanwhile, expression and localisation of endogenous YAP was also investigated to study YAP signalling in 3D co-culture PDAC models.

3.2 Validation of cell distribution and protein expression in the 3D scaffold-free co-culture models

3.2.1 Increasing ratio of stellate cells to cancer cells results in reduced spheroid expansion

Due to a lack of reliable detection methods at early stage, about 80% of patients diagnosed with PDAC present locally advanced and metastatic disease, with frequent liver metastasis [GM *et al*, 2018; Lau *et al*, 2017; Neoptolemos *et al*, 2018; Salgado *et al*, 2018; Uccello *et al*, 2018]. Hepatic stellate cells (HSCs) derived from metastatic PDAC in liver share similar features with activated pancreatic stellate cells such as profibrogenesis, contractility, and ECM producing abilities [Erkan *et al*, 2012]. The common ratio of stellate cells to cancer cells reported for modelling 3D co-culture PDAC models is 2:1 [Coleman *et al*, 2014b; Fujiwara *et al*, 2016; Lee *et al*, 2018a; Ware *et al*, 2016], which is lower than the ones detected in the clinical specimens [Neesse *et al*, 2011]. Due to higher supply of HSCs than PSCs from our collaborator, we first attempted to establish a model recapitulating liver metastatic sites in PDAC by exploring the changes in the spheroid size to determine the optimal ratio of stellate cells to cancer cells from 10:1 to 80:1, in order to achieve the a PDAC model with 10% cancer cells [Neesse *et al*, 2011].

Cell suspensions of HSCs and established pancreatic cancer cell lines were mixed in a hanging drop format to form 3D spheroids. After 4 days of culture in these hanging drops, spheroids were transferred to poly-HEMA low-attachment 96-well plates that resulted in the production of one spheroid per well. Phase-contrast imaging was used to follow spheroid growth over time with images being acquired daily from day 4 to day 7. 3D mono-culture of cancer cells were used as a negative control to study the effects of HSCs on cancer cells.

As seen in Figure 19-21, there was a reduction in sphere expansion from day 4 to day 7, as the ratio of HSCs to cancer cells was increased. Comparing spheroid sizes measured on day 4 with the ones on day 7, the expansion in spheroids prepared with an 80:1 ratio of HSCs to Capan-2 cells (40K HSCs with 500 Capan-2 cells) was 14% whereas the expansion in spheroids was 73% in spheroids prepared with a 10:1 ratio of HSCs to cancer cells (5K HSCs with 500 cancer cells). Meanwhile, 3D spheroids prepared with an 80:1 of HSCs to PANC-1 cells did not change significantly over this time frame whereas there was an expansion of 58% and 80% in the group of 10:1 HSCs to PANC-1 cells in two independent experiment. The variability observed for the 10:1 ratio suggests this ratio to be less acceptable based upon our identification of consistency as desired aspect of a viable 3D co-culture format.

Because the data presenting percentages of spheroid size normalized to the ones on day 4 in each individual experiment did not follow normal distribution and not have the same shape of distribution, mean ranks of percentages of spheroid size normalized to the ones on day 4 between groups on four different time points were compared using non-parametric Kruskal-Wallis H test. As seen in Figure 19-21, statistically significant differences in percentages were detected between different days in mono-culture of Capan-2 and PANC-1 whereas not found in mono-culture of HSCs and co-culture of cancer cells with HSCs. The spheroid size of 3D mono-culture of HSCs with the initial number of 5,000 (5K) remained basically unchanged from day 4 to day 7 while nearly 25-30% decrease were seen in mono-cultures of 20,000 (20K) and 40,000 (40K) HSCs on Day 7 compared to Day 4 (Figure 19). Compared with the ones on day 4 (Figure 20-21), the spheroid size of the 3D mono-culture of Capan-2 and PANC-1 with the initial number of 500 cells in hanging drops increased significantly from day 4 to day 7 after

dropping into 96-well plates, with a mean rank of 3.0 for Day 4, 7.5 for Day 5, 12.0 for Day 6 and 17.0 for Day 7, Kruskal-Wallis H = 17.196, p = 0.001 in Capan-2 groups; 3.0 for Day 4, 7.5 for Day 5, 13.0 for Day 6 and 16.0 for Day 7, Kruskal-Wallis H = 15.911, p = 0.001 in PANC-1 groups. Although insufficient statistically power was present in the groups of 3D co-culture spheroids, it is possible that the sample sizes in terms of independent experiments were not large enough to get sufficient information out of the datasets.

When cancer cells and stellate cells encountered in this environment, it was likely that higher number of stellate cells surrounded a few cancer cells, depriving more nutrient, oxygen and space for cancer cells to grow than lower number of stellate cells. However, cancer cells might have had developed mechanisms, for instance, becoming dormant, to survive this harsh environment. Based on the observation that the size of cancer mono-spheres increased overtime whereas the size of mono-spheres with stellate cells remained the same or reduced, the increase in size was likely to be due to the proliferation of cancer cells at the edge of the spheroids. Whether there were cancerous cores full of cancer cells inside the co-culture models would be investigated by cancer cell markers in the next section.

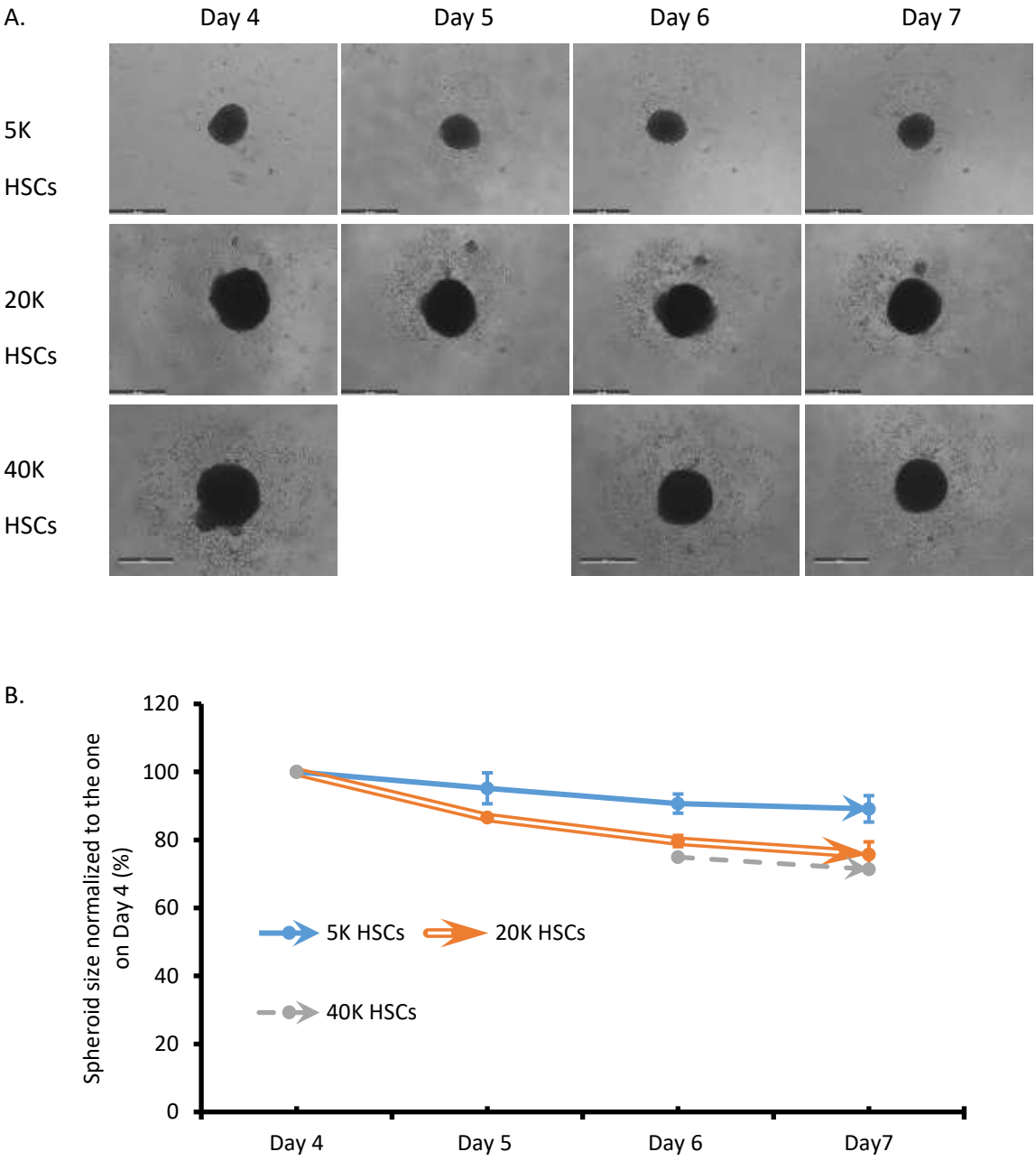

Figure 19. 3D mono-culture of hepatic stellate cells in a hanging drop format.

5,000 (5K), 20,000 (20K) and 40,000 (40K) hepatic stellate cells (HSCs) were grown in a hanging drop format to form 3D mono-cultures. After 4 days, spheroids were transferred to the poly-HEMA low-attachment 96-well plates, resulting in one spheroid per well. A. Phase-contrast live-cell images were acquired by Leica DMI4000 B (50x magnification) daily from day 4 to day 7 after spheroid transfer into 96-well plates. Results of 3D HSCs were from two independent experiments except in the instance where only one independent experiment was done in the groups of 3D culture with 40K HSCs. The images of mono-culture spheroids with 40K HSCs on Day 5 were missing when image analysis was performed. Scale bar, 500 µm. B. Percentages of spheroid sizes on Day 5, Day 6 and Day 7 normalized to the ones on day 4. 4-16 spheroids in each group from two independent experiments were used for calculation (n=2). The areas were measured using CellProfiler. The mean area in pixels of spheroids on day 5, day 6 and day 7 were divided by the mean area in pixels of spheroids on day 4 and then multiplied by 100. Graph was created by Excel, averaging the percentages in each group from two independent experiments except in the group of 40K HSCs. Error bars represented standard deviations from two independent experiments. Non-parametric Kruskal-Wallis H test was used to compare means of four groups.

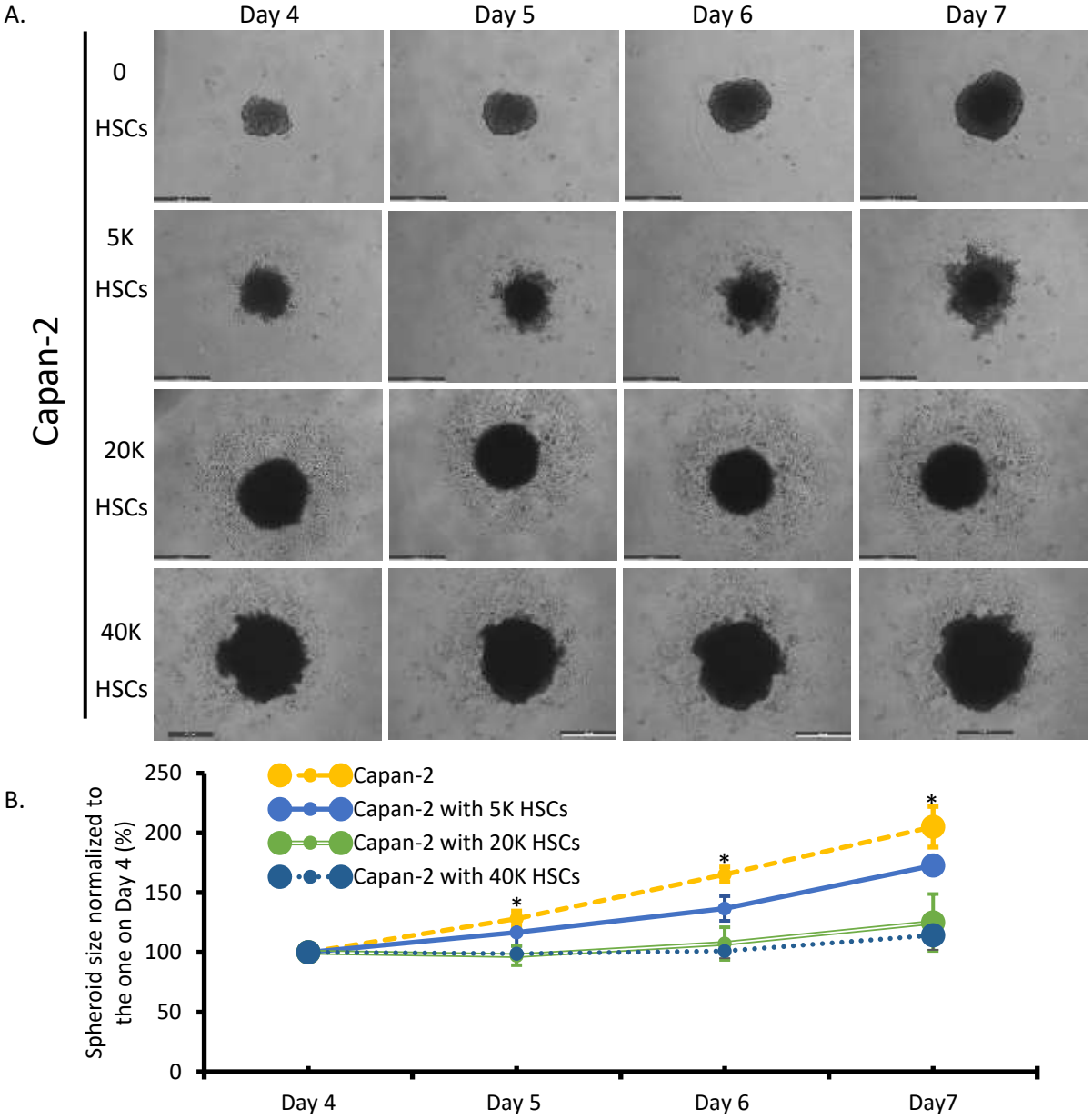

Figure 20. 3D mono-culture of Capan-2 and 3D co-culture of Capan-2 with hepatic stellate cells in a hanging drop format.

0, 5,000 (5K), 20,000 (20K) and 40,000 (40K) hepatic stellate cells (HSCs) were mixed with 500 Capan-2 cells respectively in a hanging drop format to form 3D culture models at 0, 10:1, 40:1 and 80:1 ratios of stellate cells to cancer cells. After 4 days, spheroids were transferred to the poly-HEMA low-attachment 96-well plates, resulting in one spheroid per well. A. Phase-contrast images were acquired by Leica DMI4000 B (50x magnification) daily from day 4 to day 7 after spheroid transfer into 96-well plates. Results of Capan-2 mono-culture were from five independent experiments. Results of co-culture spheroids were from 2-3 independent experiments except in the instance where only one independent experiment was done in the groups of 40K HSCs with Capan-2. Scale bar, 500 µm. B. Percentages of spheroid sizes on Day 5, Day 6 and Day 7 normalized to day 4. 4-16 spheroids in each group from 2-5 independent experiments were used for calculation (n=2-5). The areas were measured using CellProfiler. The mean area in pixels of spheroids on day 5, day 6 and day 7 were divided by the mean area in pixels of spheroids on day 4 and then multiplied by 100. Graph was created by Excel, averaging the percentages from 2-5 independent experiments in each group. Error bars represented standard deviations from 2-5 independent experiments. *P*-value was calculated using non-parametric Kruskal-Wallis H test. *: $P<0.05$.

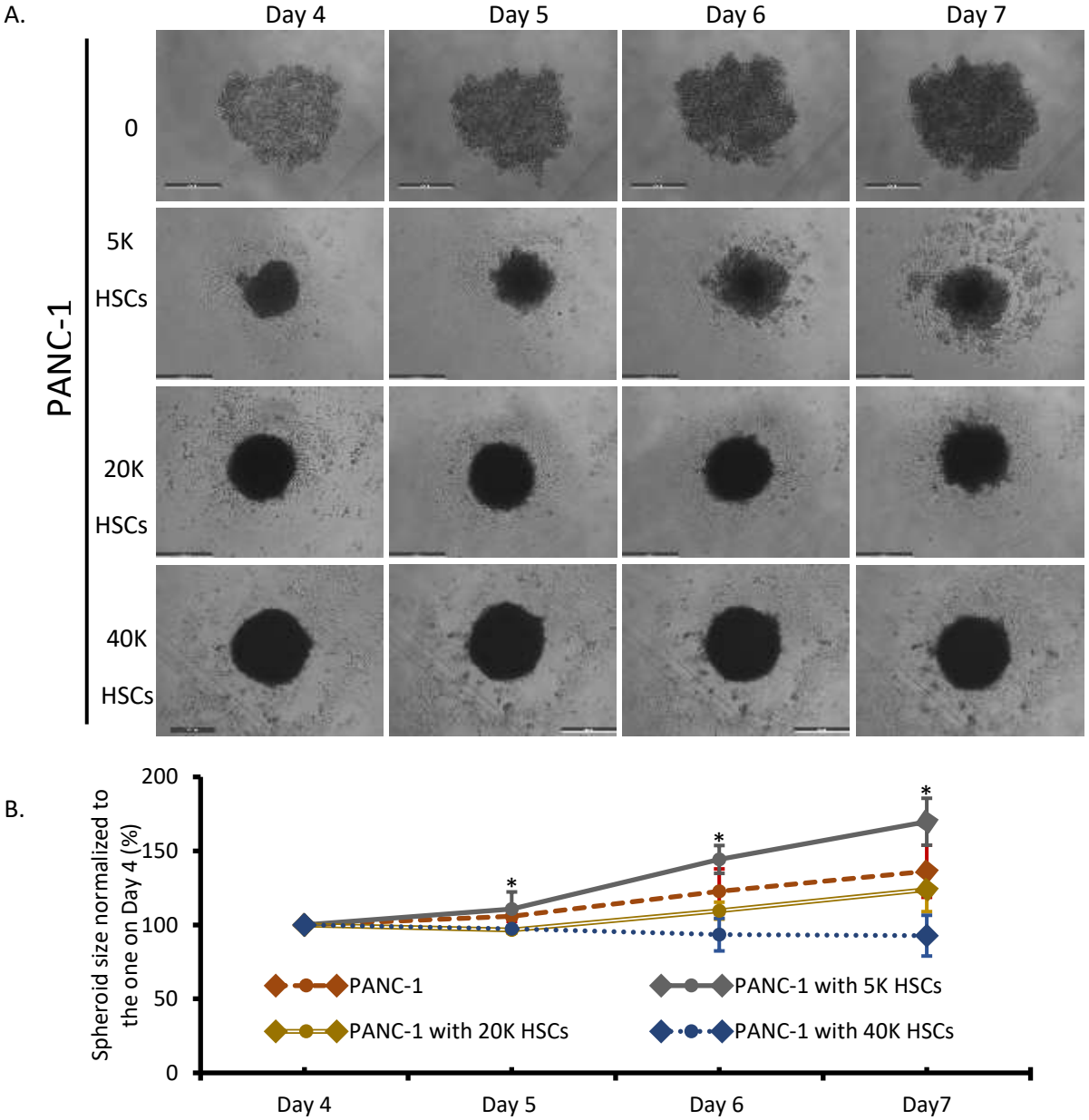

Figure 21. 3D mono-culture of PANC-1 and 3D co-culture of PANC-1 with hepatic stellate cells.

0, 5,000 (5K), 20,000 (20K) and 40,000 (40K) hepatic stellate cells (HSCs) were mixed with 500 PANC-1 cells respectively in a hanging drop format to form 3D culture models at 0, 10:1, 40:1 and 80:1 ratios of stellate cells to cancer cells. After 4 days, spheroids were transferred to the poly-HEMA low-attachment 96-well plates, resulting in one spheroid per well. A. Phase-contrast images were acquired by Leica DMI4000 B (50x magnification) daily from day 4 to day 7 after spheroid transfer into 96-well plates. Results of PANC-1 mono-culture were from five independent experiments. Results of co-culture spheroids were from 2-3 independent experiments except in the instance where only one independent experiment was done in the groups of 40K HSCs with PANC-1. Scale bar, 500 µm. B. Percentages of spheroid sizes on Day 5, Day 6 and Day 7 normalized to day 4. 4-16 spheroids in each group from 2-5 independent experiments were used for calculation (n=2-5). The areas were measured using CellProfiler. The mean area in pixels of spheroids on day 5, day 6 and day 7 were divided by the mean area in pixels of spheroids on day 4 and then multiplied by 100. Graph was created by Excel, averaging the percentages from 2-5 independent experiments in each group. Error bars represented standard deviations from 2-5 independent experiments. *P*-value was calculated using non-parametric Kruskal-Wallis H test. *: $P<0.05$.

3.2.2 Increasing ratio of stellate cells to cancer cells is associated with reduced localization of cancer cells outside hepatic stellate cells cores

Mutations within the *TP53* that affect expression and actions of p53 are associated with PDAC malignancy [Cicenas *et al*, 2017]. Although low level of p53 was detected in rat hepatic stellate cells (HSCs) [Jeong *et al*, 2005; Longxi *et al*, 2011; Zhao *et al*, 2016a], p53 expression was stronger in cancer cells than adjacent non-cancerous cells in tumour biopsies from patients with PDAC [Dong *et al*, 2000; Jeong *et al*, 2005; Zhao *et al*, 2016a]. Therefore, we chose p53 as the cancer cell marker to detect the cancer cells and cell distribution in the current 3D co-culture spheroids with human cancer cells and human hepatic stellate cells.

At first, we validated the total cellular p53 expression in mono-culture spheroids and co-culture spheroids using immunoblotting. Also, we tested whether hepatic stellate cells promote or inhibit cancer cell growth by comparing the total p53 protein changes. HSCs and cancer cells were co-cultured in hanging drops for 4 days to form 3D spheroids, transferred and grown in 96-well plates for another 3 days. 20 spheroids were collected for protein analysis by immunoblotting on day 4 and day 7. Because the spheroids collected in each group, the volume used to lyse the same number of spheroids and load the protein samples into the gel for immunoblotting was the same across mono-culture and co-culture spheroids, the total protein could be expected to be proportional to the total number of cells sampling.

As can be seen in Figure 22, p53 was not found in mono-culture spheroids of HSCs whereas there was a clear band at 55 kDa when the spheroids included Capan-2 and PANC-1 cells, suggesting that HSCs cultured in this condition did not express p53 and the p53 protein from cancer cells contributed to the p53 levels in the 3D co-culture models. The bands at 55 kDa appeared weaker when the spheroids were formed from higher ratio of HSCs to cancer cells (40:1) than the ones from lower ratio (10:1).

Because all the cells in the 3D mono-culture spheroids, 1 to 10 of total cells in the 3D co-culture spheroids, and 1 to 40 of the total cells in the 3D co-culture spheroids should be cancer cells, we postulated that fewer cells expressing p53 should be expected to drop proportionally in the co-culture models. The absolute p53 intensities of bands at 55 kDa in Figure 23, however, demonstrated that there was a nonlinear decline in p53 intensities as the number of cancer cells co-cultured with HSCs decreased. Meanwhile, the intensities of GAPDH fluctuated, sometimes constant or increased, among groups of mono-culture of cancer cells, co-culture of cancer cells with 5K HSCs and co-culture of cancer cells with 20K HSCs in Figure 24. The saturation of primary antibodies and secondary antibodies was considered to be negligible because both membranes containing groups with Capan-2 cells and PANC-1 cells respectively were incubated with the same solutions with the antibodies in one run of immunoblotting. It appeared that the decrease in p53 intensities was not proportional to the dropping of number of cancer cells in the co-culture models, indicating different growth rates in 3D mono-culture and 3D co-culture of cancer cells. After being normalized to levels of the housekeeping protein GAPDH, reduction of p53 expression was found in most co-culture spheroids composed of HSCs with cancer cells on day 4 and day 7 comparing to mono-culture spheroids of cancer cells in Figure 25. An exception was observed in one individual experiment where a higher level of p53 expression was found when spheroids of PANC-1 co-cultured with 5K HSCs on day 4 than the one of mono-culture spheroids of PANC-1 cells on day 4. The inconsistent data suggest the requirement of more independent experiments using immunoblotting to test the correlation of p53 expression with the number of HSCs

in the current models. Whether the decrease in p53 level was due to the dilution of cancer cells in the co-culture models needs to be determined.

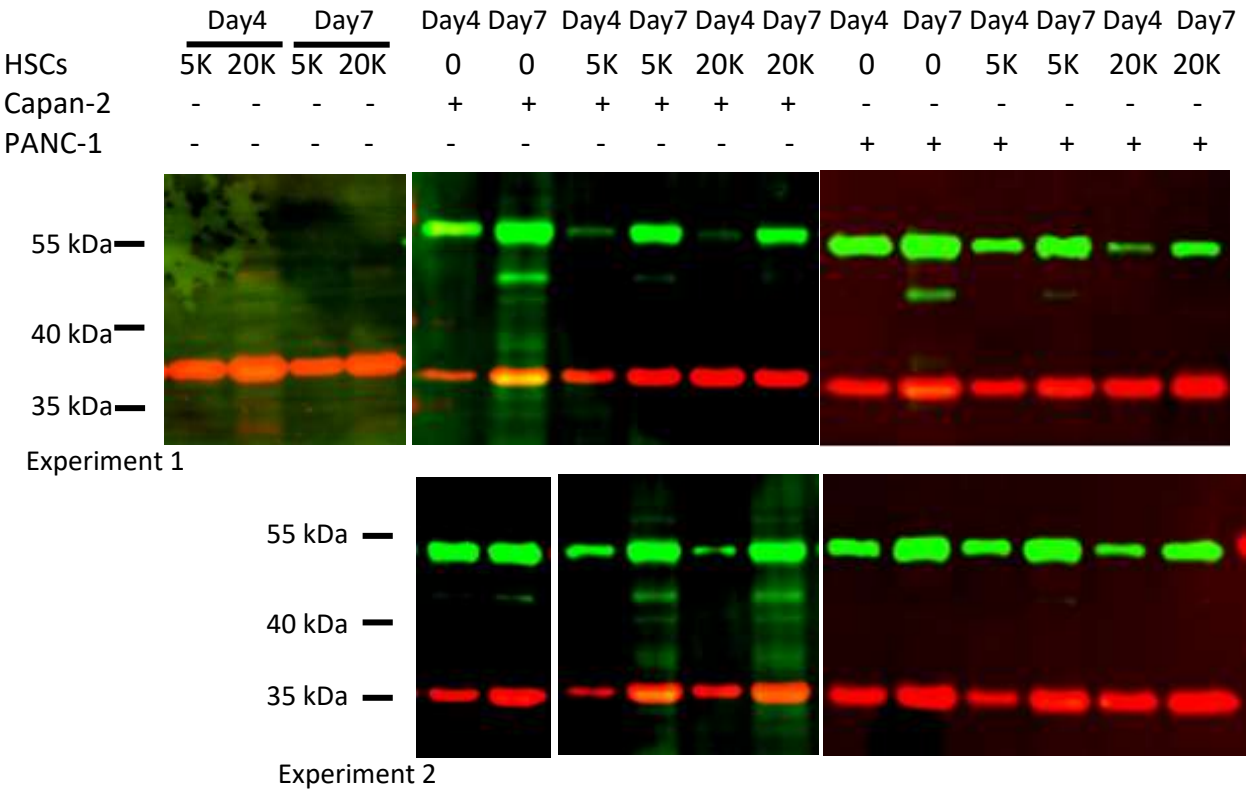

Figure 22. Immunoblotting analysis of p53 expression in 3D mono-culture and 3D co-culture.

0, 5,000 (5K) and 20,000 (20K) hepatic stellate cells (HSCs) were mixed with 500 Capan-2 or PANC-1 cells respectively in a hanging drop format to form the co-culture models at 0, 10:1 and 20:1 ratios of stellate cells to cancer cells. 3D mono-culture of HSCs were grown in parallel. After 4 days, spheroids were transferred to the polyHEMA low-attachment 96-well plates, resulting in one spheroid per well. Immunoblotting analysis of p53 were performed on the indicated time points. Twenty spheroids in each group were lysed in 100 µL RIPA buffer to extract the total protein on day 4 and day 7. 6 µL of the cell lysate was loaded into the wells of SDS-PAGE gel. Two-colour near-infrared detection was performed to detect p53 (green) and GAPDH (red) simultaneously. Two datasets from two independent experiments in 3D mono-culture of cancer cells and 3D co-culture of cancer cells with HSCs were presented. One dataset from two independent experiments in 3D mono-culture of HSCs were presented.

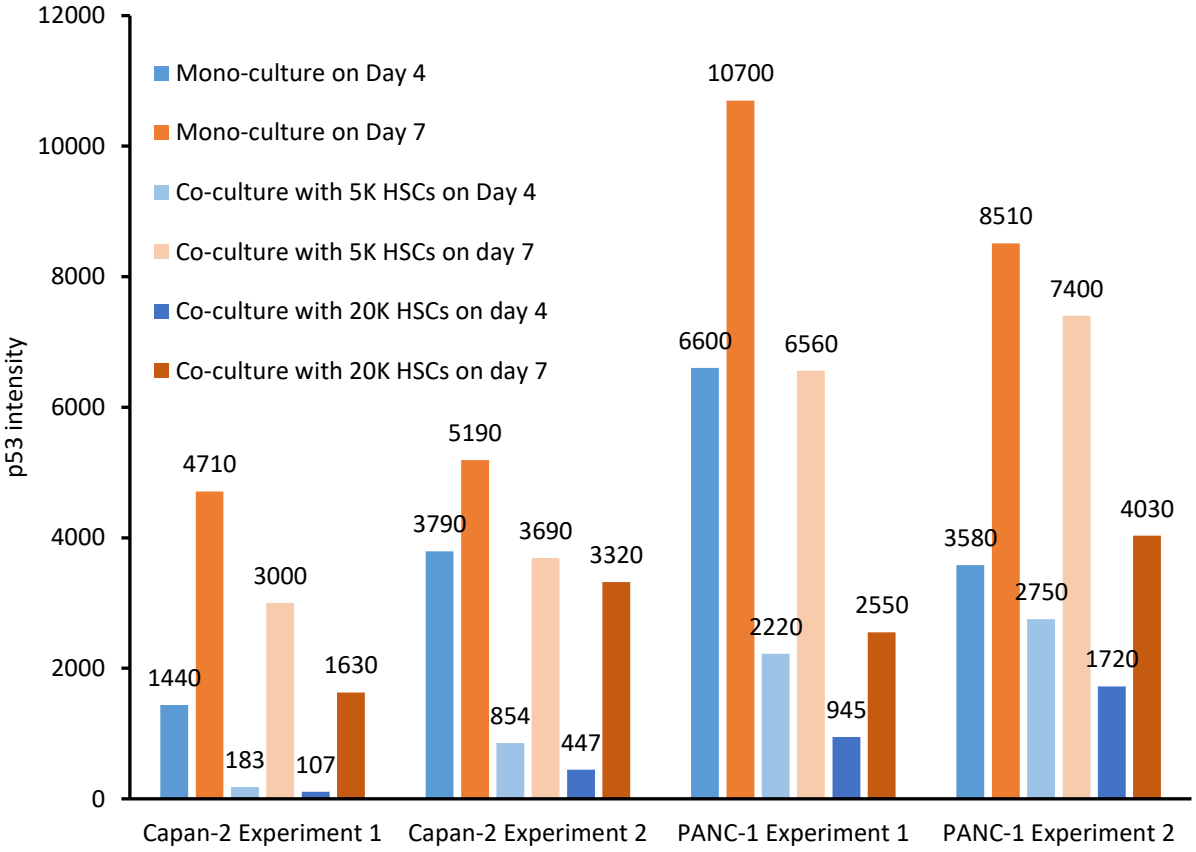

Figure 23. Quantification of absolute p53 expression in 3D mono-culture and 3D co-culture.

0, 5,000 (5K) and 20,000 (20K) hepatic stellate cells (HSCs) were mixed with 500 Capan-2 or PANC-1 cells respectively in a hanging drop format to form the co-culture models at 0, 10:1 and 20:1 ratios of stellate cells to cancer cells. After 4 days, spheroids were transferred to the polyHEMA low-attachment 96-well plates, resulting in one spheroid per well. Immunoblotting analysis of p53 expression were performed on the indicated time points. Twenty spheroids in each group were lysed in 100 µL RIPA buffer to extract the total protein on day 4 and day 7. 6 µL of the cell lysate was loaded into the wells of SDS-PAGE gel. The groups with Capan-2 cells were run on the same gel. Meanwhile, the groups with PANC-1 cells were run on the other gel. The two gels were transferred in the same blot module and the same chamber. The membranes were incubated with the same batch of dilutions of antibodies in blocking buffer. Two-colour near-infrared detection was performed to detect p53 and GAPDH simultaneously. The intensities of p53 were analysed by Licor ImageStudio and graphed using Excel. Data from two independent experiments in 3D mono-culture of cancer cells and 3D co-culture of cancer cells with HSCs were presented. The absolute values of intensities were shown.

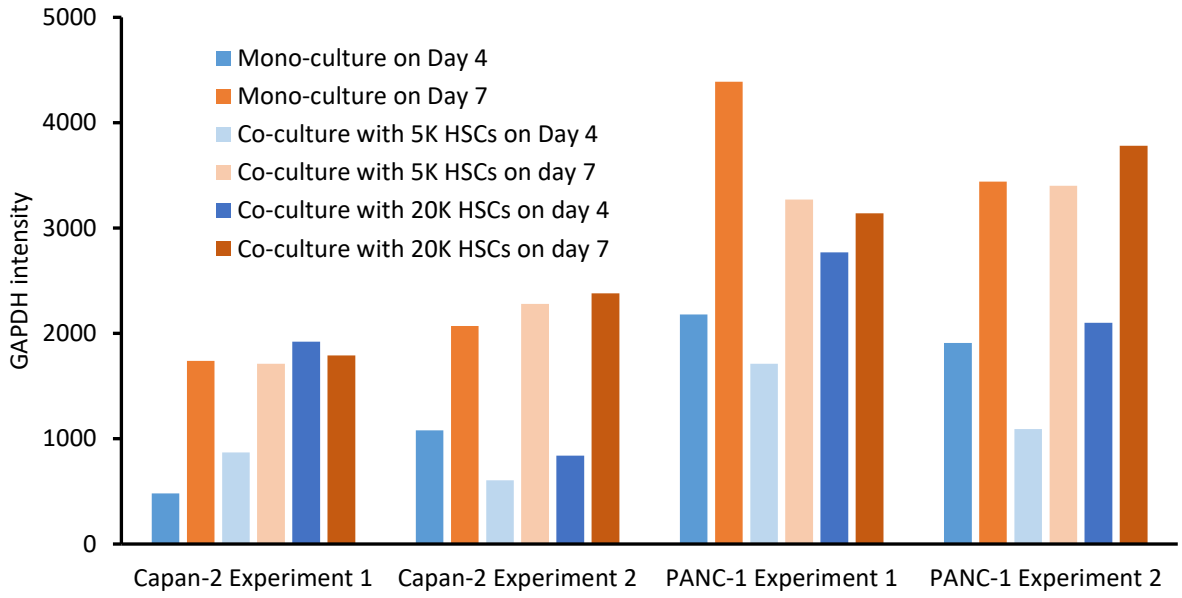

Figure 24. Quantification of absolute GAPDH expression in 3D mono-culture and 3D co-culture.

0, 5,000 (5K) and 20,000 (20K) hepatic stellate cells (HSCs) were mixed with 500 Capan-2 or PANC-1 cells respectively in a hanging drop format to form the co-culture models at 0, 10:1 and 20:1 ratios of stellate cells to cancer cells. After 4 days, spheroids were transferred to the polyHEMA low-attachment 96-well plates, resulting in one spheroid per well. Immunoblotting analysis of p53 expression were performed on the indicated time points. Twenty spheroids in each group were lysed in 100 µL RIPA buffer to extract the total protein on day 4 and day 7. 6 µL of the cell lysate was loaded into the wells of SDS-PAGE gel. The groups with Capan-2 cells were run on the same gel. Meanwhile, the groups with PANC-1 cells were run on the other gel. The two gels were transferred in the same blot module and the same chamber. The membranes were incubated with the same batch of dilutions of antibodies in blocking buffer. Two-colour near-infrared detection was performed to detect p53 and GAPDH simultaneously. The intensities of GAPDH were analysed by Licor ImageStudio and graphed using Excel. Data from two independent experiments in 3D mono-culture of cancer cells and 3D co-culture of cancer cells with HSCs were presented.

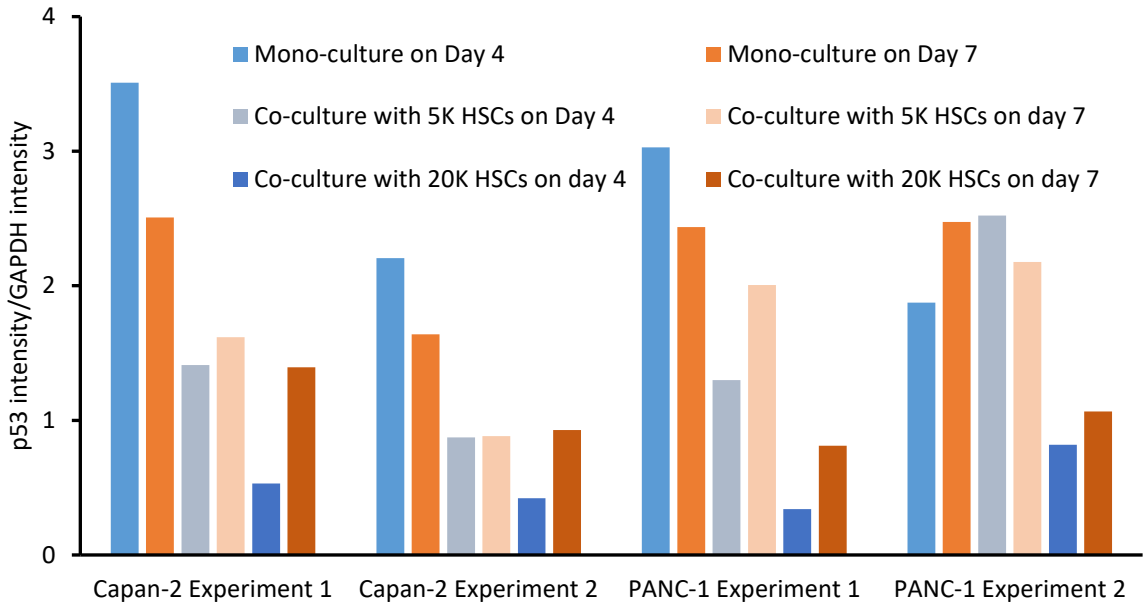

Figure 25. Normalisation of p53 expression to GAPDH in 3D mono-culture and 3D co-culture.

0, 5,000 (5K) and 20,000 (20K) hepatic stellate cells (HSCs) were mixed with 500 Capan-2 or PANC-1 cells respectively in a hanging drop format to form the co-culture models at 0, 10:1 and 20:1 ratios of stellate cells to cancer cells. After 4 days, spheroids were transferred to the polyHEMA low-attachment 96-well plates, resulting in one spheroid per well. Immunoblotting analysis of p53 expression were performed on the indicated time points. Twenty spheroids in each group were lysed in 100 µL RIPA buffer to extract the total protein on day 4 and day 7. 6 µL of the cell lysate was loaded into the wells of SDS-PAGE gel. The groups with Capan-2 cells were run on the same gel. Meanwhile, the groups with PANC-1 cells were run on the other gel. The two gels were transferred in the same blot module and the same chamber. The membranes were incubated with the same batch of dilutions of antibodies in blocking buffer. Two-colour near-infrared detection was performed to detect p53 and GAPDH simultaneously. The intensities of p53 and GAPDH were analysed by Licor ImageStudio. Normalization of p53 intensities to GAPDH intensities were calculated and graphed using Excel. Data from two independent experiments in 3D mono-culture of cancer cells and 3D co-culture of cancer cells with HSCs were presented.

The total amount of p53 analysed by immunoblotting was not able to provide us with the details of cancer cell distribution in the 3D co-culture models, such as whether cancer cells were located at the core of the spheroids. In order to investigate the distribution of cancer cells and stellate cells in these co-cultures, whole spheroids were fixed in PFA, stained for p53 and confocal laser scanning microscopy (CLSM) using Zeiss LSM880 was performed using one optical sectioning through the largest area of a spheroid, representing the detection near the core of the spheroid. As can be seen in Figure 26-28, HSCs showed little nuclear staining for p53 with the non-specific signal from p53 channel coming from the outside of the nuclei. Meanwhile, cancer cells showed strong nuclear p53 staining (Figure 27 and 28). Interestingly, the p53 expression was stronger near the edge of the spheroids than in the spheroid core. Examples where p53 staining was negative in a number of cancer cells at the edge of the spheroids with easy access to antibodies were observed, as shown in red arrows in Figure 27 and 28. It was possible that these negative staining outcomes were due to inappropriate storage of samples at the moment when the samples were not protected by low temperature, resulting in the deterioration of fluorophores. There was little possibility that the cancer cells at the edge of the spheroids co-cultured with 20K HSCs did not express p53 because p53 expression in those spheroids was detected using immunoblotting as shown in Figure 22. Another line of evidence that p53 was expressed in the co-culture models with high ratio of stellate cells to cancer cells was illustrated in Figure 29, where Capan-2 and PANC-1 cells near the edge of the spheroids co-cultured with 40K HSCs were p53 positive using higher laser power than the ones in Figure 26-28. Judging from the enlarged nuclei observed in cancer cells demonstrated by DAPI staining (red arrows), a second criterion of the nuclear size and morphology could be employed to discriminate cancer cells from HSCs. In general, the regions of cancer cells identified by this criteria were also reduced as the number of HSCs increased in the current 3D co-culture models.

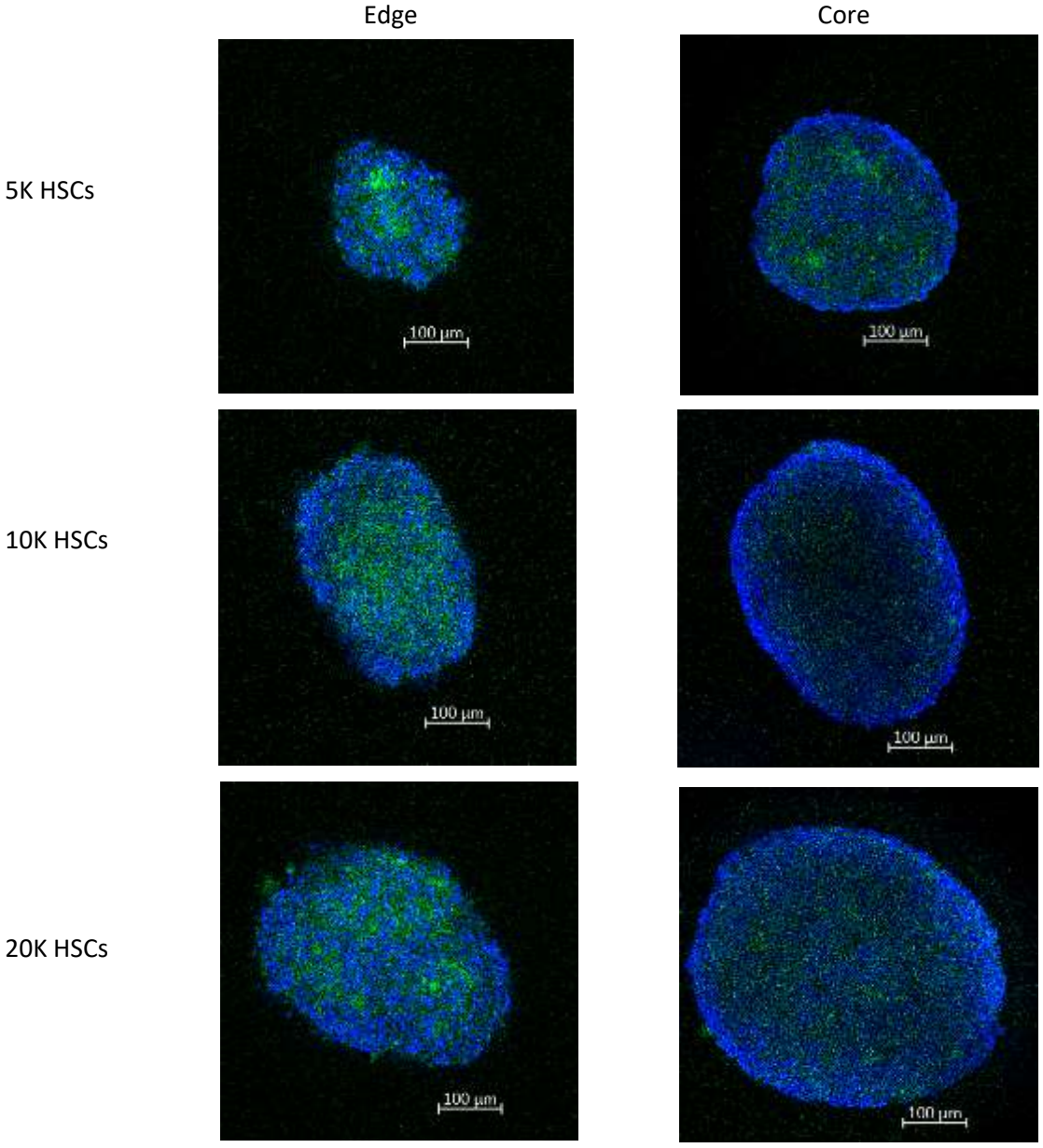

Figure 26. Immunofluorescence analysis of p53 expression in intact 3D mono-culture of hepatic stellate cells.

5,000 (5K), 10,000 (10K), and 20,000 (20K) hepatic stellate cells (HSCs) were grown in a hanging drop format to form 3D mono-culture spheroids. After 4 days, spheroids were transferred to the polyHEMA low-attachment 96-well plates, resulting in one spheroid per well. After 3 days, whole spheroids were fixed in PFA and stained with DAPI and anti-p53 antibodies using immunofluorescence. Confocal laser scanning microscopy using Zeiss LSM880 was performed on intact spheroids near the edge and the core of the spheroids. Image analysis was performed in Zen 2.3 (blue edition). Representative images from two spheroids in one independent experiment were shown (n=1). Scale bar, 100 µm.

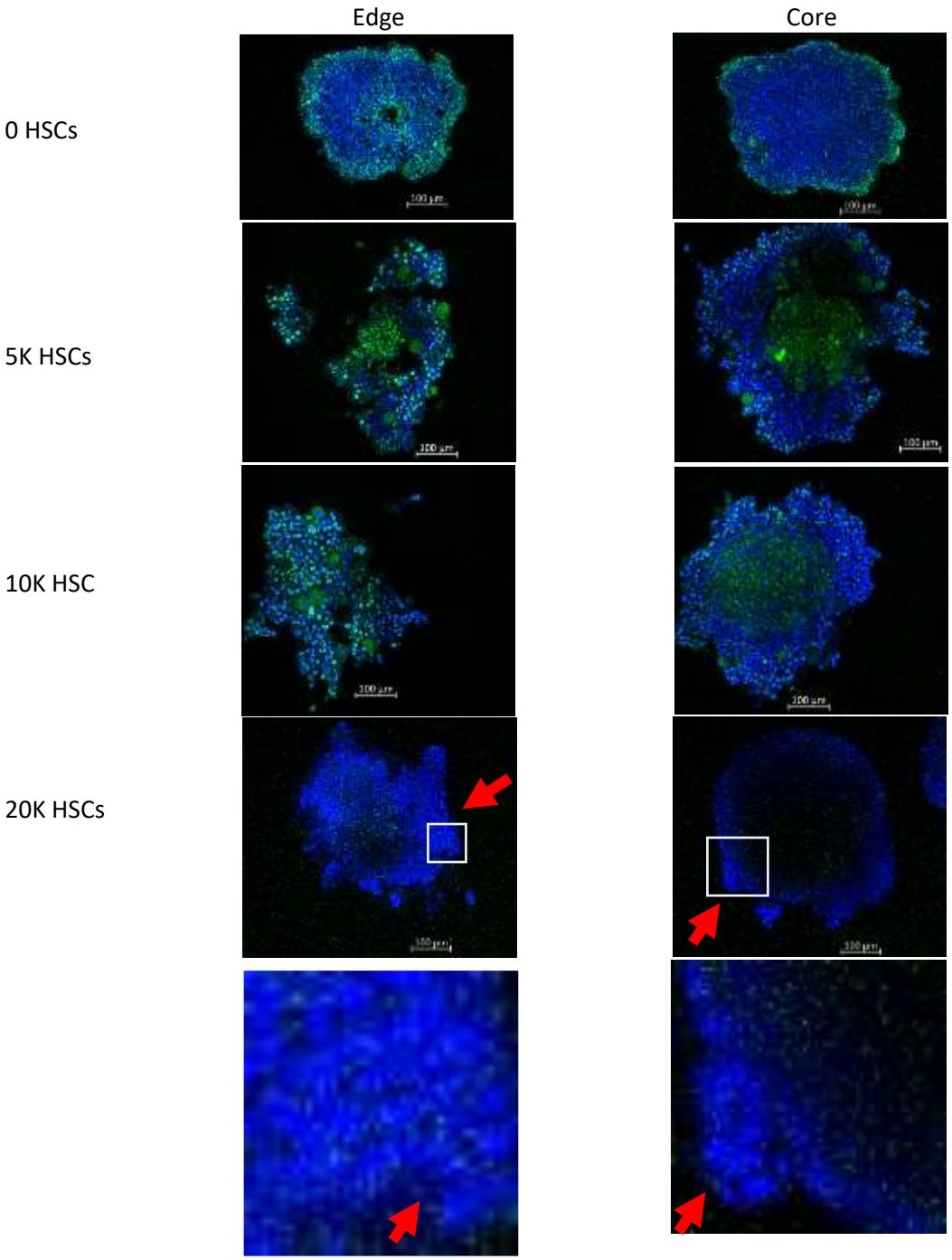

Figure 27. Immunofluorescence analysis of p53 expression in intact 3D mono-culture of Capan-2 cells and 3D co-culture of Capan-2 cells with hepatic stellate cells.

0, 5,000 (5K), 10,000 (10K), and 20,000 (20K) hepatic stellate cells (HSCs) were mixed with 500 Capan-2 respectively in a hanging drop format to form the 3D models at 0, 10:1, 20:1 and 40:1 ratios of stellate cells to cancer cells. After 4 days, spheroids were transferred to the polyHEMA low-attachment 96-well plates, resulting in one spheroid per well. After 3 days, whole spheroids were fixed in PFA and stained with DAPI and anti-p53 antibodies using immunofluorescence. Confocal laser scanning microscopy using Zeiss LSM880 was performed on intact spheroids near the edge and the core of the spheroids. Image analysis was performed in Zen 2.3 (blue edition). Representative images from two spheroids in one independent experiment were shown (n=1). Red arrows: p53 negative Capan-2 cells. Scale bar, 100 µm.

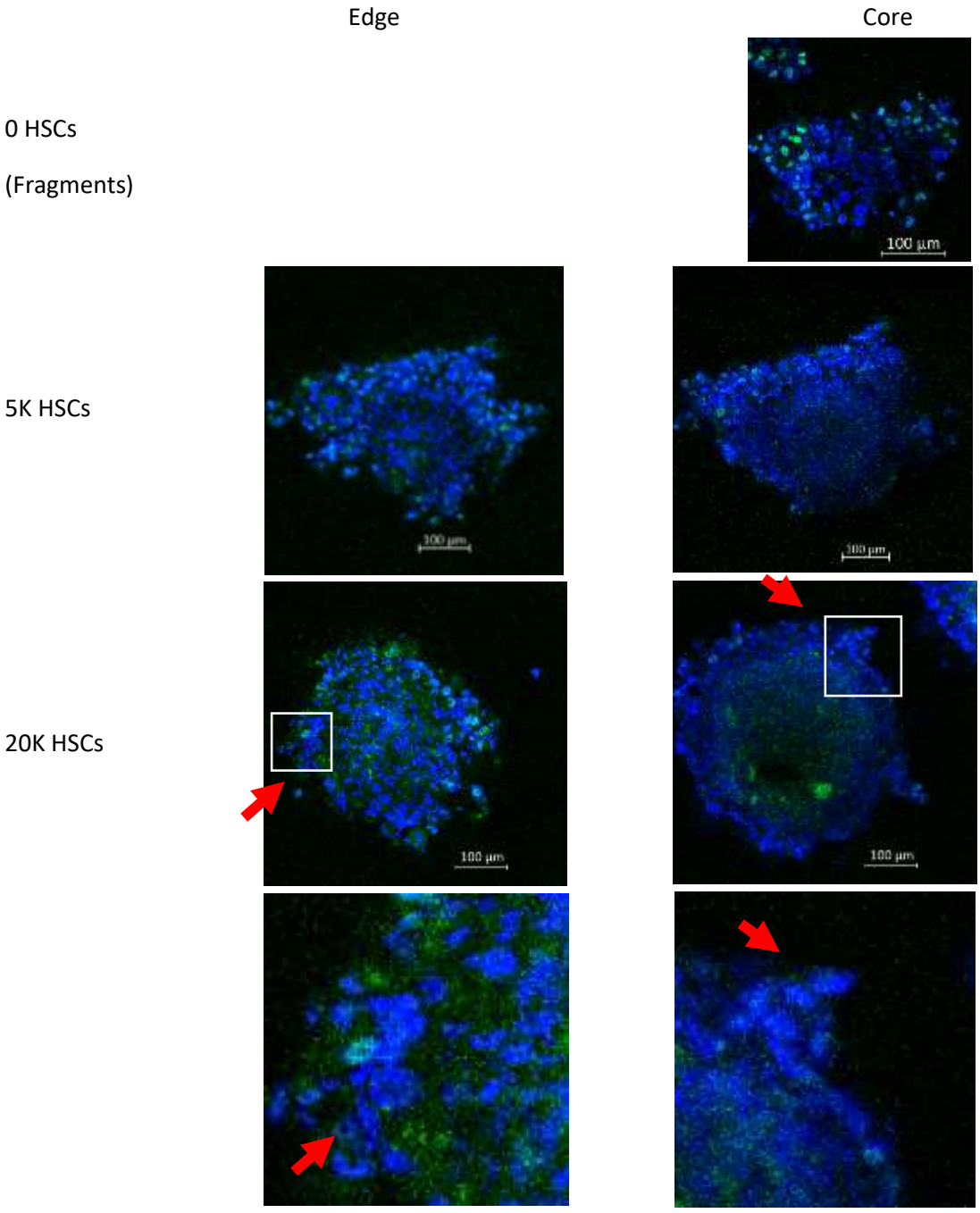

Figure 28. Immunofluorescence analysis of p53 expression in intact 3D mono-culture of PANC-1 cells and 3D co-culture of PANC-1 cells with hepatic stellate cells.

0, 5,000 (5K), and 20,000 (20K) hepatic stellate cells (HSCs) were mixed with 500 PANC-1 cells respectively in a hanging drop format to form the 3D models at 0, 10:1, and 40:1 ratios of stellate cells to cancer cells. After 4 days, spheroids were transferred to the polyHEMA low-attachment 96-well plates, resulting in one spheroid per well. After 3 days, whole spheroids were fixed in PFA and stained with DAPI and anti-p53 antibodies using immunofluorescence. Confocal laser scanning microscopy using Zeiss LSM880 was performed on intact spheroids near the edge and the core of the spheroids. Image analysis was performed in Zen 2.3 (blue edition). Representative images from two spheroids in one independent experiment were shown (n=1). Red arrows: p53 negative PANC-1 cells. Scale bar, 100 µm.

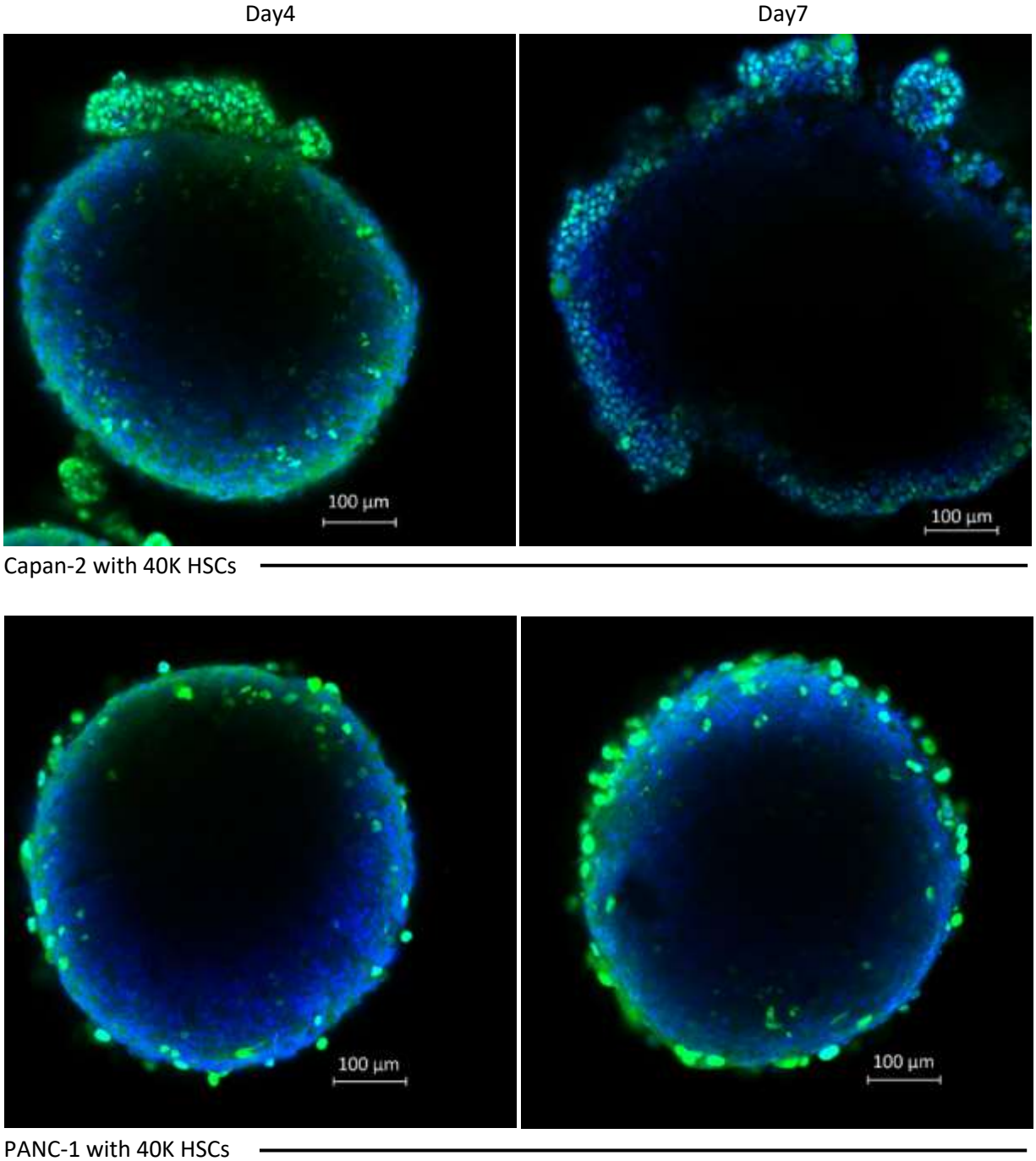

Figure 29. Immunofluorescence analysis of p53 expression in intact 3D co-culture of cancer cells with hepatic stellate cells using high laser power.

40,000 (40K) hepatic stellate cells (HSCs) were mixed with 500 Capan-2 or PANC-1 cells respectively in a hanging drop format to form the co-culture models at a 80:1 ratio of stellate cells to cancer cells. After 4 days, some spheroids were transferred to the polyHEMA low-attachment 96-well plates while the rest were fixed in PFA. After 3 days when the total growth time was 7 days, spheroids in the plates were fixed in PFA and immunofluorescence was performed on the whole spheroids collected on day 4 and day 7. Fluorescent images were acquired by confocal laser scanning microscopy (CLSM) using Zeiss LSM880. Image analysis was performed in Zen 2.3 (blue edition). Staining with DAPI (blue) and for p53 (green) was shown. Laser power for CLSM was over 30%. Representative images were from two spheroids in one independent experiment. Scale bar, 100 µm.

The immunofluorescence microscopy was optimized by an optical clearing protocol of samples and the use of multi-photon (MP) imaging was attempted to test the performance in detecting thick specimen. An effort was also made to examine potential antibody staining differences due to the antibody penetration between the core and edge of spheroids by acquiring images using CLSM and MP procedures to allow for improved p53 visualization at the spheroid core. As seen in Figure 30, clearing with ethanol and mixture of benzyl alcohol and benzyl benzoate at 1:2 (v/v, BABB) allowed improved consistency for nuclear staining with DAPI and p53 immuno-staining at the spheroid core. With the help from Anne Gesell in Microscopy and Analysis Suit (MAS), wavelengths were optimised with scanning from 690 – 980 nm between 10 to 40 nm wavebands for 3-coloured MP imaging using DAPI, anti-p53 antibodies and anti-YAP antibodies as representatives to incubate a co-culture spheroids with PANC-1 cells and 5K HSCs. The image acquired at 950 nm with the BP filter of 500-550 nm exhibited the best signal from the staining for p53 with least interference from the staining of DAPI and for YAP (Figure 31). As a result, when the secondary antibodies linked to Alexa Fluor 488 were used in combination with primary anti-p53 antibodies, 950 nm and the BP filter of 500-550 nm was selected as the optimal excitation and emission wavelengths.

After optical clearing, CLSM and MP imaging were performed and p53 intensities were calculated by matching same cell outcomes identified by the CellProfiler software as shown in Figure 32. Nine cells in the spheroid core region were considered representatives of cancer cells positively stained with p53. Seventeen cells were selected in the region of the spheroid edge as representatives of cancer cells positively stained with p53. Because the data presenting p53 intensities divided by areas did not follow normal distribution and not have the same shape of distribution, mean ranks were compared using non-parametric Kruskal-Wallis H test. By comparing all the values of the p53 intensity divided by the area used to extract the intensity in each individual cell, there was no significant difference between the p53 expression levels in the cells near the core of the spheroids compared to those at the edge of the spheroids by Kruskal-Wallis H test with mean rank of 29.65 for the cells in the core by CLSM scanning, 25.13 for the cells near the edge by CLSM scanning, 23.12 for the cells in the core by MP scanning and 22.13 for the cells near the edge by MP scanning (p = 0.519). Henceforth, MP scanning will not be conducted in the following sections whereas optical clearing with CLSM will be used due to the improvement in the visualization of 3D spheroids.

Taken together, two to four cells could be demonstrated to be p53 positive inside the stellate cells core, indicating the presence of cancer cells among stellate cells. However, no cancer cell clusters with more than ten cells or ductal structures were formed in the co-culture spheroids even when the ratio of stellate cells to cancer cells reached 80:1. We decided to discontinue the work presented in this section to explore other approaches in the next sections because of two major reasons: 1) the data presented in this section failed to indicate any potential for the stellate cells to wrap around the cancer cells in scaffold-free conditions to form multiple layers of stellate cells around cancer cells core; 2) the number of stellate cells required in the models may be too high, possibly resulting in consuming unnecessary large number of stellate cells in one run.

An intact spheroid without optical clearing

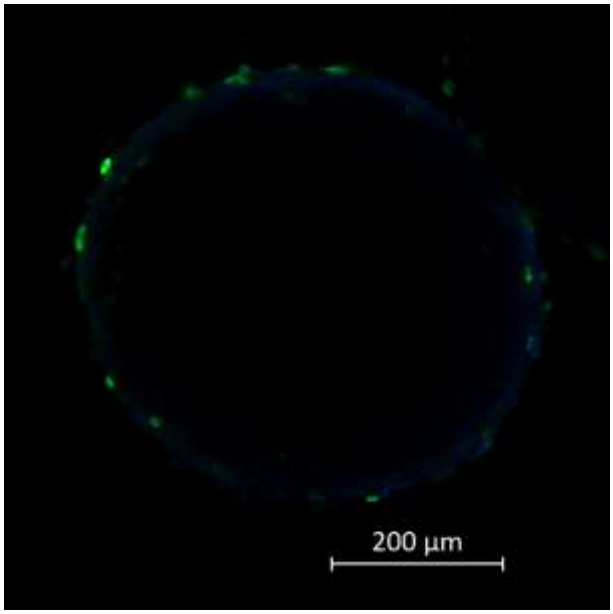

An intact spheroid with optical clearing

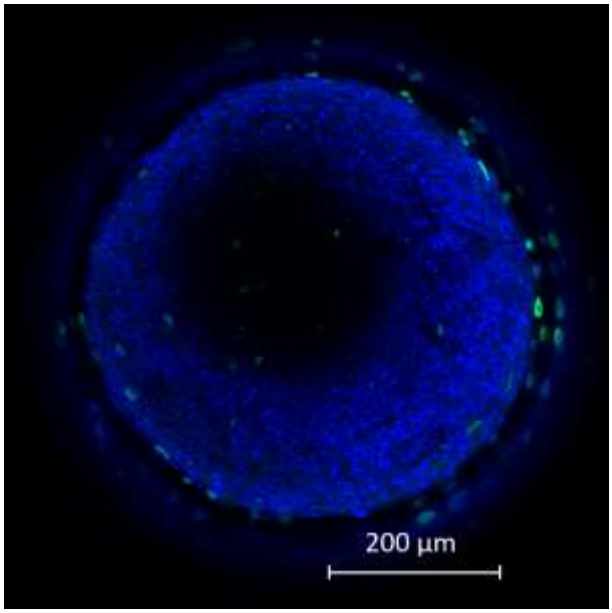

Figure 30. Effects of optical clearing on large intact spheroids.

40,000 (40K) hepatic stellate cells (HSCs) were mixed with 500 PANC-1 cells respectively in a hanging drop format to form the co-culture models at a 80:1 ratio of stellate cells to cancer cells. After 4 days, spheroids were fixed in PFA and immunofluorescence was performed on the whole intact spheroids. Spheroids were stained with anti-p53 antibodies (green) and DAPI (blue). Spheroids with or without optical clearing using mixture of benzyl alcohol and benzyl benzoate at 1:2 (v/v, BABB) were scanned near the core by confocal laser scanning microscopy using Zeiss LSM880. Image analysis was performed in Zen 2.3 (blue edition). Histogram indicated consistent brightness and contrast were used to export the images. Representative images were from six spheroids of 40K HSCs with Capan-2 cells in one independent experiment. Scale bar, 200 µm.

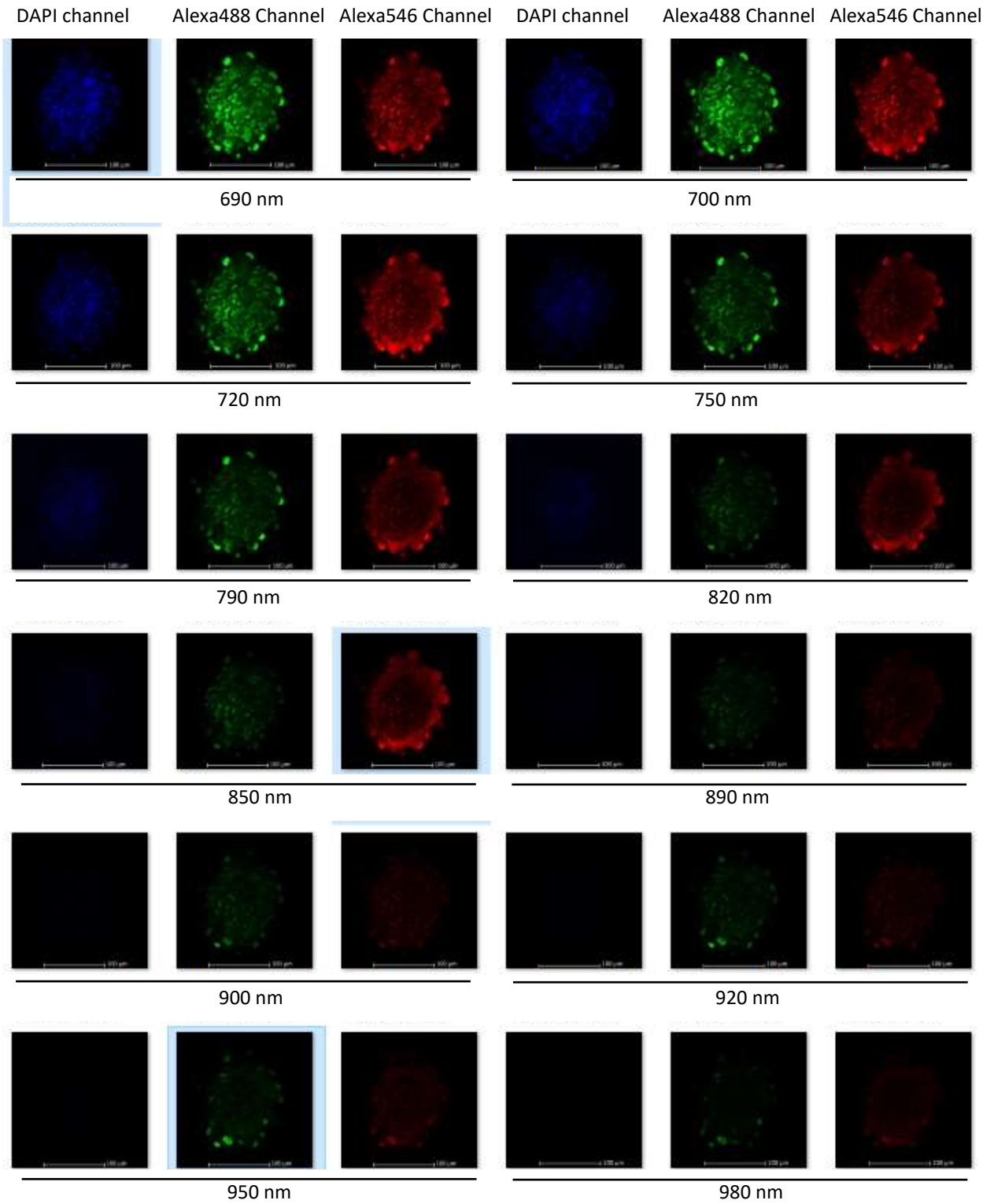

Figure 31. Multi-photon scanning from 690 – 980 nm of a co-culture spheroid.

5,000 (5K) hepatic stellate cells were mixed with 500 PANC1 cells respectively in a hanging drop format. After 4 days, whole spheroids were fixed in PFA and stained with DAPI, anti-p53 antibodies with secondary antibody conjugated to Alexa Fluo 488 (green) and anti-YAP antibodies with secondary antibody conjugated to Alexa Fluo 546 (red), using immunofluorescence. Optical clearing with BABB was performed. Multi-photon microscopy using Zeiss LSM880 with Spectra Physics multiphoton lasers was performed near the core of an intact spheroid, with 10-40 nanometre wavebands from 690 – 980 nm on one optical slide. Image analysis was performed in Zen 2.3 (blue edition). Representative images from one spheroids in one independent experiment were shown (n=1). Scale bar, 100 µm.

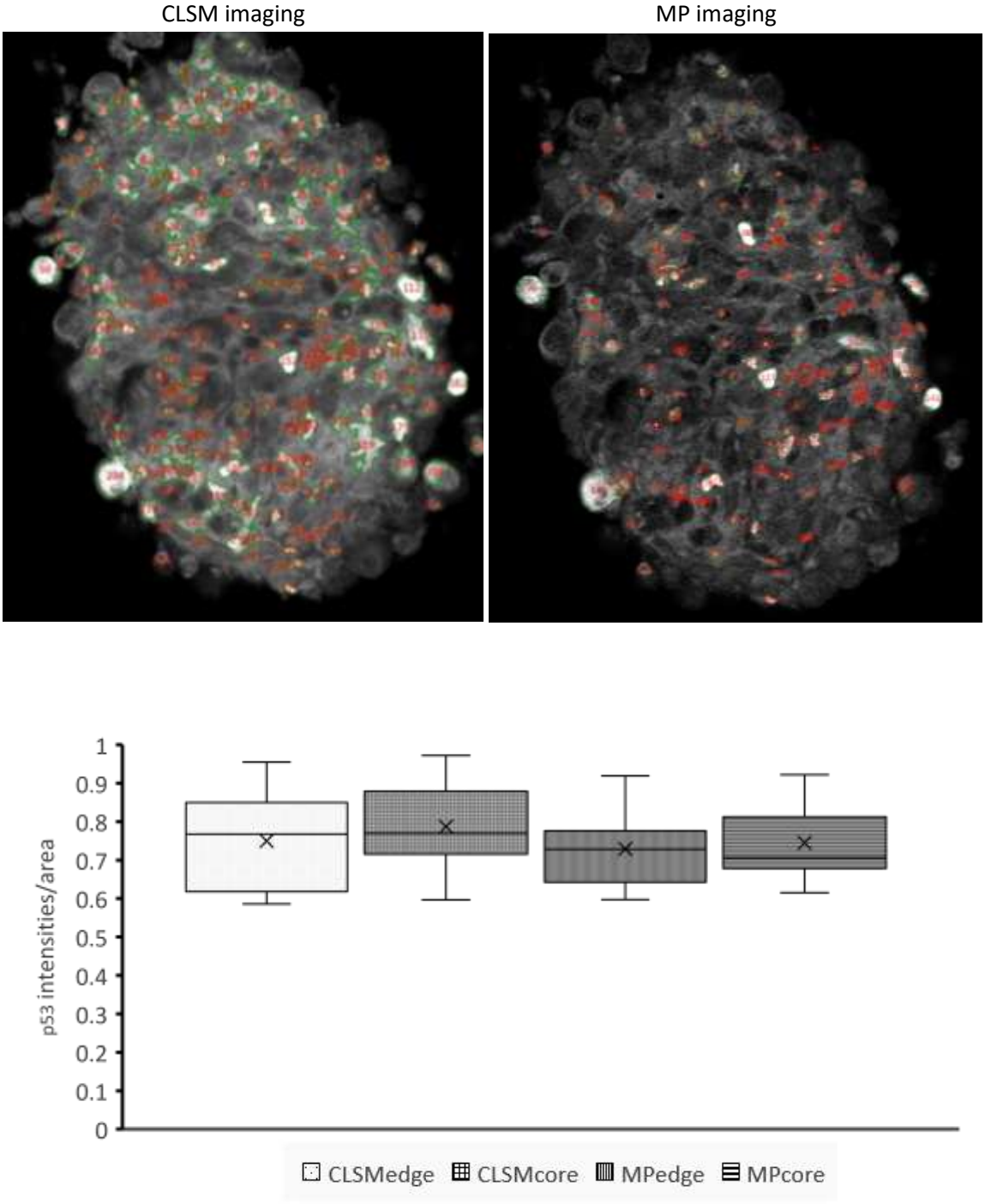

Figure 32. Semi-quantification of p53 expression in a co-culture spheroid.

Co-culture spheroids of 500 PANC-1 cells and 5,000 (5K) HSCs were grown in a hanging drop format for 4 days and stained with anti-p53 antibodies only. Optical clearing with BABB was performed. Confocal laser scanning microscopy (CLSM) and multi-photon microscopy (MP) were performed on the same focal plane position of the spheroid. Intensities and areas of every single cell in the two images presented were generated by CellProfiler. Whisker box graph was made from one optical section of a spheroid with all the values of intensity divided by respective area from nine cells near the core of the spheroid (CLSMcore and MPcore) and seventeen cells near the edge of the spheroid (CLSMedge and MPedge). Mean markers were shown. Median was exclusive from quartile calculation. Mean ranks were compared using non-parametric Kruskal-Wallis H test.

3.2.3 αSMA is not only a marker for hepatic stellate cells but is also found in pancreatic cancer cells

Alpha smooth muscle actin (αSMA) has been widely accepted as a marker for activated stellate cells [Erkan *et al*, 2008; Jiang *et al*, 2018; Ozdemir *et al*, 2014; Wei *et al*, 2017]. In order to detect the stellate cells in the 3D co-culture models and validate the presence and activation status of the hepatic stellate cells (HSCs), we investigated αSMA expression patterns alongside cancer cell distributions using the p53 marker. Also, we intended to test whether cancer cells could promote the proliferation of HSCs by using total αSMA protein levels.

Two different antibodies were used to detect αSMA: one is a rabbit polyclonal antiserum made from immunogens overlapping with amino acids 1-100 of the N-terminus of αSMA (rabbit anti-αSMA) and the other is a goat antiserum raised against a synthetic peptide (EEEDSTALVC) that emulates amino acids 3 to 12 of αSMA (goat anti-αSMA).

As seen in Figure 33 and 34, a clear band at 42 kDa could be detected using rabbit anti-αSMA in all spheroids including mono-spheroids with cancer cells only. The pattern was the same using goat anti-αSMA antiserum except that there was no band near 42 kDa in Capan-2 mono-culture spheroids. The goat anti-αSMA antiserum, however, was able to stain Capan-2 cells and PANC-1 cells using immunofluorescence microscopy with a non-specific goat IgG being used as a negative control. Therefore, αSMA was expressed in both HSCs and cancer cells grown in the current co-culture models.

As αSMA could also be detected in mono-spheroids with cancer cells only, no conclusion could be drawn from the immunoblotting results. Thus, more specific markers for HSCs were needed.

A.

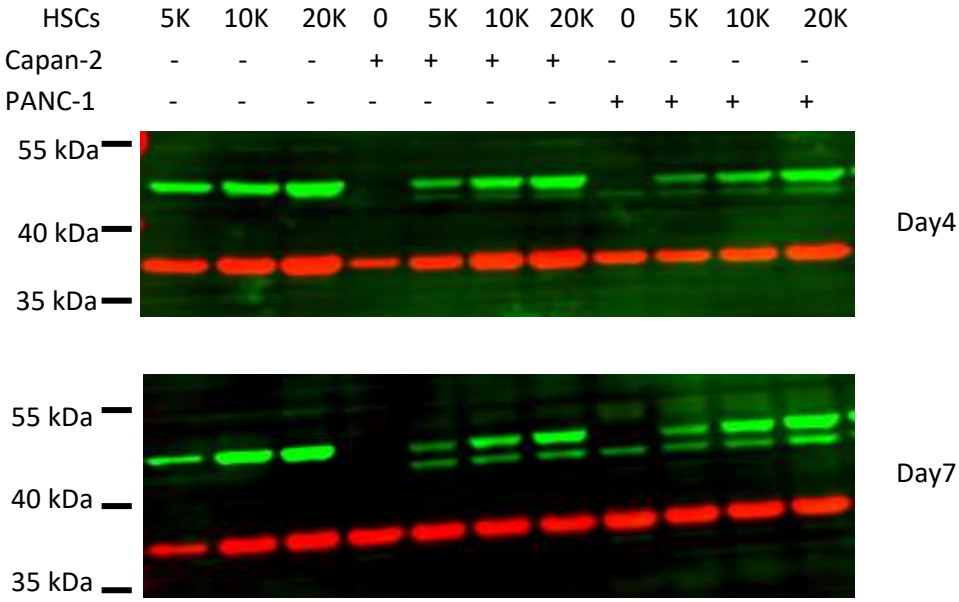

B.

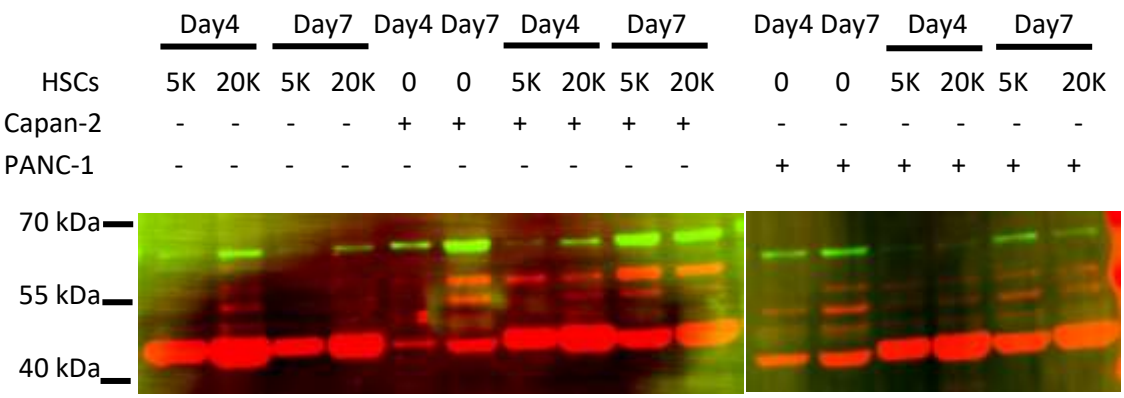

Figure 33. Immunoblotting analysis of αSMA in 3D mono-culture and 3D co-culture.

0, 5,000 (5K), 10,000 (10K), and 20,000 (20K) hepatic stellate cells (HSCs) were mixed with 500 Capan-2 or PANC-1 cells respectively to form the co-culture models at 0, 10:1, 20:1 and 40:1 ratios of stellate cells to cancer cells in a hanging drop format. After 4 days, spheroids were transferred to the poly-HEMA low-attachment 96-well plates, resulting in one spheroid per well. The spheroids were grown for another 3 days. Immunoblotting analysis of αSMA using two different antibodies on the indicated time points was performed. Two-colour near-infrared detection by immunoblotting was used to detect αSMA using goat anti-αSMA antibodies (green) and GAPDH (red) in A) or αSMA using rabbit anti-αSMA (red) and HDAC1 (green) in B). Representatives were from two independent experiments (n=2).

Figure 34. Immunofluorescence analysis of αSMA expression near the core of the spheroids.

40K HSCs, 500 Capan-2 cells and 500 PANC-1 cells were grown respectively in a hanging drop format to form 3D mono-culture spheroids. After 4 days, the whole spheroids were fixed in PFA and stained with goat anti-αSMA antibodies or goat IgG, followed by incubation of donkey anti-goat secondary antibodies conjugated to Alexa-Fluor 488. Fluorescent images were acquired by confocal laser scanning microscopy using Zeiss LSM880 with the same power at 488 nm and the signals from Alexa Fluor 488 were coloured white. Image analysis were performed using Zen 2.3 (blue edition). Consistent whiteness in Histogram among the images was used. The patterns were observed in at least three different experiments. Scale bar, 200 µm.

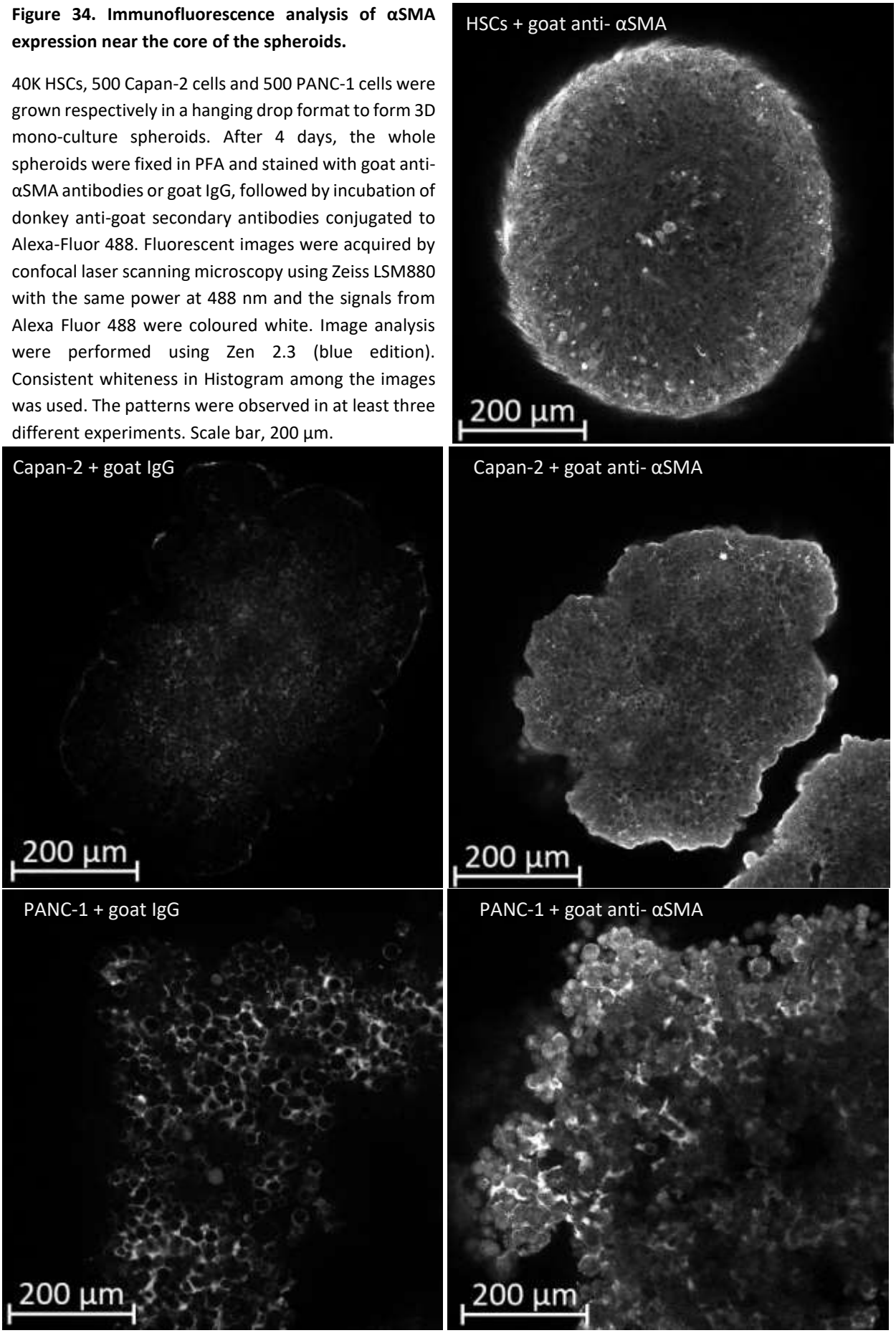

3.2.4 YAP mainly localizes in the cytoplasm near the edge of 3D spheroids while cancer cells at the edge occasionally presented with nuclear localisation of YAP

Nuclear accumulation of YAP is considered to be one of the driving forces that can promote cancer cell growth. However, signalling through cell-cell contact inhibits YAP nuclear translocation, leading to its cytoplasmic retention. Intense cell-cell contact interactions can be established in the co-culture models presented here. Based on the data showing the spheroid expansion in the 3D mono-culture and co-culture, we also investigated YAP localization during this process.

Total YAP expression in whole spheroids was examined by immunoblotting using the antibodies raised against YAP of human origin. 65 kDa is generally accepted as the molecular weight of YAP [Basu *et al*, 2003; Sudol, 1994; Tomlinson *et al*, 2010], which is different from the molecular weights listed in Uniprot website. According to the Uniprot website (http://www.uniprot.org/uniprot/P46937), there are 9 isoforms of YAP produced by alternative splicing, with the molecular weights of 36 kDa, 48 kDa, 49 kDa, 50 kDa, 50.47 kDa, 53 kDa, 54.46 kDa, and 55 kDa. As illustrated in Figure 35, multiple bands could be detected ranging from 40 kDa to 100 kDa with distinct bands pattern. There were two weak bands at 55 kDa and 65 kDa detected in 3D mono-culture of HSCs, 3D mono-culture of Capan-2 cells and 3D co-culture of HSCs with Capan-2 cells. By comparison, the 55 kDa and 65 kDa bands in 3D mono-culture of PANC-1 cells and 3D co-culture of HSCs with PANC-1 cells were stronger than the ones in HSCs and Capan-2 cells. The bands at 48 kDa in Capan-2 groups were stronger than the ones in PANC-1 groups. The exact molecular weights of bands between 48 to 55 kDa need further verification. The band observed between 70 kDa and 100 kDa was postulated to be the phosphorylated YAP, as 75 kDa was reported to be the phosphorylated YAP in breast cancer cells [Lee *et al*, 2018b], liver cancer cells [Jeric *et al*, 2016], and kidney cells [Matsudaira *et al*, 2017]. This assumption should be verified by using commercially available antibodies against phosphorylated YAP, which needs further investigation. The bands indicating YAP expression seen in the co-culture models were postulated to come mainly from cancer cells because the bands seen in mono-culture of HSCs were much weaker than the ones in mono-culture of cancer cells. Therefore, the co-culture of cancer cells with HSCs was able to reduce YAP expression in cancer cells, indicating the possibility of HSCs to reduce the proliferative ability of cancer cells. However, considering the possible differences in total cell numbers between mono-culture and co-culture, the lack of nutrients due to the consumption by HSCs in the co-culture models could also be responsible for the reduced proliferation of cancer cells.

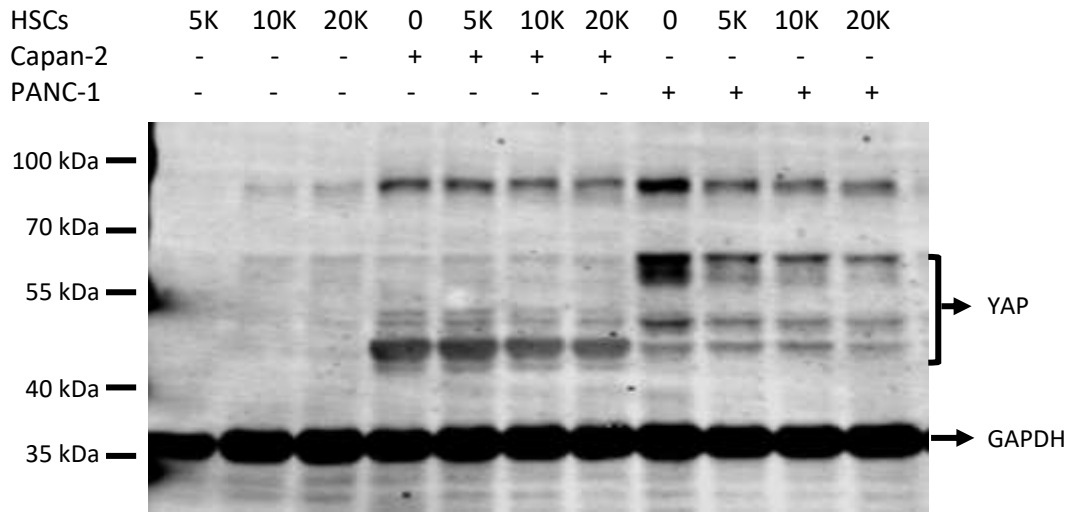

Figure 35. Endogenous YAP expression detected by immunoblotting in 3D spheroids.

0, 5,000 (5K), 10,000 (10K), and 20,000 (20K) hepatic stellate cells (HSCs) were mixed with 500 Capan-2 or PANC-1 cells respectively to form the 3D co-culture models at 0, 10:1, 20:1, and 40:1 ratios of stellate cells to cancer cells using the hanging drop method. 3D mono-culture of HSCs were grown in parallel. After 4 days, spheroids were transferred to the poly-HEMA low-attachment 96-well plates, resulting in one spheroid per well. After 3 days when the total growth time was 7 days, YAP expression were analysed by immunoblotting. Two-colour near-infrared detection was performed to detect YAP and GAPDH simultaneously. The band patterns of YAP expression in 3D mono-culture of 20K HSCs, Capan-2 cells or PANC-1 cells and 3D co-culture of 20K HSCs with Capan-2 or PANC-1 cells respectively were observed in three independent experiments. The band patterns of YAP expression in 3D mono-culture of 5K HSCs and 10K HSCs were observed in one independent experiments. The band patterns of YAP expression in 3D co-culture of Capan-2 cells with 5K or 10K HSCs respectively were observed in one independent experiments. The band patterns of YAP expression in 3D co-culture of PANC-1 cell with 5K or 10K HSCs respectively were observed in one independent experiments.

Total YAP expression is insufficient to study YAP localisation in each individual cell, especially as two cell types were involved in the current co-culture models. Hence, confocal laser scanning immunofluorescence microscopy was conducted to analyse YAP localisation in single cell in the models. Initial images acquired to examine intracellular YAP distribution suggested extensive nuclear localization as demonstrated in Figure 36. However, later it was found that there was spectral overlapping with DAPI staining because staining spheroids with DAPI only also elicited fluorescent signals in YAP channel (Figure 36), which turned out to be false nuclear expression of YAP. This was verified by examining spheroids labelled for YAP but without DAPI staining, showing that YAP was found to mainly localize in the cytoplasm of the majority of cancer cells in 3D mono-cultures of Capan-2 and PANC-1 cells as well as co-culture spheroids prepared from PANC-1 cells mixed with 5K HSCs, all being cultured using the hanging drop protocol for 4 days (Figure 37-39). As seen in Figure 40, spectral unmixing can separate DAPI overlapping with YAP, resulting in a YAP cytoplasmic localisation similar to the spheroids stained with single anti-YAP antibodies.

Additional efforts were made to describe accurately the subcellular distribution of YAP in the cancer cells of these 3D spheroid systems. The images were acquired using two tracks with DAPI channel and Alexa546 channel which was used to detect YAP expression while Alexa488 channel and Alexa647 channel in the other track as dual tracking in Figure 36-40. Multitracking mode separating each channel into one track individually was utilized, so as for the emitted photons from DAPI, Alexa Fluo 488, Alexa Fluo 546, Alexa Fluo 647 to be collected in individual track. Combined channels mode as in Figure 36-40 and multitracking mode as in Figure 41 were used to capture the same optical section of the spheroid stained with DAPI, anti-YAP antibodies and 2^{nd} antibodies conjugated to Alexa Fluo 546. As seen in Figure 41, YAP nuclear expression was dramatically reduced (green arrows) using multitracking mode, indicating multitracking was able to minimize the negative effect of spectral overlapping on YAP expression. We next assessed the effect of unmixing on the images acquired using multitracking with ACE unmixing. Meanwhile, single dye spectrum acquired using the same CLSM setting for manual unmixing was generated by staining the spheroids with single DAPI, anti-YAP antibodies, anti-p53 antibodies, respectively. As illustrated in Figure 42 and 43, ACE unmixing and manual unmixing did not improve multitracking imaging but led to signal loss (red arrows). Moreover, the unmixing steps had added unnecessary steps that would slow down the image analysis. These outcomes did not favour the continuation of ACE or manual unmixing. There was little artefacts and background staining involved in the current imaging methods as confirmed by negative controls in Figure 44-46. Taken together, multitracking scanning by CLSM will be the optimal method for future fluorescence imaging in the current study.

As seen in the Figure 37-39 and 42 (green arrow heads), there were a few cancers cells with nuclear localisation of YAP.

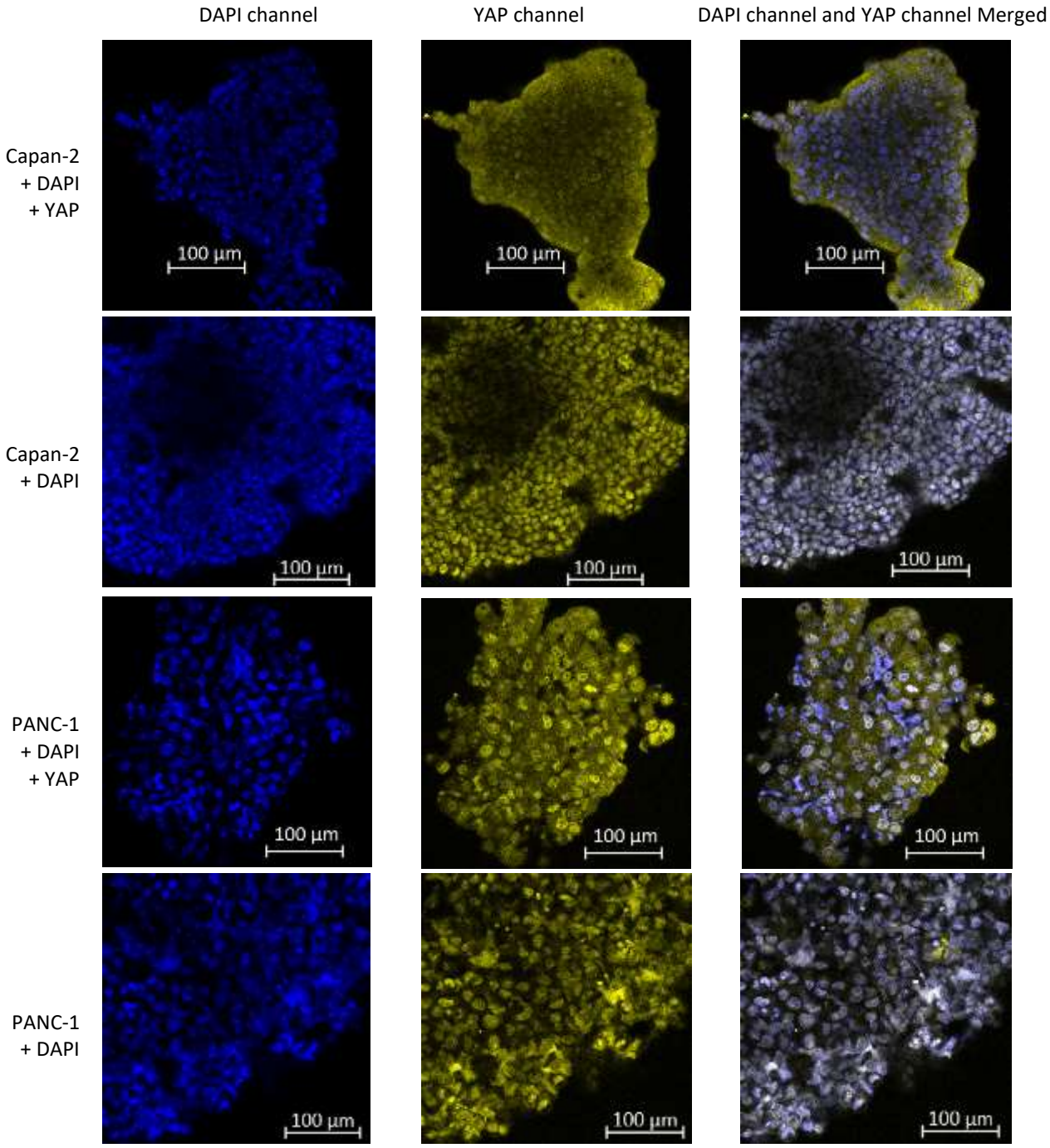

Figure 36. Effects of spectral overlapping on YAP subcellular localisation.

3D mono-culture of 500 Capan-2 and PANC-1 cells respectively were grown in a hanging drop format. After 4 days, whole spheroids were fixed in PFA and stained with DAPI alone or both DAPI and anti-YAP antibodies, followed by incubation of secondary antibodies conjugated to Alexa Fluor 546. Fluorescent images were acquired by confocal laser scanning microscopy using Zeiss LSM880 with excitation at 405 nm and 561 nm simultaneously. DAPI channel (blue) collecting photons resulted from the emission from DAPI was combined with YAP channel (yellow) collecting photons resulted from the emission from Alexa Fluor 546 in one track. The pattern was observed in three independent experiments.

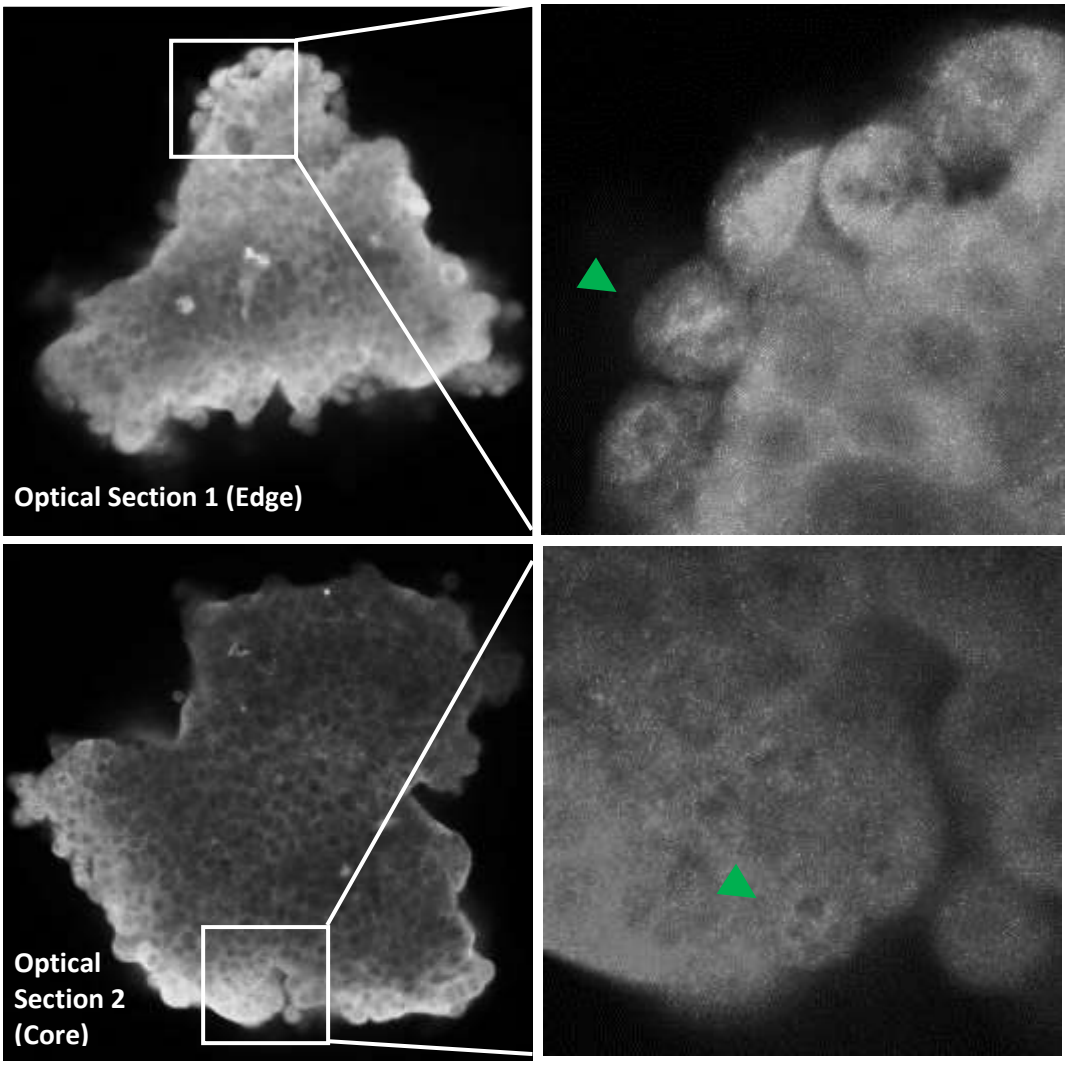

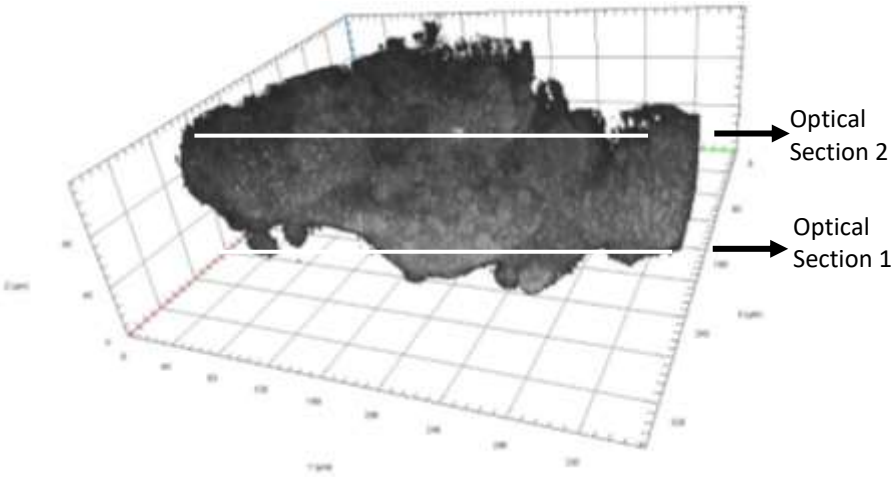

Figure 37. Subcellular localisation of YAP in 3D mono-culture of Capan-2 cells detected by immunofluorescence with anti-YAP antibodies only.

3D mono-culture of 500 Capan-2 cells were grown in a hanging drop format for 4 days, fixed in PFA and then stained with anti-YAP antibodies, followed by incubation of secondary antibodies conjugated to Alexa Fluor 546. Images with one optical section or Z-stack images were acquired with excitation at 405 nm and 561 nm simultaneously. DAPI channel (blue) collecting photons resulted from the emission from DAPI was combined with YAP channel (yellow) collecting photons resulted from the emission from Alexa Fluor 546 in one track, consistent with the setting in Figure 36. 3D rendering was done by Zen 2.3 (blue edition) using Z-stack images of spheroids stained with DAPI and YAP, exporting only images in YAP channel. Representative images from two spheroids in two independent experiments were shown. Green arrow heads: nuclear YAP localisation.

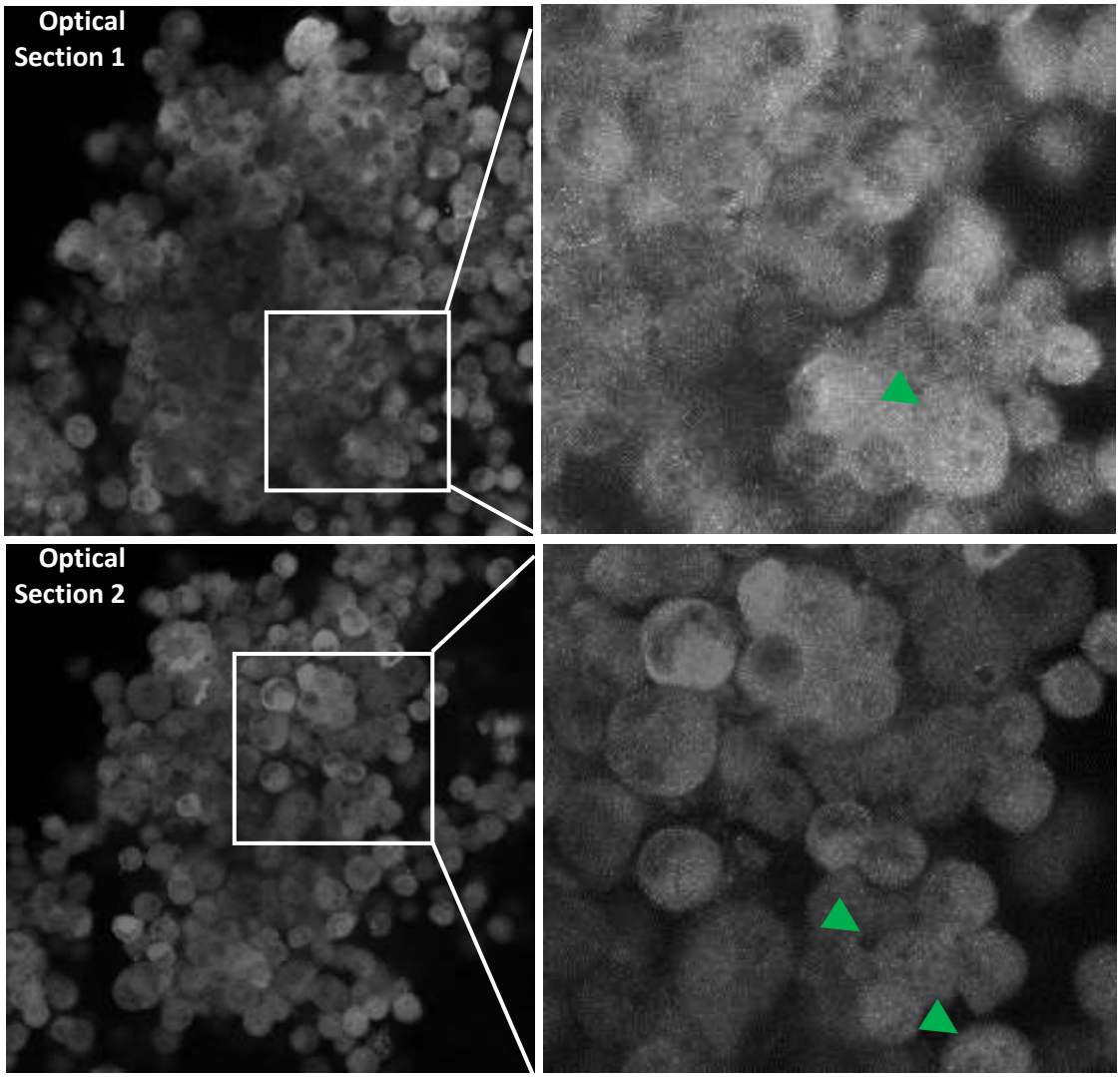

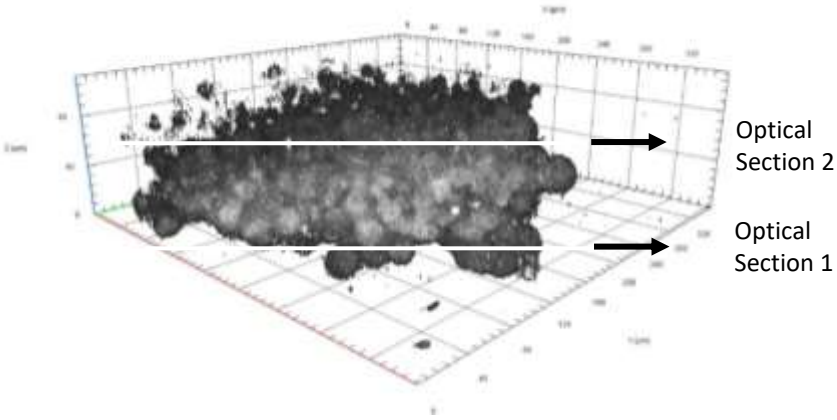

Figure 38. Subcellular localisation of YAP in 3D mono-culture of PANC-1 cells detected by immunofluorescence with anti-YAP antibodies only.

3D mono-culture of 500 PANC-1 cells were grown in a hanging drop format for 4 days, fixed in PFA and then stained with anti-YAP antibodies, followed by incubation of secondary antibodies conjugated to Alexa Fluor 546. Images with one optical section or Z-stack images were acquired with excitation at 405 nm and 561 nm simultaneously. DAPI channel (blue) collecting photons resulted from the emission from DAPI was combined with YAP channel (yellow) collecting photons resulted from the emission from Alexa Fluor 546 in one track, consistent with the setting in Figure 36. 3D rendering was done by Zen 2.3 (blue edition) using Z-stack images of spheroids stained with DAPI and YAP, exporting only images in YAP channel. Representative images from two spheroids in two independent experiments were shown. Green arrow heads: nuclear YAP localisation.

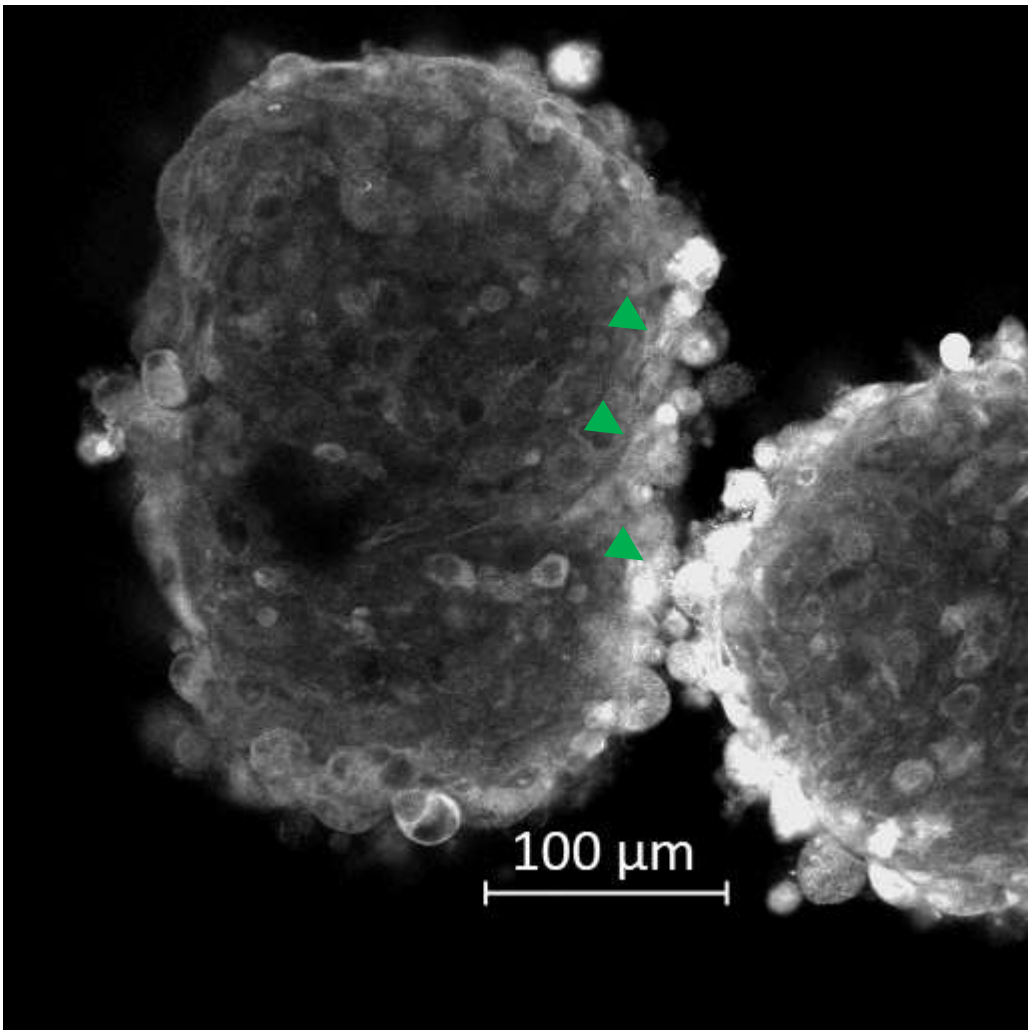

Figure 39. Subcellular localisation of YAP in 3D co-culture of PANC-1 cells with hepatic stellate cells detected by immunofluorescence with anti-YAP antibodies only.

3D co-culture of 500 PANC-1 cells with 5,000 hepatic stellate cells (HSCs) were grown in a hanging drop format for 4 days, fixed in PFA and then stained with anti-YAP antibodies, followed by incubation of secondary antibodies conjugated to Alexa Fluor 546. Images with one optical section were acquired with excitation at 405 nm and 561 nm simultaneously. DAPI channel (blue) collecting photons resulted from the emission from DAPI was combined with YAP channel (yellow) collecting photons resulted from the emission from Alexa Fluor 546 in one track, consistent with the setting in Figure 36. Only the image in YAP channel was exported. Representative images from two spheroids in one independent experiments were shown. Green arrow heads: nuclear localisation of YAP.

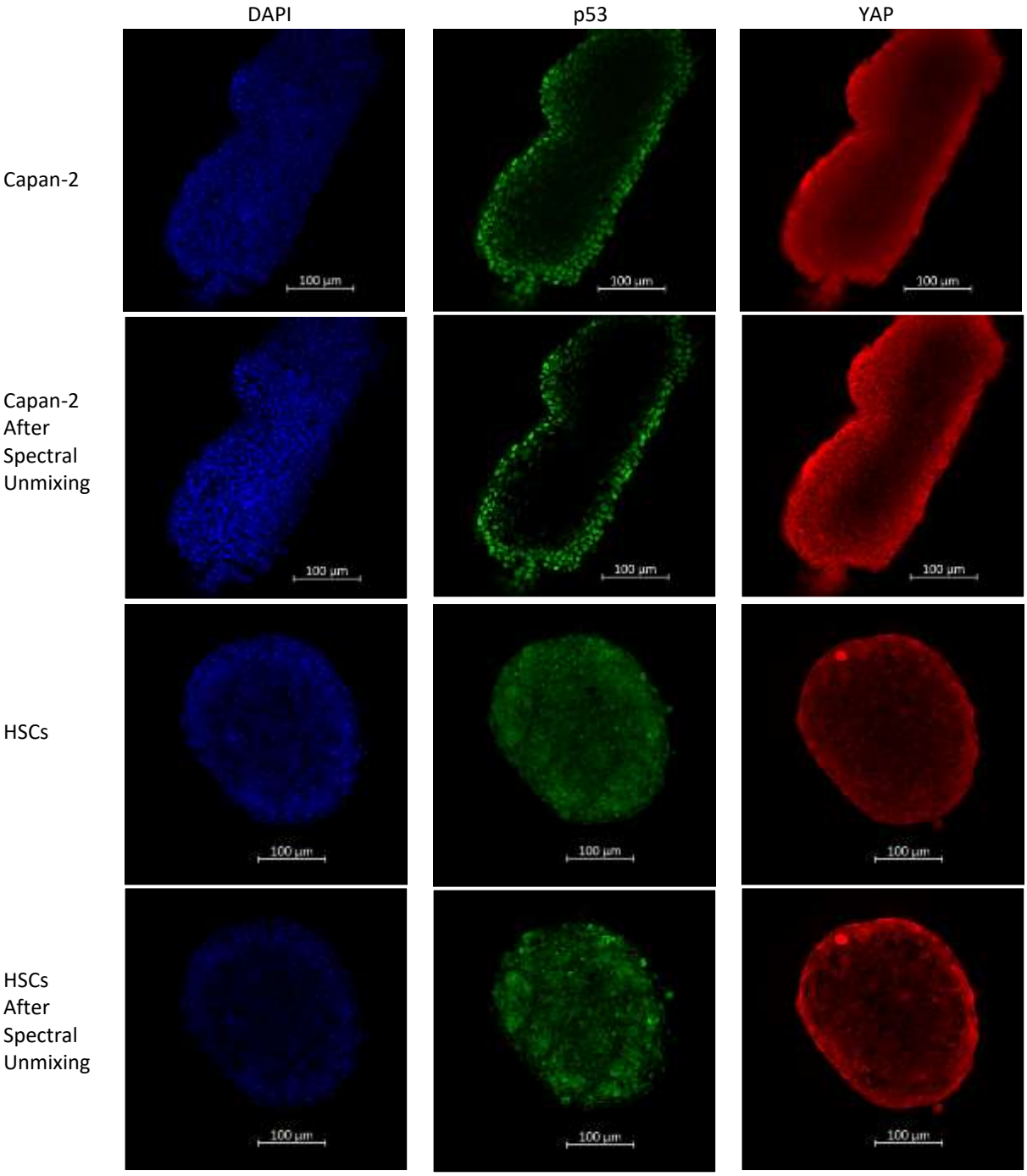

Figure 40. Effects of linear unmixing on detecting DAPI, expression of p53 and subcellular localisation of YAP in the nucleus and cytoplasm with multi-coloured imaging.

3D mono-cultures of 500 Capan-2 cells or 5,000 HSCs were grown in a hanging drop format for 4 days, fixed in PFA and then stained with DAPI (blue), anti-p53 antibodies (green) and anti-YAP antibodies (red). Optical clearing by ethanol and BABB was performed. Images with one optical section were acquired with excitation at 405 nm and 561 nm simultaneously. DAPI channel (blue) collecting photons resulted from the emission from DAPI was combined with YAP channel (yellow) collecting photons resulted from the emission from Alexa Fluor 546 in one track. Linear unmixing was done in Zen 2.3 (blue edition) using Automatic Component Extraction (ACE).

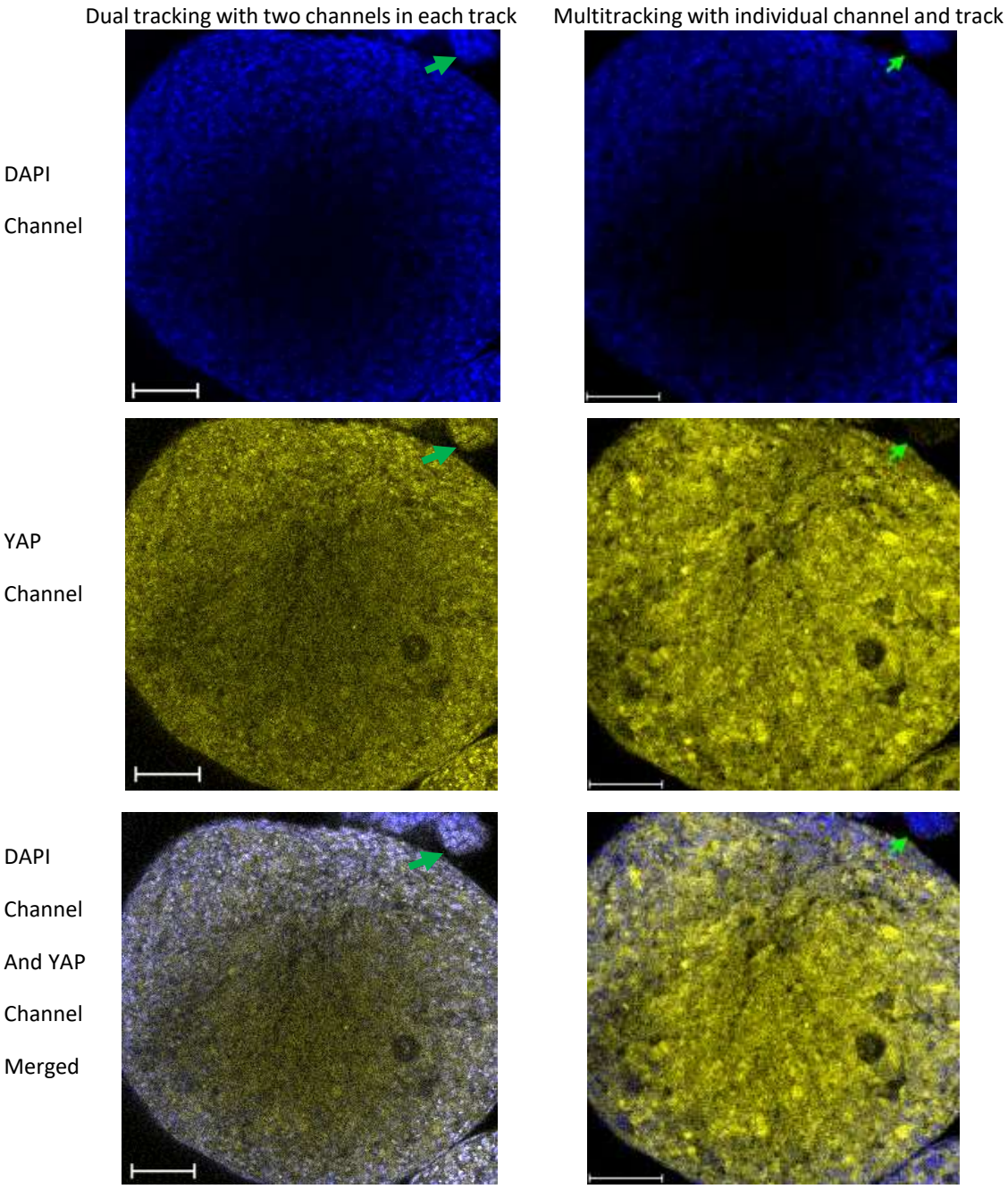

Figure 41. Effects of multitracking on detecting DAPI and subcellular localisation of YAP in the nucleus and cytoplasm with multi-coloured imaging.

3D co-cultures of 500 Capan-2 cells mixed with 40,000 hepatic stellate cells (HSCs) were grown in a hanging drop format for 4 days, fixed in PFA and then stained with DAPI (blue), anti-p53 antibodies (channel not shown) and anti-YAP antibodies (yellow). Optical clearing by ethanol and BABB was performed. Images with one optical section were acquired with excitation at 405 nm and 561 nm simultaneously. DAPI channel (blue) collecting photons resulted from the emission from DAPI was combined with YAP channel (yellow) collecting photons resulted from the emission from Alexa Fluor 546 in one track, as shown in the left panel. Multitracking mode was used in the right panel, separating DAPI channel from YAP channel. Green arrows indicated the disappearance of emitted photons from exciting DAPI fluorophore. Scale bar, 100 µm.

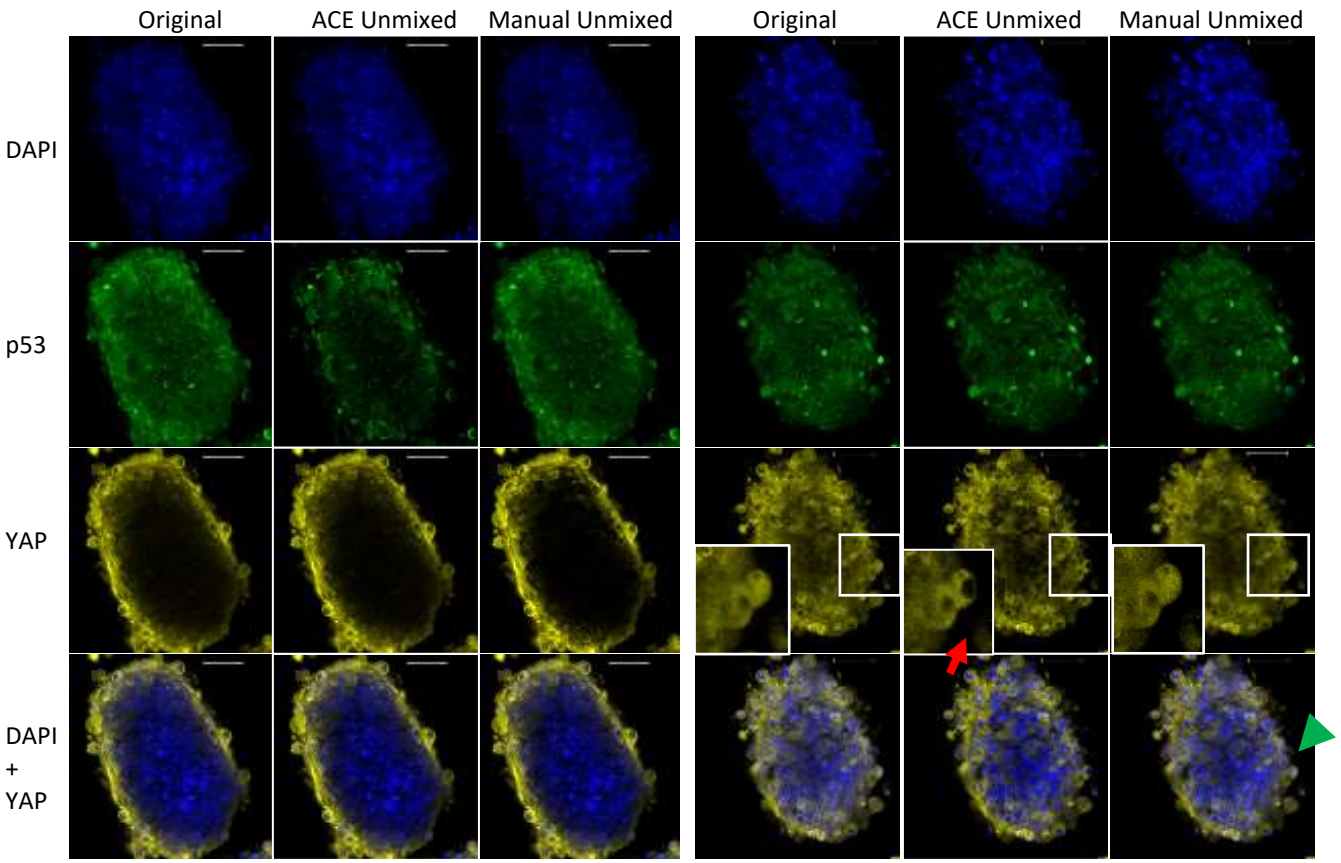

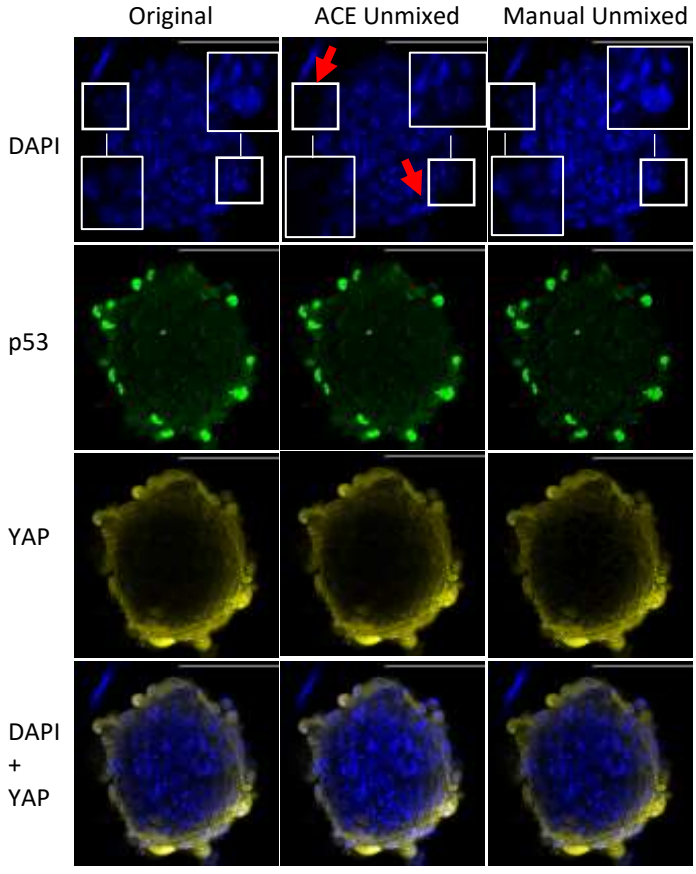

Figure 42. Effects of ACE unmixing and manual unmixing with multi-coloured imaging on detecting DAPI, p53 and subcellular localisation of YAP in the nucleus and cytoplasm of 3D co-culture with PANC-1 cells and 5K hepatic stellate cells.

Co-culture of 500 PANC-1 cells mixed with 5K hepatic stellate cells (HSCs) were grown in a hanging drop format for 4 days and then stained with DAPI (blue), and for p53 (green) and YAP (yellow). Optical clearing by ethanol and BABB was performed. Fluorescent images were acquired by confocal laser scanning microscopy using Zeiss LSM880. ACE unmixing was done in Zen 2.5 (blue edition). Single dye spectrum was generated by staining the spheroids with single dye and acquired using the same CLSM setting for manual unmixing, which was done in Zen 2.5 (blue edition). Red arrows indicated undesired signal loss after ACE unmixing. Green arrow heads: nuclear localisation of YAP. Scale bar, 50 µm.

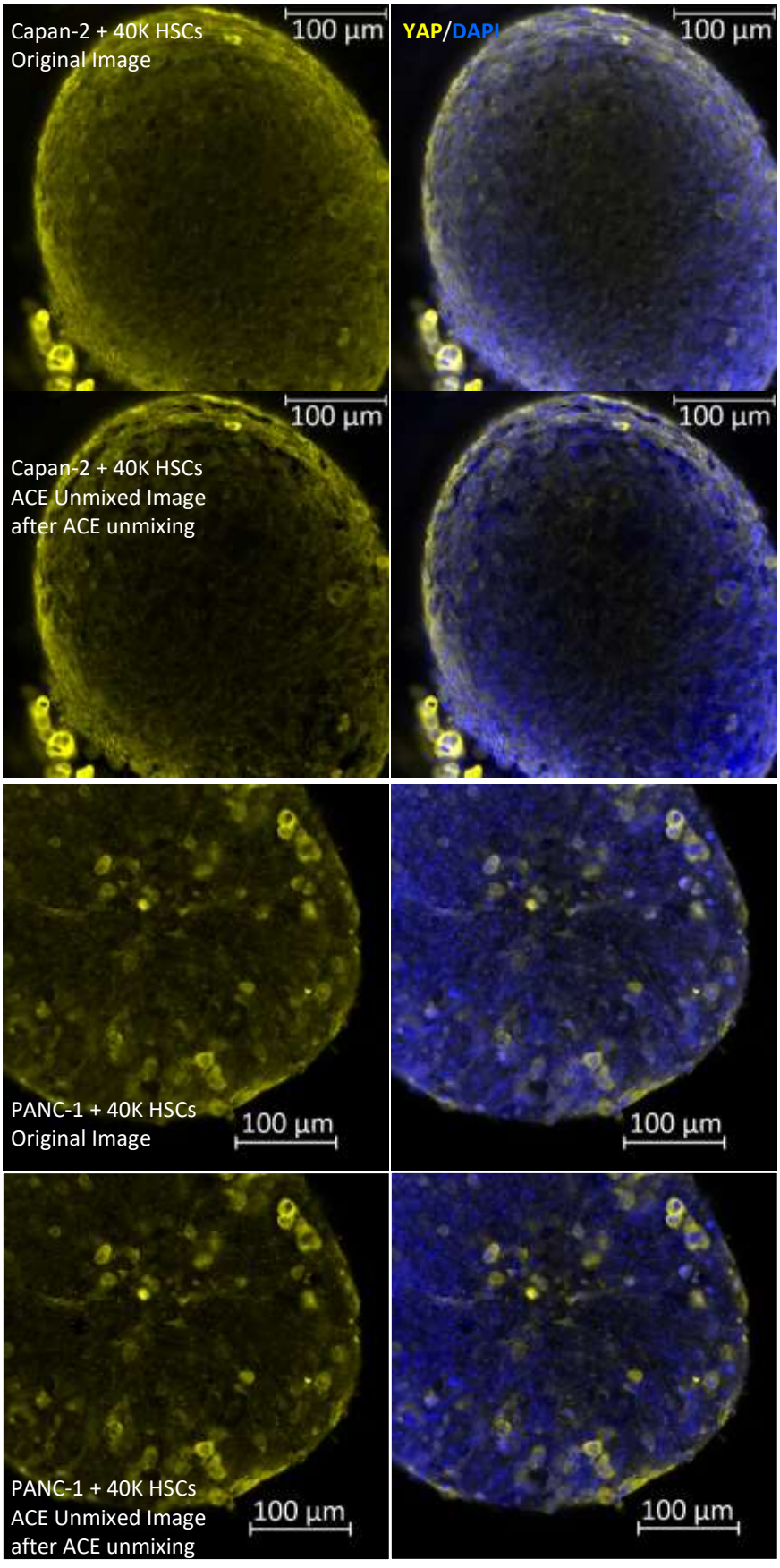

Figure 43. Effects of ACE unmixing with multi-coloured imaging on detecting DAPI and subcellular localisation of YAP in the nucleus and cytoplasm of 3D co-culture with cancer cells and 40K hepatic stellate cells.

Co-culture of 500 Capan-2 cells or PANC-1 cells mixed with 40K hepatic stellate cells (HSCs) were grown in a hanging drop format for 4 days and then stained with DAPI (blue), p53 (not shown) and YAP (yellow). Optical clearing by ethanol and BABB was performed. Fluorescent images were acquired by confocal laser scanning microscopy using Zeiss LSM880. ACE unmixing was done in Zen 2.5 (blue edition). Scale bar, 100 µm

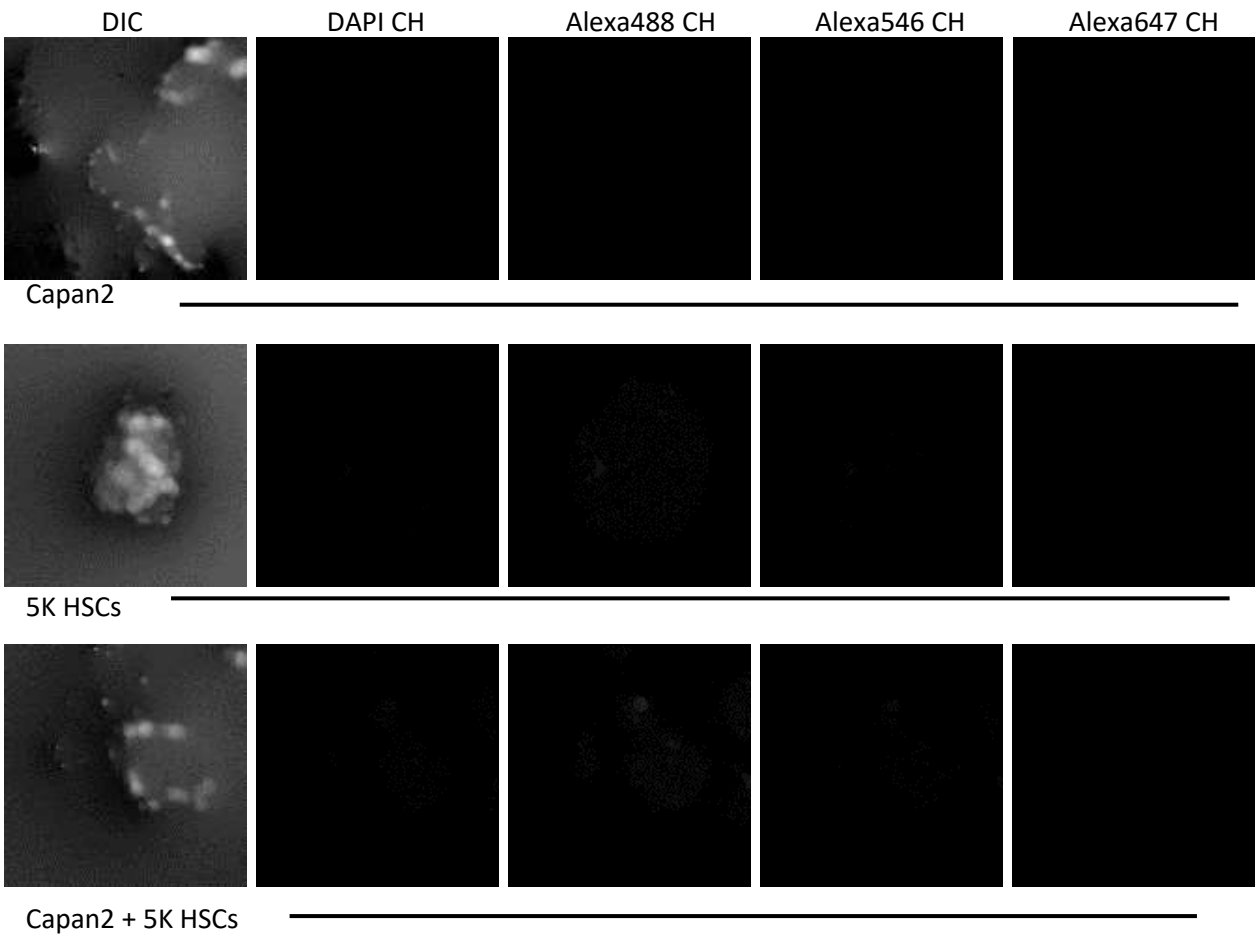

Figure 44. Representative images of 3D spheroids without fluorophores.

3D mono-culture of Capan-2 cells or 5,000 (5K) hepatic stellate cells (HSCs) respectively and 3D co-culture of 500 Capan-2 cells mixed with 5K HSCs were grown in a hanging drop format. After 4 days, whole spheroids were fixed in PFA and optical clearing by ethanol and BABB was performed. Confocal laser scanning microscopy with multitracking was performed on spheroids without any staining of fluorophores. Excitation wavelengths were 405nm, 488nm, 561nm and 633nm with the same laser powers and gains as the ones used in Figure 42-43. Images exported were coloured black and white. CH: channel. DIC: Differential interference contrast.

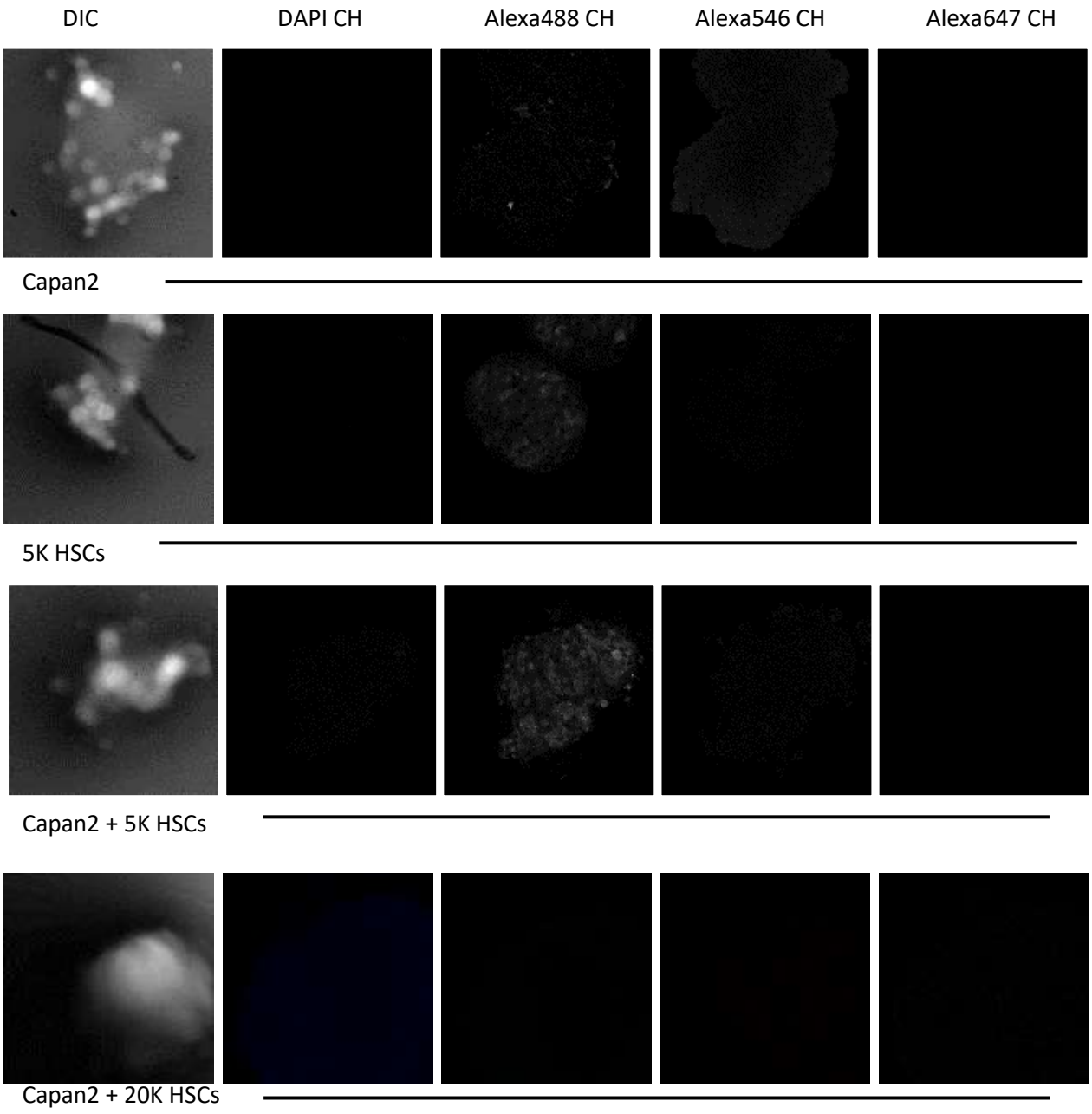

Figure 45. Representative images of 3D spheroids stained with 2nd antibodies conjugated to fluorophores.

3D mono-culture of Capan-2 cells or 5,000 (5K) hepatic stellate cells (HSCs) respectively and 3D co-culture of 500 Capan-2 cells mixed with 5K HSCs or 20K HSCs respectively were grown in a hanging drop format. After 4 days, spheroids were fixed in PFA and incubated with 2nd antibodies conjugated to Alexa Fluo 488, Alexa Fluo 546 and Alexa Fluo 647 respectively. Optical clearing by BABB and confocal laser scanning microscopy with multitracking were performed. Excitation wavelengths were 405 nm, 488 nm, 561 nm and 633 nm with the same laser powers and gains as the ones used in Figure 42-43. Images exported were coloured black and white. CH: channel. DIC: Differential interference contrast.

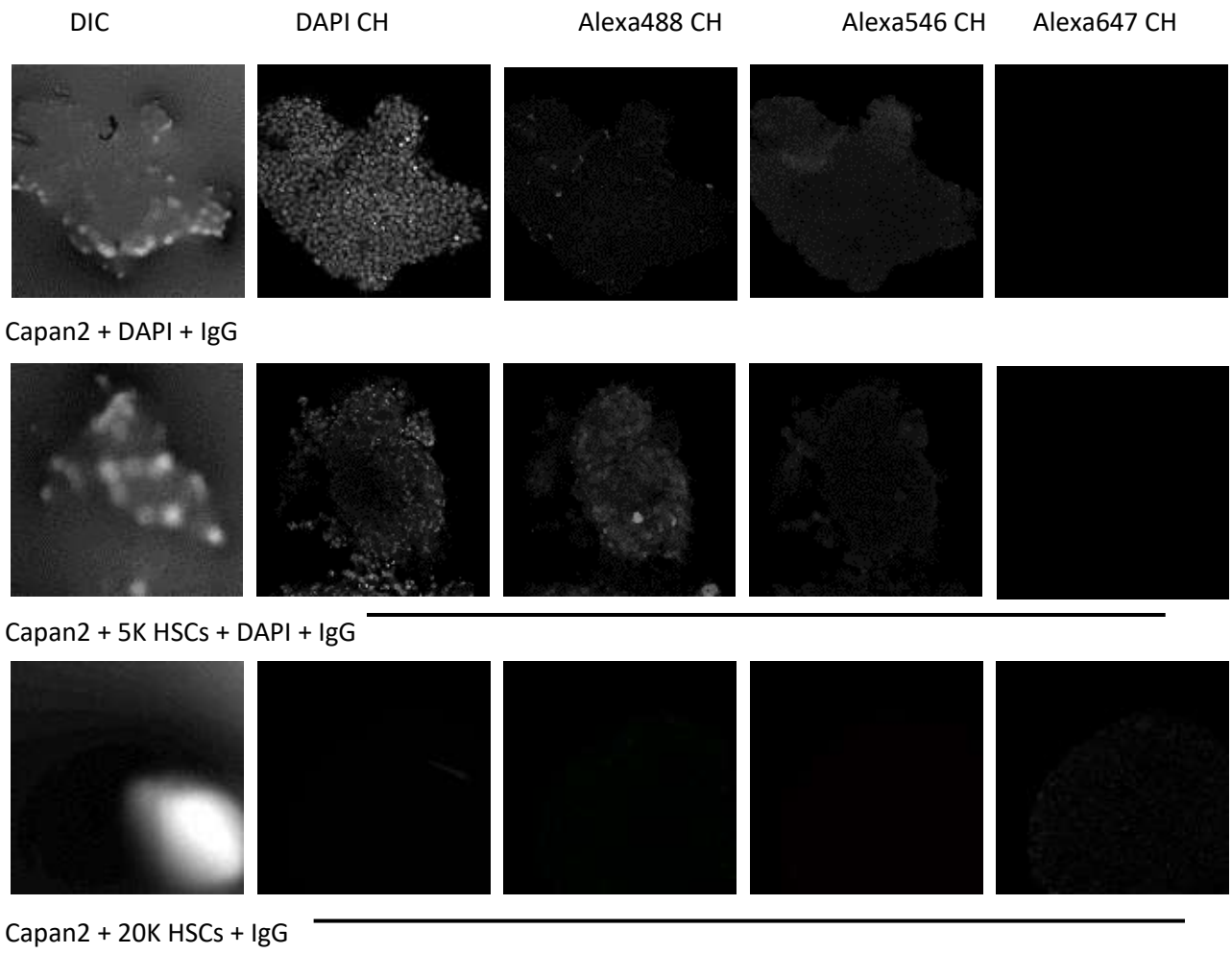

Figure 46. Representative images of 3D spheroids stained with DAPI, IgGs and 2nd antibodies conjugated to fluorophores.

3D mono-culture of Capan-2 cells and 3D co-culture of 500 Capan-2 cells mixed with 5,000 (5K) hepatic stellate cells (HSCs) or 20K HSCs respectively were grown in a hanging drop format. After 4 days, whole spheroids were fixed in PFA and incubated with DAPI, IgGs, 2nd antibodies conjugated to Alexa Fluo 488, Alexa Fluo 546 and Alexa Fluo 647 respectively except that DAPI was missing by accidence in 3D co-culture of 500 Capan-2 cells mixed with 20K HSCs. Optical clearing by BABB and confocal laser scanning microscopy with multitracking were performed. Excitation wavelengths were 405 nm, 488 nm, 561 nm and 633 nm with the same laser powers and gains as the ones used in Figure 42-43. Images exported were coloured black and white. CH: channel. DIC: Differential interference contrast.

From these method improvements, it appeared that YAP was mainly localized in the cytoplasm for the 3D mono-culture and co-culture spheroids grown using the hanging drop protocol for 4 days. Semi-quantification of YAP intensities by CellProfiler in Figure 47. YAP intensities in the nucleus, cytoplasm and the whole cells were measured in at least 25 cells near the edge of the spheroid and the core of the spheroid in the mono-culture of Capan-2 cells and HSCs using one optical slide. The YAP expression in the whole cell between the cells located near the core of the spheroid and the ones located near the edge of the spheroid was compared using total YAP intensity. Meanwhile, the intensity ratios of YAP intensity measured in the nucleus (nuclear YAP intensity) to total YAP intensity in the whole cell were compared to the intensity ratios of YAP intensity measured in the cytoplasm (cytoplasmic YAP intensity) to total YAP intensity in the whole cell, in order to compare the relative amount of YAP localisation in the nucleus between the cytoplasm.

Because the data representing YAP intensities and ratios did not follow normal distribution and not have the same shape of distribution, mean ranks of the datasets were compared using a non-parametric Mann-Whitney U test in Figure 47. Comparing the total YAP intensities in the whole cells near the edge and the cores, the cells near the edge exhibited significantly higher YAP expression (mean rank of 25.55 for Capan-2 cells near the core and 62.91 for Capan-2 cells near the edge while mean rank of 16.07 for HSCs in the core and 44.74 for HSCs near the edge, $p < 0.001$). The ratio of cytoplasmic YAP intensities was significantly higher than the ratio of nuclear YAP intensities in the Capan-2 cells near the edge of the spheroids (mean rank of 47.60 for ratio of cytoplasmic YAP intensity and 23.40 for nuclear intensities of YAP, $p < 0.001$), HSCs near the core of the spheroids (mean rank of 42.50 for ratio of cytoplasmic YAP intensity and 14.50 for nuclear intensities of YAP, $p < 0.001$), and HSCs near the edge of the spheroids (mean rank of 52.86 for ratio of cytoplasmic YAP intensity and 18.14 for nuclear intensities of YAP, $p < 0.001$). However, there was no significant difference between the ratio of cytoplasmic YAP intensities and the ratio of nuclear YAP intensities in the Capan-2 cells located near the core of the spheroid ($p = 0.443$). There was obvious cytoplasmic localisation of YAP and nuclear exclusion of YAP in the Figure 37 and 40, showing 3D mono-culture of Capan2 cells. Therefore, the image processing needs further refinement.

Figure 47 Semi-quantification of YAP subcellular expression in 3D mono-culture of Capan-2 cells and hepatic stellate cells in scaffold-free conditions.

3D Mono-cultures of 500 Capan-2 cells or 5,000 hepatic stellate cells (HSCs) were grown in a hanging drop method for 4 days and then stained with DAPI (blue), and YAP (red). Optical clearing by ethanol and BABB was performed. CLSM with dual tracking was performed near the core of the Capan2 and HSCs spheroids. Linear unmixing was done in Zen 2.3 (blue edition) using Automatic Component Extraction (ACE). Intensities of YAP in single cell on one optical section from one spheroid in one independent experiment were generated by CellProfiler (A). Whisker box graph was made from all the values of total YAP intensity in the whole cell (B) or the intensity ratios of nuclear YAP intensity to total YAP intensity in the whole cell or cytoplasmic YAP intensity to total YAP intensity in the whole cell (C) from at least twenty cells near the core of the spheroid and the edge of the spheroid, using Excel. Mean markers were shown. Median was exclusive from quartile calculation. Dots indicated the values in cells automatically generated by Excel. Non-parametric Mann-Whitney U test was used to calculate the *p* values. Nu: nucleus, Cy: cytoplasm, W: whole cell.

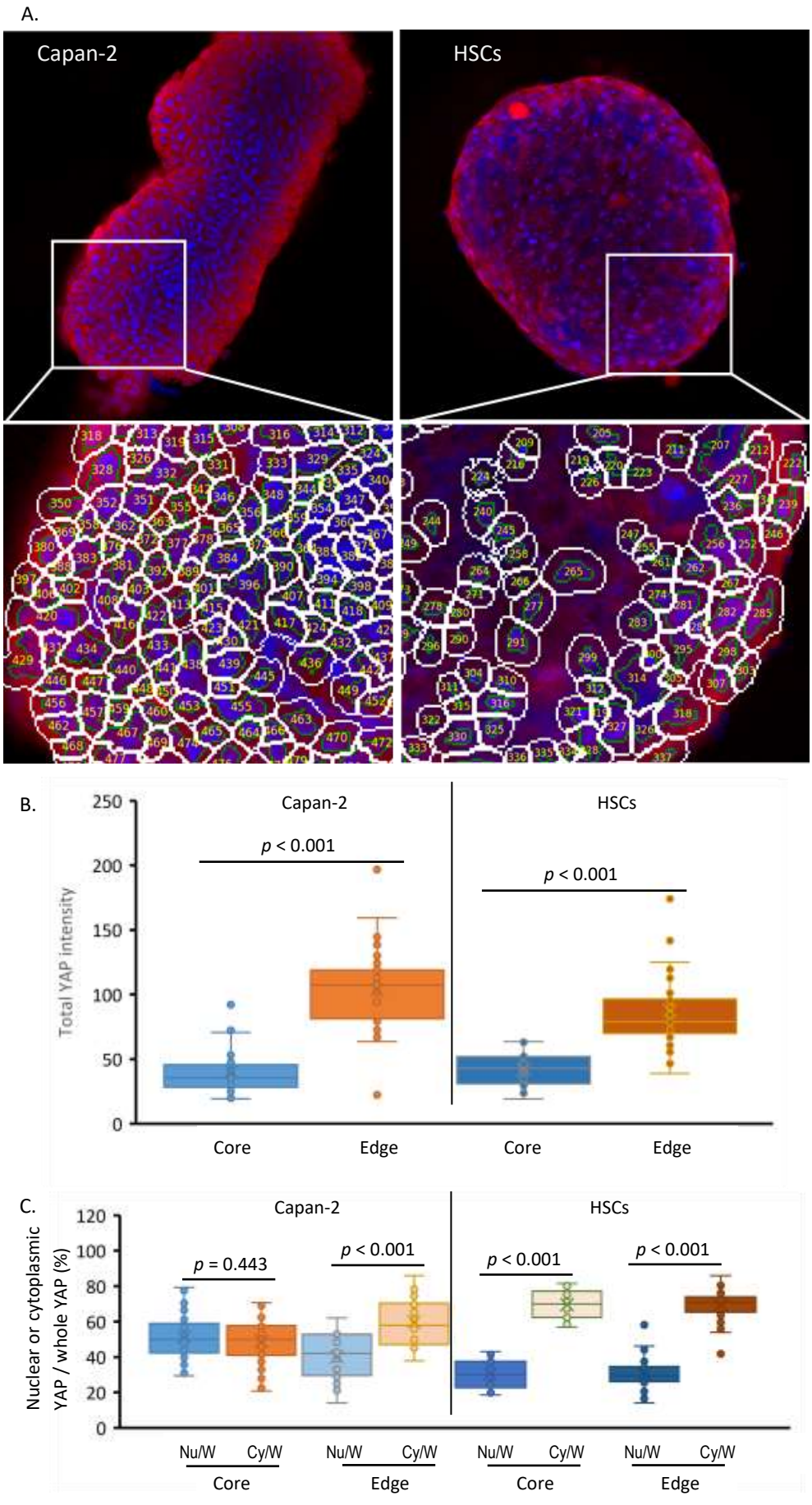

3.3 Step-wise process of coating pre-formed 3D cancer cell spheroids with stellate cells

We next attempted to establish a 3D co-culture model by first forming cancer cell spheroids and then placing these into a stellate cells suspension in standard cell culture medium. 500 Capan-2 or PANC-1 cells per 40 µL, the same number as what was used in section 3.2, were seeded into the inlet of the GravityPLUS™ HangingDrop Plate. After 4 days, each droplet containing a single cancer spheroid was pushed into a stellate cells suspension containing hepatic stellate cells (HSCs) introduced into the wells of polyHEMA low-attachment plates. The number of HSCs placed into these wells were calculated to achieve 10:1, 20:1 and 40:1 ratios of stellate cells to cancer cells. Our previous data suggested that the average cancer cell number in Capan-2 and PANC-1 3D spheroids formed by the hanging drop protocol was approximately 2,000 cells on day 4. Therefore, the cell numbers of HSCs in suspension ranged from 20,000 to 100,000 cells per well were used.

As illustrated in Figure 48, HSCs in the low-attachment plates formed a single spheroid by themselves without centrifugation, presenting a dark area in the well. As shown in Figure 49 and 50, compared to the dark area indicating the HSCs, the cancer mono-culture spheroids presented as a lighter area in the well. On the first day (Day 4) when the cancer spheroid was dropped in the stellate cells suspension, no more than one third of spheroids dropped into the HSCs spheroid region (images in the solid outline) whereas the rest of the spheroids only touched the edge of HSCs spheroid (images in the dotted outline). We expected the HSCs could migrate towards the cancer spheroids. However, more wells were observed with the light area touching the dark area in the wells on day 5 and day 6, indicating the majority of cancer cell spheroids situated at the edge of the HSCs spheroids. The different brightness and contrast between the cancer cell spheroids and the HSCs spheroids were sufficient to distinguish the cancers area from the HSCs area, thereby eliminating the need for immunofluorescence analysis of p53 expression. In sum, this approach of using pre-formed 3D mono-cultures of pancreatic cancer cells and then co-mixing these with HSCs suspension failed for produce a co-culture organization that emulated PDAC tumours.

A.

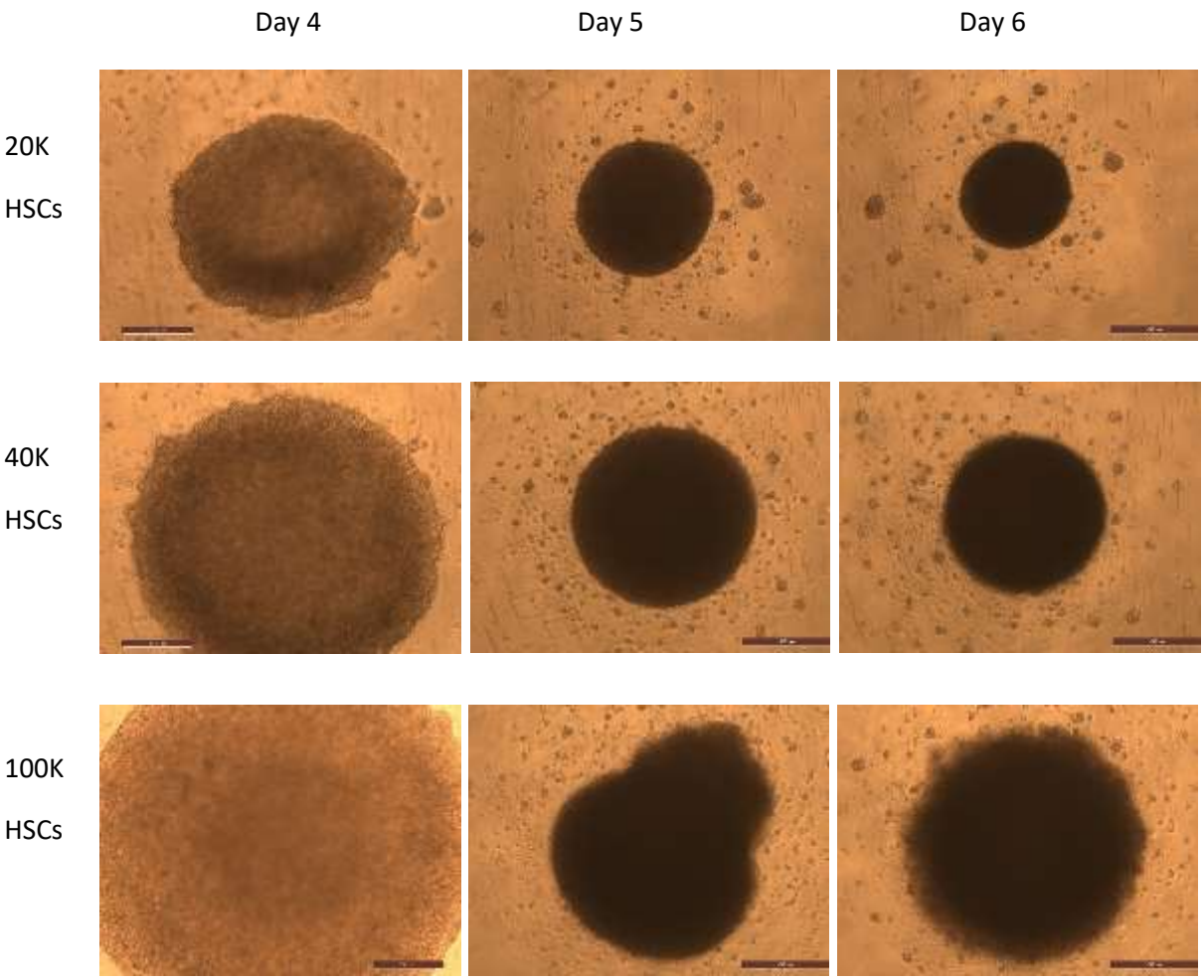

Figure 48. Spheroid formation of hepatic stellate cells suspension in scaffold-free condition.

20,000 (20K), 40,000 (40K), 100,000 (100K) cells per well of hepatic stellate cells (HSCs) suspensions were seeded in the poly-HEMA low-attachment 96-well plates with standard cell culture medium. The experiment was done in parallel with dropping cancer spheroids to HSCs suspensions. Day 4 indicated the day when cancer spheroids pre-formed in hanging drops were dropped to the HSCs suspension. Images were acquired by Leica DMI4000 B (50x magnification). Representative images shown were from six wells in one independent experiment. Scale bar, 500 µm.

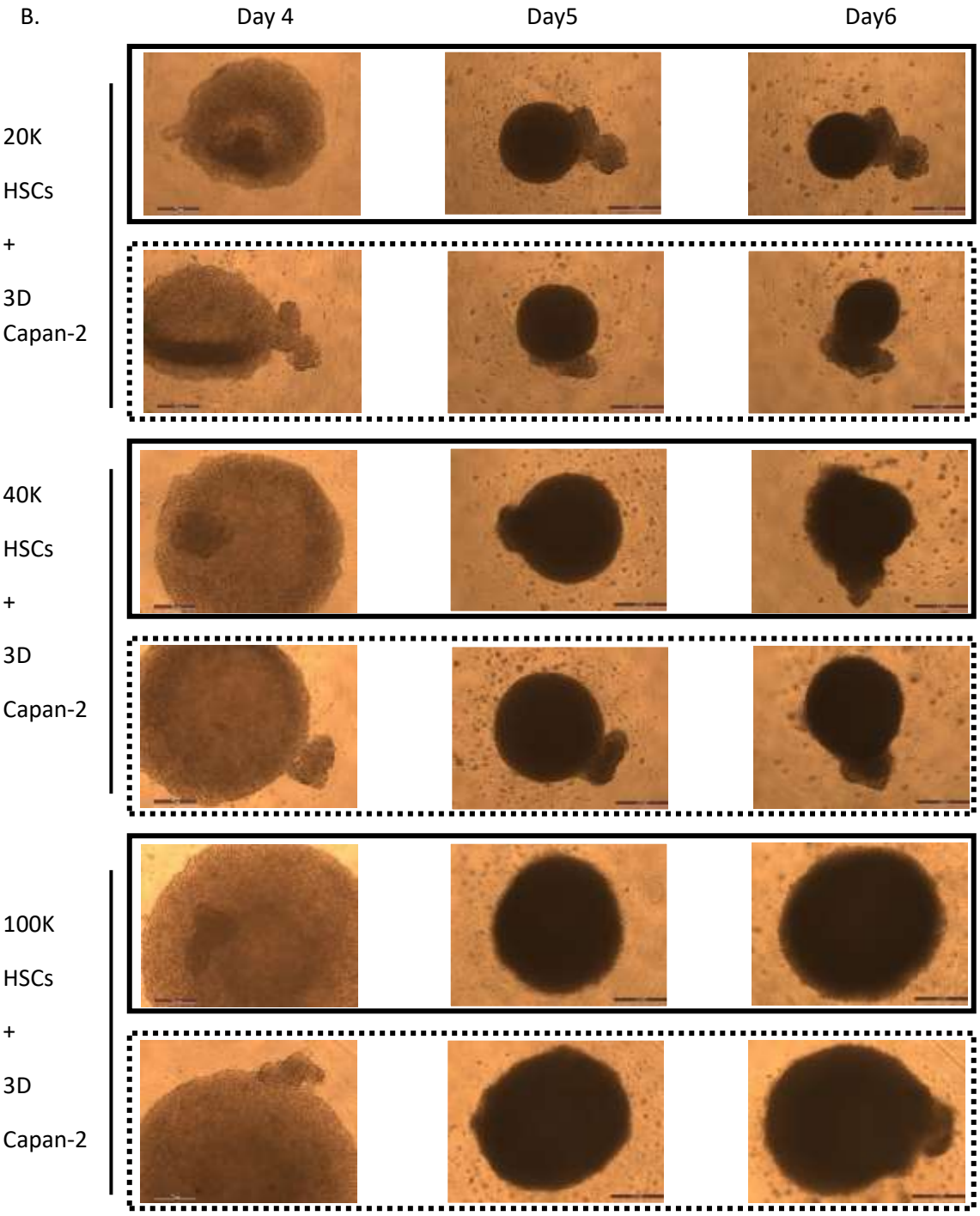

Figure 49. Dropping 3D Capan-2 mono-spheroids into hepatic stellate cells suspension in scaffold-free condition.

3D Capan-2 spheroids were first grown in a hanging-drop format for 4 days and then put into the wells of polyHEMA low-attachment 96-well plate where 20,000 (20K), 40,000 (40K), 100,000 (100K) cells per well of hepatic stellate cells (HSCs) suspensions were seeded respectively in standard cell culture medium at 10:1, 20:1 and 40:1 ratios of stellate cells to cancer cells according the cancer cell count on day 4. Images were acquired by Leica DMI4000 B (50x magnification). Images in the solid outline represented the spheroids dropped into the HSCs spheroid region on day 4 whereas the images in the dotted outline represented the edge of some cancer spheroids only touched the edge of HSCs spheroids on day 4. Representative images shown were from six wells in one independent experiment. Scale bar, 500 µm.

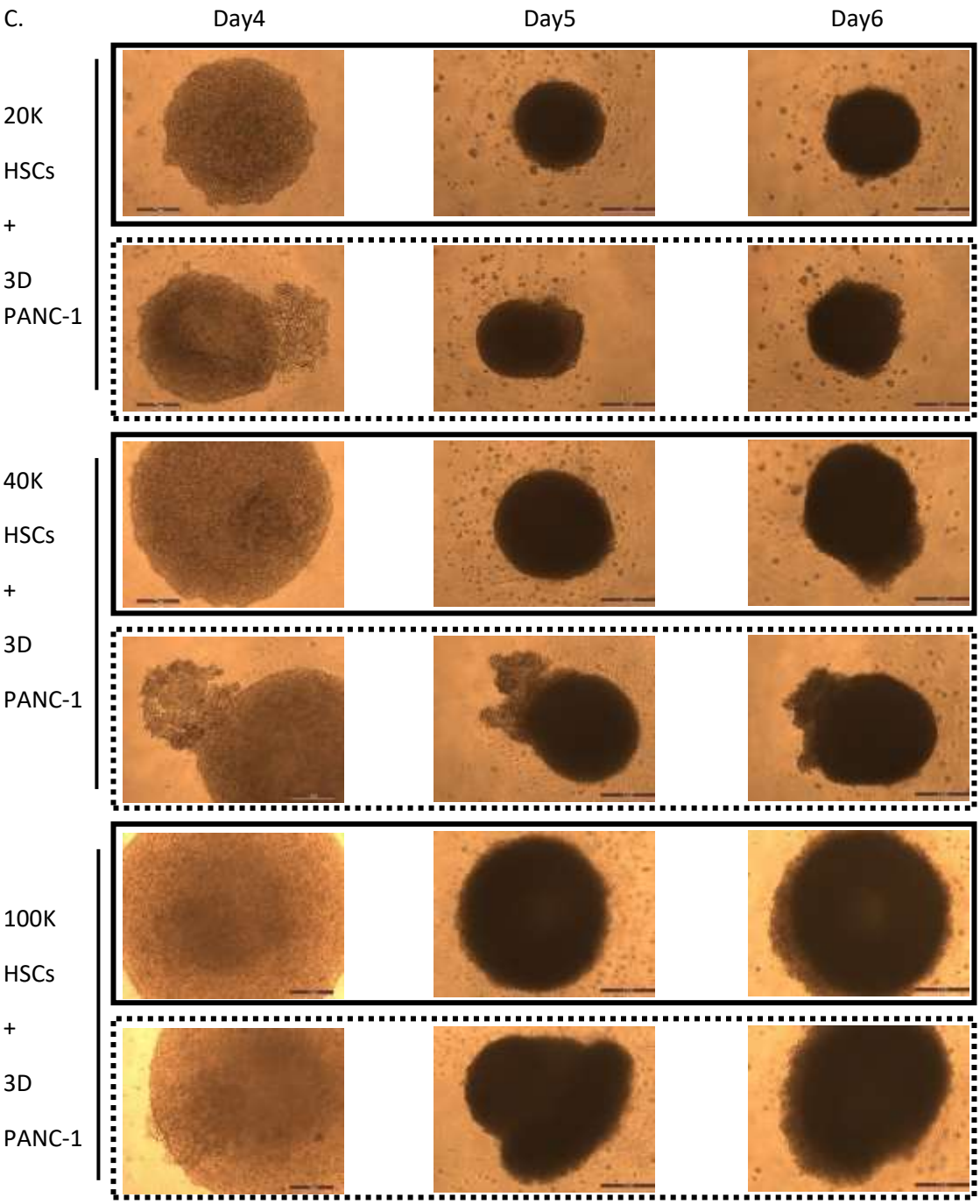

Figure 50. Dropping 3D PANC-1 mono-spheroids into hepatic stellate cells suspension in scaffold-free condition.

3D PANC-1 spheroids were first grown in a hanging-drop format for 4 days and then put into the wells of polyHEMA low-attachment 96-well plate where 20,000 (20K), 40,000 (40K), 100,000 (100K) cells per well of hepatic stellate cells (HSCs) suspensions were seeded respectively in standard cell culture medium at 10:1, 20:1 and 40:1 ratios of stellate cells to cancer cells according the cancer cell count on day 4. Images were acquired by Leica DMI4000 B (50x magnification). Images in the solid outline represented the spheroids dropped into the HSCs spheroid region on day 4 whereas the images in the dotted outline represented the edge of some cancer spheroids only touched the edge of HSCs spheroids on day 4. Representative images shown were from six wells in one independent experiment. Scale bar, 500 µm.

3.4 Discussion

In this chapter, increasing ratio of stellate cells to cancer cells led to reduced spheroid expansion and fewer cancer cells near the edge of the spheroids. However, localization of cancer cells occurred outside stellate cells cores, which was opposite to the cell distribution in PDAC. One possible reason why cancer cells wrapped around the stellate cells was that the stellate cells derived from PDAC patients in the current models tend to attach to stellate cells themselves in the scaffold-free condition.

Efforts were made in this chapter to optimise the microscopic scanning of the 3D spheroids with the size around 500 µm with the methods causing as little damage to the 3D structure as possible and minimizing the steps involved in the traditional histology methods to increase efficiency. Multiphoton scanning has been considered to improve the light penetration and reduce the light scattering in thick tissue compared to CLSM [Tauer, 2002]. However, by comparing p53 expression by CLSM scanning and MP scanning after optical clearing with ethanol and BABB, there was no significant difference between the p53 expression levels in the cells near the core and the edge of the spheroids. Besides, the lasers excitation mode in Zeiss LSM 880 currently used for MP scanning is not as fast as CLSM scanning. Henceforth, optical clearing with ethanol and BABB using CLSM will be utilized as the standard imaging technique to acquire the images in the next sections.

Our data indicate the p53 was not detected in patient-derived hepatic stellate cells grown in 3D mono-culture and 3D co-culture. This is inconsistent with the findings in hepatic stellate cells isolated from rat [Huang *et al*, 2018; Longxi *et al*, 2011; Nishizawa *et al*, 2016]. Immunoblotting demonstrated a baseline level of p53 expression in 2D primary isolated rat HSCs while the staining of p53 *in vivo* was weak [Nishizawa *et al*, 2016]. Primary rat HSCs grown in 2D for 3 days exhibited p53 expression detected by immunoblotting [Huang *et al*, 2018]. As far as we know, there has been no report on p53 expression in patient-derived HSCs in pancreatic cancer. Whether the growth conditions change p53 expression and 2D culture promotes p53 expression in HSCs remain to be determined.

Our data suggest that the decrease in p53 intensities was not proportional to the reduced number of cancer cells in the 3D co-culture models analysed by immunoblotting, indicating that different growth rates may be present in 3D mono-culture of cancer cells and 3D co-culture of cancer cells and HSCs. Different growth rates have been observed between stromal cells and cancer cells not only in 2D culture but also in 3D culture [Hoarau-Vechot *et al*, 2018]. After robust data could be obtained to verify the reliable markers for cancer cells in the co-culture models, stringent experiments need to be designed to determine the initial ratio of HSCs to cancer cells so that a 3D co-culture model matching the growth conditions in patients with PDAC could be achieved.

Of note, contradictory data on p53 expression was found in this section in the images used to quantify p53 expression (Figure 32) where strong p53 staining was detected in the core of the spheroid and the images showing p53 expression in Figure 27-29 where weak p53 staining was detected in the core of the spheroid. One of the reasons could be the position of the scanning in the spheroids. It could be an isolated incident that the scanning happened to be a position where high p53 expression in the cancer cells between the core and the edge of the spheroids. Also, the judgements of the operators on positioning the core of the spheroids are critical. In general, more data in this chapter support that p53 expression was reduced in the cells grown further away from the edge of the 3D spheroids.

The data on the association of increasing ratio of stellate cells to cancer cells with reduced p53 expression seemed to support the inhibitory role of stellate cells on cancer cell proliferation [Ozdemir *et al*, 2014; Rhim *et al*, 2014]. However, the observations and assessments were undertaken in the environment of small volume that led to severe nutrient depletion and metabolites accumulation. Meanwhile, it was possible that ECM levels in the environment where stellate cells and cancer cells were only together for 4 days had not reached the same level as the ones in patients with PDAC. Further models with realistic cells and ECM composition are needed to elucidate the cancer-supportive or cancer-suppressive roles of stellate cells in different context and stage in PDAC.

Although our data is consistent with the commonly acknowledged fact that αSMA is a marker for activated stellate cells [Erkan *et al*, 2008; Jiang *et al*, 2018; Ozdemir *et al*, 2014; Wei *et al*, 2017], the two pancreatic cancer cell lines, Capan-2 and PANC-1 cells, also exhibited strong expression of αSMA. This unexpected finding might suggest that the anti-αSMA antibodies used in the current project would not be able to distinguish between some subsets of HSCs and pancreatic cancer cells. Since EMT is common in PDAC, αSMA expression in Capan-2 and PANC-1 cells can be considered as the biomarker of EMT cells [Hill *et al*, 2017].

In this section, YAP mainly localizes in the cytoplasm near the edge of 3D spheroids while cancer cells at the edge occasionally presented with nuclear localisation of YAP. The data validate that cell-cell contact promote YAP cytoplasmic localization [Gumbiner *et al*, 2014], which is one of the reasons that more cancer cells with nuclear exclusion of YAP could be seen. The YAP expression in the wholes cells near the edge of the spheroids was higher than the ones near the core of the spheroids, indicating cells near the edge of the spheroids subjected to less cell-cell contact inhibition and more nutrients accessibility than the ones near the core. This is one of the possibilities that Capan-2 spheroids expanded significantly. However, even though HSCs spheroids exhibited the same YAP expression pattern as the Capan2 spheroids, their sizes remained the same over time, indicating that YAP expression may not promote cell growth in certain cell types. Interestingly, in spite of higher ratio of cytoplasmic YAP intensities near the edge of the spheroids, Capan2 spheroids did not enter a growth arrest state as suggested by the findings in 2D culture [Cravo *et al*, 2015], indicating that pancreatic cancer cells grown in 3D culture might require a lower level of nuclear localisation of YAP as a driving force for proliferation.

There are a few limitations in the current chapter. For instance, the work presented fail to recreate a model that is the formation of a single sphere/tumouroid consisted of stellate cells surrounding the cancer cells in each well to lay the foundation to perform high throughput drug screening. More optical sections are needed to quantify the protein expression to determine whether the antibodies are able to evenly bind to the antigens from the edge to the core of the spheroids. The current study lacked the measurement of ECM in the current models. It is necessary to characterize the collagens, fibronectin, laminins and hyaluronic acid (HA) in PDAC models using specific antibodies or HA detection kits to access if the models truly recapitulate the abundant ECM found in patients with PDAC.

Chapter 4. Effect of an artificial ECM on YAP signalling in a 3D mono-culture model of pancreatic cancer cells

Graphical Abstract

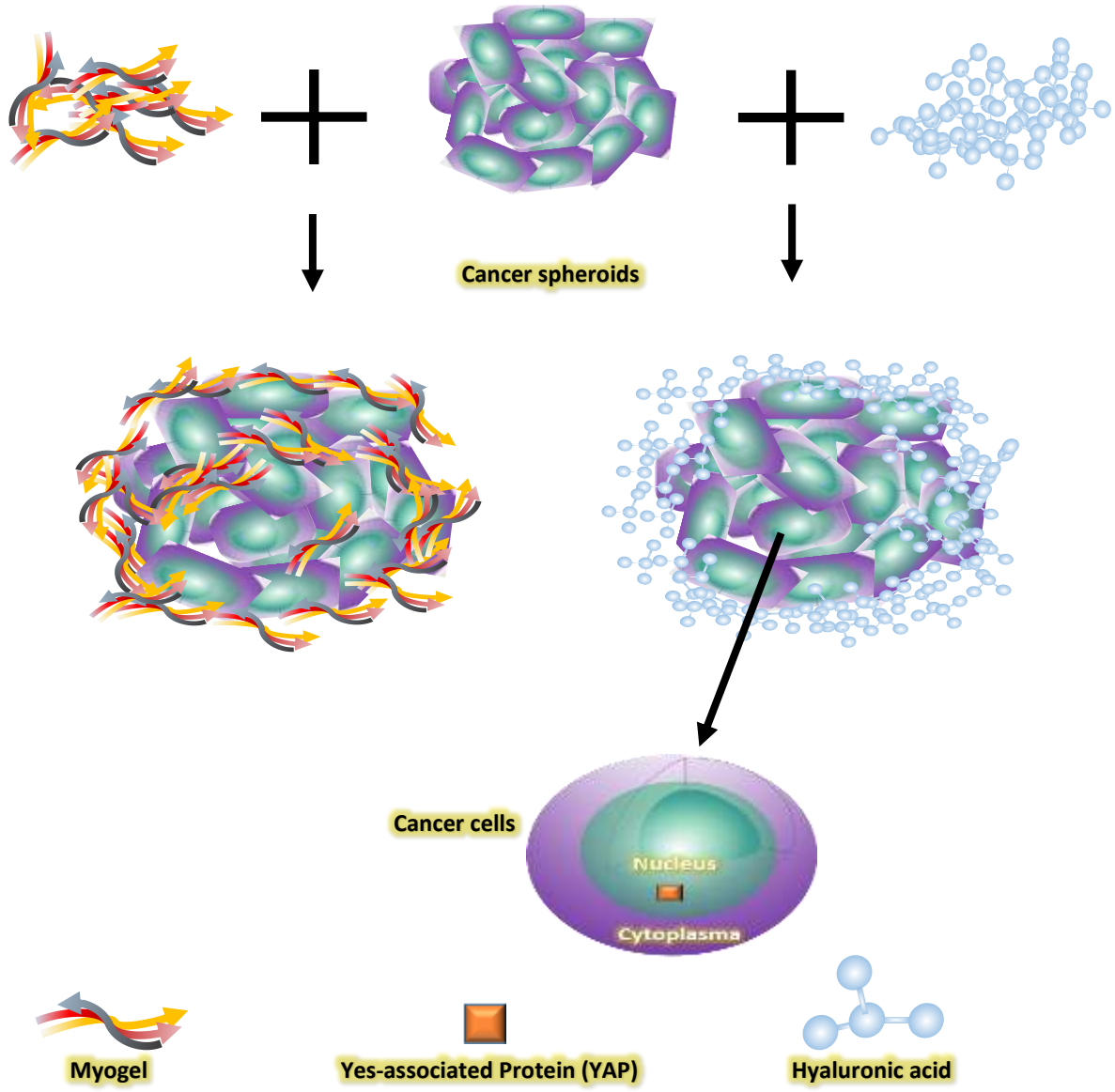

Figure 51. Diagram of effects of an artificial ECM on YAP signalling in a 3D mono-culture model of pancreatic cancer cells

Highlights

Myogel was prepared as a source of ECM elements. Collagen I, collagen IV, fibronectin and laminin could be detected in Myogel. Myogel was biocompatible with certain subtypes of PDAC cells.

Unmodified hyaluronic acid was biocompatible with Capan-2 and PANC-1 cells and could promote nuclear accumulation of YAP.

4.1 YAP signalling in the 3D model with pancreatic cancer cells and Myogel

4.1.1 Background

Since mouse models and commercial matrices used in 3D culture and organoids are expensive, it would be beneficial to explore other alternatives to reduce the cost of current pancreatic cancer models, especially in the context of screening large databases of potential novel therapeutics in conditions that represent the pancreatic cancer tumour microenvironment [Baker *et al*, 2016]. In 3D culture and organoids, rat collagen I and Matrigel (mouse sarcoma-derived products) are used to recreate an extracellular matrix (ECM) environment containing collagen I, collagen IV, fibronectin, and laminin that are present in the pancreatic cancer tumour microenvironment [Laklai *et al*, 2016; Ohlund *et al*, 2009]. A decellularized ECM preparation obtained from skeletal muscle, termed Myogel, can be prepared from a wide variety of animal sources in large quantities as an inexpensive source of ECM constituents. Myogel contains collagen I, collagen IV, laminin, and fibronectin, making it a promising scaffold element for tissue engineering [Abberton *et al*, 2008; Wolf *et al*, 2012] supports the growth of many cell types, including C2C12 myoblasts, human perivascular stem cells, NIH 3T3 fibroblasts, NIH 3T3-L1 cells, HMEC endothelial cells, primary muscle progenitor cells, primary aortic smooth muscle cells, and corneal epithelial cells [Abberton *et al*, 2008; DeQuach *et al*, 2012; Francis *et al*, 2009; Stern *et al*, 2009; Wolf *et al*, 2012].

Collagens in Myogel were reported to be between 27-72% of the total ECM extract [Abberton *et al*, 2008; Stern *et al*, 2009], allowing it to be compressed and manipulated to create different levels of external pressures. The collagen content was 486.7 ± 133 µg per mg of the porcine skeletal muscle (PSM) extract [Abberton *et al*, 2008], higher than the one (0.029 µg per mg) in porcine pancreas [Mirmalek-Sani *et al*, 2013]. The investigation of cell proliferation and cell migration using Myogel [Cheema *et al*, 2013; Nyga *et al*, 2013] could provide novel insights into using Myogel as a potential alternative matrix to culture pancreatic cancer cells and pancreatic stellate cells to mimic the PDAC tumour microenvironment. Further, Myogel from PSM could potentially provide a relatively inexpensive source for ECM elements that could act as an alternative matrix to mimic the pancreatic cancer tumour microenvironment.

4.1.2 Myogel characterization

Myogel was prepared as indicated in Materials and Methods. The total protein concentration of Myogel in the preparations that were examined ranged from 5 mg/mL to 9 mg/mL. De-cellularization was confirmed by DAPI staining as illustrated in Figure 52 A. The nuclei of muscle cells and the PANC-1 cells were able to be stained with DAPI while the intact nuclei and the tissue structure were not seen in the Myogel compared with the porcine skeletal muscle tissue.

MS/MS was performed to characterize the components within Myogel. Collagen I from rat tail was used as a control to test the ability of MS method to detect collagen I. The results indicated that Myogel components included myosins 1, 2, 4, and 7 as well as actins, glyceraldehyde-3-phosphate dehydrogenase, and Troponin T. In addition, an array of proteins from other species such as human, cow, chicken, mouse, rat, rabbit, and horse were also present, possibly due to the similarity of their mass. Unexpectedly, collagen I, collagen IV, fibronectin and Laminins were not identified in the Myogel using MS/MS.

Immunoblotting was also used to detect ECM components in Myogel using specific antibodies. Rat tail collagen I, Matrigel® containing collagen IV and Laminins, and fibronectin from bovine serum were used as positive controls. As illustrated in Figure 52 B, weak bands of collagen I, collagen IV, fibronectin and Laminin β-2 could be detected in these Myogel preparations using respective antibodies, indicating its potential to mimic the complexities of ECM in pancreatic cancer microenvironment. However, as the amount of detected ECM components was very low, further extraction and purification methods are needed to increase the concentration of collagen I, collagen IV, fibronectin and laminins in Myogel preparations that might be useful to mimic an ECM for 3D co-culture spheroids.

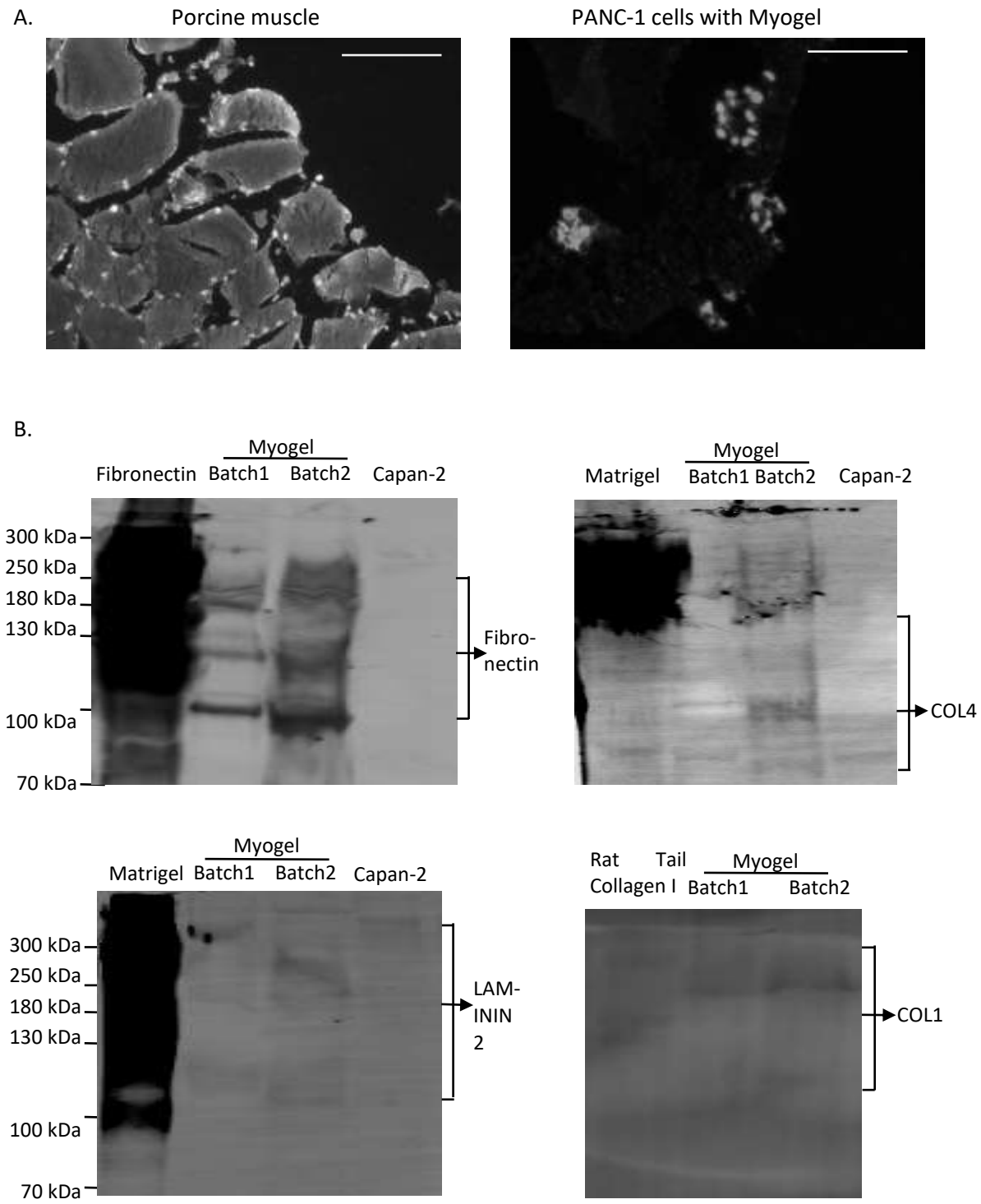

Figure 52. Myogel Characterization.

A. DAPI staining of porcine muscle, PANC-1 cells grown with Myogel for 10 days. Porcine muscle and the PANC-1 cells with Myogel were fixed in PFA, embedded in wax and sectioned in 5 µm per slide by microtome. After deparaffinization, DAPI (white) was incubated with the slides and images were acquired using Leica DMI4000 B (100x magnification). Scale bar, 100 µm. B. Immunoblotting of Myogel with antibodies against collagen I (COL1), collagen IV (COL4), fibronectin and Laminin β-2 (LAMININ2). Rat tail collagen I, Matrigel® and fibronectin from bovine serum were used as positive controls. Capan-2 cells were used as negative control.

4.1.3 Biocompatibility of Capan-2 and PANC-1 cells and spheroids with Myogel

We next mixed the Myogel preparation with Capan-2 or PANC-1 cell suspensions. Meanwhile, Capan-2 and PANC-1 spheroids prepared using the hanging drop protocol were transferred into 96-well plates, one spheroid per well coated with Myogel. Sphere growth and cell viability at 2 and 4 days after the cells and spheroids were put into Myogel were analysed. The cell suspension in Myogel was used to test the viability and proliferation of single cancer cell in Myogel so as to validate the ability of Myogel to support pancreatic cell growth and spheroids formation. The pre-formed spheroids in Myogel were used to test the potential of Myogel as a matrix for modelling cell invasion in ECM.

As shown in Figure 53 A, compared to the single layer of cells grown as 2D in standard cell culture medium, the Capan-2 cells suspension in Myogel formed multiple spheres and spheroid expansion could be seen on day 4. The spheroid expansion pattern in Capan-2 and PANC-1 was similar between the pre-formed spheroids dropped to the standard culture medium and the spheroids dropped to Myogel. Comparing the sizes of the spheroids on two different days and in two different growth conditions, there was no significant difference between spheroids grown in medium on day 2 and day 4 ($p > 0.05$). The sizes of Capan-2 spheroids increased significantly when cultured with Myogel for 4 days compared to 2 days ($p = 0.01$). However, the sizes of PANC-1 spheroids remained the same when cultured with Myogel for 4 days compared to 2 days ($p = 0.26$). Interestingly, there was no significant difference between Capan-2 spheroids grown in medium and in Myogel ($p = 0.72$) whilst significant increase could be seen in PANC-1 spheroids in Myogel compared to the ones in medium ($p = 0.04$).

As shown in Figure 54, the fluorescence intensity detected by incubation with resazurin, as a measurement of cell viability, was higher in spheroids grown in Myogel on Day 4 than those examined at Day 2 ($p < 0.05$) in Capan-2 groups. Moreover, there was no significant difference between the cell viability of 3D Capan-2 spheroids in Myogel and those incubated in standard cell culture medium ($p = 0.202$).

PANC-1 cell suspensions in Myogel, however, failed to form multiple spheres similar to those seen in Capan-2 group (Figure 53). As can be seen in Figure 54, the cell viability of PANC-1 cells suspension dropped significantly on Day 4 compared to Day 2 ($p < 0.05$). Also, there was significantly decrease in cell viability in PANC-1 spheroids grown 4 days in Myogel compared to the ones grown in medium ($p < 0.05$). Of note, cell viability was markedly increased on Day 4 in PANC-1 cell spheroids in Myogel compared with the ones on Day 2 in one independent experiment ($p < 0.05$) while remained statistically unchanged in another ($p = 0.86$, Exp2), indicating the variability among individual experiments. The batch difference, the unknown factors and proteins due to insufficient purification of Myogel preparation might cause the inconsistency in the biocompatibility of Myogel with PANC-1 cells and inhibition of cell viability in PANC-1 cells.

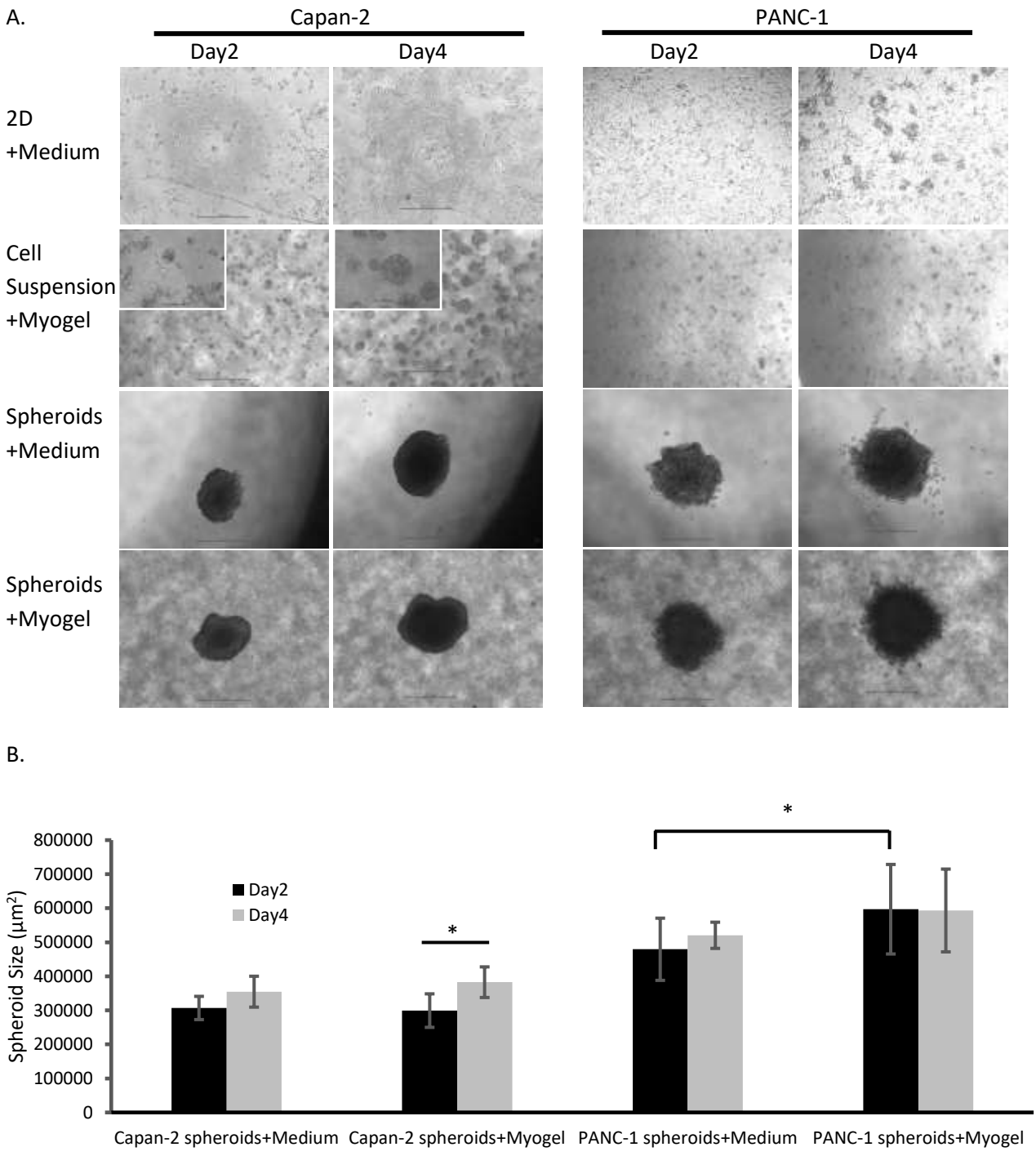

Figure 53. 2D and 3D culture in Myogel.

A. Representative phase-contrast imaging of 2D and 3D culture of Capan-2 and PANC-1 cells grown with or without Myogel in 96-well plates. Images were acquired using Leica DMI4000 B (50x and 100x magnification). Scale bars, 500 µm; 100 µm (insert). N=2. B. Graph of areas in µm^2 of Capan-2 and PANC-1 spheroids on Day 2 and Day 4. The areas were measured using CellProfiler. Error bars and graph were generated in Excel. Error bars represented standard deviations from 5-9 spheroids in each group from one independent experiment (n=1). *P*-value was calculated by two-tailed two-sample equal variance t-Test if the sample size between two groups were the same or unequal variance t-Test if the sample size between two groups were not the same using Excel. *: $p < 0.05$.

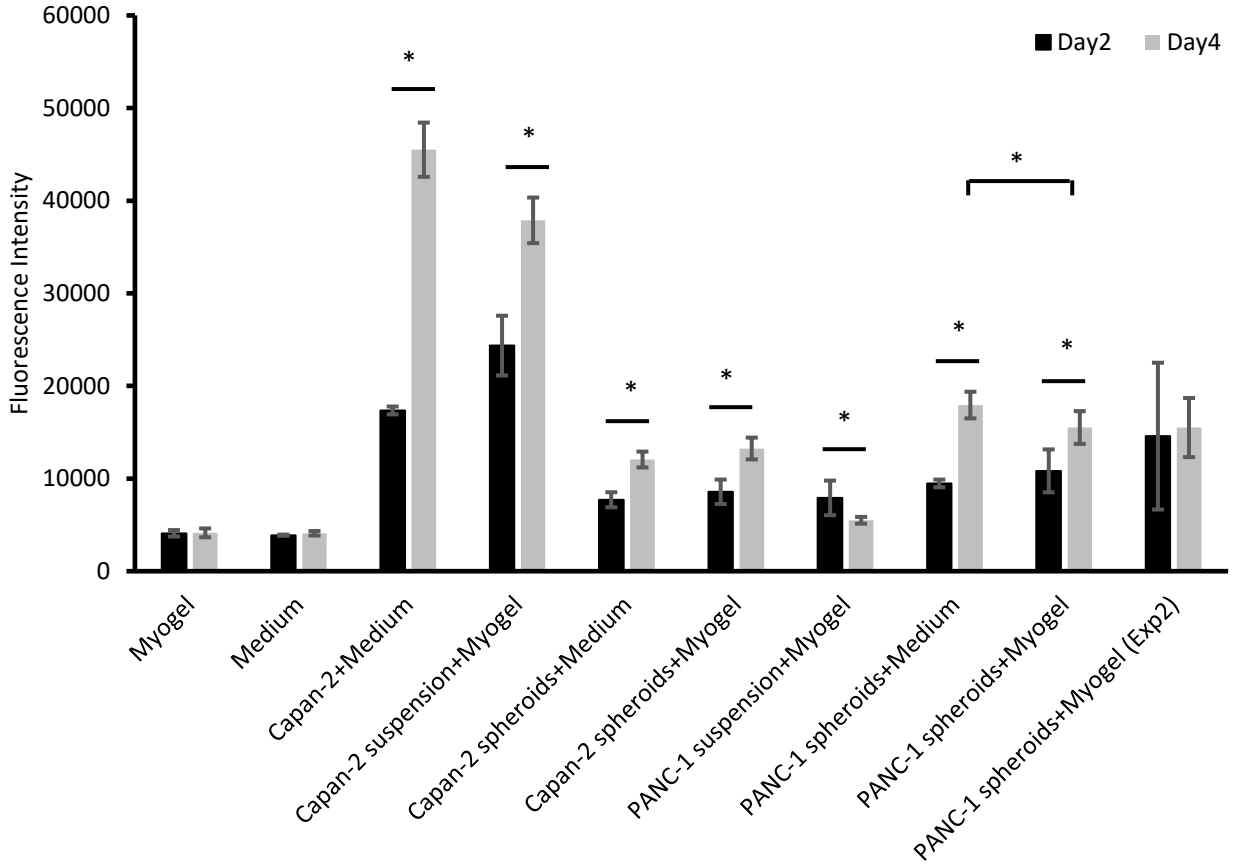

Figure 54. Cell viability of Capan-2 and PANC-1 cells and spheroids with Myogel by AlamarBlue® assay.

2D and 3D culture of Capan-2 cells and PANC-1 cells were grown with or without Myogel in 96-well plates. Fluorescence intensities in five-six wells detected by incubation with resazurin in cell suspensions and spheroids with or without Myogel in one independent experiment were calculated except three wells were managed to be detected in Exp2. Error bars indicated standard deviation of five or six wells in one independent experiment except three wells in Exp2. *P*-value was calculated by two-tailed two-sample equal variance t-Test if the sample size between two groups were the same or unequal variance t-Test if the sample size between two groups were not the same using Excel. Error bars and graph were generated in Excel. *: $p < 0.05$.

4.1.4 YAP signalling in Capan-2 spheroids and PANC-1 spheroids grown in Myogel

YAP expression and localization was investigated in 3D mono-culture of Capan-2 and PANC-1 grown in Myogel. As illustrated in Figure 55, there was no striking difference in YAP expression between Capan-2 spheroids and PANC-1 spheroids grown in standard cell culture medium and Myogel for 2 days.

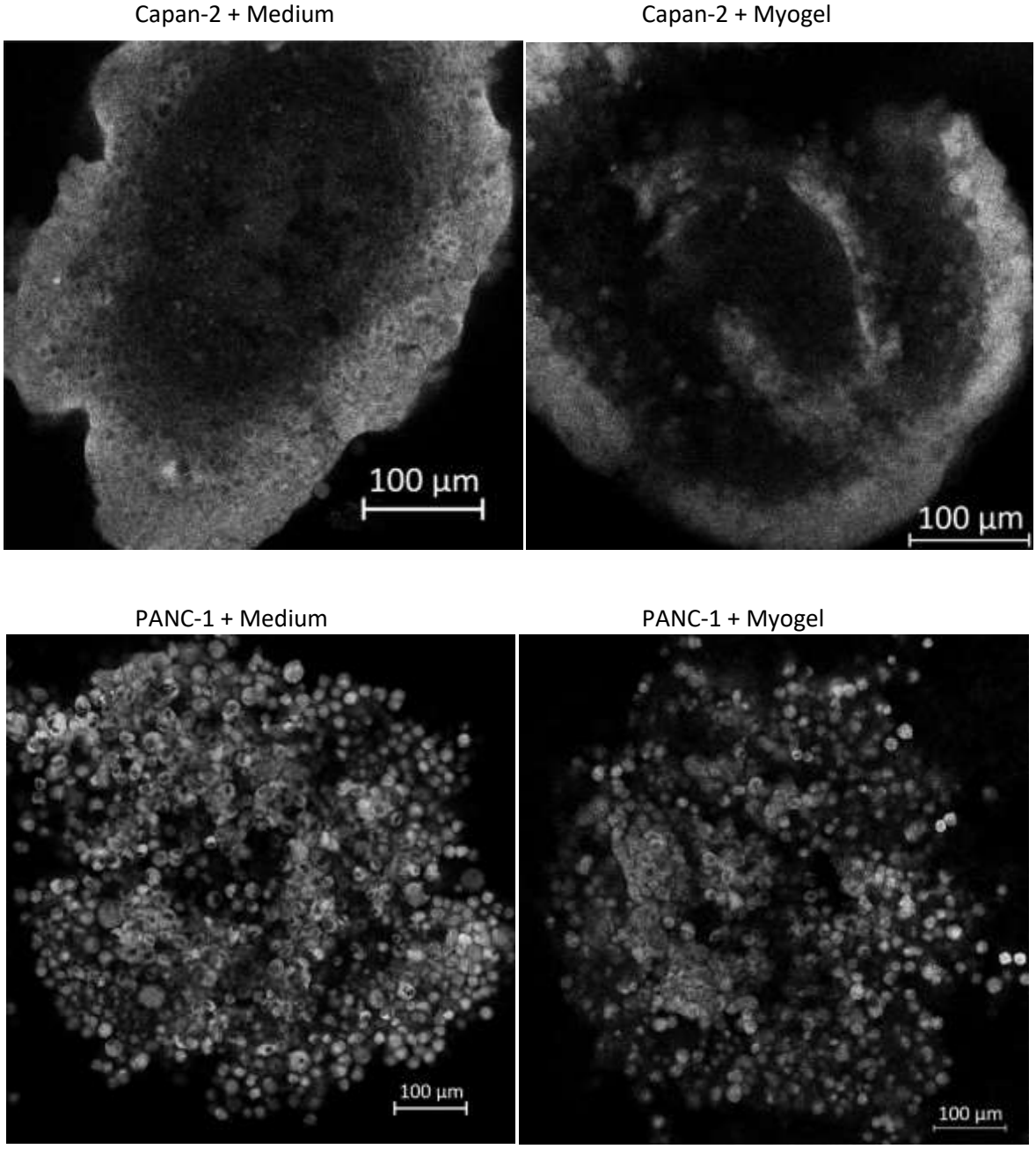

Figure 55. Subcellular localization of YAP in 3D mono-culture of Capan-2 spheroids and PANC-1 spheroids with or without Myogel.

500 Capan-2 cells and PANC-1 cells were seeded in a hanging drop format for 4 days and then spheroids were dropped to standard cell culture medium with or without Myogel. After 2 days, immunofluorescence microscopy with single anti-YAP antibodies was performed. Fluorescent images were acquired by confocal laser scanning microscopy using Zeiss LSM880. Image analysis was performed using Zen 2.3 (blue edition). N=1. Scale bars, 100 µm.

4.2 YAP signalling in a 3D model containing pancreatic cancer cells and HA

4.2.1 Background

Hyaluronic acid (HA) is accumulated in 80-87% of PDAC and contributes to the high interstitial fluid pressure that hinders drug delivery to these tumours [Kultti *et al*, 2012; Sato *et al*, 2016b]. Pancreatic cancer cells and the tumour-stromal interactions induce the production of HA in the PDAC microenvironment [Mahlbacher *et al*, 1992; Sato *et al*, 2016a]. HA metabolism results in small HA fragments to large molecular weight polymers (2,000–25,000 disaccharide unit) in the cancer microenvironment, which can bind to cell surface receptors such as EGFR and CD44, to stimulate cell proliferation [Kultti *et al*, 2012]. Meanwhile, HA crosslinks naturally with collagens and fibronectin in the ECM to promote cell invasion [Kultti *et al*, 2012]. Through these interactions, HA activates a focal adhesion kinase (FAK), Ras GTPases, and modulates actin cytoskeleton [Kultti *et al*, 2012] as events that are associated with YAP signalling. Therefore, incorporating HA in the culture system could provide a highly promising approach to study YAP signalling in these *in vitro* 3D models of PDAC.

HA-based hydrogels have been widely used to establish 3D cancer models, most of which utilized chemically-modified products. PDAC cells have been shown to be viable in thiol-modified HA and models have demonstrated epigenomic and metabolic changes in the stromal compartment of these systems [Sherman *et al*, 2017]. The effects of by-products and residual materials generated by these chemical crosslinking reactions can affect genetic changes and protein expression that might alter PDAC properties [Burdick *et al*, 2011]. Such possible events warrant further investigation. Meanwhile, HA isolated from microbial fermentation, such as *Streptococcus equi*, can be used to examine the feasibility using unmodified HA to develop 3D models to mimic PDAC tumours. In this section, studies were performed to identify optimised condition for using HA and to study the impact of this ECM element on YAP signalling *in vitro*.

4.2.2 Spheroid expansion in HA

There were limited data on the 3D culture of Capan-2 and PANC-1 cells in HA. HA present in human PDAC and human normal pancreas is reported to range from 0.029 ± 0.003 to 0.388 ± 0.032 mg per g wet tissue [Ozcelikkale *et al*, 2017]. Such a large range of potential HA levels did not provide much guidance in the selection of HA concentrations to include in the 3D culture format. Thus, an empirical approach was taken to select an HA concentration that might be useful in establishing a 3D cancer format for future screening of potential anticancer agents.

3D mono-culture spheroids composed of Capan-2 or PANC-1 cancer cells were formed using the hanging-drop protocol. At day 4, these spheroids were dropped into the wells of polyHEMA low-attachment plates containing 1, 3, or 5 mg/mL HA in PBS. An HA stock solution was prepared at 10 mg/mL in PBS. It should be noted that the introduction of HA reduced the volume of culture medium in the final culture conditions, where the higher HA content correlated with lower levels of nutrients coming from the amount of culture media replaced by HA solution. As a result, wells with the same volume of PBS as the ones in the highest HA concentration (5 mg/mL) used in the present study served as controls, acknowledging this discrepancy in potential nutrient composition.

As shown in Figure 56 and 57, compared to spheroids dropped into the wells on day 4, there was no marked difference between the spheroid expansions over 5 days grown in PBS: medium mixture and spheroids grown in standard culture medium (the difference in the size was due to the manual variability between independent experiments). Cancer cell mono-culture spheroids in the wells containing the PBS without HA (controls) were indistinguishable from those wells with normal culture medium as detected by phase-contrast imaging. This indicates that the reduction in nutrients on this occasion had no significant impact on gross aspects of these 3D cancer cell spheroids. Of note, small clusters of PANC-1 cells could be seen after 1 day in the 3 and 5 mg/mL HA whereas none were observed in the 0 and 1 mg/mL HA (Figure 57).

5 mg/mL HA was chosen for the following sections because it could mimic more challenging barrier for therapeutic agents to penetrate than 1 and 3 mg/mL HA.

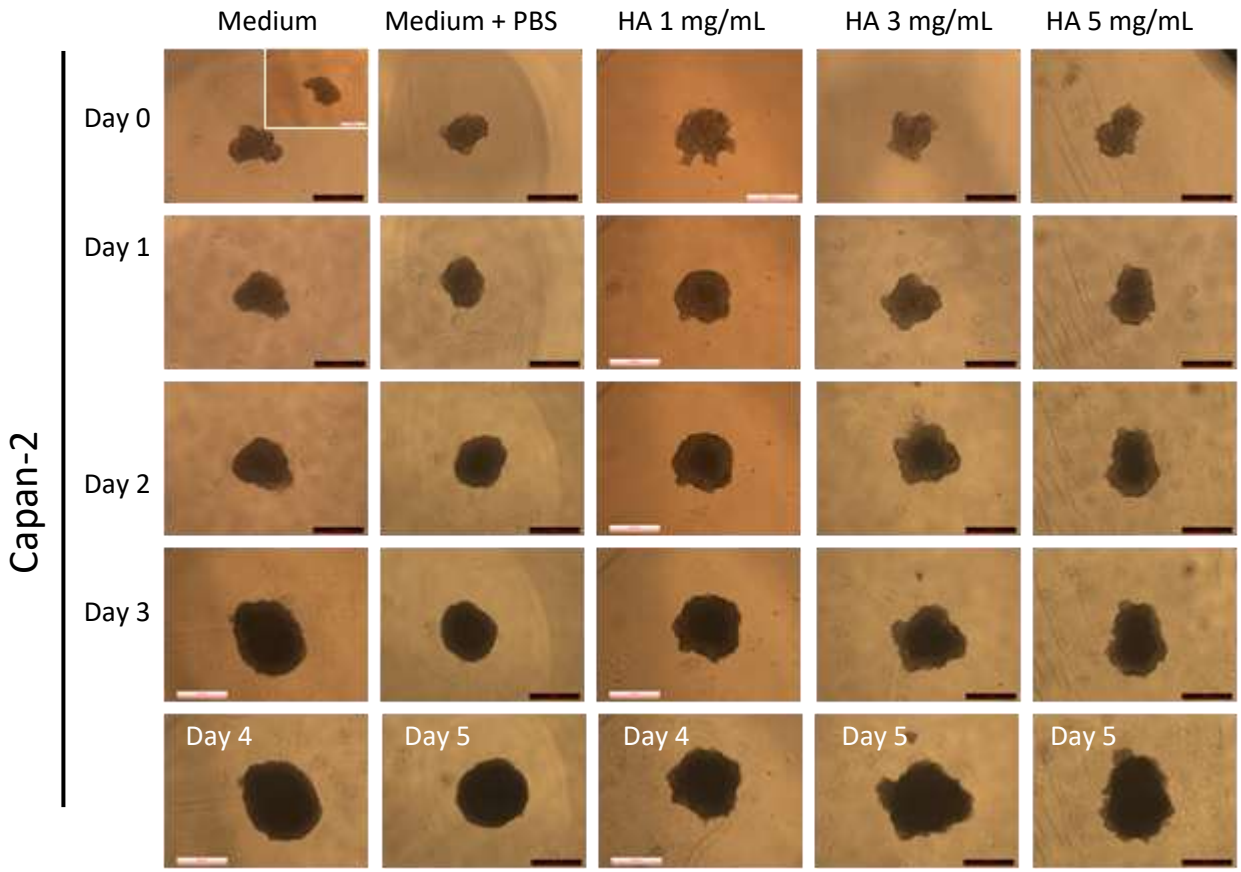

Figure 56. Capan-2 spheroid expansion in hyaluronic acid.

500 Capan-2 cells were seeded in GravityPLUS™ HangingDrop plates and after 4 days the droplets were pushed to the wells containing 0, 1, 3, and 5 mg/mL hyaluronic acid (HA) in polyHEMA low-attachment plates. The wells with the same volume of PBS (the solvent used to dissolve HA) as the ones in the highest concentration of HA (5 mg/mL) were included to examine the reduction of nutrients in the culture environment. Images were acquired by Leica DMI4000 B (50x magnification) manually at the time points indicated after dropping Capan-2 spheroids into the polyHEMA low-attachment plates. Representative images from six spheroids in the same group from one independent experiment were shown. The insert image of Capan-2 with medium on Day 0 was captured in the same well as the one on Day 3 and Day 4. Scale bar, 500 µm.

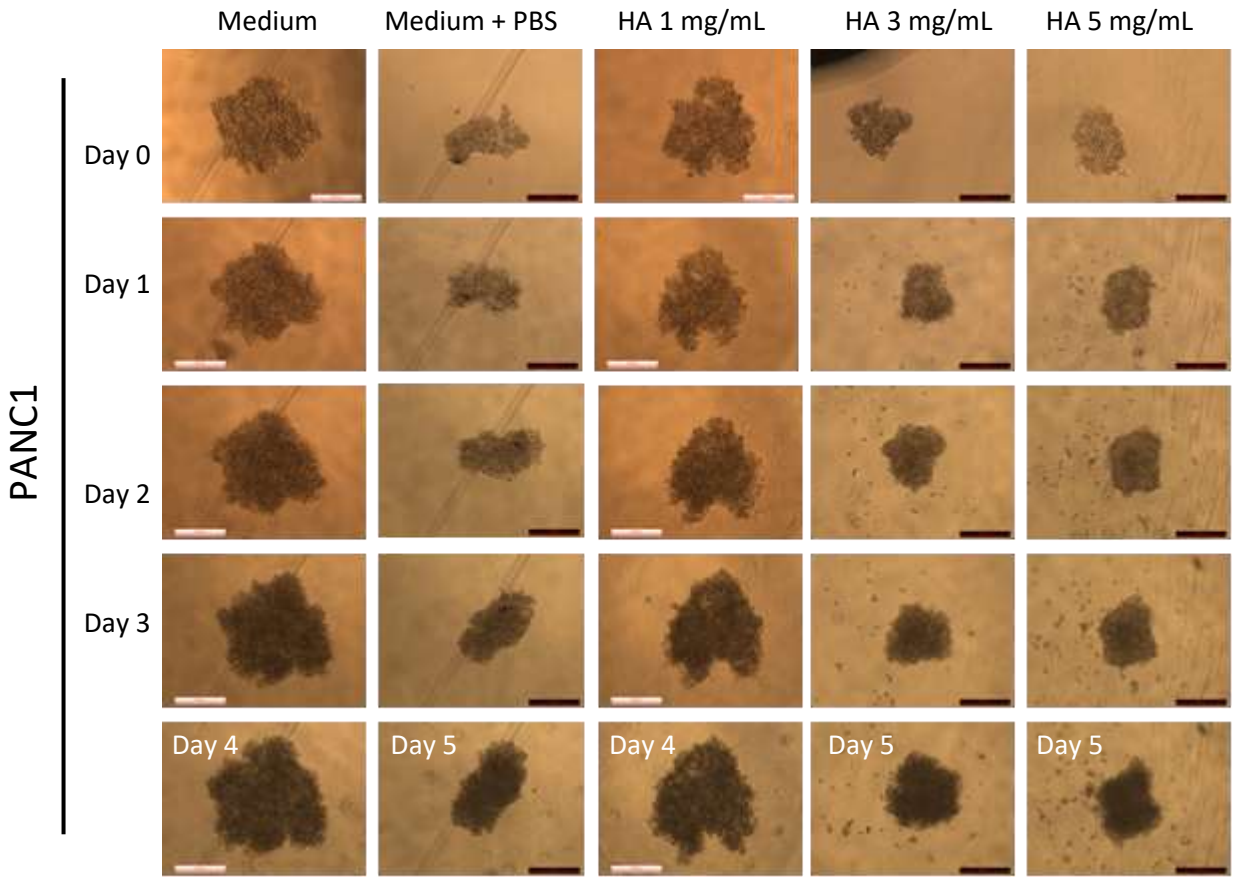

Figure 57. PANC-1 spheroid expansion in hyaluronic acid.

500 PANC-1 cells were seeded in GravityPLUS™ HangingDrop plates and after 4 days the droplets were pushed to the wells containing 0, 1, 3, and 5 mg/mL hyaluronic acid (HA) in polyHEMA low-attachment plates. The wells with the same volume of PBS (the solvent used to dissolve HA) as the ones in the highest concentration of HA (5 mg/mL) were included to examine the reduction of nutrients in the culture environment. Images were acquired by Leica DMI4000 B (50x magnification) manually at the time points indicated after dropping PANC-1 spheroids into the polyHEMA low-attachment plates. Representative images from six spheroids in the same group from one independent experiment were shown. Scale bar, 500 µm.

4.2.3 YAP subcellular localisation in 3D cultures of cancer cells with hyaluronic acid

YAP expression and localization was investigated in Capan-2 and PANC-1 spheroids grown in the presence of hyaluronic acid (HA). 500 Capan-2 or PANC-1 cells were seeded in GravityPLUS^{TM} HangingDrop plates for 4 days and spheroids were dropped to 96-well plates containing medium with or without 5 mg/mL HA. After 2 days, whole spheroids were fixed in PFA, and immunofluorescence staining with anti-YAP antibodies and DAPI followed by optical clearing was performed.

After 2 days in HA, nuclear and cytoplasmic localisation of YAP, both at the edge and the core of the spheroids, changed in the spheroids with HA compared to the ones grown in medium without HA (Figure 58). There appeared to be more signals near the core of the spheroids when cultured with HA than the ones without HA (Figure 58). Semi-quantification of YAP was conducted in one Capan-2 spheroid in the presence of HA (Figure 59). Unfortunately, DAPI staining of the spheroids cultured with medium was missing during sampling, causing unavailability of semi-quantification of YAP in the spheroids without HA. Because the data representing YAP intensities and ratios did not follow normal distribution and not have the same shape of distribution, mean ranks of the datasets were compared using a non-parametric Mann-Whitney U test in Figure 59. Comparing the total YAP intensities in the whole cells near the edge and the core, the cells near the edge exhibited significantly higher YAP expression (mean rank of 25.35 for Capan-2 cells near the core and 77.31 for Capan-2 cells near the edge, $p < 0.001$). The ratio of cytoplasmic YAP intensities was significantly lower than the ratio of nuclear YAP intensities in the Capan-2 cells near the core of the spheroids (mean rank of 28.17 for ratio of cytoplasmic YAP intensity and 68.83 for nuclear intensities of YAP, $p < 0.001$), and Capan2 cells near the edge of the spheroids (mean rank of 44.24 for ratio of cytoplasmic YAP intensity and 74.76 for nuclear intensities of YAP, $p < 0.001$). The data indicated cells with nuclear accumulation of YAP were found in the current optical section of 3D Capan-2 spheroid cultured in HA.

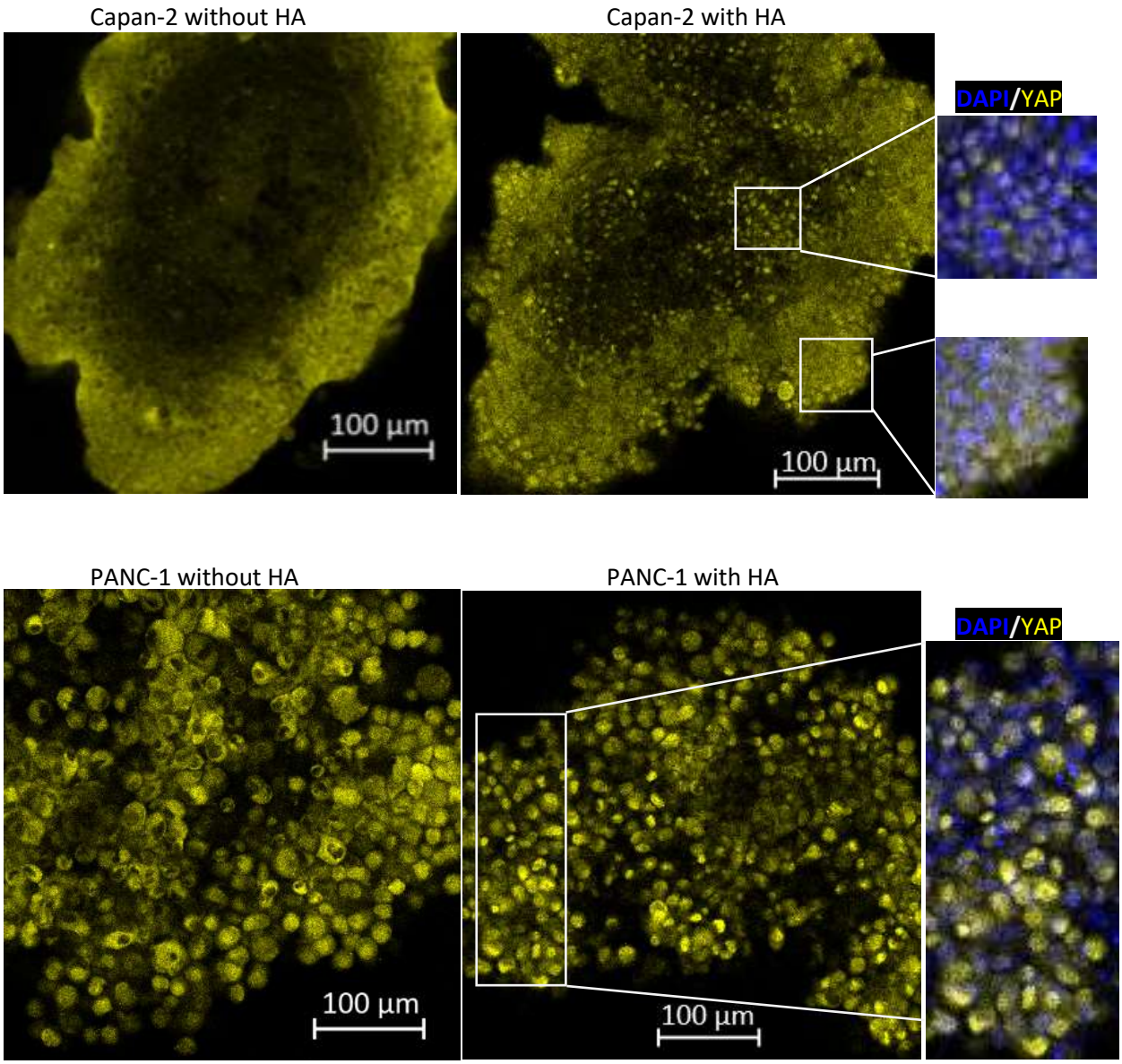

Figure 58. Subcellular localization of YAP in 3D mono-culture of Capan-2 spheroids and PANC-1 spheroids with or without hyaluronic acid.

500 Capan-2 cells or PANC-1 cells were seeded in GravityPLUS^{TM} HangingDrop plates for 4 days and spheroids were dropped to 96-well plates containing medium with or without 5 mg/mL hyaluronic acid (HA). After 2 days, immunofluorescence staining with anti-YAP antibodies (yellow) and DAPI (blue) followed by optical clearing was performed. Fluorescent images were acquired by confocal laser scanning microscopy using Zeiss LSM880 with optical sectioning near the core of each spheroid. Image analysis was performed using Zen 2.3 (blue edition). Representative images were from three spheroids in one independent experiment.

A.

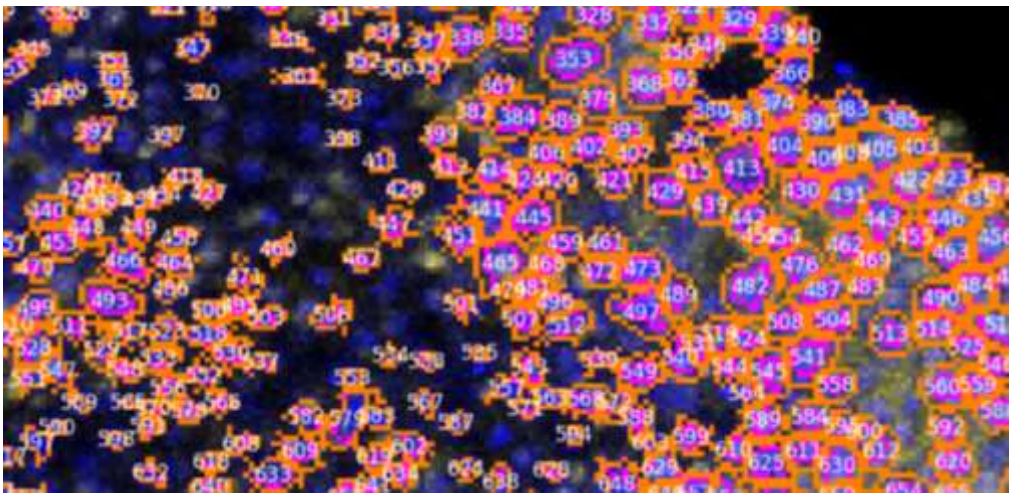

B.

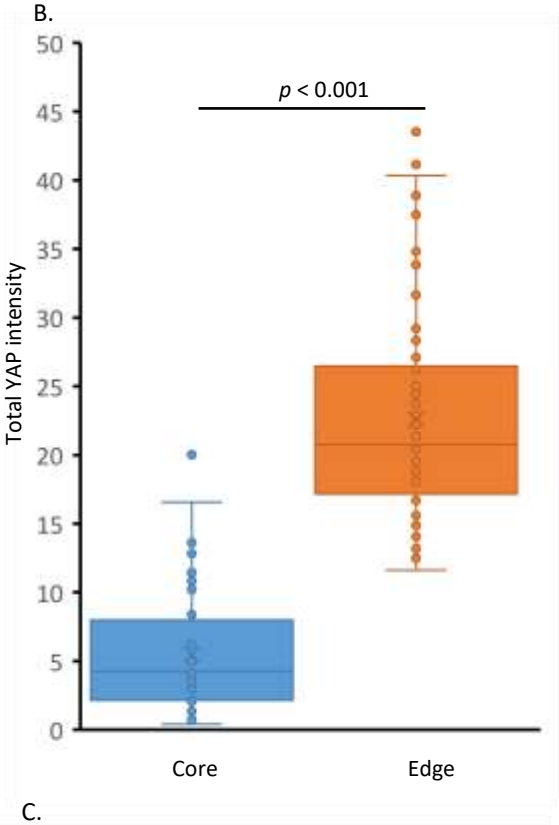

C.

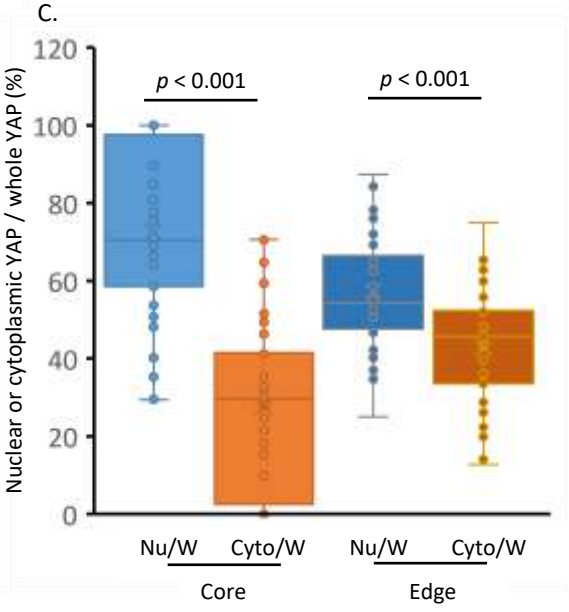

Figure 59. Semi-quantification of YAP subcellular expression in 3D mono-culture of Capan-2 spheroids with hyaluronic acid.

500 Capan-2 cells were seeded in GravityPLUS™ HangingDrop plates for 4 days and spheroids were dropped to medium with 5 mg/mL hyaluronic acid. After 2 days, immunofluorescence staining with anti-YAP antibodies (yellow) and DAPI (blue) followed by optical clearing was performed. Fluorescent images were acquired by confocal laser scanning microscopy using Zeiss LSM880 with optical sectioning near the core of each spheroids. Image analysis was performed using Zen 2.3 (blue edition). Semi-quantification of YAP expression was analysed by CellProfiler. A representative field of view in an image processed by CellProfiler was shown, depicting the outlined nuclear areas and the cytoplasmic areas labelled with numbers (A). Whisker box graph was made from all the values of total YAP intensity in the whole cell of each individual cell (B) or the intensity ratios of nuclear YAP intensity to total YAP intensity in the whole cell of each individual cell or cytoplasmic YAP intensity to total YAP intensity in the whole cell of each individual cell (C) from around 45-60 cells near the core of the spheroid and the edge of the spheroid, using Excel. Mean markers were shown. Median was exclusive from quartile calculation. Dots indicated the values in cells automatically generated by Excel. Non-parametric Mann-Whitney U test in SPSS was used to calculate the *p* values. Nu: nucleus; Cy: cytoplasm; W: whole cell.

4.3 Discussion

Rat Collagen I and mouse Matrigel® are biomaterials that have been used to mimic the ECM in 3D PDAC models and patient-derived organoids [Baker *et al*, 2016]. Batch-to-batch differences and the variability of animal-derived factors obtained by various isolation methods raise uncertainties to their long-term use in *in vitro* models to the tumour environment in patients with PDAC [Baker *et al*, 2016]. There is a need to reduce the cost of the PDAC models considering the demand for high-throughput assays. In this chapter, the feasibility of Myogel and unmodified HA in establishing 3D PDAC models and studying YAP signalling was investigated.

The commonly used commercially available materials to mimic ECM are extractions from rat tails and the Engelbreth-Holm-Swarm (EHS) mouse sarcoma. They usually come from companies as solutions so they may not be ideal to recapture the 3D structure of tumours because they lose the architecture of intact cells. But gelation occurs when they are put in the environment with 5% CO_2 at 37 °C, recovering certain degree of the ECM structure in cancer microenvironment. The idea of extraction from porcine skeletal muscle (PSM) follows similar principles so as to produce ECM macromolecules to form ECM structure.

Since pancreatic cancer originated from the pancreas, assumptions can be made to extract ECM from the porcine pancreas as a more feasible approach not only to obtain ECM macromolecules but also other factors that may be essential for the growth and maintenance of pancreatic cancer cells than from PSM. However, The collagen content was 486.7 ± 133 µg per mg of PSM extract [Abberton *et al*, 2008], higher than the one (0.029 µg per mg) in porcine pancreas [Mirmalek-Sani *et al*, 2013]. Compared to the higher amount of skeletal muscle per animal than the pancreas per animal, extraction from skeletal muscle may be more efficient than that from the pancreas and compliant with the emerging trend of replacement, reduction and refinement of animal use in scientific research [Brown *et al*, 2018; Tannenbaum *et al*, 2015].

There were two commonly used methods to prepare Myogel. One method is to use trypsin and detergents such as SDS and Triton™ X-100 to treat the tissue, which requires multiple freeze-thaw steps and lengthy incubation of the tissue with SDS solutions and Triton-100 solution to decellularize the tissue [DeQuach *et al*, 2012; Stern *et al*, 2009; Wolf *et al*, 2012]. The other method is based on homogenization [Abberton *et al*, 2008], which is tested for reproducibility in this section and considered to be more efficient and less harsh for ECM proteins than the first method to preserve the ECM macromolecules. The resulting total protein concentration of Myogel could reach about 9 mg/mL, which could be close to the commercially available protein concentration in Matrigel®. The serious batch variation could be due to the human error. However, collagens, fibronectin and laminin were not detected by mass spectrometry whereas peptide signatures following trypsin hydrolysis of the Myogel prepared in these studies indicated large amount of myosin proteins. While immunoblotting studies detected collagens, fibronectin and laminin in the Myogel preparation isolated for these studies, the presence of collagens, fibronectin and laminin could not be verified by mass spectrometry. There are three probable reasons why the peptides unique to collagens, fibronectin and laminin were not observed by mass spectrometry: 1) the energy used to charge the peptides derived from digested Myogel may not have been sufficient to ionize all the peptides from collagens, fibronectin and laminins for detection; 2) the shotgun MS could have been overlooked the presence of peptides from collagens, fibronectin and laminins due to multiple peptides at much higher content from myosin proteins being

eluted at the same time; 3) no collagens, fibronectin and laminin could be extracted using the current method.

Two models to test the biocompatibility of Myogel with pancreatic cancer cells were used in the current study. One model is to use the cell suspension in Myogel to test the viability and proliferation of single cancer cell in Myogel so as to validate the ability of Myogel to support pancreatic cell growth and spheroids formation. The other model is to use the pre-formed spheroids in Myogel so as to test the potential of Myogel as a matrix for modelling cell invasion in ECM. Because PANC-1 cells are isolated from a patient with metastatic PDAC and possess high invasiveness in ECM [Deer *et al*, 2010], it was expected that the spheroids would expand in Myogel compared to the ones grown in the medium. Significant increase could be seen in PANC-1 spheroids in Myogel compared to the ones in medium. However, the sizes of PANC-1 spheroids remained the same when cultured with Myogel for 4 days compared to 2 days. The data are not consistent with each other, possibly due to an isolated event if sufficient independent experiments could be attained. Single Capan-2 cell formed 3D structures in Myogel after 2 days whereas it sometimes took 10 days for single PANC-1 cell to form 3D structures. Despite that 3D Capan-2 and PANC-1 spheroids were able to expand in Myogel and the cell viability increased after 2 days, YAP expression and localisation was not affected by Myogel, which was supposed to have the components to induce YAP nuclear translocation [Miroshnikova *et al*, 2017; Rice *et al*, 2017]. Taken together, purification of Myogel by enrichment of ECM may worth exploring in the future.

It is possible that large molecules of HA could be fragmented during heating. HA is reported to be metabolised into small HA fragments to large molecular weight polymers (2,000–25,000 disaccharide unit) in the cancer microenvironment, which can bind to cell surface receptors such as EGFR and CD44, to stimulate cell proliferation [Kultti *et al*, 2012]. Weighing the risk of contamination to affect the cell growth and considering the reported method of sterilising HA by heating [Madihally *et al*, 1999], high temperature sterilization method was used to ensure the aseptic quality of HA solution because of the difficulty during filtering and uncertainty of HA concentration after filtering. After autoclaving, the HA solution still maintains the viscosity, creating a viscous environment to test the drug diffusion. Obvious spheroid expansion could be seen in both 3D Capan-2 and PANC-1 in unmodified HA derived from *Streptococcus equi* over 5 days. Meanwhile, after semi-quantification of YAP in 3D Capan-2 spheroids, more YAP translocated into the nucleus in the presence of HA compared to the ones in the Chapter 3, consistent with the findings indicating that HA can activate upstream regulators in YAP signalling to promote the nuclear accumulation of YAP [Kultti *et al*, 2012]. It also recapitulated YAP signalling as a driving force for aggressive cell proliferation in PDAC. Thus, the present study offered direct evidence on unmodified HA from *Streptococcus equi* as a biomaterial to recreate PDAC environments.

One major limitation of the studies described in this chapter is that they only examined YAP signalling in the context of cancer cell-ECM interaction, lacking stellate cells and immune cells that are present in the PDAC tumour environment. At present, it is unclear which receptors, cell junction proteins, growth factors, chemokines, and cytokines that might be provided by stellate cells and immune cells are needed to recapitulate the complex networks affecting YAP signalling in PDAC tumours. Another limitation of this chapter is the lack of analysis of ECM by MassSpec in each batch of Myogel preparation.

Chapter 5. YAP signalling in 3D co-culture models of pancreatic cancer cells, stellate cells and ECM-like materials

Graphical abstract

First trial: spheroids dropped into a stellate cells (SCs) suspension with hyaluronic acid (HA)

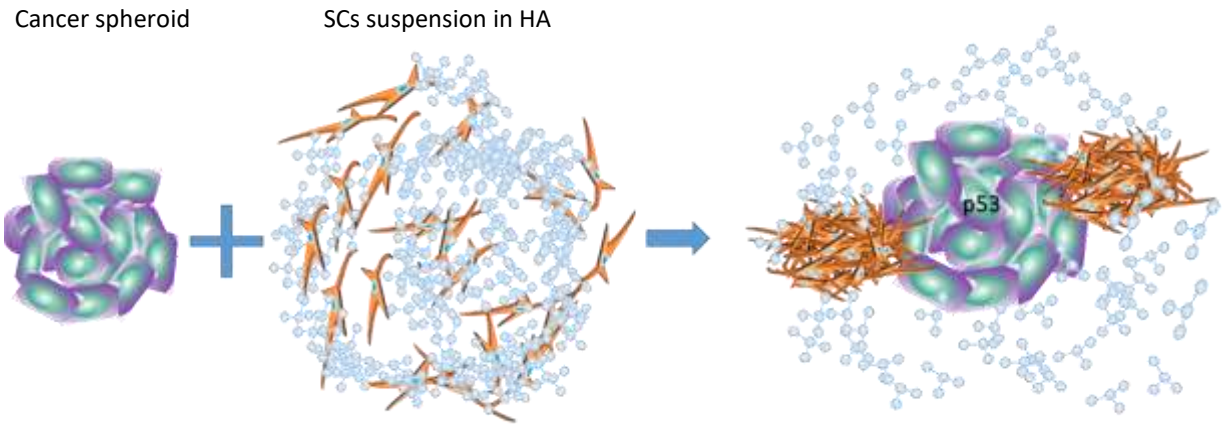

Second trial: spheroids dropped to a SCs suspension with HA and collagen I

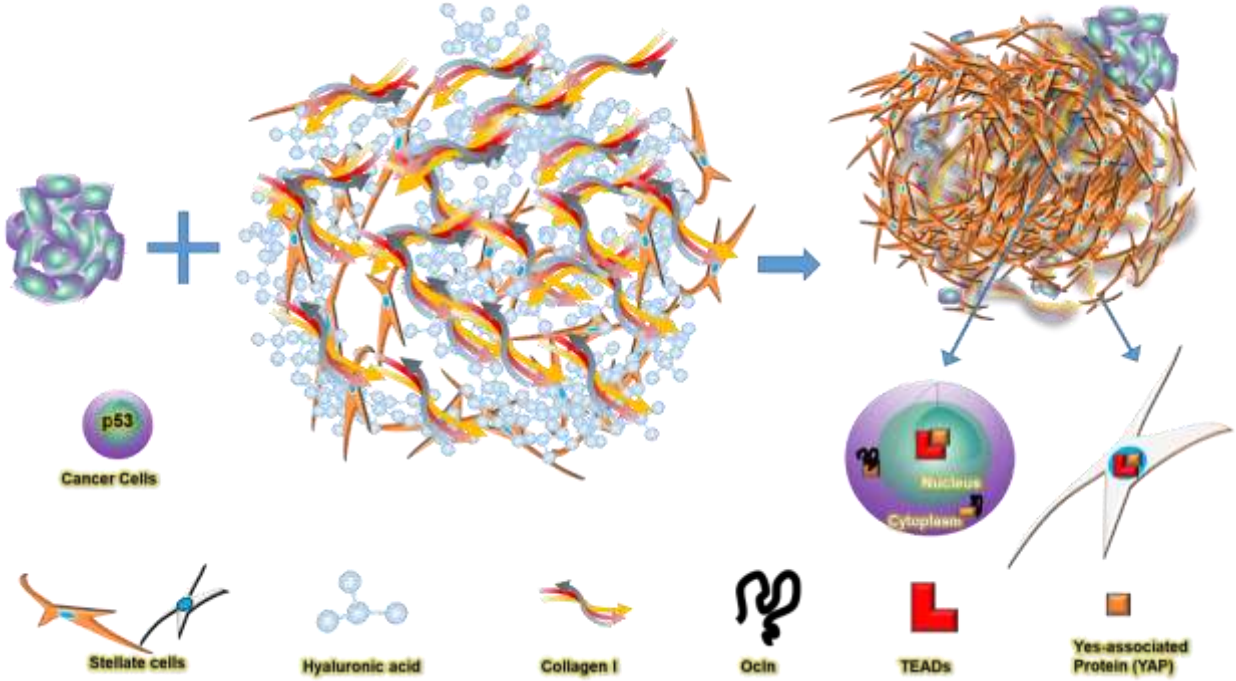

Figure 60. Diagram of YAP signalling in 3D co-culture models of pancreatic cancer spheroids dropping into stellate cells suspensions with ECM-like materials.

Third trial: cancer cells, stellate cells (SCs) and collagen I mixture (initial test of anti-cancer agents)

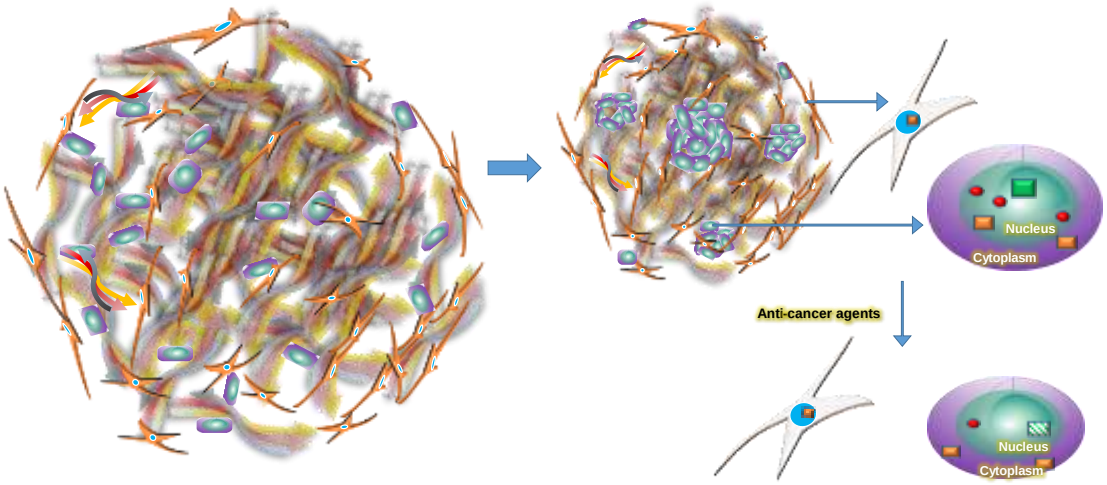

Fourth trial: cancer cells, SCs, HA and collagen I mixture

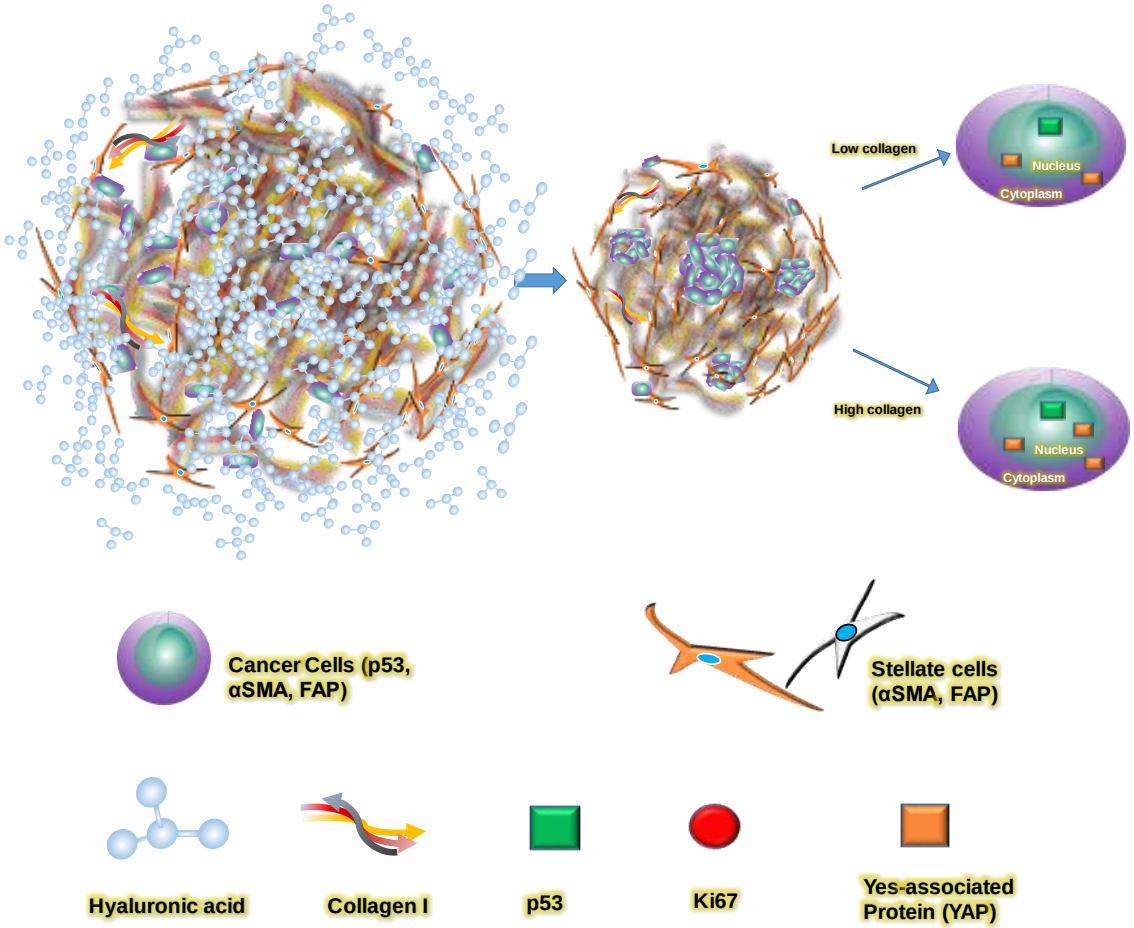

Figure 61. Diagram of YAP signalling in 3D co-culture models of pancreatic cancer cells mixing with stellate cells and ECM-like materials.

Highlights

Dropping of PDAC spheroids into a stellate cells suspension in HA or HA with collagen I was able to establish a 3D co-culture model where only some of the cancer cells contacted with stellate cells without the multi-layered stellate cell barrier around the cancer cells core.

Growing PDAC cells and stellate cells in a collagen I matrix with or without HA formed a single spheroid in each well of 96-well plates, resulting in multiple cancer cell cores inside the 3D co-culture models that resembled the fibrotic cancer microenvironment in patients with advanced and metastatic PDAC.

Dynamic YAP subcellular localisation was found in these PDAC and stellate cell 3D co-culture models.

Reduction of p53 expression correlated with YAP cytoplasmic localisation in the 3D co-culture models of PDAC cells and stellate cells.

Potential anti-cancer compounds Pseudopterosin A-D and Tylophorinine, derived from natural products, reduced p53, Ki67 and YAP expression in the 3D co-culture models of PDAC cells and stellate cells.

5.1 Background

Based on our previous work, direct co-culture of PDAC cells and stellate cells in scaffold-free conditions failed to form spheroids organized into stellate cells surrounding the cancer cells in each well. Additionally, dropping cancer cell mono-culture spheroids into a scaffold-free stellate cells suspension was not able to establish this organization where stellate cells could wrap around a cancer cells core. Unmodified hyaluronic acid was found to be biocompatible with PDAC cells and able to affect YAP signalling. Therefore, in the work reported below, we aimed to build an easy-to-use model for high-throughput assay by mixing cancer cells, stellate cells, HA, and collagen I in various ways. These studies focused on stabilizing 3D spheroids in the desired organization of cancer cells and stellate cells using ECM surrogate materials. Only those approaches considered to potentially provide a consistent, efficient, and economical method that could provide clinical relevance.

5.2 Spheroid formation and cell distribution in 3D co-culture models of stellate cells to cancer cells at a 10:1 cell ratio with hyaluronic acid

5.2.1 Dropping cancer cell spheroids into hepatic stellate cells suspensions in hyaluronic acid

In our opinion, having a single spheroid per well will benefit the standardization of spheroid size in high-throughput assay, consistent with other studies on 3D culture in micropatterning [Hirschhaeuser *et al*, 2010] and forming 3D culture using centrifugation [Friedrich *et al*, 2009]. In order to determine the optimal concentration of hyaluronic acid (HA) to suspend stellate cells to provide conditions for attachment to and engulfment of a cancer cells spheroid, we mixed the stellate cells suspension with an HA preparation to produce a final concentration of 0, 1, 3, or 5 mg/mL HA in each well in 96-well polyHEMA plates. The goal was to identify conditions leading to the formation of multilayers of stellate cells surrounding a cancer cells core. Each cancer cell mono-culture spheroid was pushed from a hanging drop plate to individual well containing a stellate cells suspension in HA, resulting in dropping one spheroid per well.

As shown in Figure 62, stellate cells in 1 mg/mL HA settled to the bottom of wells approximately 2 hours after seeding when being captured by the microscope on day 4, whereas stellate cells in either 3 mg/mL or 5 mg/mL HA initiated aggregation into small spheres suspending in the medium 4 hours after seeding (Figure 65). As illustrated in Figure 63 and 64, one large spheroid with multiple small spheroids nearby could be detected after Capan-2 and PANC-1 spheroids dropped into the HSCs suspension with HA. Stellate cells and clusters of stellate cells surrounding the cancer cells spheroid in HA started to attach to cancer spheroids 4 hours after seeding into the wells containing 3 mg/mL or 5 mg/mL HA (Figure 65). We expected the stellate cell spheres would move towards the cancer spheroids to form one single spheroid in each well over time. However, there was no single spheroid formed in each well 4 days (Day 8) and 8 days (Day 12) after seeding into the wells containing 1 mg/mL or 5 mg/mL HA (Figure 63 and 64).

After quantification of the largest spheroid in the field of view, the sizes of the HSCs mono-culture in 1 mg/mL HA and the co-culture of PANC-1 with HSCs and 1, 3, or 5 mg/mL HA declined whereas the ones of the co-culture of Capan-2 with HSCs and 1, 3, or 5 mg/mL HA rose from day 4 to day 5. Sizes of spheroids from day 5 to day 12 remained unchanged (Figure 62-64).

5 mg/mL HA was chosen for the following sections because it could mimic more challenging barrier for therapeutic agents to penetrate than 1 and 3 mg/mL HA.

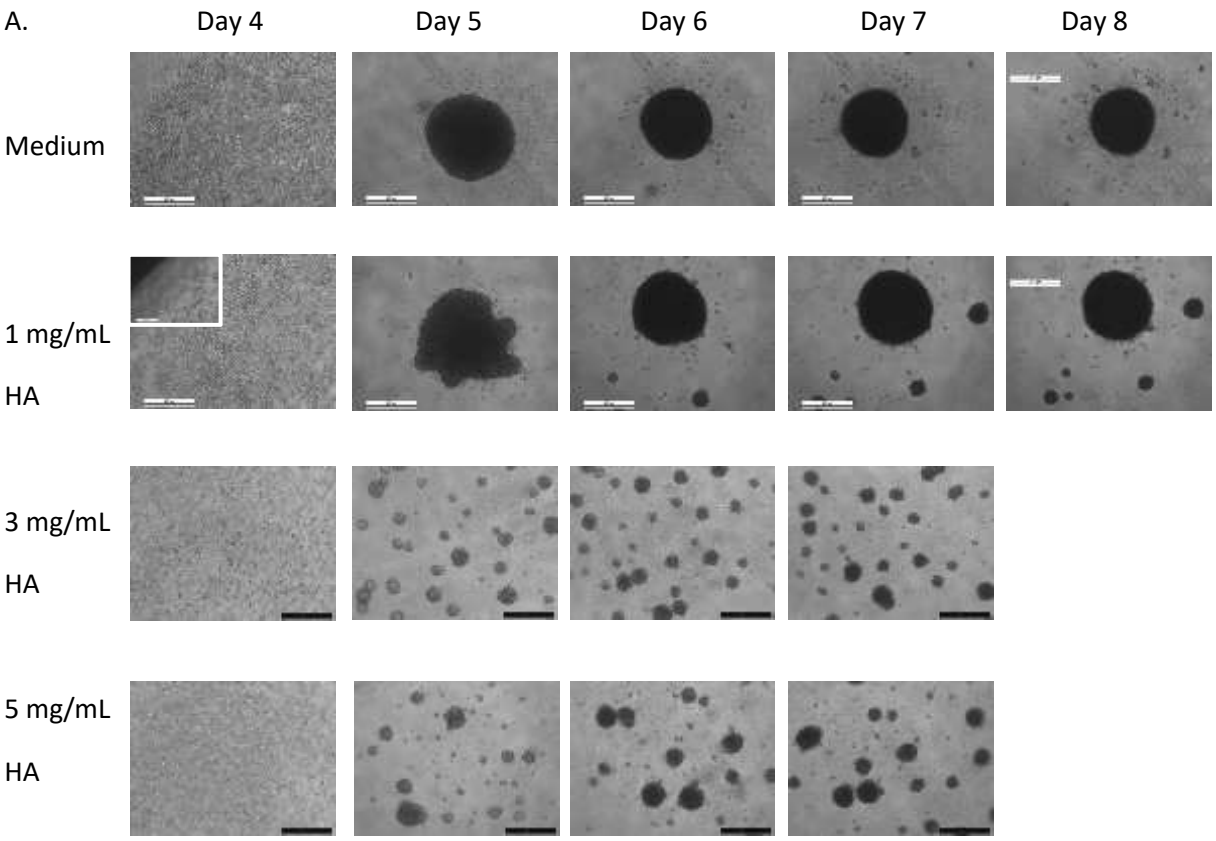

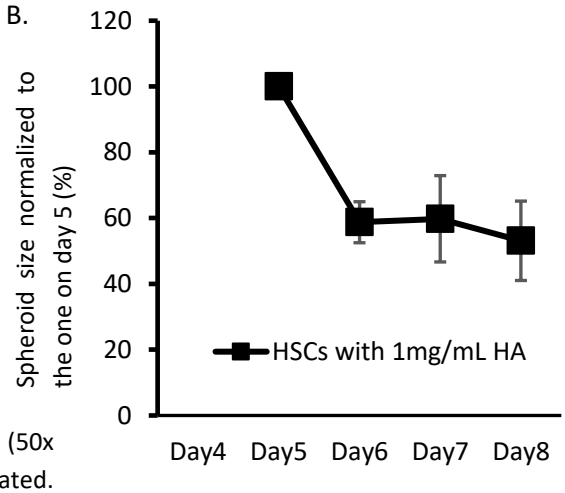

Figure 62. Sphere-forming assays in hepatic stellate cells with different concentration of hyaluronic acid over time.

20,000 cells per well of hepatic stellate cells (HSCs) suspensions were seeded in the poly-HEMA low-attachment 96-well plates with either no hyaluronic acid (Medium), 1 mg/mL hyaluronic acid (HA), 3 mg/mL HA, or 5 mg/mL HA respectively. The experiment was done in parallel with dropping cancer cell spheroids to HSCs suspensions. Day 4 indicated the day when cancer cell spheroids pre-formed in hanging drops were dropped to the HSCs suspension with HA. A. Phase-contrast images were taken by Leica DMI4000 B (50x magnification) manually at the time points indicated. Representative images from five spheroids in the same group from one independent experiment were shown except that representative images of spheroids with 5 mg/mL HA were from two independent experiments. Scale bar, 500 µm. B. The percentages of spheroid sizes on Day 4, Day 6 and Day 7 normalized to the ones on day 5. The areas were measured using CellProfiler. The mean areas in pixels of spheroids on day 4, day 6 and day 7 were divided by the mean areas in pixels of spheroids in the same well on day 5 and then multiplied by 100. Graph was created by Excel, using the means of the percentages in 5-6 spheroids. Error bars represented standard deviations from the percentages of 5-6 spheroids in one independent experiment. Only one spheroid on day 4 was found during data processing and thus the dataset on day 4 was not included.

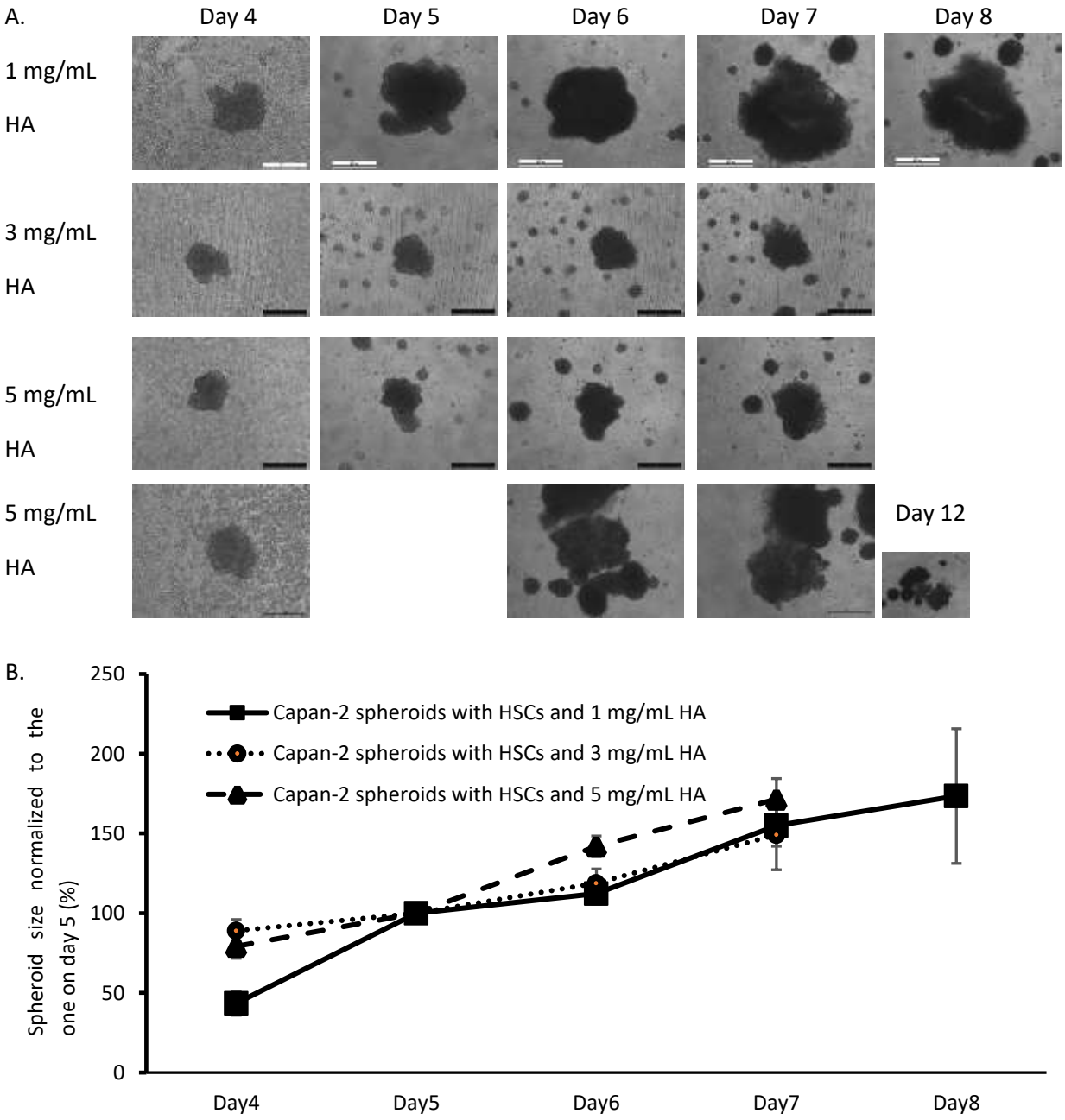

Figure 63. Sphere-forming assays in Capan-2 spheroids with different concentration of hyaluronic acid over time.

500 Capan-2 cells were seeded in hanging drops and after 4 days each droplet was pushed into a well containing 20,000 cells per well of hepatic stellate cells (HSCs) suspensions and either 1 mg/mL hyaluronic acid (HA), 3 mg/mL HA, or 5 mg/mL HA respectively. Day 4 indicated the day when cancer cell spheroids pre-formed in hanging drops were dropped to the HSCs suspension with HA. A. Phase-contrast images were taken by Leica DMI4000 B (50x magnification) manually at the time points indicated. Representative images from five spheroids in the same group from one independent experiment were shown except that representative images of spheroids with 5 mg/mL HA were from two independent experiments. Scale bar, 500 µm. B. The percentages of spheroid sizes on Day 4, Day 6 and Day 7 normalized to the ones on day 5. The areas were measured using CellProfiler. The mean areas in pixels of spheroids on day 4, day 6 and day 7 were divided by the mean areas in pixels of spheroids in the same well on day 5 and then multiplied by 100. Graph was created by Excel, using the means of the percentages in 5-6 spheroids. Error bars represented standard deviations from the percentages of 5-6 spheroids in one independent experiment.

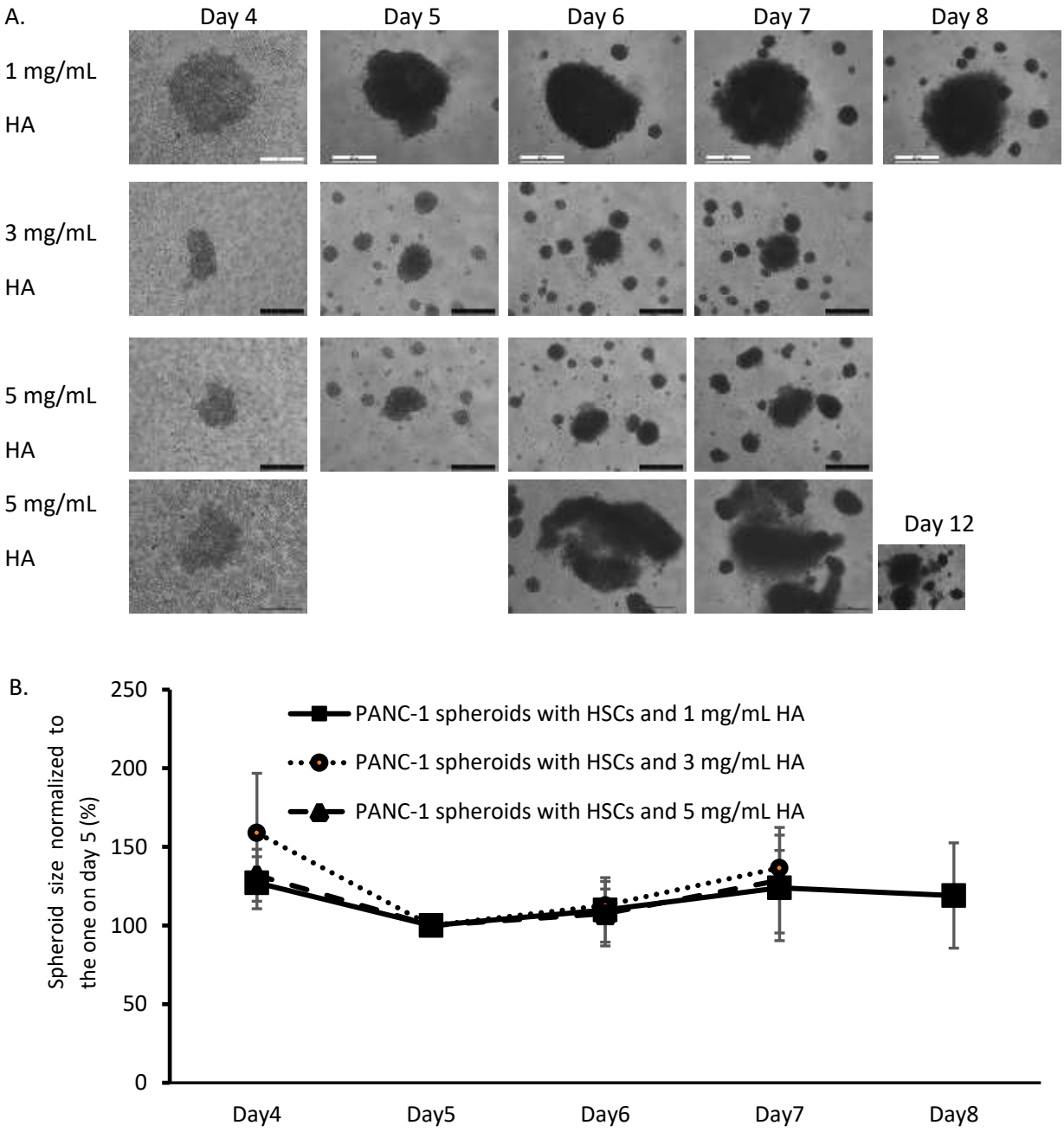

Figure 64. Sphere-forming assays in PANC-1 spheroids with different concentration of hyaluronic acid over time.

500 PANC-1 cells were seeded in hanging drops and after 4 days each droplet was pushed into a well containing 20,000 cells per well of hepatic stellate cells (HSCs) suspensions and either 1 mg/mL hyaluronic acid (HA), 3 mg/mL HA, or 5 mg/mL HA respectively. Day 4 indicated the day when cancer cell spheroids pre-formed in hanging drops were dropped to the HSCs suspension with HA. A. Phase-contrast images were taken by Leica DMI4000 B (50x magnification) manually at the time points indicated. Representative images from five spheroids in the same group from one independent experiment were shown except that representative images of spheroids with 5 mg/mL HA were from two independent experiments. Scale bar, 500 µm. B. The percentages of spheroid sizes on Day 4, Day 6 and Day 7 normalized to the ones on day 5. The areas were measured using CellProfiler. The mean areas in pixels of spheroids on day 4, day 6 and day 7 were divided by the mean areas in pixels of spheroids in the same well on day 5 and then multiplied by 100. Graph was created by Excel, using the means of the percentages in 5-6 spheroids. Error bars represented standard deviations from the percentages of 5-6 spheroids in one independent experiment.

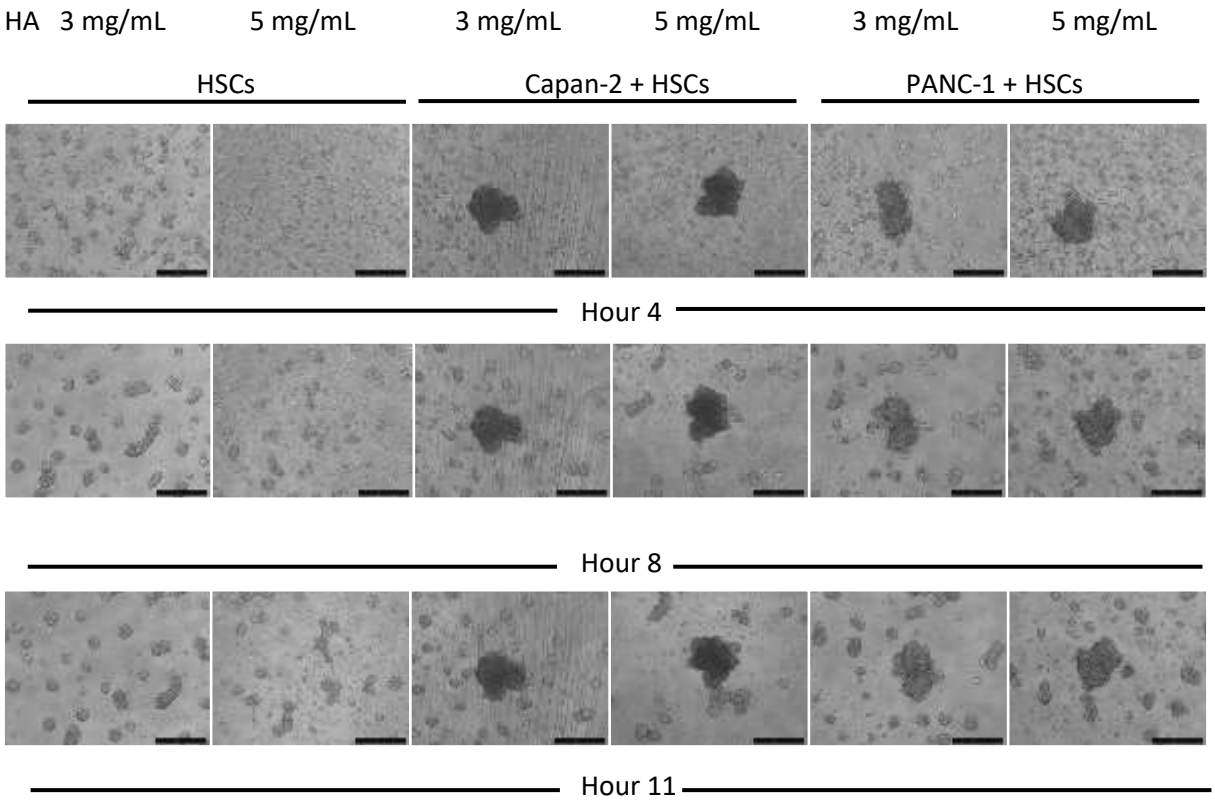

Figure 65. Sphere-forming assays in different concentration of hyaluronic acid in 12 hours.

500 Capan-2 cells or 500 PANC-1 cells were seeded in hanging drops and after 4 days each droplet was pushed into a well containing 20,000 hepatic stellate cells (HSCs) and 3 mg/mL hyaluronic acid (HA), or 5 mg/mL HA respectively. Wells with HSCs only were also included. Phase-contrast images were taken by Leica DMI4000 B (50x magnification) manually at the time points indicated. Representative images from five spheroids in the same group from one independent experiment were shown. Scale bar, 500 μm.

5.2.2 Stellate cells attaching to areas at the edge of 3D cancer cell spheroids

Although the protocol described above resulted in multiple spheroids in each well, it might be possible that a thin layer of stellate cells wrapped around each cancer spheroid. In order to evaluate the cell type distribution in this co-culture model, the largest spheroid present in each well was fixed in PFA and stained with anti-p53 antibodies and DAPI to differentially detect cancer cells and stellate cells. As illustrated in Figure 66, areas that stained with only DAPI with indication of HSCs with small nuclei constituted a small proportion of these spheroids. The green staining of HSCs with small nuclei was found mainly in the cytoplasm, possibly due to non-specific binding of antibodies and autofluorescence in the cytoplasm of HSCs. The cancer cells areas illustrated strong nuclear staining of p53 in green. The distribution of p53 and DAPI labelling was consistent with only a few stellate cells attaching at the surface of cancer cell spheroids by 2 days after the spheroids were dropped into the stellate cells suspension.

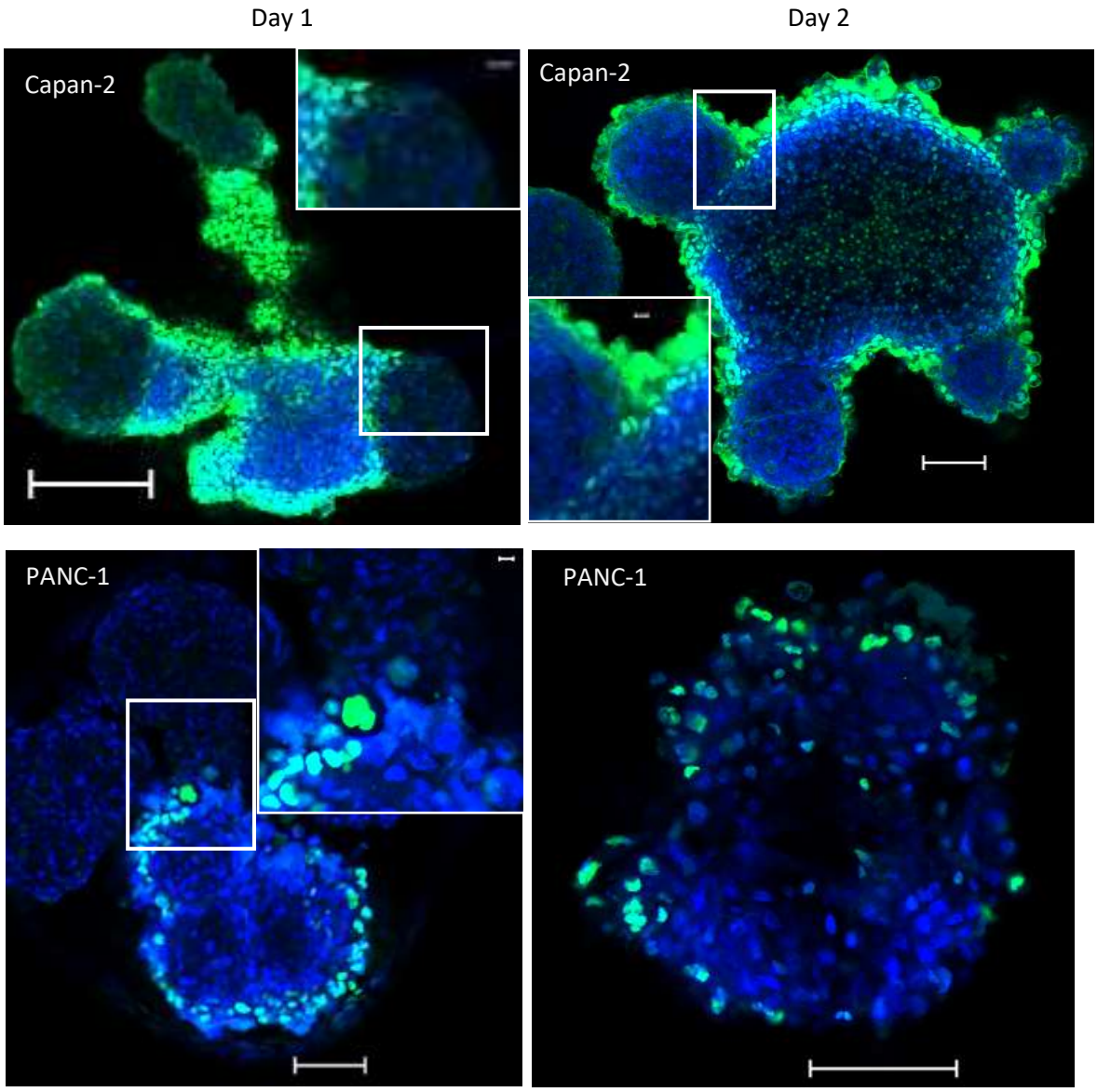

Figure 66. Stellate cells attached at the surface of the cancer cell spheroids.

500 cancer cells were seeded in hanging drops and after 4 days these droplets were pushed into the wells with 20,000 stellate cells and 5 mg/mL HA per well. On day 1 and day 2 after dropping, the largest spheroid in each well was collected and stained with DAPI (blue), and for p53 (green). Confocal laser scanning microscopy using Zeiss LSM880 was used to acquire images. Image analysis was performed using Zen 2.3 (blue edition). Images shown were representatives of three spheroids from one independent experiment. Scale bar, 100 µm; insert, 10 µm.

5.3 Spheroid formation, cell distribution and protein expression in 3D co-culture models of stellate cells to cancer cells at a 10:1 cell ratio with HA and COL I

5.3.1 A single spheroid could be formed after dropping a cancer cell spheroid into a stellate cells suspension in hyaluronic acid and collagen I

Pre-formed cancer cell spheroids failed to form a single spheroid when dropped into a hepatic stellate cells (HSCs) suspension in HA. Further, stellate cells formed only a thin and inconsistent sheet of cells at the surface of these cancer spheroids. Based upon this outcome, we explored the formation of a co-culture system that included collagen I. 500 cancer cells were seeded and cultured using the hanging drop protocol. After 4 days, droplets were pushed into wells containing 20,000 stellate cells, 5 mg/mL HA and 0.3 mg/mL collagen I per well. As seen in Figure 67 (inserts), there appeared to be collagen fibre contraction 4 hours after spheroids were dropped into individual well containing pancreatic stellate cells (PSCs). During this time, stellate cells and cancer cells came together to form a single spheroid in each well which was reproducible in the case of Capan-2 spheroids with HSCs, Capan-2 spheroids with PSCs, PANC-1 spheroids with HSCs, and PANC-1 spheroids with PSCs. No difference could be observed between the sizes of spheroids 48 hours after dropping into PSCs and the ones 72 hours after dropping into PSCs (Figure 67).

Of note, as shown in the Figure 67, there were some wells with spheroids attached to the wall that appeared to result in a possibly flatten oval shape (red arrow heads). Thus, not all the 3D co-culture models of cancer cells, stellate cells and matrices were spheroidal in shape in the current section. Also, there were cancer cells spheroids that may have fallen outside the stellate cells spheroids when dropped into the wells (red arrows). This may have led to the formation of cancer cell spheroids without the surrounding layer of stellate cells. Therefore, it appears that further optimisation is needed to improve the protocol.

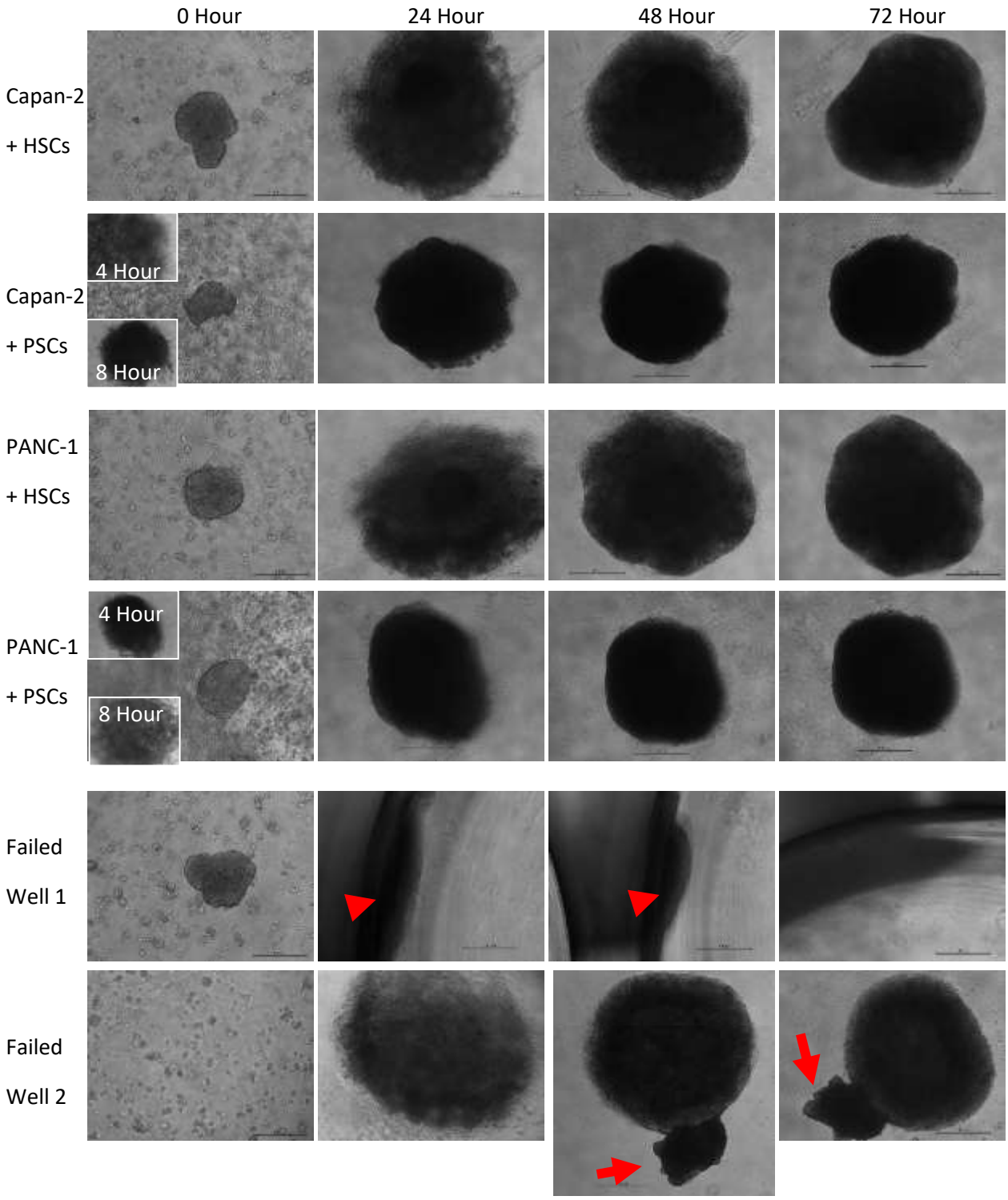

Figure 67. Single spheroid formation after cancer cell spheroids were dropped into a stellate cells suspension in hyaluronic acid and collagen I.

500 cancer cells were seeded in hanging drops and after 4 days the droplets were pushed into wells with 20,000 pancreatic stellate cells (PSCs) or hepatic stellate cells (HSCs), 5 mg/mL HA and 0.3 mg/mL collagen I per well. Images were acquired by Leica DMI4000 B (50x magnification) manually as indicated time points. Representative images shown were from five wells in two independent experiments. Red arrow heads: a spheroid attached to the wall. Red arrows: a cancer cells spheroid appeared outside a stellate cells spheroid. Scale bar, 500 µm.

5.3.2 Stellate cells fail to engulf whole cancer spheroids and form multi-layered cells surrounding cancer spheroids

In the previous sections, stellate cells (SCs) formed small spheres scattered in the wells and distanced themselves from the large spheroids in an environment with only hyaluronic acid (HA). Although there were some small SCs spheroids attaching to the large spheroids, they remained static in a way that they still adhered to themselves without transforming into layers of cells to cover the cancer cells spheroids in HA. This is inconsistent with the theory that SCs could be mobilised by cancer cells in the tumour microenvironment and the histology reported in PDAC [Dong *et al*, 2000; Erkan *et al*, 2008; Jeong *et al*, 2005; Khan *et al*, 2017; Zhang *et al*, 2007; Zhao *et al*, 2016a]. One of the reasons may be the lack of protein-based macromolecules such as collagens to provide a scaffold to aid the migration of SCs towards the cancer cells spheroids. We next evaluated cell type distribution in the co-culture models with HA and collagen I to test the hypothesis that collagens can facilitate the attachment of SCs to the cancer cells spheroids.

On day 2 and 3 after dropping cancer cells spheroids into a SCs suspension in HA and collagen I, whole spheroids in each group were fixed in PFA and stained for p53 with DAPI to discriminate SCs from cancer cells using confocal microscopy. As demonstrated in Figure 68, a fraction of the large spheroid presented with strong p53 staining (red arrows), indicating cells located in the fraction are mostly cancer cells. The green staining of SCs with small nuclei was found mainly in the cytoplasm, possibly due to non-specific binding of antibodies and autofluorescence in the cytoplasm of SCs. Compared to SCs spheroids discontinuously touching the edge of cancer cells spheroids in Figure 66, SCs formed a continuous layer around the region of the cancer cells spheroids in Figure 68. However, parts of the region of the cancer cells spheroids were devoid of SCs, resulting in direct exposure to medium and easy access to oxygen and nutrient for cancer cells located in those parts. This situation is not consistent with where cancer cells are grown in patients with PDAC, possibly altering the phenotypes and cell signalling in PDAC cells. The attachment of SCs to the cancer cells spheroids has been improved with the addition of collagen I; however, no defined cancer cells core surrounded by multi-layered of SCs could be detected on day 2 or day 3, suggesting further optimisation is needed.

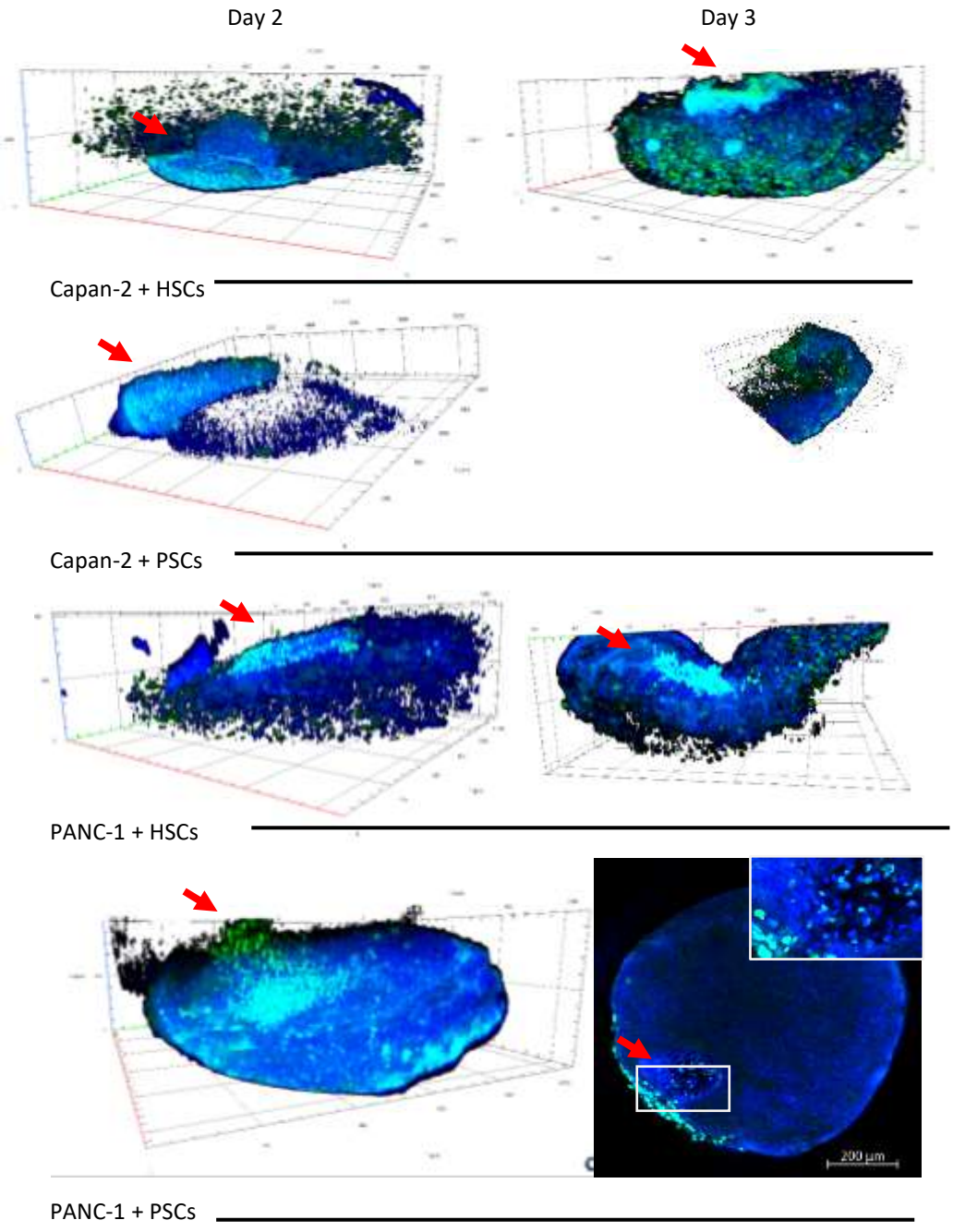

Figure 68. Stellate cells failed to engulf cancer cells spheroids and form a multi-layered cells surrounding a cancer cells core in hyaluronic acid and collagen I. Refer to separate files. Pay attention to lines.

Spheroids were formed from 500 cancer cells in hanging drops for 4 days and pushed into a hepatic stellate cells (HSCs) suspension or a pancreatic stellate cells (PSCs) suspension (20,000 cells per well) with 5 mg/mL hyaluronic acid (HA) and 0.3 mg/mL collagen I. On day 2 or 3 after cancer spheroids were dropped into HSCs or PSCs in HA and collagen I, whole spheroids in each group were fixed in PFA and then stained with DAPI (blue), and for p53 (green). Z-stack imaging was performed by confocal microscopy (Zeiss LSM880) to acquire the entire spheroids. Image analysis and 3D rendering were done in Zen 2.3 (blue edition). Red arrows: fractions of cancer cells. Representative images were from two spheroids in two independent experiments. Scale bars of X, Y, and Z axes: 200 µm; exception: 50 µm in the Capan-2+PSCs group on day 3.

5.3.3 Increased nuclear YAP levels were observed in cancer cells co-cultured with stellate cells, hyaluronic acid and collagen I

We next evaluated key components in YAP signalling in this co-culture spheroid model. Whole spheroids co-cultured with cancer cells and pancreatic stellate cells (PSCs) were fixed in PFA 3 days after dropping cancer spheroids into PSCs and stained for Ocln, TEADs and YAP. As seen in Figure 69-74, unlike the YAP expression and localization pattern in the section 3.2.4 where YAP staining appeared like a ring around the nuclei, high level of YAP could be detected inside p53 positive cancer cell nuclei (white arrows) and the elongated nuclei of PSCs (white arrow heads) located at the edge of the spheroids or at the core of the spheroids. Cytoplasmic accumulation of YAP could still be detected in some PANC-1 cells near the edge of the spheroid in Figure 70.

Semi-quantification of YAP by CellProfiler was conducted on one optical section of the co-culture spheroids with Capan-2 cells or PANC-1 cells with PSCs (Figure 71 and 72). The image exported from p53 channel was also used in the module 'IdentifyPrimaryObjects' due to signal loss near the core of the spheroid in DAPI channel. Because the data representing YAP intensities and ratios did not follow normal distribution and not have the same shape of distribution, mean ranks of the datasets were compared using a non-parametric Mann-Whitney U test. Comparing the total YAP intensities in the whole cancer cells near the edge and the cores, cancer cells near the edge exhibited significantly higher YAP expression (mean rank of 4.63 for Capan-2 cells near the core and 9.67 for Capan-2 cells near the edge, $p = 0.025$; mean rank of 10 for PANC-1 cells near the core and 25 for PANC-1 cells near the edge, $p < 0.001$). There was no significant difference between the ratios of cytoplasmic YAP intensity to total YAP intensity of the whole cell and the ratios of nuclear YAP intensity to total YAP intensity of the whole cell in Capan-2 cells near the core of the spheroids (mean rank of 9.5 for ratios of cytoplasmic YAP intensity and 7.5 for nuclear YAP intensity, $p = 0.401$), Capan2 cells near the edge of the spheroids (mean rank of 2.33 for ratios of cytoplasmic YAP intensity and 4.67 for nuclear YAP intensity, $p = 0.127$), and PANC-1 cells near the edge of the spheroids (mean rank of 12.27 for ratio of cytoplasmic YAP intensity and 10.73 for nuclear YAP intensity, $p = 0.577$). However, the mean ratios of nuclear YAP intensities was significantly higher than the one of cytoplasmic YAP intensities in PANC-1 cells near the core of the spheroids (mean rank of 10.16 for ratios of cytoplasmic YAP intensity and 28.84 for nuclear YAP intensity, $p < 0.001$). Compared to the data in Figure 47 where a 3D mono-culture spheroid of Capan-2 was measured, the overall level of cytoplasmic YAP dropped while the level of nuclear YAP increased, suggesting a shift in the subcellular localisation of YAP. The data indicated more cancer cells with nuclear localisation of YAP in the core of the spheroid were found in the current optical sections of 3D co-culture models. The core of these spheroids was considered to be more hypoxic than the rest of the spheroids with reduced nutrient access [Hoarau-Vechot *et al*, 2018]. These results from analysing the co-culture of PANC-1 cells with PSCs, HA and COL I suggest that cancer cells in this environment might develop some mechanisms to induce nuclear accumulation of YAP to sustain cell growth and survival, possibly through overcoming reduced oxygen and/or nutrient access [Enzo *et al*, 2015; Mo *et al*, 2015; Wang *et al*, 2015].

Ocln is found to interact with YAP in the cytoplasm and the membrane of cancer cells [Cravo *et al*, 2015]. Interestingly, Ocln was not only found in cancer cells but also in PSCs in the current section (Figure 69 and 70). Ocln is reported to be undetectable in fibroblasts [Dorfel *et al*, 2012]. One of the reasons for the Ocln expression in PSCs was that the antibodies against Ocln used in the present study

were able to bind to certain proteins in PSCs non-specifically, similar to the situation of the green signals from p53 in the cytoplasm of stellate cells. Moreover, Ocln was detected in the nucleus and the cytoplasm of cancer cells and co-localized with YAP in both location (Figure 69 and 70), possibly indicating the destruction of tight junctions during EMT in PDAC cells causing fragments of TJ proteins scattering in the nucleus and cytoplasm that happened to be in the same location with YAP distribution if the unspecific staining was not taken into account.

TEADs are the binding partners of YAP in the nucleus to promote cell growth [Abylkassov *et al*, 2016]. As shown in Figure 73 and 74, TEADs could be detected in both cancer cells and PSCs, co-localizing with nuclear YAP.

The data in the current section was obtained in only one optical section in one spheroids from one independent experiment. Further explorations on the interaction of TEADs, Ocln and YAP are needed.

Blue: DAPI; green: p53; Red: Ocln; yellow: YAP.

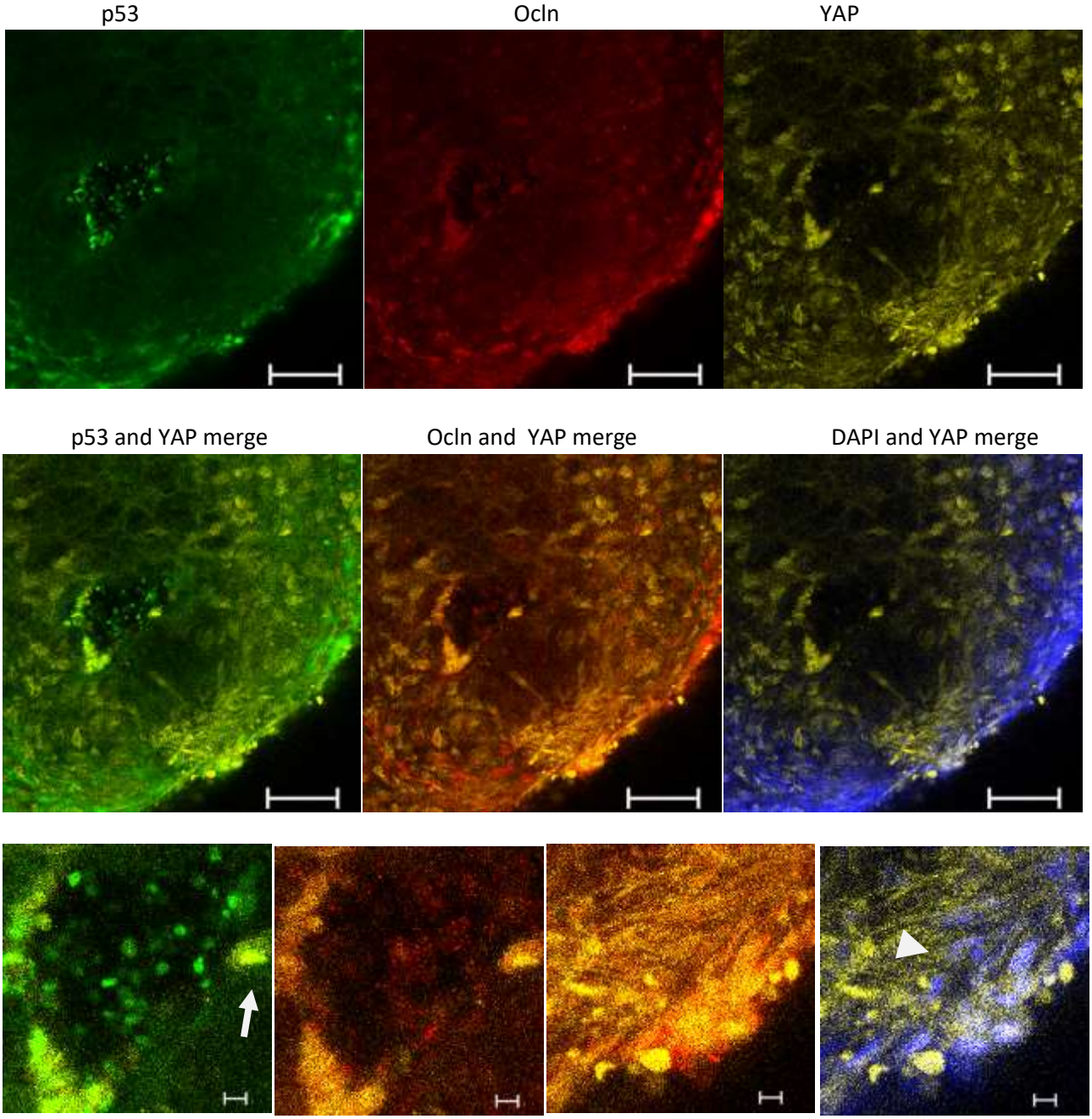

Figure 69. Ocln and YAP expression and co-localisation in 3D co-culture models of Capan-2 with PSCs, HA and COL I.

Spheroids were formed from 500 Capan-2 cells in hanging drops for 4 days and pushed into the pancreatic stellate cells (PSCs) suspension (20,000 cells per well) with HA and COL I. On day 3 after cancer spheroids were dropped into PSCs with HA and COL I, whole spheroids in each group were fixed in PFA and stained with DAPI (blue), anti-Ocln antibodies (red), anti-YAP antibodies (yellow), and anti-p53 antibodies (green). Confocal microscopy with multitracking scanning using Zeiss LSM880 was performed. Image analysis was done in Zen 2.3 (blue edition). White arrows: nuclear localisation of YAP in cancer cells; white arrow heads: nuclear localisation of YAP in PSCs. Two spheroids were scanned in one independent experiment. Scale bar, 100 µm; insert: 10 µm.

Blue: DAPI; green: p53; Red: Ocln; yellow: YAP.

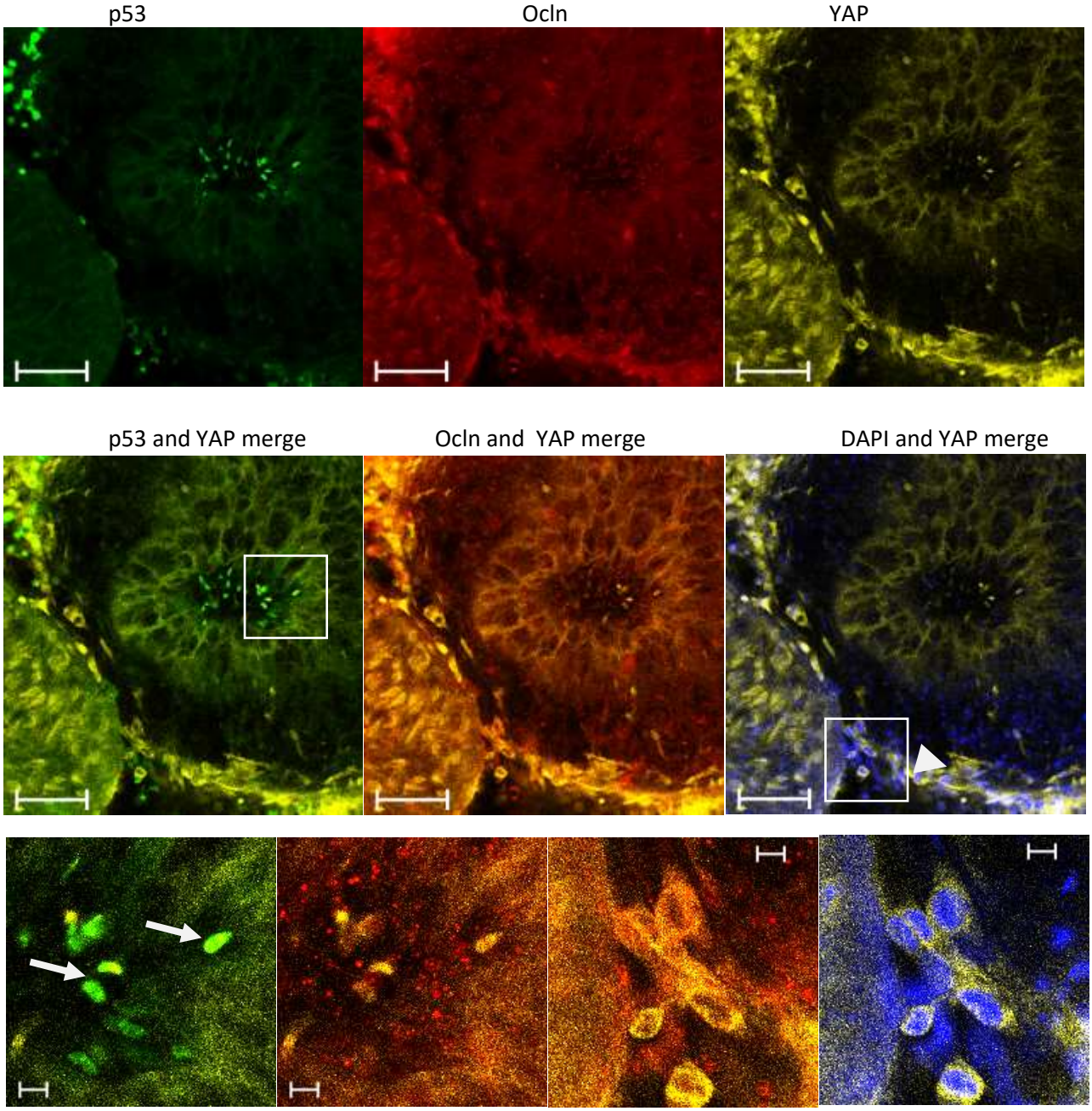

Figure 70. Ocln and YAP expression and co-localisation in 3D co-culture models of PANC-1 with PSCs, HA and Col I.

Spheroids were formed from 500 PANC-1 cells in hanging drops for 4 days and pushed into the pancreatic stellate cells (PSCs) suspension (20,000 cells per well) with HA and COL I. On day 3 after cancer spheroids were dropped into PSCs with HA and COL I, whole spheroids in each group were fixed in PFA and stained with DAPI (blue), anti-Ocln antibodies (red), anti-YAP antibodies (yellow), and anti-p53 antibodies (green). Confocal microscopy with multitracking scanning using Zeiss LSM880 was performed. Image analysis was done in Zen 2.3 (blue edition). White arrows: nuclear localisation of YAP in cancer cells; white arrow heads: nuclear localisation of YAP in PSCs. Two spheroids were scanned in one independent experiment. Scale bar, 100 µm; insert: 10 µm.

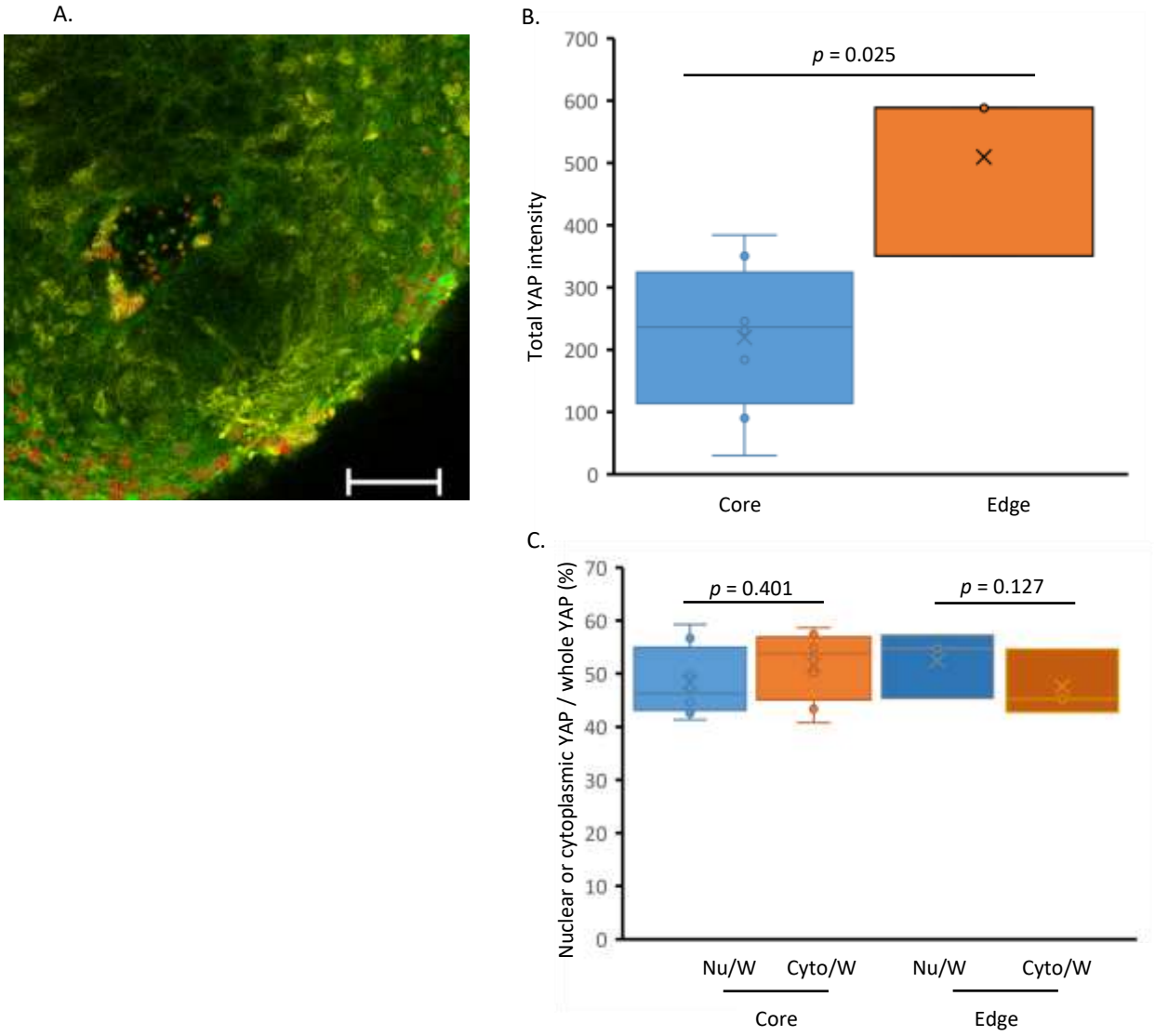

Figure 71. Semi-quantification of YAP subcellular expression in 3D co-culture models of Capan-2 with PSCs, HA and Col I.

Spheroids were formed from 500 Capan-2 cells in hanging drops for 4 days and pushed into the pancreatic stellate cells (PSCs) suspension (20,000 cells per well) with HA and collagen I. On day 3 after cancer spheroids were dropped into PSCs with HA and Col I, whole spheroids in each group were fixed and stained with anti-YAP antibodies (yellow), and anti-p53 antibodies (green). Confocal microscopy with multitracking scanning using Zeiss LSM880 was performed. Image analysis was done in Zen 2.3 (blue edition). Quantification of YAP was performed by CellProfiler. A. A representative field of view in an image processed by CellProfiler, depicting the outlined nuclear areas and the cytoplasmic areas labelled with numbers. Whisker box graph was made from all the values of total YAP intensity in the whole cells (B) or the intensity ratios of nuclear YAP intensity to total YAP intensity in the whole cell or cytoplasmic YAP intensity to total YAP intensity in the whole cell (C) from around 3-8 cells near the core of the spheroid and the edge of the spheroid, using Excel. Mean markers were shown. Median was exclusive from quartile calculation. Dots indicated the values in cells automatically generated by Excel. Non-parametric Mann-Whitney U test in SPSS was used to calculate the *p* values. Nu: nucleus, Cy: cytoplasm, W: whole cell.

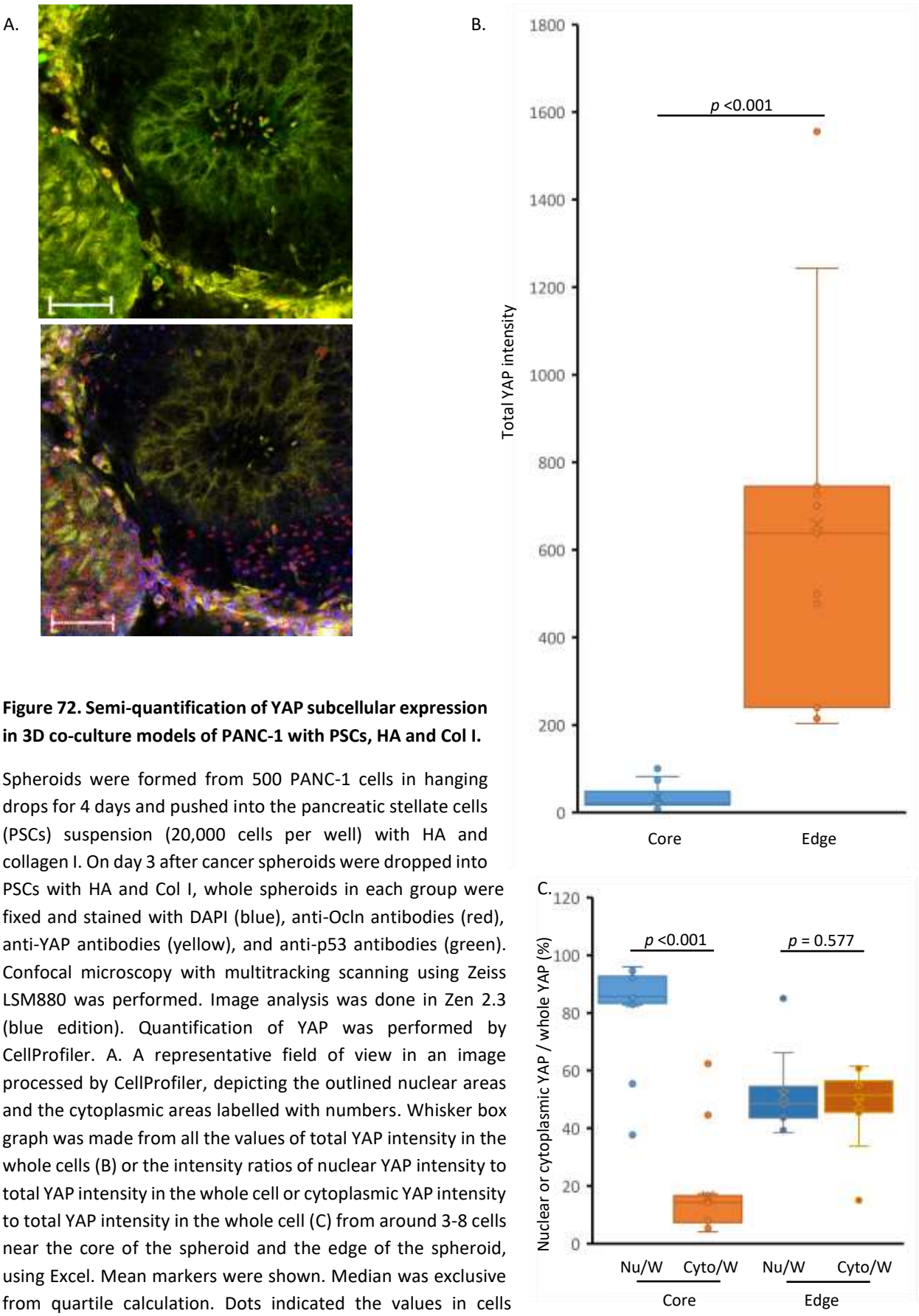

Figure 72. Semi-quantification of YAP subcellular expression in 3D co-culture models of PANC-1 with PSCs, HA and Col I.

Spheroids were formed from 500 PANC-1 cells in hanging drops for 4 days and pushed into the pancreatic stellate cells (PSCs) suspension (20,000 cells per well) with HA and collagen I. On day 3 after cancer spheroids were dropped into PSCs with HA and Col I, whole spheroids in each group were fixed and stained with DAPI (blue), anti-Ocln antibodies (red), anti-YAP antibodies (yellow), and anti-p53 antibodies (green). Confocal microscopy with multitracking scanning using Zeiss LSM880 was performed. Image analysis was done in Zen 2.3 (blue edition). Quantification of YAP was performed by CellProfiler. A. A representative field of view in an image processed by CellProfiler, depicting the outlined nuclear areas and the cytoplasmic areas labelled with numbers. Whisker box graph was made from all the values of total YAP intensity in the whole cells (B) or the intensity ratios of nuclear YAP intensity to total YAP intensity in the whole cell or cytoplasmic YAP intensity to total YAP intensity in the whole cell (C) from around 3-8 cells near the core of the spheroid and the edge of the spheroid, using Excel. Mean markers were shown. Median was exclusive from quartile calculation. Dots indicated the values in cells automatically generated by Excel. Non-parametric Mann-Whitney U test in SPSS was used to calculate the *p* values. Nu: nucleus, Cy: cytoplasm, W: whole cell.

Blue: DAPI; green: p53; Red: TEADs; yellow: YAP.

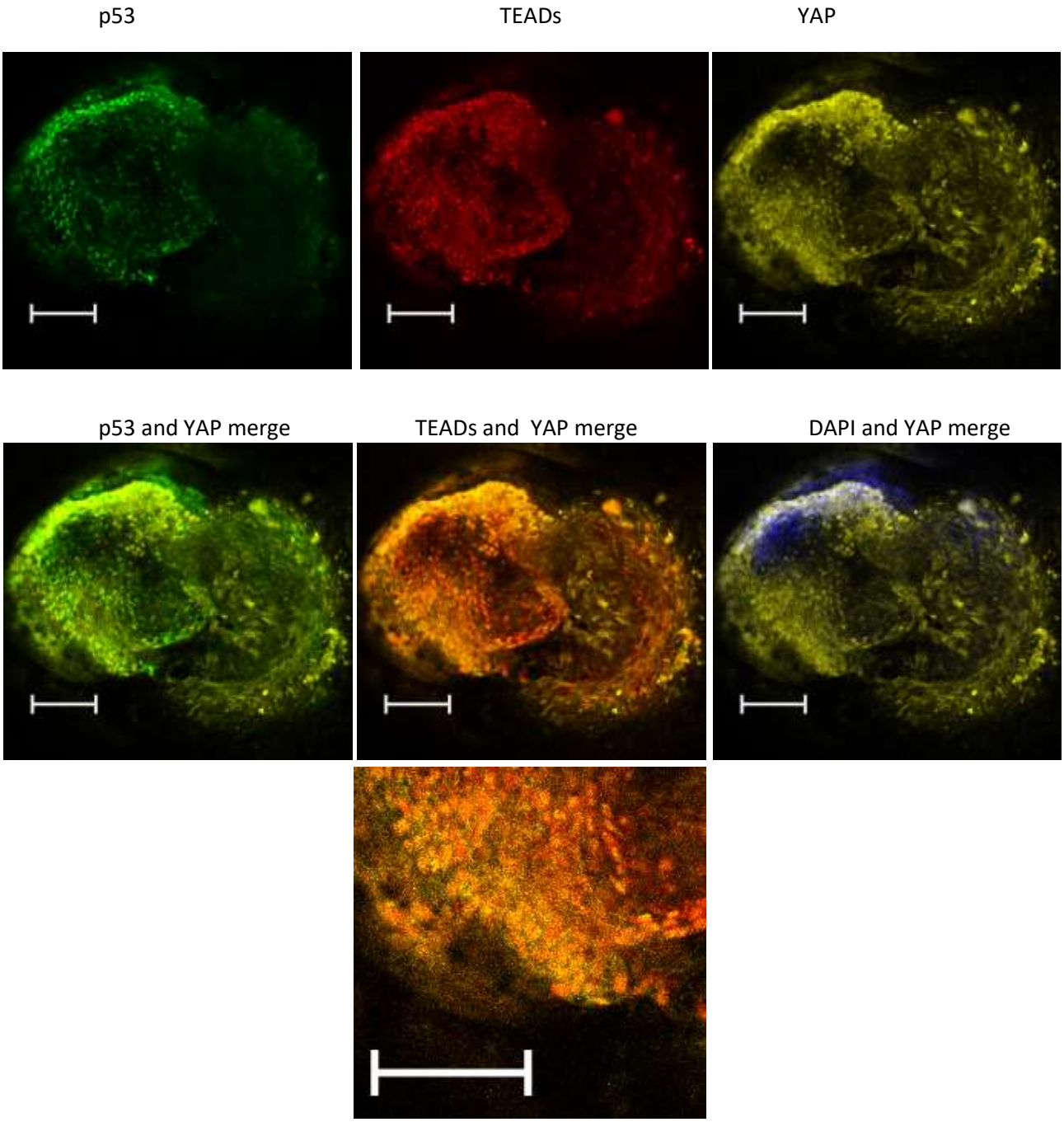

Figure 73. TEADs and YAP expression and co-localisation in 3D co-culture models of Capan-2 with PSCs, HA and Col I.

Spheroids were formed from 500 Capan-2 cells in hanging drops for 4 days and pushed into the pancreatic stellate cells (PSCs) suspension (20,000 cells per well) with HA and COL I. On day 3 after cancer spheroids were dropped into PSCs with HA and COL I, whole spheroids in each group were fixed in PFA and stained with DAPI (blue), anti-pan-TEADs antibodies (red), anti-YAP antibodies (yellow), and anti-p53 antibodies (green). Confocal microscopy with multitracking scanning using Zeiss LSM880 was performed. Image analysis was done in Zen 2.3 (blue edition). Two spheroids were scanned in one independent experiment. Scale bar, 100 µm.

Blue: DAPI; green: p53; Red: TEADs; yellow: YAP. PANC-1 + PSCs

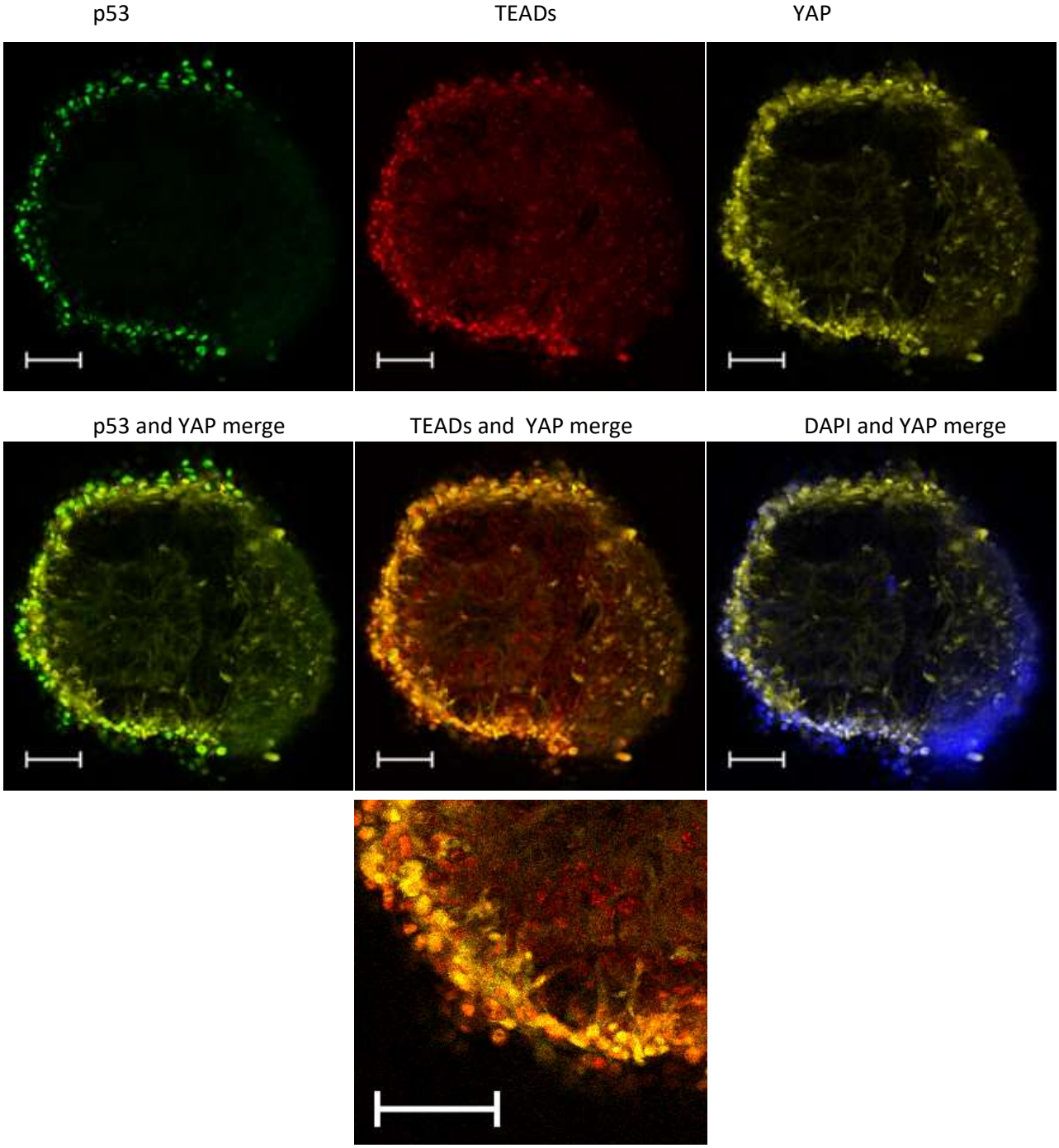

Figure 74. TEADs and YAP expression and co-localisation in co-culture models of PANC-1 with PSCs, HA and Col I.

Spheroids were formed from 500 PANC-1 cells in hanging drops for 4 days and pushed into the pancreatic stellate cells (PSCs) suspension (20,000 cells per well) with HA and COL I. On day 3 after cancer spheroids were dropped into PSCs with HA and COL I, whole spheroids in each group were fixed in PFA and stained with DAPI (blue), anti-pan-TEADs antibodies (red), anti-YAP antibodies (yellow), and anti-p53 antibodies (green). Confocal microscopy with multitracking scanning using Zeiss LSM880 was performed. Image analysis was done in Zen 2.3 (blue edition). Two spheroids were scanned in one independent experiment. Scale bar, 100 µm.

5.4 Spheroid formation, cell distribution and protein expression in 3D co-culture models of stellate cells to cancer cells at a 2:1 cell ratio with COL I

5.4.1 Sphere-forming assays and cancer cell distribution in different amount of collagen I with or without HA

Efforts were undertaken to explore the direct mixture of a stellate cells suspension with a cancer cells suspension at a 2:1 ratio of stellate cells to cancer cells at several collagen I contents per well with or without HA. The following matrix conditions were tested: a) 0.3 mg/mL collagen I and 3.5 mg/mL HA in 100 µL; b) 0.3 mg/mL collagen I and 3.5 mg/mL HA in 50 µL; c) 0.3 mg/mL collagen I in 50 µL; d) 0.1 mg/mL collagen I in 50 µL.

As shown in Figure 75 and 76, spheroids were larger in 0.3 mg/mL collagen I when cultured in 100 µL compared to those cultured in 50 µL. Spheroids were smaller in 0.1 mg/mL collagen I than in 0.3 mg/mL of the same volume. There was no marked difference in spheroid size when cultured in 0.3 mg/mL collagen I with or without HA. Quantification of the sizes by CellProfiler was not appropriate due to the incomplete areas of the whole spheroids using the current microscope. Based on the clear distinct brightness and contrast in the areas of the spheroids in the wells, these studies suggested that collagen I is the key factor to determine 3D co-culture spheroid size.

As seen in Figure 77 and 78, multiple cancer cell cores/clusters with positive staining of p53 were formed in the spheroids with 0.3 mg/mL collagen I and 0.1 mg/mL collagen I after 4 days of culture. We had intended to use a CellTiter-GLO 3D assay to assess cell viability in these spheroids as a way to assess the impact of potential anti-cancer compounds in high-throughput assay. According to the manufacturer of this commercial method, 3D spheroids larger than 500 µm in diameter may not be accurately assessed. For this reason, the condition of 50 µL of 0.1 mg/mL collagen I per well was chosen for the following sections.

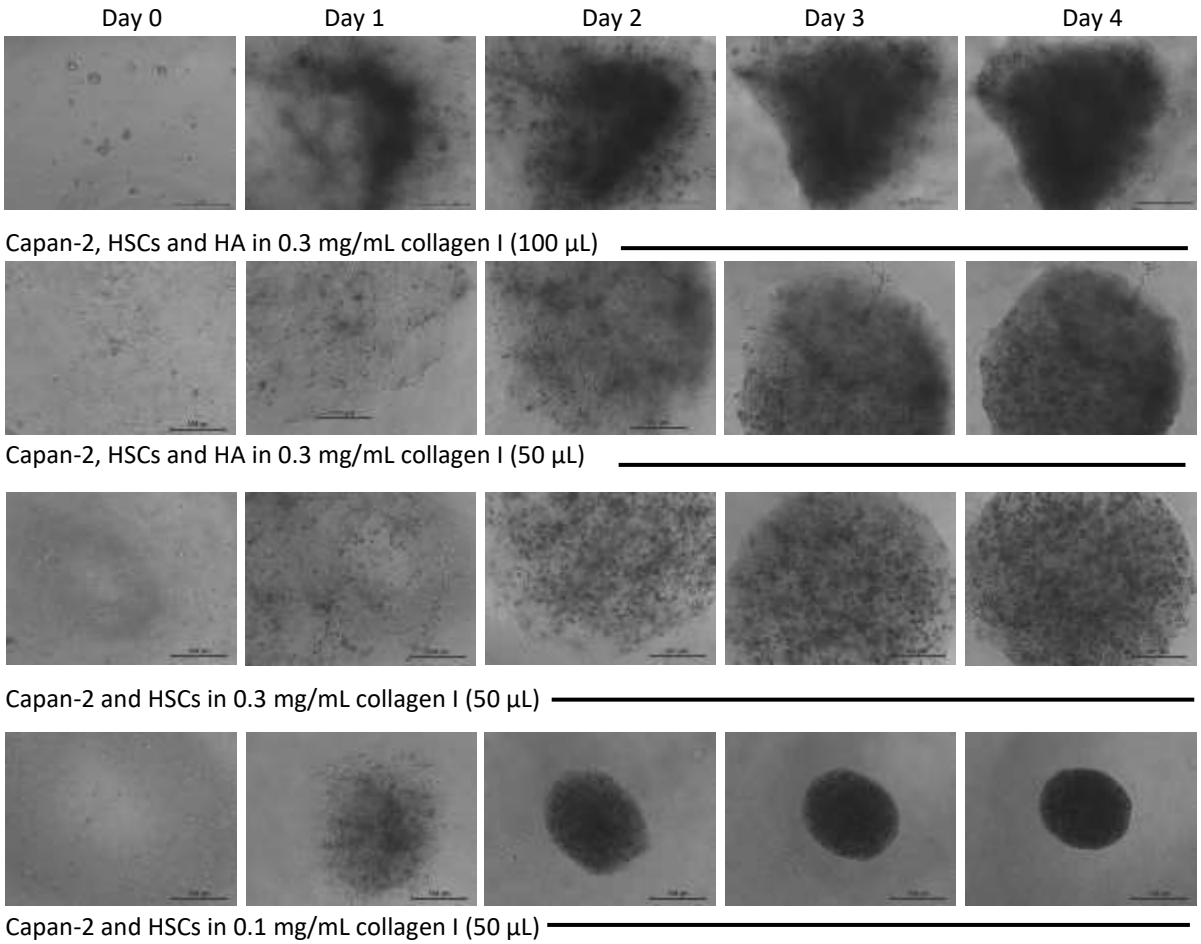

Figure 75. Spheroid formation in 3D co-culture spheroids with Capan-2 cells, stellate cells, different amount of collagen I with or without HA.

500 Capan-2 cells and 1,000 hepatic stellate cells (HSCs) were mixed in 100 µL or 50 µL of collagen I with or without HA as indicated. Phase-contrast images were acquired by Leica DMI4000 B (50x magnification) manually at the indicated time points for 4 days. Data shown were representative images from two independent experiments with three spheroids in each experiment. Scale bar, 500 µm.

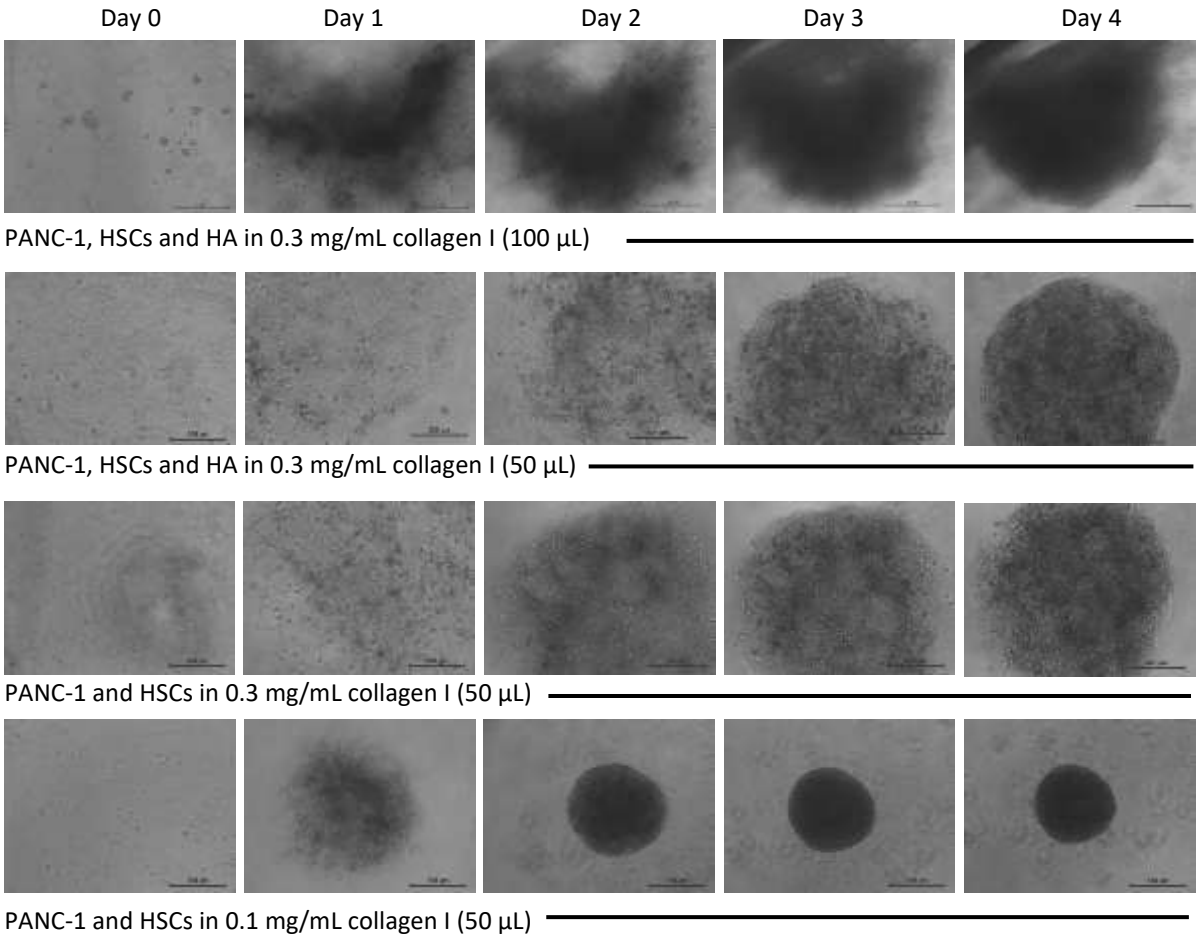

Figure 76. Spheroid formation in 3D co-culture spheroids with PANC-1 cells, stellate cells, different amount of collagen I with or without HA.

500 PANC-1 cells and 1,000 hepatic stellate cells (HSCs) were mixed in 100 µL or 50 µL of collagen I with or without HA as indicated. Phase-contrast images were acquired by Leica DMI4000 B (50x magnification) manually at the indicated time points for 4 days. Data shown were representative images from two independent experiments with three spheroids in each experiment. Scale bar, 500 µm.

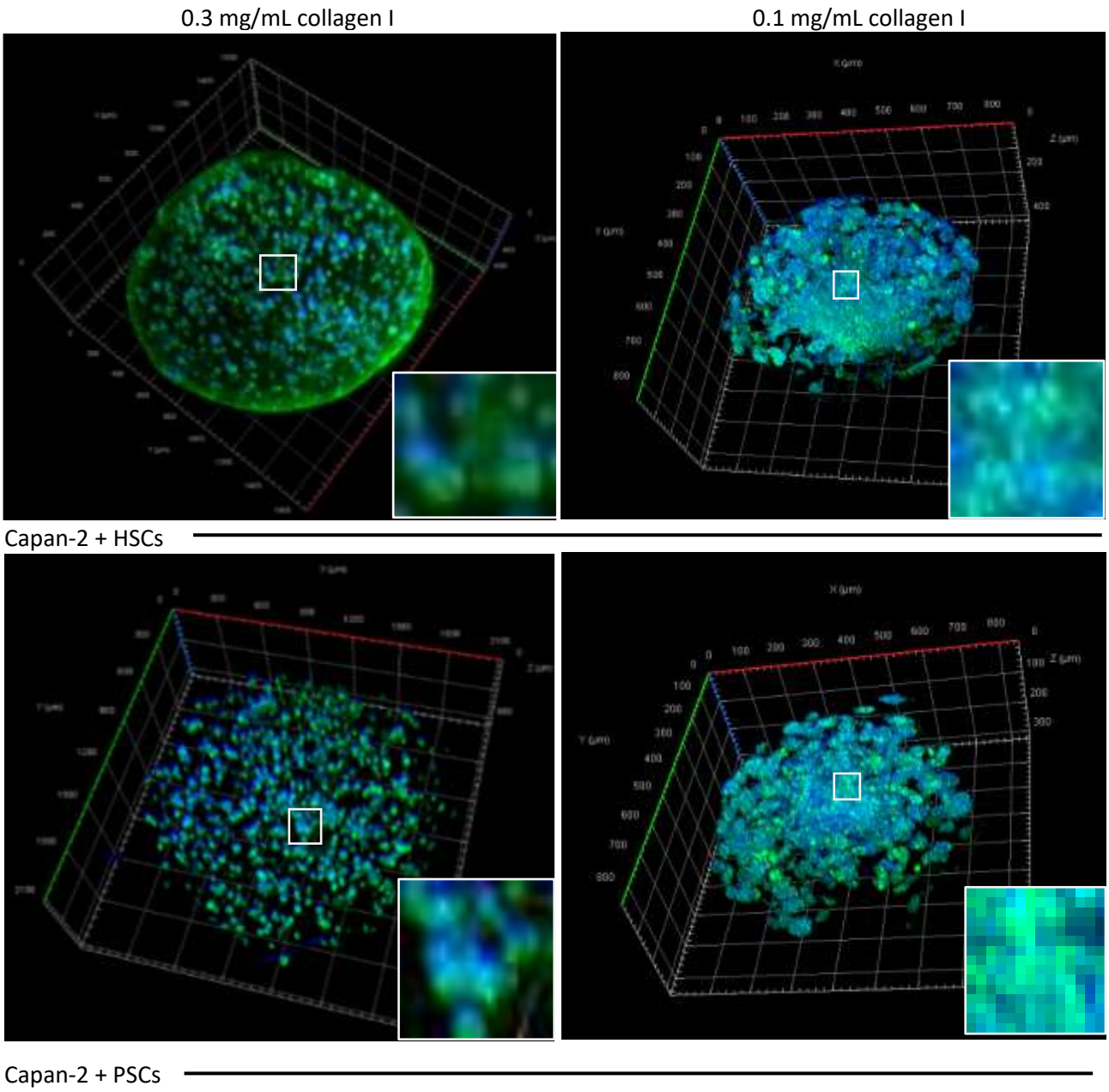

Figure 77. Expression of p53 in 3D co-culture spheroids of Capan-2 cells with stellate cells, different amount of collagen I.

500 Capan-2 cells and 1,000 hepatic stellate cells (HSCs) or pancreatic stellate cells (PSCs) were mixed in 50 µL of 0.3 or 0.1 mg/mL collagen I as indicated. On day 4, whole spheroids were fixed in PFA and stained with anti-p53 antibodies (green) and DAPI (blue). Z-stacking was performed using confocal microscope Zeiss LSM880 and 3D rendering was done in Zen 2.3 (blue edition). Insert: representative area of cancer cells cores/clusters with positive staining of p53. Scale bars of X, Y, and Z axes: 100 µm.

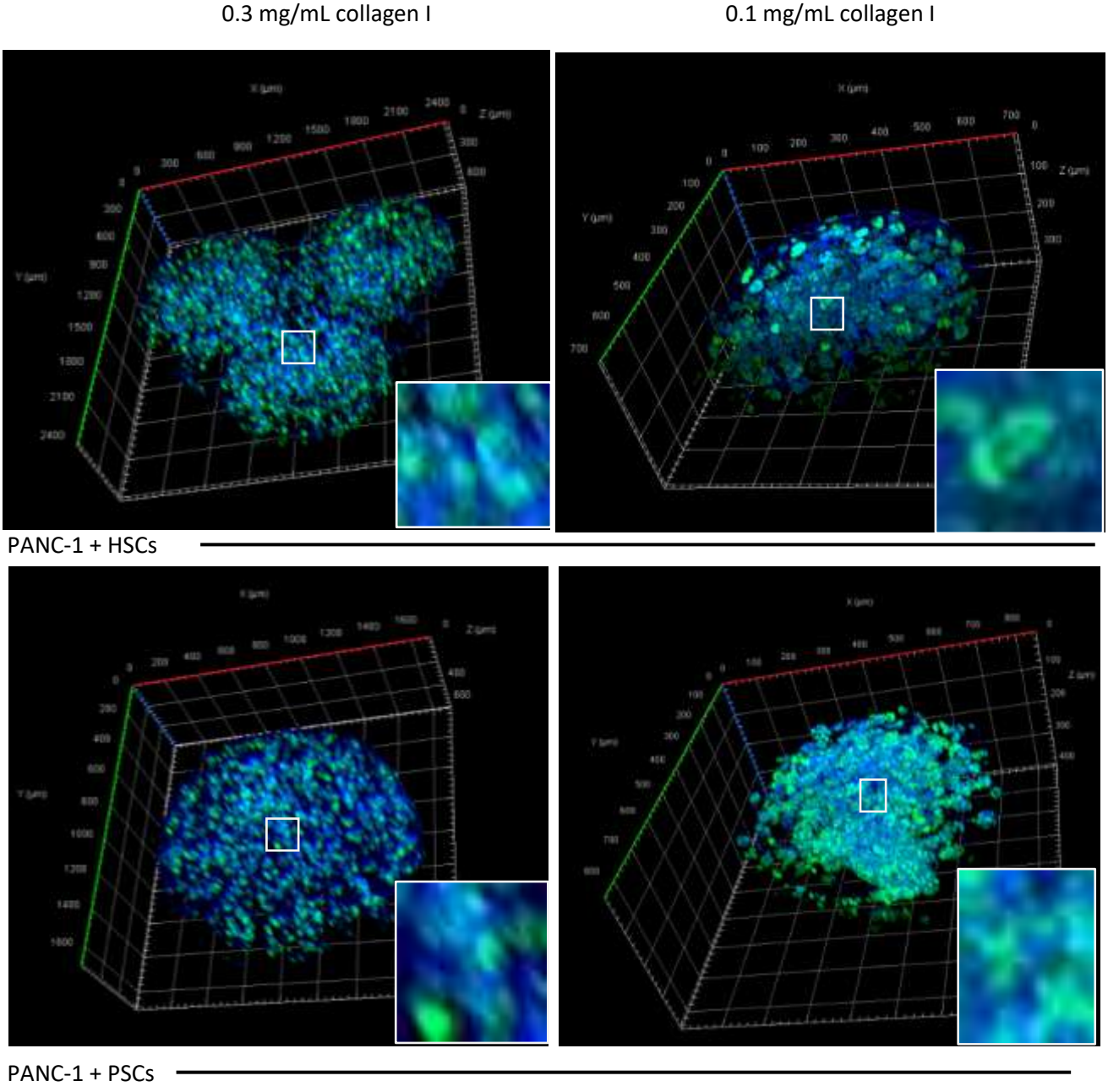

Figure 78. Expression of p53 in 3D co-culture spheroids of PANC-1 cells with stellate cells, different amount of collagen I.

500 PANC-1 cells and 1,000 hepatic stellate cells (HSCs) or pancreatic stellate cells (PSCs) were mixed in 50 µL of 0.3 or 0.1 mg/mL collagen I as indicated. On day 4, whole spheroids were fixed in PFA and stained with anti-p53 antibodies (green) and DAPI (blue). Z-stacking was performed using confocal microscope Zeiss LSM880 and 3D rendering was done in Zen 2.3 (blue edition). Insert: representative area of cancer cells cores/clusters with positive staining of p53. Scale bars of X, Y, and Z axes: 100 µm.

5.4.2 Stellate cells could be seen scattered in the 3D co-culture models with 0.1 mg/mL collagen I

Although αSMA was found to be present in 3D mono-culture of Capan-2 and PANC-1 cells grown in a scaffold-free condition, we would like to test whether the expression of αSMA in a 3D co-culture system with collagen I would be consistent with its expression pattern in a 3D mono-culture system. The morphology of stellate cells in 2D observed by phase-contrast microscopy is drastically different from the one of Capan-2 and PANC-1 cells in 2D. However, phase-contrast imaging is not able to capture the cell distribution in 3D thick specimen due to the limited penetration of visible lights. The fluorescent staining of αSMA analysed by confocal microscopy would allow deeper detection of different cell types in thick specimen after optical clearing with BABB.

Expression of αSMA was evaluated in 3D co-culture spheroids prepared from 500 cancer cells and 1,000 stellate cells in 50 µL of media containing 0.1 mg/mL collagen I. Whole spheroids grown for 4 days were fixed in PFA and stained with DAPI, and for αSMA and p53. CLSM Z-stack imaging was performed. 3D rendering is used to reconstruct the 3D co-culture models from the Z-stack images. 3D rendering has been performed to provide 3D structure of blood and lymphatic vessels [Oren *et al*, 2018], to reconstruct thick mouse inner ears [Kopecky *et al*, 2012], and analyse 3D cancer microenvironment in a whole mouse tumour [Lee *et al*, 2017]. The integrated 3D rendering module in the software Zen (blue edition) developed by an optical and optoelectronic company Zeiss, together with a software company arivis AG, allows fast processing of multiple optical slicing images acquired using Z-stacking scanning (https://blogs.zeiss.com/microscopy/news/en/solutions-for-the-visualization-and-analysis-of-big-image-data-in-life-sciences/?doing_wp_cron=1544695322.6736040115356445312500). Hundreds of 2D images resulting from optical sectioning of an intact spheroid using the CLSM with multiple channels can be displayed and handled in the module and the reconstruction of the spheroids can be presented with scaled axes.

As shown in Figure 79 and 80, there were regions with high levels of p53 expression or strong DAPI staining with enlarged nuclei, indicating clusters of cancer cells in the core of the spheroids. Consistent with studies described in section 3.2.3, αSMA expression could be found in the cytoplasm of cancer cells. There were also αSMA-positive fibre-like cells with long stretches of cytoplasm and small nuclei that did not stain for p53, indicating the presence of stellate cells.

Among three independent experiments, around 50% of the time, spheroids formed a big cancer core and the rest formed multiple cancer cell clusters, for both Capan-2 and PANC-1 co-culture systems.

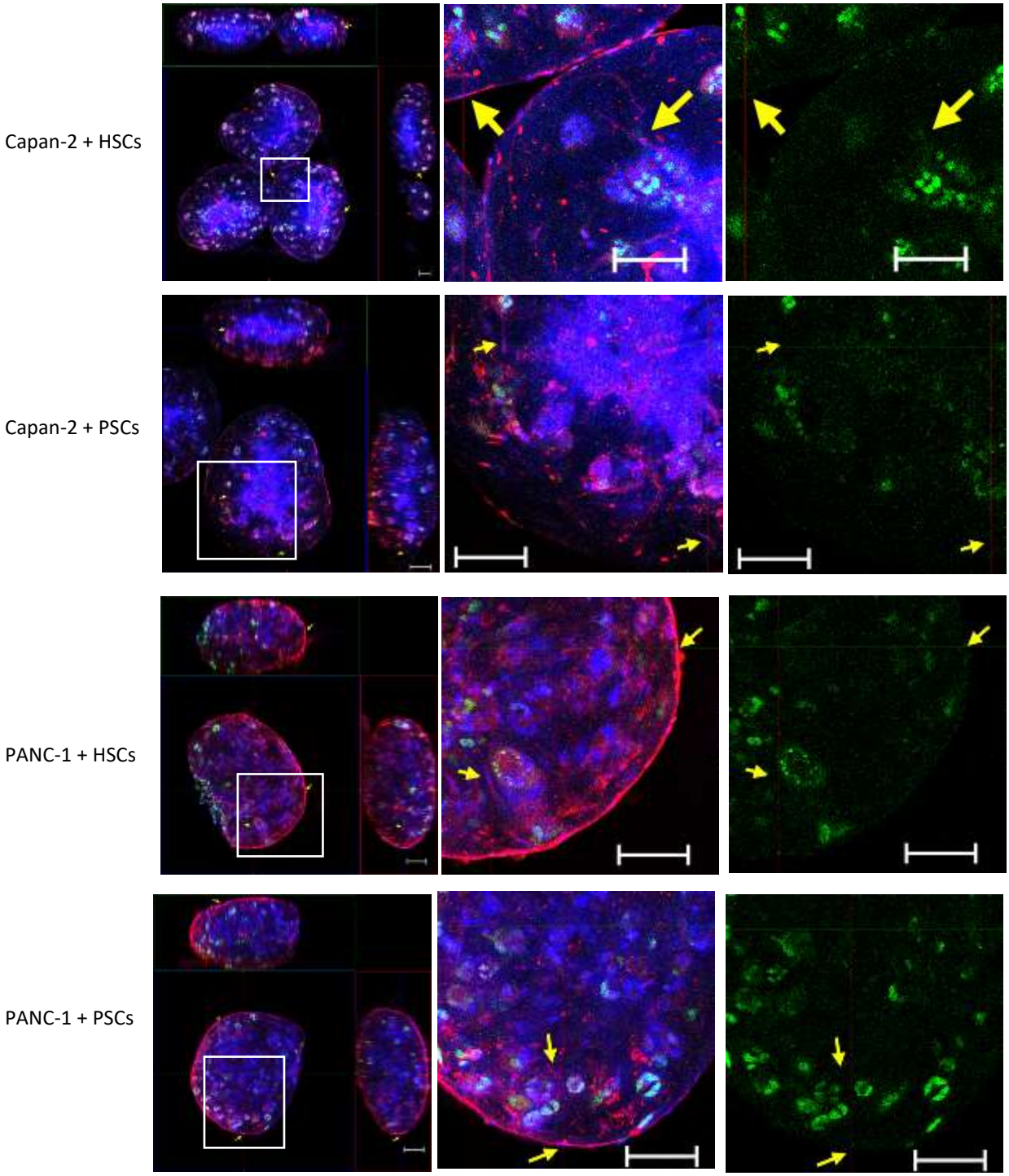

Figure 79. Orthogonal view of stellate cells distributed throughout co-culture spheroids with cancer cells, stellate cells and collagen I.

Spheroids from 500 cancer cells and 1,000 hepatic stellate cells (HSCs) or pancreatic stellate cells (PSCs) in 50 µL of 0.1 mg/mL collagen I were grown for 4 days. The whole spheroids were fixed in PFA and then stained with DAPI (blue), and for αSMA (red) and p53 (green). After optical clearing with BABB, Z-stack imaging using confocal laser scanning microscopy was performed. Image analysis of orthogonal view was done in Zen 2.3 (blue edition). Yellow arrows indicated stellate cells. Scale bar, 100 µm.

Figure 80. 3D rendering of stellate cells distributed throughout co-culture spheroids with cancer cells, stellate cells and collagen I.

Spheroids from 500 cancer cells and 1,000 hepatic stellate cells (HSCs) or pancreatic stellate cells (PSCs) in 50 µL of 0.1 mg/mL collagen I were grown for 4 days. The whole spheroids were fixed in PFA and then stained with DAPI (blue), and for αSMA (red) and p53 (green). After optical clearing with BABB, Z-stack imaging using confocal laser scanning microscopy was performed. Image analysis of 3D rendering was done in Zen 2.3 (blue edition). Yellow arrows indicated stellate cells. Scale bars of X, Y, and Z axes: 100 µm.

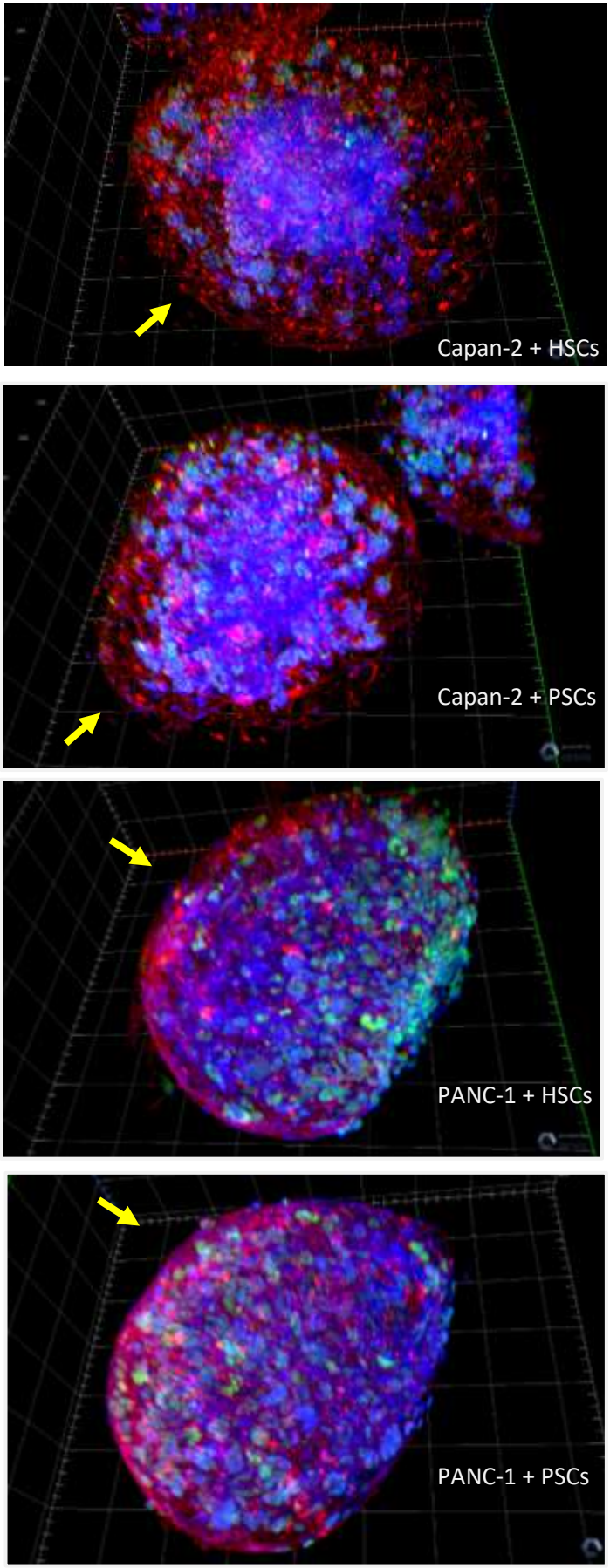

5.4.3 Initial test of potential anti-cancer agents on p53, Ki67 and YAP expression in 3D co-culture models

The data presented above suggest that we have developed a 3D co-culture spheroid model that resembles the organization of cancer cells and stellate cells present in the pancreatic cancer microenvironment. Also, the protocol for building the models is reproducible in our collaborators' lab where the natural products are being investigated as potential anti-cancer agents, two of which are Pseudopterosin A-D (PsA-D) and Tylophorinine. PsA-D are a mixture of four amphilectane-containing compounds, each of which is acetylated at different locations in one attached xylose sugar. PsA-D possess growth-inhibitory activity and can reduce invasiveness in triple negative breast cancer by targeting NF-κB signalling and glucocorticoid receptor alpha *in vitro* [Sperlich *et al*, 2017; Sperlich *et al*, 2018]. Tylophorinine and tylophorine are two interesting natural products that have drawn medicinal chemists' attention on biosynthesis and extraction [Gantait et al, 2017; Govindachari et al, 1965]. A tylophorine analogue, DCB-3503, can inhibit pancreatic cancer cell growth by targeting the abnormal cell-cycle signalling in PANC-1 and HPAC pancreatic cancer cell lines, providing a promising new compound to be tested in PDAC [Shiah et al, 2006]. Thus, we carried out an initial investigation using this model to examine its capacity to screen potential anti-cancer agents, PsA-D and Tylophorinine, with collaboration across different labs.

According to the cell viability results from our collaborators Janina Betz, Julia Sperlich, and Nicole Teusch from Technische Hochschule Köln, University of Technology, Arts and Sciences in Germany, 70 µM Pseudopterosin A-D (PsA-D) or 0.1 µM Tylophorinine were added to the spheroids on day 4. 100 µM gemcitabine was used as a positive control and 0.7% DMSO was used as a solvent control. After 3 days, phase-contrast imaging and immunofluorescence with CLSM were performed to evaluate the effects of these agents on the phenotypic changes of the spheroids.

As illustrated in Figure 81, phase-contrast images showed no striking differences in co-culture spheroids after 3 days in any of the treatment or control groups other than the PsA-D treatment group where the surface of these spheroids became less organized, indicating possible cell damage.

Spheroids were then stained with DAPI, and for p53, Ki67 and YAP. CLSM Z-stack imaging was performed to detect the distribution of p53 and Ki67 expression in the entire spheroid (Figure 82). Due to limitations of the microscope being used, the 10x objective lens was not able to acquire clear and reliable images for anti-YAP antibodies incubated with secondary antibodies conjugated to Alexa Fluo 647. Airyscan with super-resolution was required to localize YAP definitely in the nuclei and the cytoplasm of these cells (Figure 84, 86, and 88). Meanwhile, multi-coloured imaging with Airyscan was also performed to detect Ki67 and p53 in the spheroids simultaneously to validate the expression of Ki67 and p53 using higher resolution imaging compared to conventional CLSM (Figure 83, 85, and 87).

As shown from 3D rendering of the entire intact spheroids from all the 2D images from the whole spheroids in Figure 82, obvious reduction of Ki67 and p53 expression could be detected after treatments with PsA-D and Tylophorinine on the spheroids, without the aid for quantification. Data from 3D reconstruction of spheroids stained for p53 and Ki67 provided sufficient information to draw conclusions and thereby further quantification by CellProfiler was not conducted at this point. It was observed that 70 µM PsA-D or 0.1 µM Tylophorinine both reduced the p53 and Ki67 to a greater extent in co-culture models with Capan-2 cells than with PANC-1 cells, using the conventional CLSM (Figure

82), and CLSM with Airyscan (Figure 83, 85, and 87). These data indicated that cancer cells having similarities to Capan-2 cells may be more sensitive to PsA-D and Tylophorinine treatment than those similar to PANC-1 cells. At this time it is unclear what genotypic/phenotypic characteristic(s) is critical to the discrimination made by these two potential anti-cancer agents.

In these studies, we observed cells with nuclear localisation of YAP near the edge of the untreated spheroids (Figure 86 and 88). Meanwhile, cells with cytoplasmic localisation of YAP were also detected, both near the edge and the core of the untreated spheroids (Figure 86 and 88). Homogenous YAP expression in the nucleus and the cytoplasm seemed to be the main event, indicating a dynamic YAP signalling in the 3D co-culture models of PDAC cells, stellate cells and collagen I. Factors that might regulate this dynamic nuclear and cytoplasmic localisation of YAP in this 3D co-culture models, such as hypoxia or nutrient limitation, is presently unclear. Treatments with 70 µM PsA-D for 3 days, however markedly reduced YAP nuclear and cytoplasmic expression (Figure 84, 86, and 88). Cells with nuclear localization with YAP after treatment of 100 µM Gemcitabine 0.1 µM Tylophorinine for 3 days were also observed (Figure 84, 86, and 88). However, only one optical section could be acquired with Airyscan for each spheroid during the limited time possible, which failed to represent a true and complete reflection of hundreds of sections in the whole spheroids.

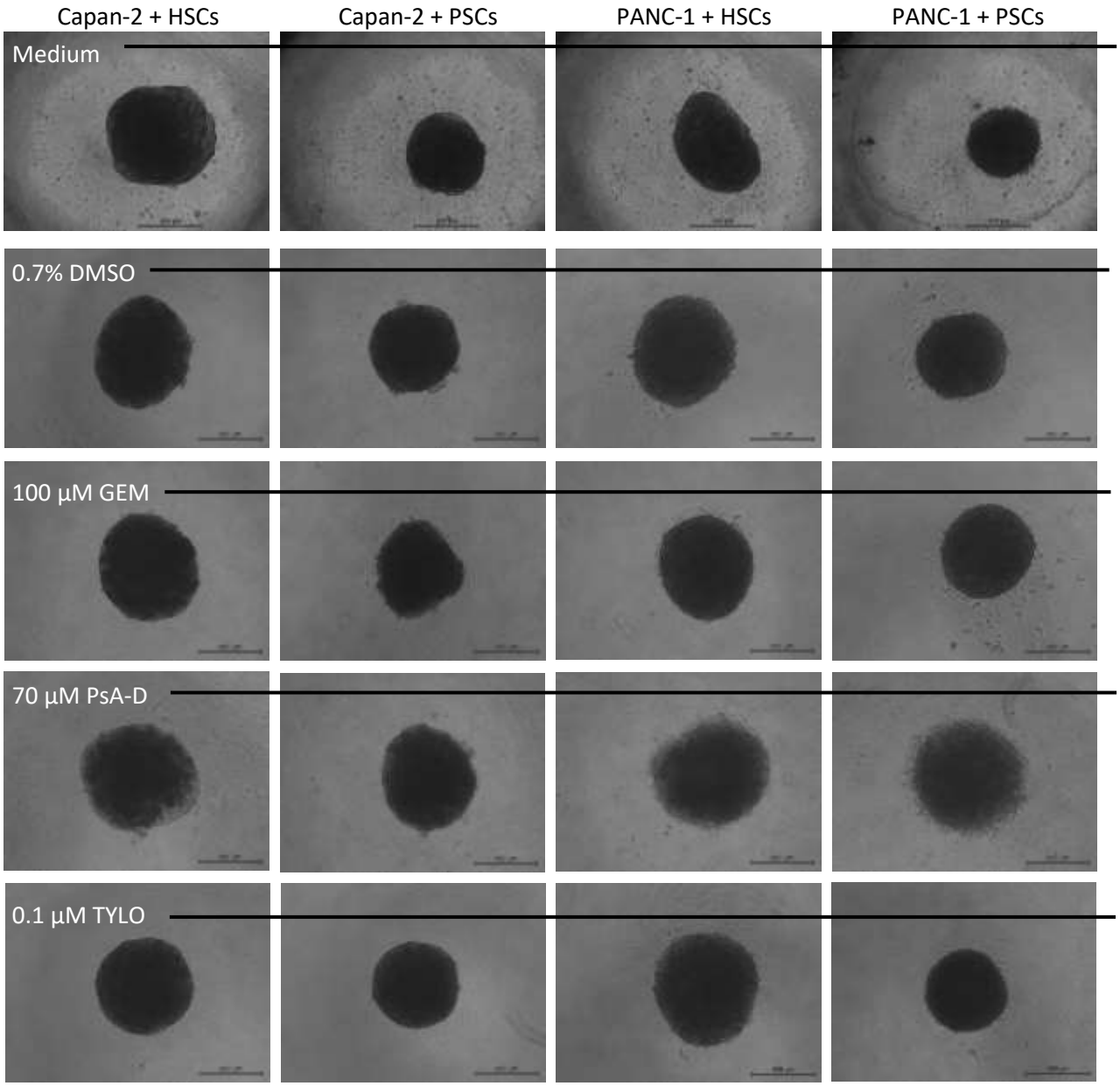

Figure 81. Phase-contrast imaging of the 3D co-culture models with or without treatments.

Spheroids with 500 cancer cells and 1,000 hepatic stellate cells (HSCs) or pancreatic stellate cells (PSCs) in 50 µL of 0.1 mg/mL collagen I were grown for 4 days and then treated with medium, 70 µM Pseudopterosin A-D (PsA-D) and 0.1 µM Tylophorinine (TYLO), 100 µM gemcitabine (GEM) as a positive control, and 0.7% DMSO as a solvent control. After 3 days with or without treatments, phase-contrast imaging by Leica DMI4000 B (50x magnification) was performed to evaluate the effects of the anti-cancer agents on spheroid sizes and morphological changes. Representative images from three independent experiments with three spheroids in each experiment were shown in the spheroids treated with 70 µM PsA-D, 0.1 µM TYLO, and 0.7% DMSO. Representative images from one independent experiments with three spheroids in each experiment were shown in the spheroids treated with 100 µM GEM and medium. Scale bar, 500 µm.

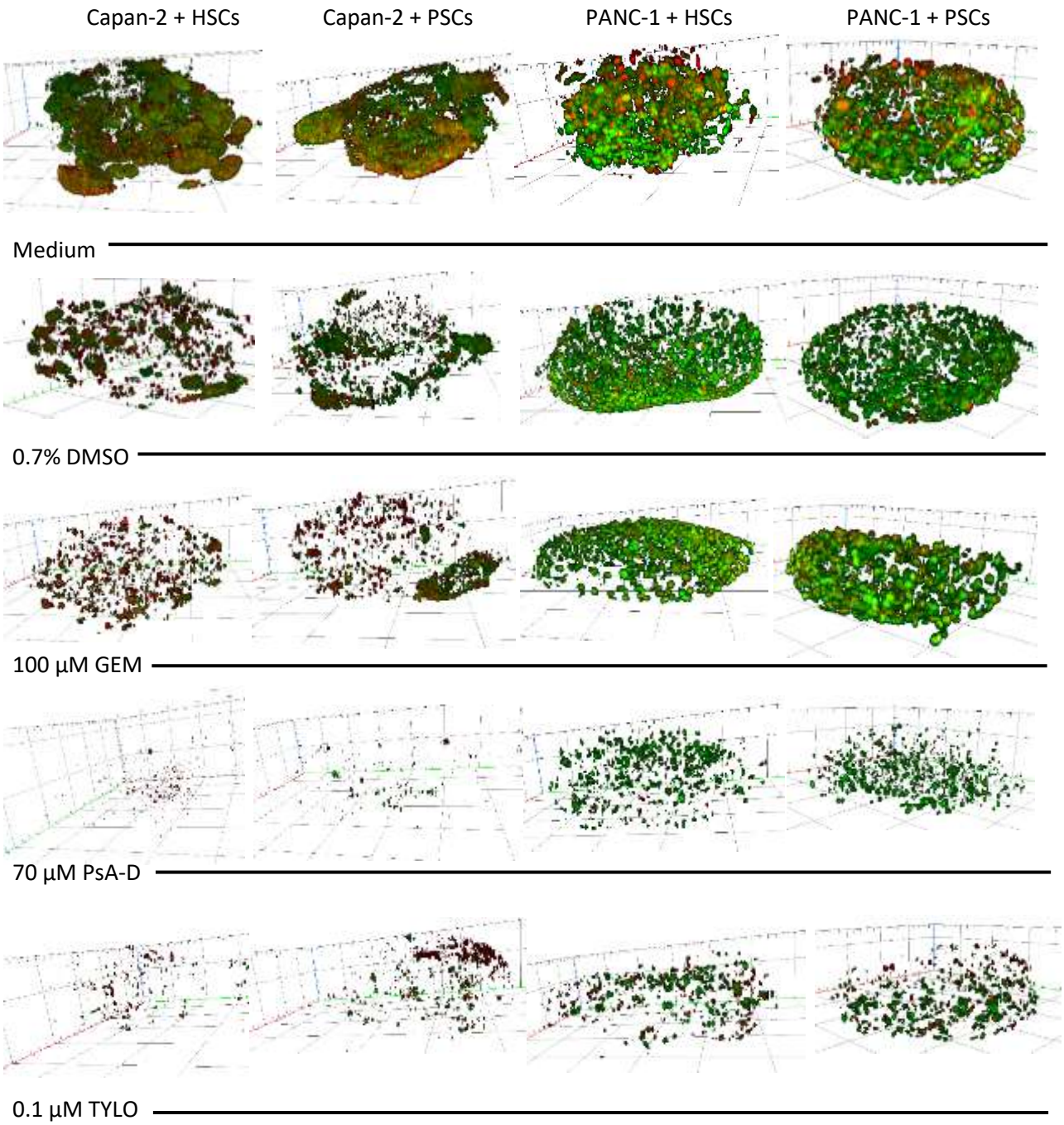

Figure 82. 3D rendering of entire spheroids showing p53 and Ki67 staining.

Spheroids with 500 cancer cells and 1,000 hepatic stellate cells (HSCs) or pancreatic stellate cells (PSCs) in 50 µL of 0.1 mg/mL collagen I were grown for 4 days and then treated with medium, 70 µM Pseudopterosin A-D (PsA-D) and 0.1 µM Tylophorinine (TYLO), 100 µM gemcitabine (GEM) as a positive control, and 0.7% DMSO as a solvent control. After 3 days with or without treatments, whole spheroids were fixed in PFA and immunofluorescence of DAPI (not shown), p53 (green), Ki67 (red) and YAP (not shown) was used to assess co-localization events. CLSM with Zeiss LSM880 was performed using a 10x objective lens. Image analysis and 3D rendering were done in Zen 2.3 (blue edition). Representative images from three independent experiments with three spheroids in each experiment were shown in the spheroids treated with 70 µM PsA-D, 0.1 µM TYLO, and 0.7% DMSO. Representative images from one independent experiments with three spheroids in each experiment were shown in the spheroids treated with 100 µM GEM and medium. Scale bars of X, Y, and Z axes: 100 µm.

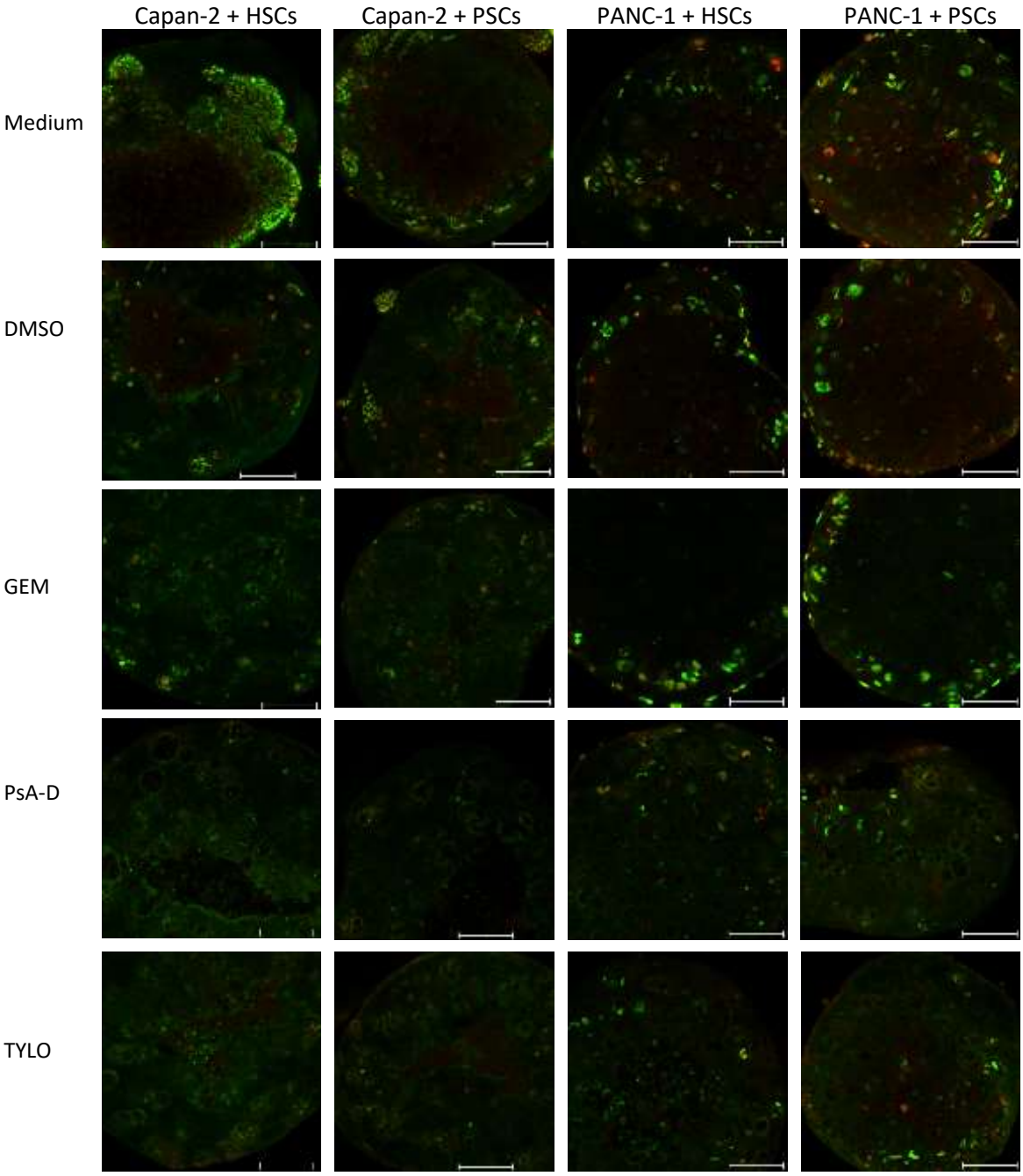

Figure 83. Effect of potential anti-cancer agents on Ki67 and p53 expression in 3D co-culture models: Airyscan imaging on whole spheroids.

Spheroids with 500 cancer cells and 1,000 hepatic stellate cells (HSCs) or pancreatic stellate cells (PSCs) in 50 µL of 0.1 mg/mL collagen I were grown for 4 days and then treated with medium, 70 µM Pseudopterosin A-D (PsA-D) and 0.1 µM Tylophorinine (TYLO), or 100 µM gemcitabine (GEM) as a positive control, and 0.7% DMSO as a solvent control. After 3 days with or without treatments, immunofluorescence with Airyscan imaging on intact spheroids was performed with Zeiss LSM880 using a 10x objective lens and four fluorescent dyes. DAPI (blue) and YAP (orange) were illustrated. Image analysis was done in Zen 2.3 (blue edition). Representative images from three independent experiments with three replicates in each experiment were shown in spheroids treated with PsA-D, TYLO, and DMSO. Representative images from one independent experiment with three replicates in each experiment were shown in spheroids treated with GEM and medium. Scale bar, 100 µm.

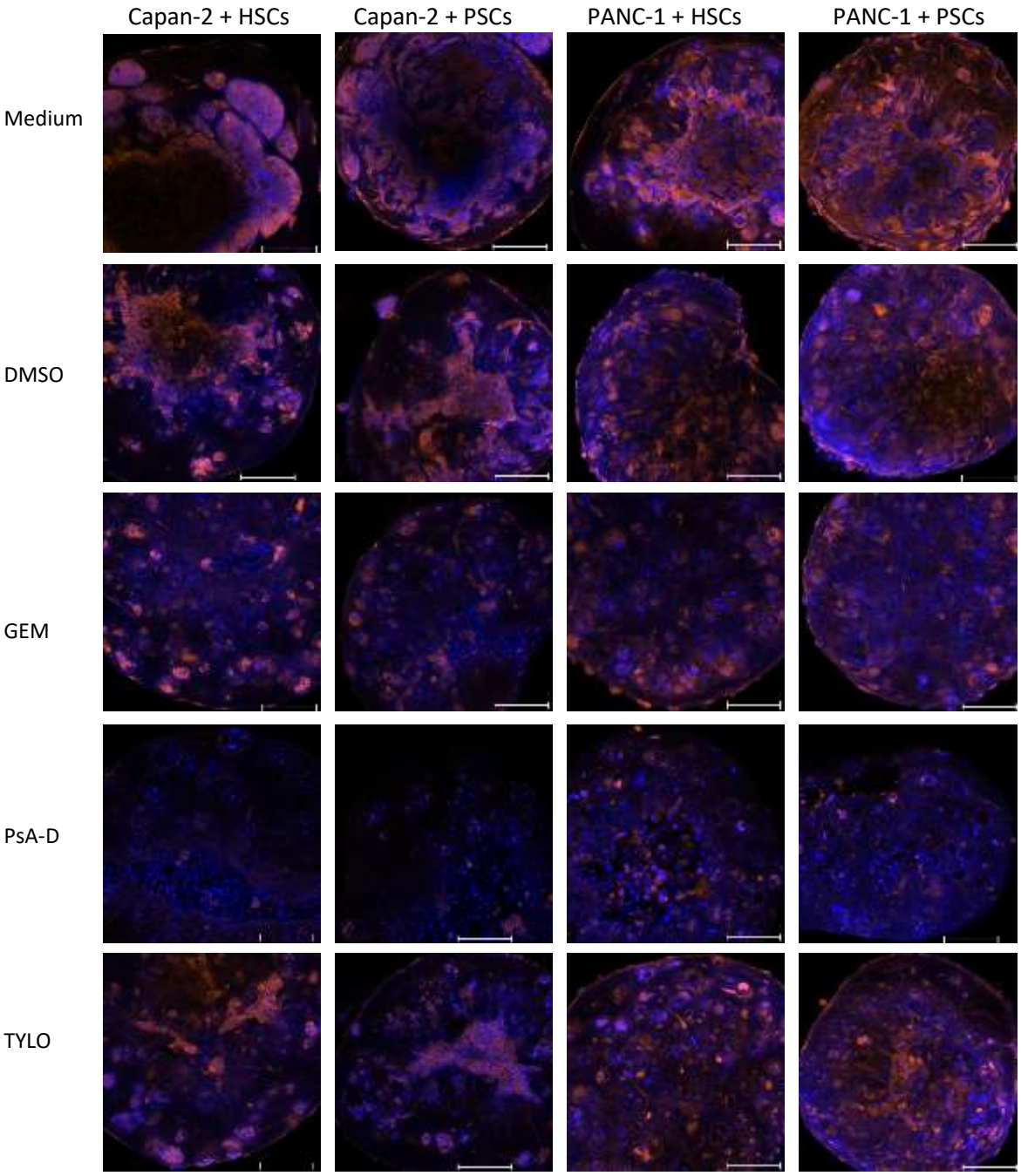

Figure 84. Effect of potential anti-cancer agents on YAP expression in 3D co-culture models: Airyscan imaging on whole spheroids.

Spheroids with 500 cancer cells and 1,000 hepatic stellate cells (HSCs) or pancreatic stellate cells (PSCs) in 50 µL of 0.1 mg/mL collagen I were grown for 4 days and then treated with medium, 70 µM Pseudopterosin A-D (PsA-D) and 0.1 µM Tylophorinine (TYLO), or 100 µM gemcitabine (GEM) used as a positive control. 0.7% DMSO was used as a solvent control. After 3 days with or without treatments, immunofluorescence with Airyscan imaging on intact spheroids was performed with Zeiss LSM880 using a 10x objective lens and four fluorescent dyes. DAPI (blue) and YAP (orange) were illustrated. Image analysis was done in Zen 2.3 (blue edition). Representative images from three independent experiments with three replicates in each experiment were shown in spheroids treated with PsA-D, TYLO, and DMSO. Representative images from one independent experiment with three replicates in each experiment were shown in spheroids treated with GEM and medium. Scale bar, 100 µm.

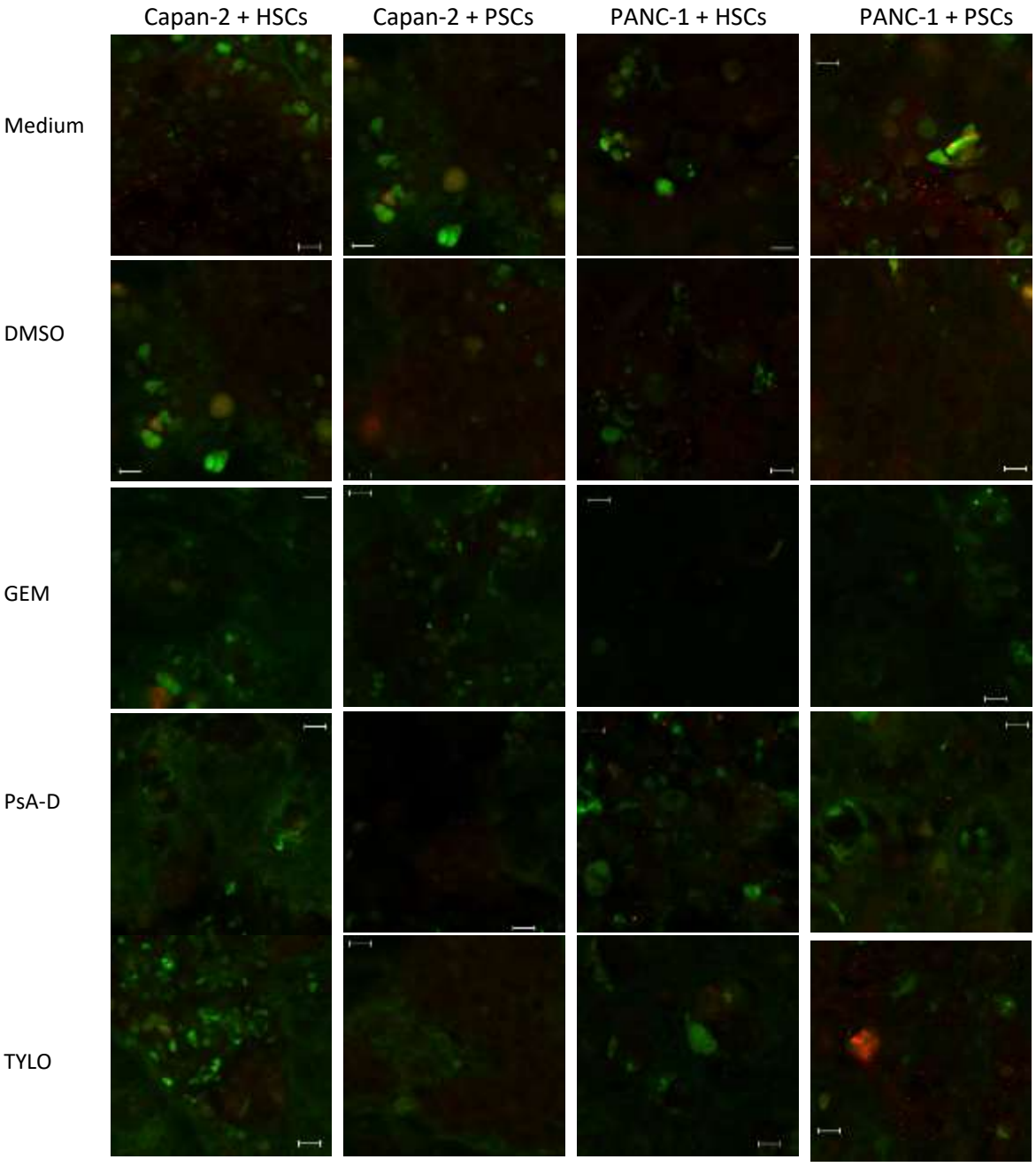

Figure 85. Effect of potential anti-cancer agents on Ki67 and p53 expression in 3D co-culture models of PDAC: Airyscan imaging near the core of intact spheroids.

Spheroids with 500 cancer cells and 1,000 hepatic stellate cells (HSCs) or pancreatic stellate cells (PSCs) in 50 µL of 0.1 mg/mL collagen I were grown for 4 days and then treated with medium, 70 µM Pseudopterosin A-D (PsA-D) and 0.1 µM Tylophorinine (TYLO), or 100 µM gemcitabine (GEM) as a positive control, and 0.7% DMSO as a solvent control. After 3 days with or without treatments, immunofluorescence with Airyscan imaging on intact spheroids was performed with Zeiss LSM880 using a 10x objective lens and four fluorescent dyes. Ki67 (red) and p53 (green) were illustrated. Image analysis was done in Zen 2.3 (blue edition). Representative images from three independent experiments with three spheroids treated with PsA-D, TYLO, and DMSO in each experiment were shown. Representative images from one independent experiment with three spheroids treated with GEM and medium in each experiment were shown. Scale bar, 10 µm.

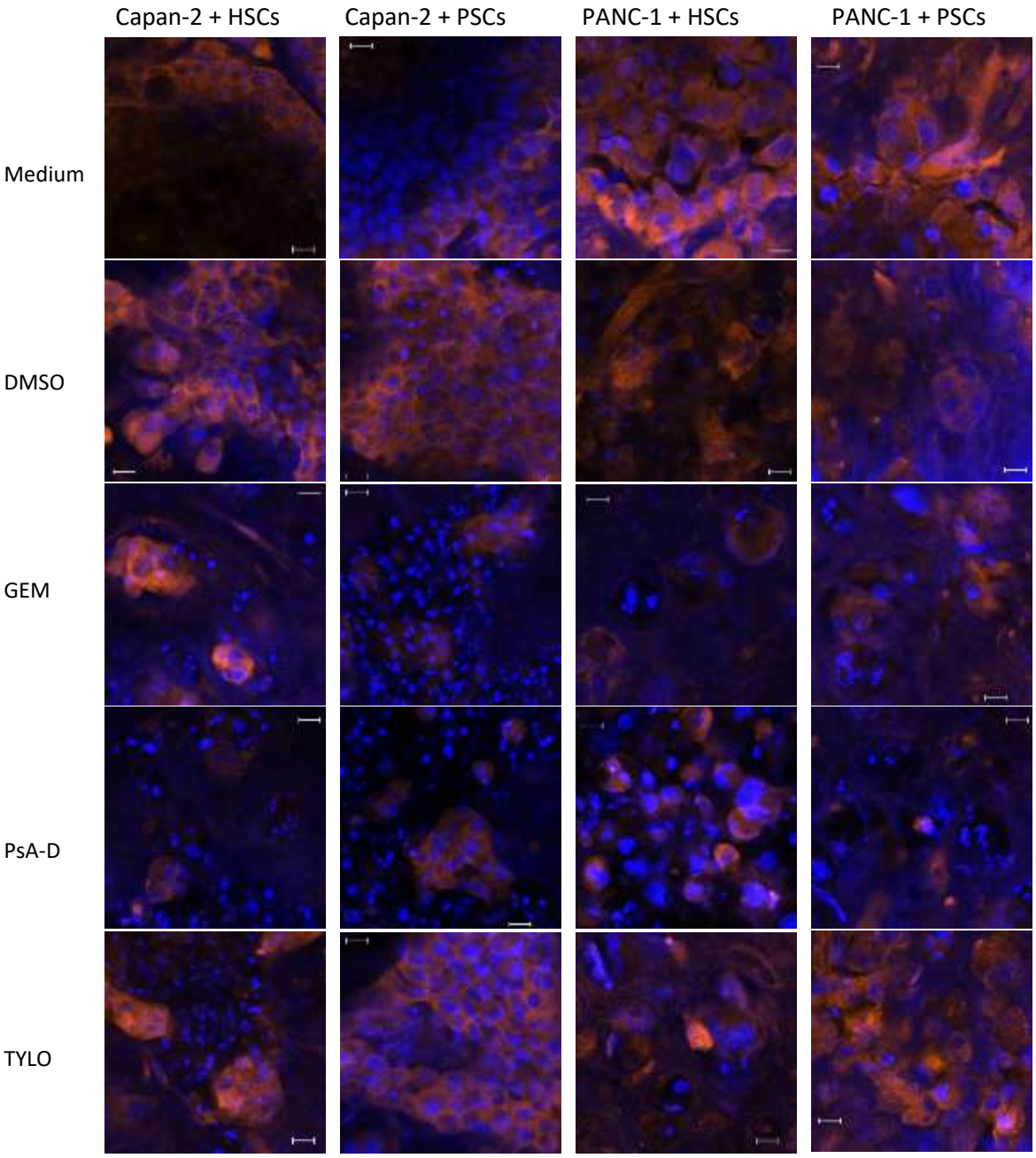

Figure 86. Effect of potential anti-cancer agents on YAP expression in 3D co-culture models of PDAC: Airyscan imaging near the core of intact spheroids.

Spheroids with 500 cancer cells and 1,000 hepatic stellate cells (HSCs) or pancreatic stellate cells (PSCs) in 50 µL of 0.1 mg/mL collagen I were grown for 4 days and then treated with medium, 70 µM Pseudopterosin A-D (PsA-D) and 0.1 µM Tylophorinine (TYLO), or 100 µM gemcitabine (GEM) used as a positive control. 0.7% DMSO was used as a solvent control. After 3 days with or without treatments, immunofluorescence with Airyscan imaging on intact spheroids was performed with Zeiss LSM880 using a 10x objective lens and four fluorescent dyes. DAPI (blue) and YAP (orange) were illustrated. Image analysis was done in Zen 2.3 (blue edition). Representative images from three independent experiments with three replicates in each experiment were shown in spheroids treated with PsA-D, TYLO, and DMSO. Representative images from one independent experiment with three replicates in each experiment were shown in spheroids treated with GEM and medium. Scale bar, 10 µm.

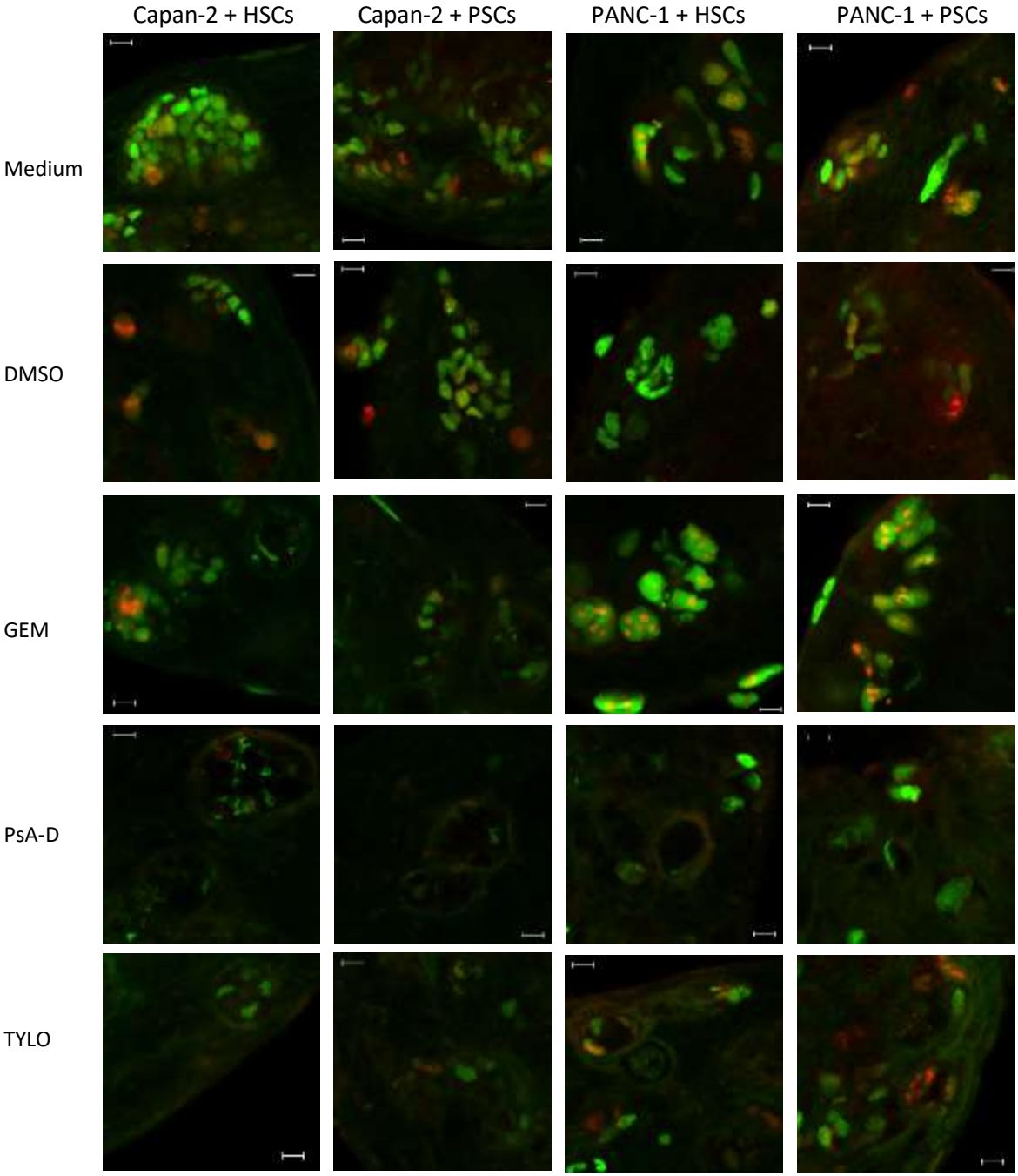

Figure 87. Effect of potential anti-cancer agents on Ki67 and p53 expression in 3D co-culture models of PDAC: Airyscan imaging near the edge of intact spheroids.

Spheroids with 500 cancer cells and 1,000 hepatic stellate cells (HSCs) or pancreatic stellate cells (PSCs) in 50 µL of 0.1 mg/mL collagen I were grown for 4 days and then treated with medium, 70 µM Pseudopterosin A-D (PsA-D) and 0.1 µM Tylophorinine (TYLO), or 100 µM gemcitabine (GEM) as a positive control, and 0.7% DMSO as a solvent control. After 3 days with or without treatments, immunofluorescence with Airyscan imaging on intact spheroids was performed with Zeiss LSM880 using a 10x objective lens and four fluorescent dyes. Ki67 (red) and p53 (green) were illustrated. Image analysis was done in Zen 2.3 (blue edition). Representative images from three independent experiments with three spheroids treated with PsA-D, TYLO, and DMSO in each experiment were shown. Representative images from one independent experiment with three spheroids treated with GEM and medium in each experiment were shown. Scale bar, 10 µm.

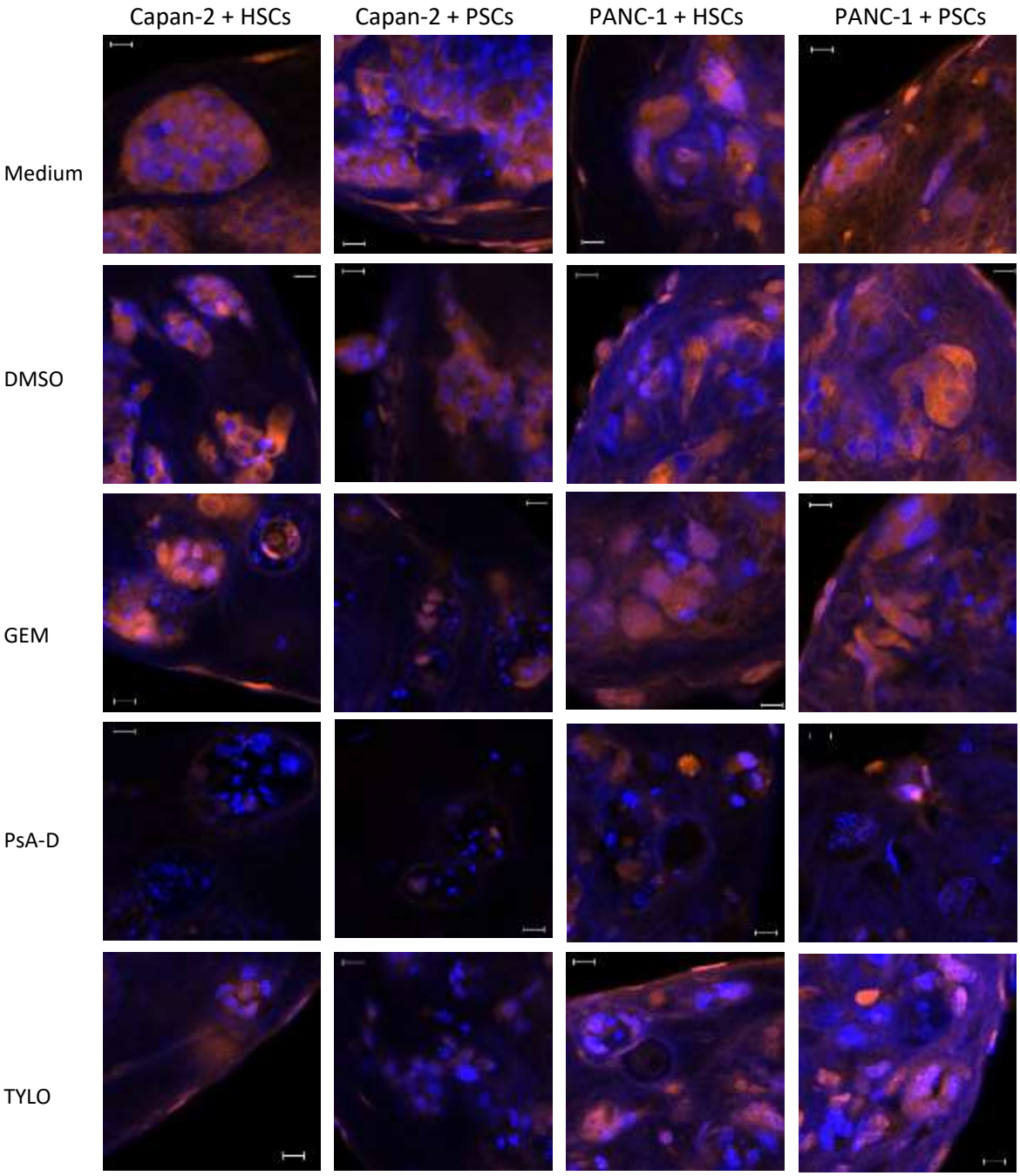

Figure 88. Effect of potential anti-cancer agents on YAP expression in 3D co-culture models of PDAC: Airyscan imaging near the edge of intact spheroids.

Spheroids with 500 cancer cells and 1,000 hepatic stellate cells (HSCs) or pancreatic stellate cells (PSCs) in 50 µL of 0.1 mg/mL collagen I were grown for 4 days and then treated with medium, 70 µM Pseudopterosin A-D (PsA-D) and 0.1 µM Tylophorinine (TYLO), or 100 µM gemcitabine (GEM) as a positive control, and 0.7% DMSO as a solvent control. After 3 days with or without treatments, immunofluorescence with Airyscan imaging on intact spheroids was performed with Zeiss LSM880 using a 10x objective lens and four fluorescent dyes. DAPI (blue) and YAP (orange) were illustrated. Image analysis was done in Zen 2.3 (blue edition). Representative images from three independent experiments with three spheroids treated with PsA-D, TYLO, and DMSO in each experiment were shown. Representative images from one independent experiment with three spheroids treated with GEM and medium in each experiment were shown. Scale bar, 10 µm.

5.5 Spheroid formation, cell distribution and protein expression in 3D co-culture models of stellate cells to cancer cells at a 2:1 cell ratio with HA and COL I

5.5.1 Correlation of spheroid size with collagen content in hyaluronic acid

Efforts were also undertaken to explore the direct mixture of stellate cells suspension with cancer cells suspension at a 2:1 ratio of stellate cells to cancer cells with 0.03 mg/mL, 0.05 mg/mL, 0.1 mg/mL, and 0.3 mg/mL collagen I (COL I) with 3.5 mg/mL hyaluronic acid (HA) to form 3D co-culture models in a 50 µL volume.

As seen in Figure 89-92, after cells, HA and COL I were mixed and grown for 1 day, dark areas could be detected in the wells with 0.1 mg/mL and 0.3 mg/mL COL I. At the same time, irregular spheroids could be found in the wells with 0.03 mg/mL and 0.05 mg/mL COL I. On day 3, spheroids with smooth edge could be formed in the wells with 0.03 mg/mL, 0.05 mg/mL, and 0.1 mg/mL COL I. On day 4, the areas of spheroids in the wells with 0.3 mg/mL COL I were smaller compared to the ones on day 3. After measuring the sizes on day 4 by CellProfiler, the mean areas of spheroids to the concentration of COL I were plotted in Figure 89-92. The R^2 of the plots were 1 for Capan-2 cells with hepatic stellate cells (HSCs), 0.985 for Capan-2 cells with pancreatic stellate cells (PSCs), 0.9962 for PANC-1 cells with HSCs and 0.9988 for PANC-1 with PSCs combinations (Figure 89-92). The data indicated the correlation of spheroid size with collagen content in the current study.

Consistent with data presented in section 5.4.1, higher amounts of collagen resulted in a larger spheroid size. This observation was consistent for studies performed on Capan-2 cells with HSCs, Capan-2 cells with PSCs, PANC-1 cells with HSCs and PANC-1 with PSCs.

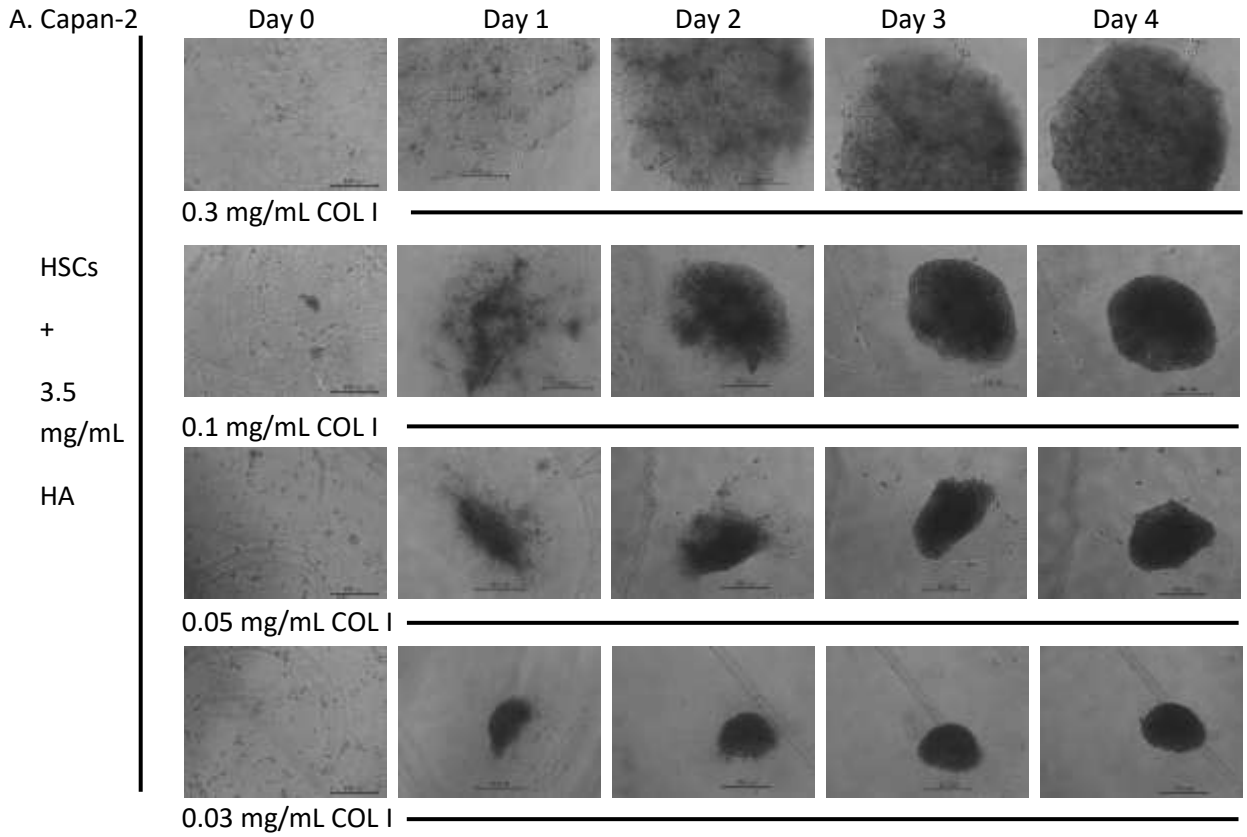

B.

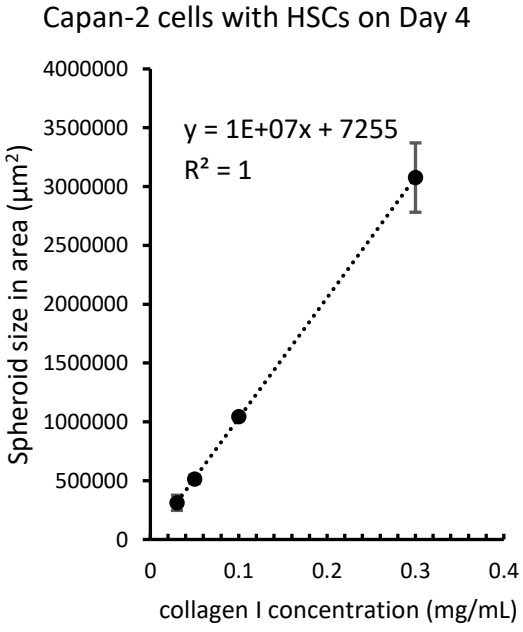

Figure 89. Correlation of spheroid size with collagen I content in 3D co-cultures of Capan-2 cells, hepatic stellate cells, collagen I and hyaluronic acid.

500 Capan-2 cells and 1,000 hepatic stellate cells (HSCs) were mixed in 50 µL of 0.03 mg/mL, 0.05 mg/mL, 0.1 mg/mL and 0.3 mg/mL collagen I with 3.5 mg/mL hyaluronic acid as indicated. A. Images were acquired by Leica DMI4000 B (50x magnification) manually and daily for 4 days. Data shown were representative images from two independent experiments with three spheroids in each experiment. Scale bar, 500 µm. B. Spheroid sizes on day 4 were measured using CellProfiler. The areas (μm^2) of spheroids cultured in different concentrations of collagen I on day 4 were graphed. Error bars represented standard deviations from three spheroids from one independent experiment. The R^2 used to measure linearity of was calculated by Excel.

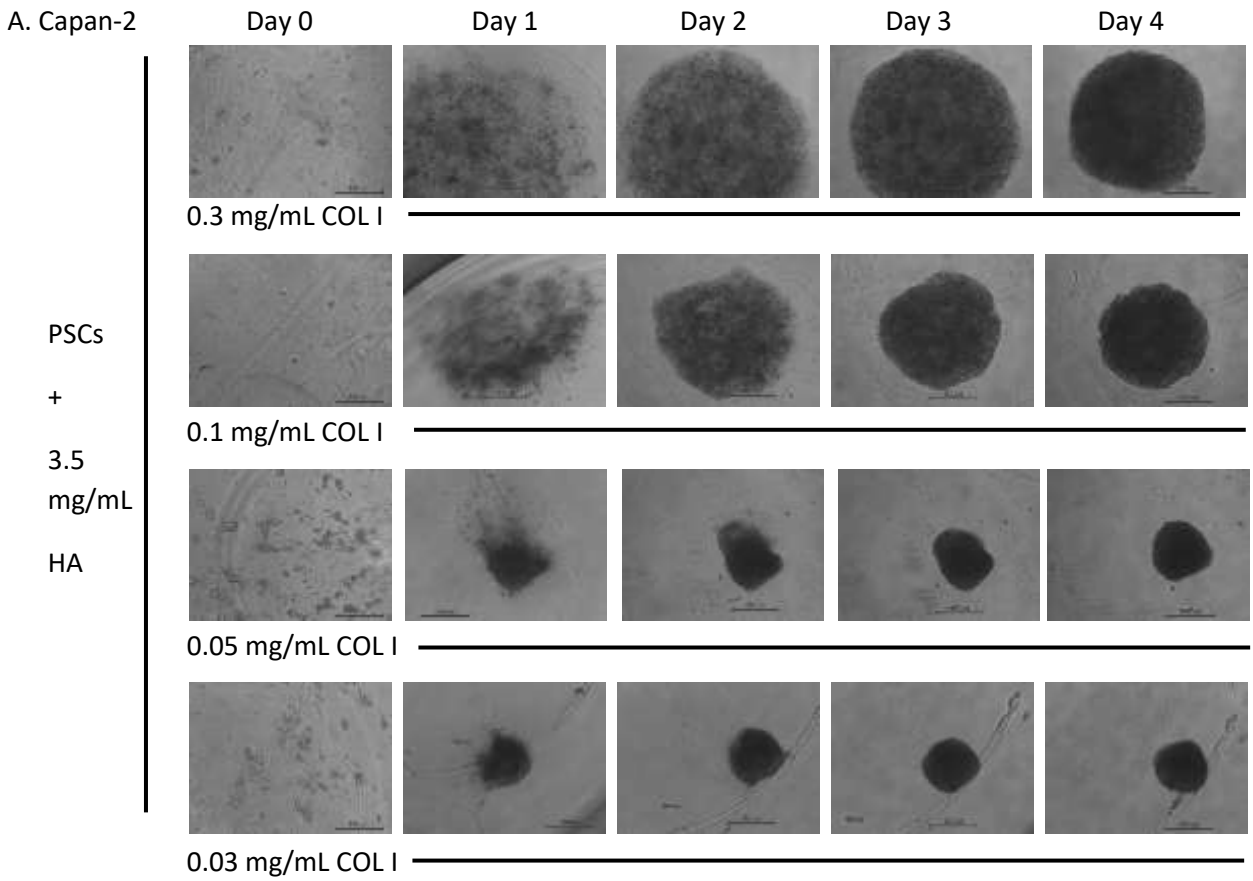

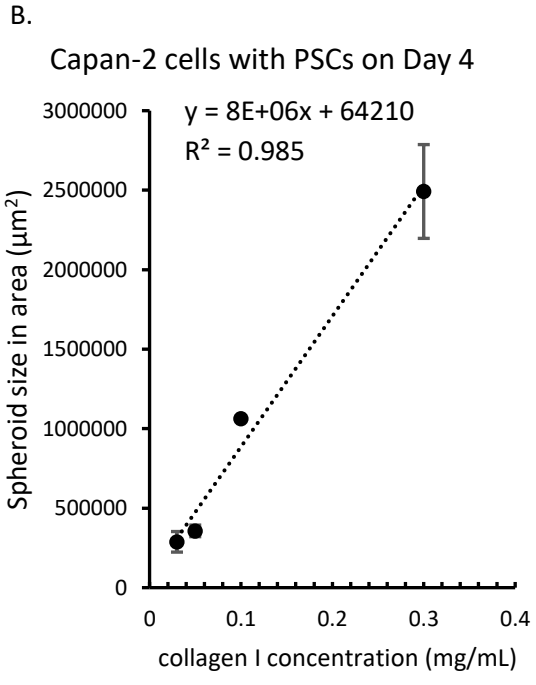

Figure 90. Correlation of spheroid size with collagen I content in 3D co-cultures of Capan-2 cells, pancreatic stellate cells, collagen I and hyaluronic acid.

500 Capan-2 cells and 1,000 pancreatic stellate cells (PSCs) were mixed in 50 µL of 0.03 mg/mL, 0.05 mg/mL, 0.1 mg/mL and 0.3 mg/mL collagen I with 3.5 mg/mL hyaluronic acid as indicated. A. Images were acquired by Leica DMI4000 B (50x magnification) manually and daily for 4 days. Data shown were representative images from two independent experiments with three spheroids in each experiment. Scale bar, 500 µm. B. Spheroid sizes on day 4 were measured using CellProfiler. The areas (μm^2) of spheroids cultured in different concentrations of collagen I on day 4 were graphed. Error bars represented standard deviations from three spheroids from one independent experiment. The R^2 used to measure linearity of was calculated by Excel.

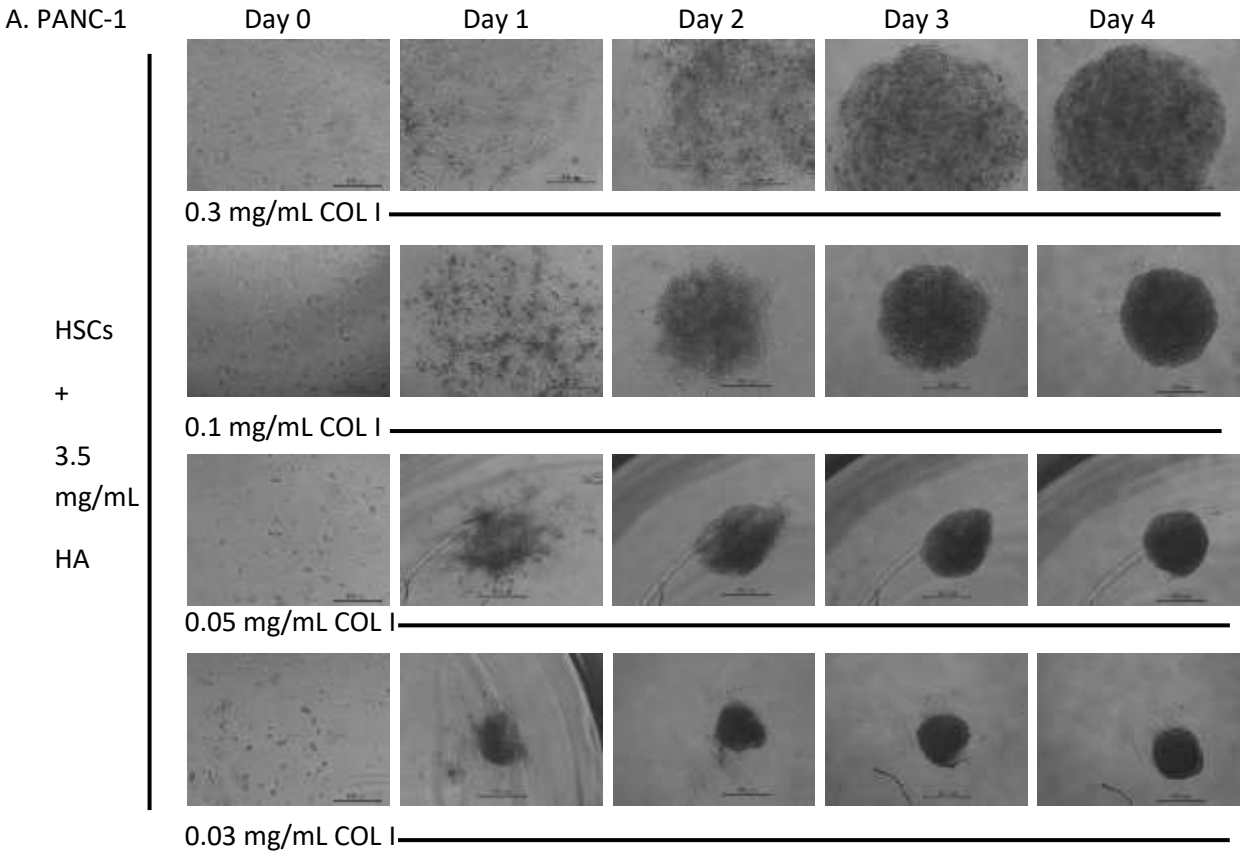

B.

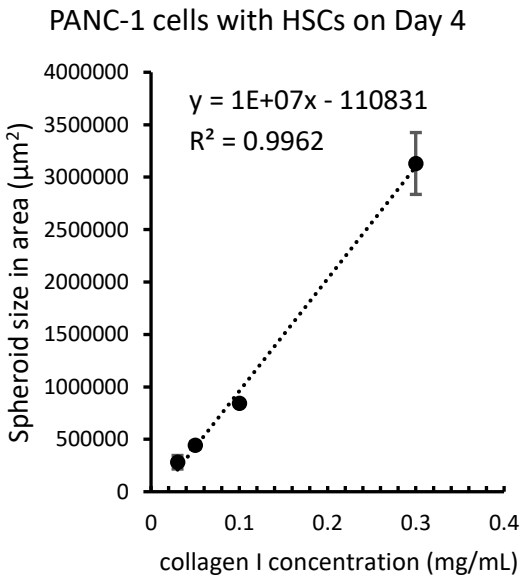

Figure 91. Correlation of spheroid size with collagen I content in 3D co-cultures of PANC-1 cells, hepatic stellate cells, collagen I and hyaluronic acid.

500 PANC-1 cells and 1,000 hepatic stellate cells (HSCs) were mixed in 50 µL of 0.03 mg/mL, 0.05 mg/mL, 0.1 mg/mL and 0.3 mg/mL collagen I with 3.5 mg/mL hyaluronic acid as indicated. A. Images were acquired by Leica DMI4000 B (50x magnification) manually and daily for 4 days. Data shown were representative images from two independent experiments with three spheroids in each experiment. Scale bar, 500 µm. B. Spheroid sizes on day 4 were measured using CellProfiler. The areas (μm^2) of spheroids cultured in different concentrations of collagen I on day 4 were graphed. Error bars represented standard deviations from three spheroids from one independent experiment. The R^2 used to measure linearity of was calculated by Excel.

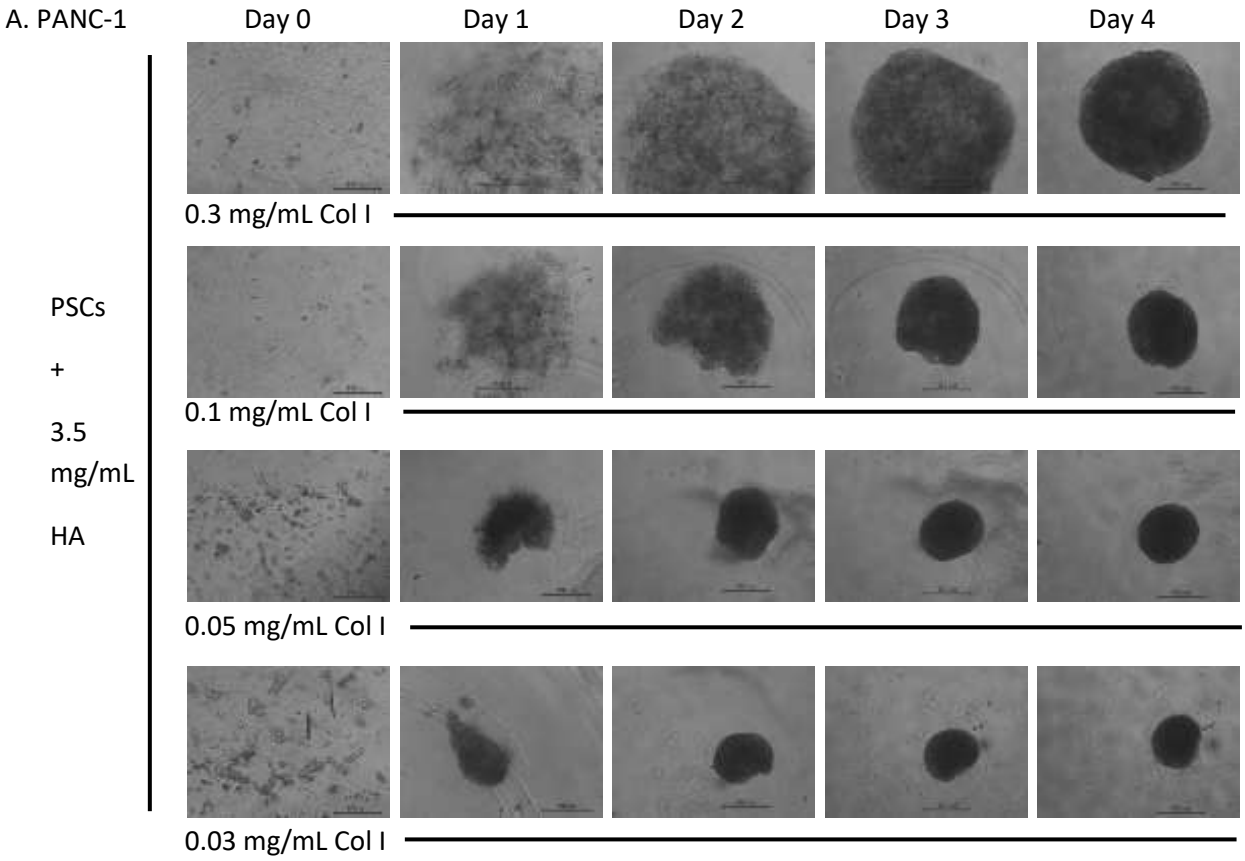

B.

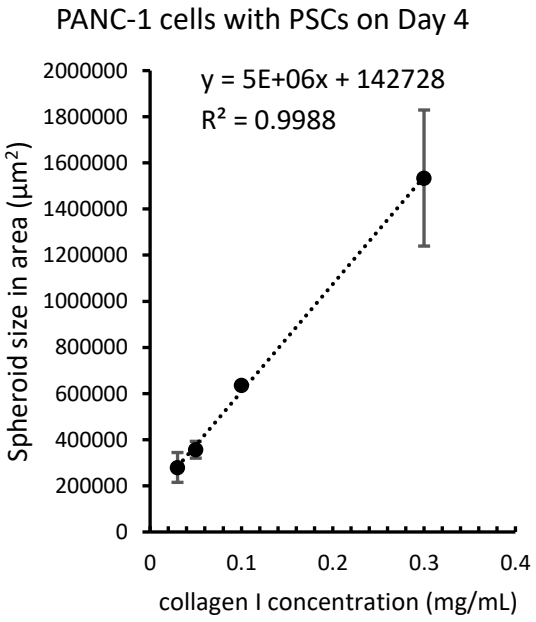

Figure 92. Correlation of spheroid size with collagen I content in 3D co-cultures of PANC-1 cells, pancreatic stellate cells, collagen I and hyaluronic acid.

500 PANC-1 cells and 1,000 pancreatic stellate cells (PSCs) were mixed in 50 µL of 0.03 mg/mL, 0.05 mg/mL, 0.1 mg/mL and 0.3 mg/mL collagen I with 3.5 mg/mL hyaluronic acid as indicated. A. Images were acquired by Leica DMI4000 B (50x magnification) manually and daily for 4 days. Data shown were representative images from two independent experiments with three spheroids in each experiment. Scale bar, 500 µm. B. Spheroid sizes on day 4 were measured using CellProfiler. The areas (μm^2) of spheroids cultured in different concentrations of collagen I on day 4 were graphed. Error bars represented standard deviations from three spheroids from one independent experiment. The R^2 used to measure linearity of was calculated by Excel.

5.5.2 FAP and p53 expression in 3D co-culture models in collagen I and hyaluronic acid

Previously in section 3.2.3 and section 5.4.2, αSMA was demonstrated not to be a specific marker for stellate cells because Capan-2 and PANC-1 were also positively stained by anti-αSMA antibodies. Fibroblast activation protein (FAP) has also been regarded as a marker for CAFs in PDAC [Brennen *et al*, 2012; Lo *et al*, 2017], thus being selected for testing to determine if it could be specifically expressed in stellate cells but not in Capan-2 and PANC-1 cells.

As seen in Figure 93-95, FAP was detected in hepatic stellate cells, pancreatic stellate cells and cancer cells, although the stellate cells could be distinguished by their stretched cytoplasm. The staining pattern of DAPI, FAP and p53 was similar to the one of DAPI, αSMA and p53 in section 5.4.2. There was no marked difference in stellate cell distribution between all the experiment groups. Higher level of p53 expression was seen near the edge of the spheroids than the core of the spheroids.

Currently it is unknown whether growing Capan-2 and PANC-1 cells in 2D, either with or without stellate cells could affect FAP expression. Further explorations are required to test the expression of FAP in 2D and 3D culture.

Figure 93. FAP and p53 expression in the 3D co-culture models with 0.1 mg/mL collagen I and hyaluronic acid.

500 cancer cells and 1,000 hepatic stellate cells (HSCs) or pancreatic stellate cells (PSCs) were mixed in 50 µL of 0.1 mg/mL collagen I with 3.5 mg/mL hyaluronic acid, grown for 4 days and then stained with DAPI (blue), and for FAP (red) and p53 (green). Images were acquired by CLSM using Zeiss LSM880 with 10x or 20x objective lens and image analysis was done in Zen 2.3 (blue edition). Scale bar, 100 µm.

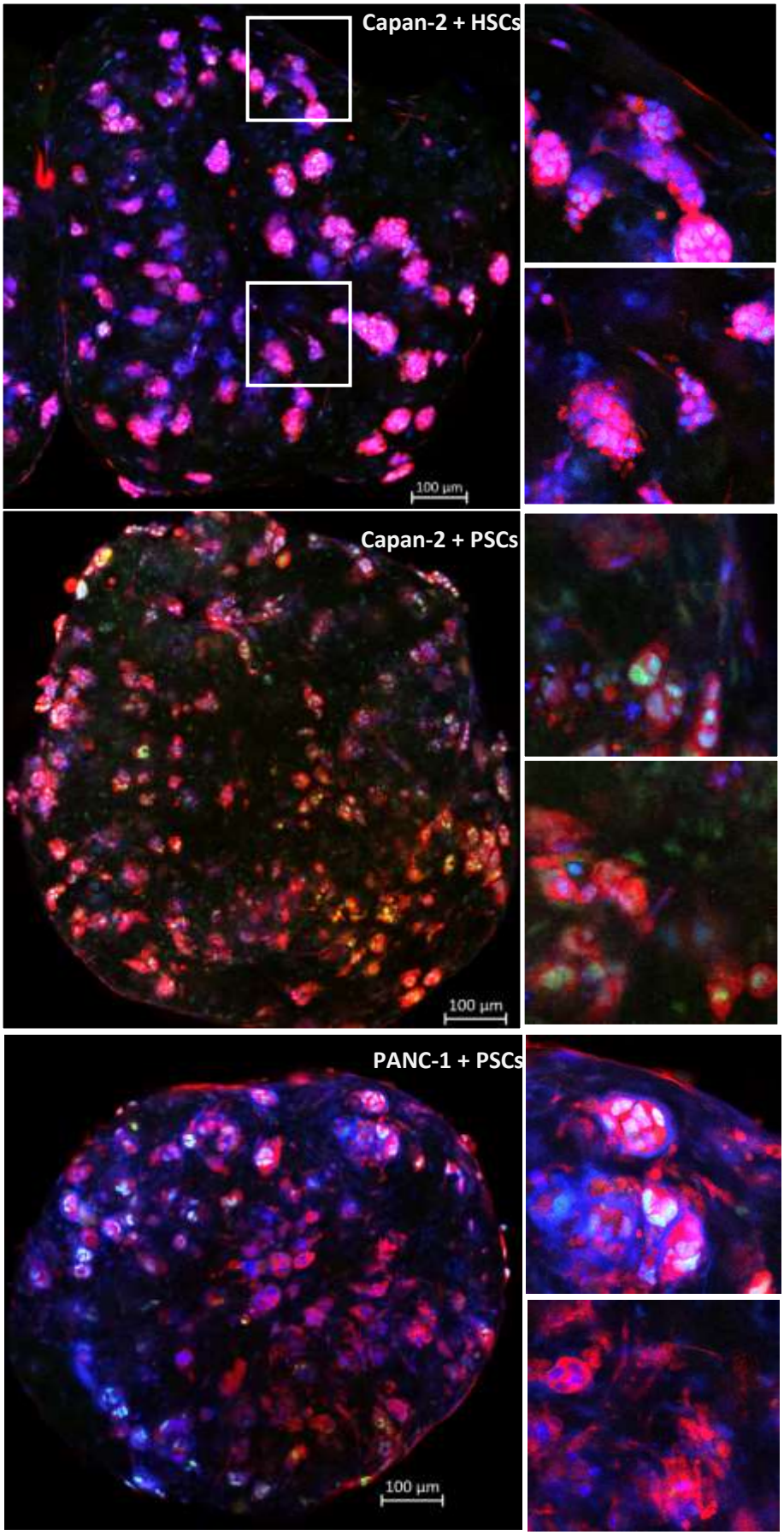

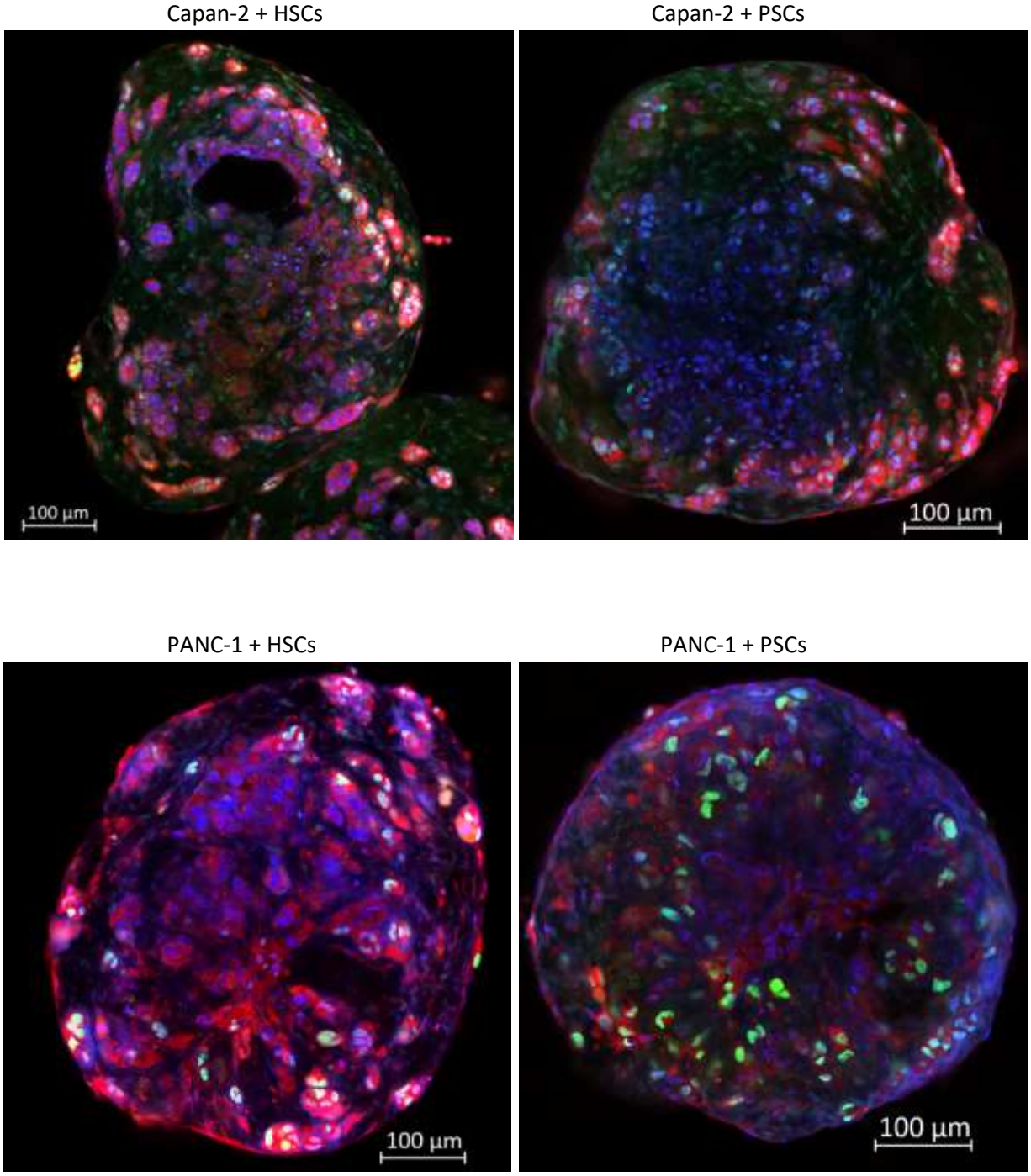

Figure 94. FAP and p53 expression in the 3D co-culture models with 0.05 mg/mL collagen I and hyaluronic acid.

500 cancer cells and 1,000 hepatic stellate cells (HSCs) or pancreatic stellate cells (PSCs) were mixed in 50 µL of 0.05 mg/mL collagen I with 3.5 mg/mL hyaluronic acid, grown for 4 days and then stained with DAPI (blue), and for FAP (red) and p53 (green). Images were acquired by CLSM using Zeiss LSM880 with 10x or 20x objective lens and image analysis was done in Zen 2.3 (blue edition). Scale bar, 100 µm.

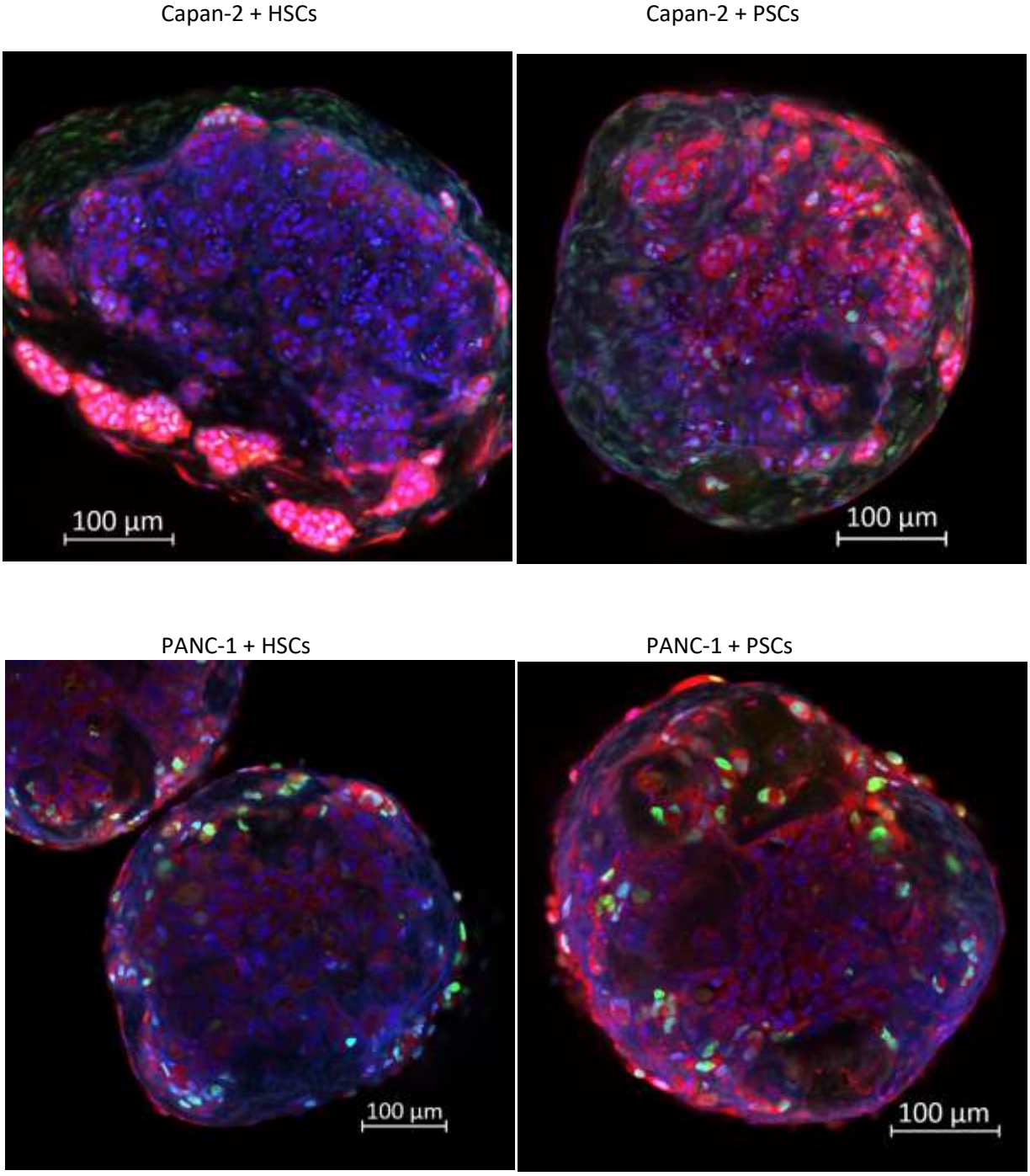

Figure 95. FAP and p53 expression in the 3D co-culture models with 0.03 mg/mL collagen I and hyaluronic acid.

500 cancer cells and 1,000 hepatic stellate cells (HSCs) or pancreatic stellate cells (PSCs) were mixed in 50 µL of 0.03 mg/mL collagen I with 3.5 mg/mL hyaluronic acid, grown for 4 days and then stained with DAPI (blue), and for FAP (red) and p53 (green). Images were acquired by CLSM using Zeiss LSM880 with 10x or 20x objective lens and image analysis was done in Zen 2.3 (blue edition). Scale bar, 100 µm.

5.5.3 Effects of different amounts of collagen I with or without hyaluronic acid on YAP subcellular localisation

Next we also explored various factors such as hyaluronic acid (HA) and different types of stellate cells on YAP expression and localisation by multi-coloured imaging with confocal microscopy. As shown in Figure 96-97, co-localisation of YAP and p53 could be detected near the edge of the spheroids with different concentration of collagen I (COL I), indicating nuclear localisation of YAP. In particular, co-localisation of YAP and p53 was more commonly seen in 3D co-culture spheroids with Capan-2 cells and 0.1 mg/mL COL I than the ones with Capan-2 cells and 0.03-0.05 mg/mL COL I, or the ones with PANC-1 cells. The core of spheroids with 0.03 or 0.05 mg/mL COL I presented with cytoplasmic accumulation of YAP, indicating the translocation of YAP out of the nucleus.

As demonstrated in Figure 98 and 99, semi-quantification of YAP by CellProfiler was conducted on one optical section of the 3D co-culture spheroids with Capan-2 cells with pancreatic stellate cells (PSCs) and hepatic stellate cells (HSCs). Because the data representing YAP intensities and ratios did not follow normal distribution and not have the same shape of distribution, mean ranks of the datasets were compared using a non-parametric Mann-Whitney U test.

Comparing all the total YAP intensities in the whole cancer cell of each individual cell near the edge and the cores, there was no significant difference between the cancer cells near the core of the spheroids and the edge in the spheroids in HA and 0.1 mg/mL COL I (mean rank of 82.94 for Capan-2 cells near the core and 79.99 for Capan-2 cells near the edge of the spheroids co-cultured with HSCs, $p = 0.689$; mean rank of 105.60 for Capan-2 cells near the core and 112.39 for Capan-2 cells near the edge of the spheroids co-cultured with PSCs, $p = 0.449$), regardless of the cell type of stellate cells. However, significantly reduction of total YAP intensities was found in the cancer cells near the core of the spheroid compared with the ones near the edge of the spheroids co-cultured with 0.1 mg/mL COL I only (mean rank of 61.73 for Capan-2 cells near the core and 84.86 for Capan-2 cells near the edge, $p = 0.002$), suggesting the possible role of HA to induce YAP expression in Capan-2 cells in the current 3D co-culture models.

We hypothesized that the differential expression of YAP in the cells near the core and the edge of the spheroids would correlate with the concentration of COL I. When the concentration of COL I was reduced to 0.05 mg/mL COL I, there was no significant difference between the cancer cells near the core of the spheroids and the edge in the spheroids co-cultured with HA and 0.05 mg/mL COL I (mean rank of 73.70 for Capan-2 cells near the core and 82.77 for Capan-2 cells near the edge of the spheroids co-cultured with HSCs, $p = 0.231$). However, cancer cells near the core exhibited significantly lower YAP expression than the ones near the edge of the spheroids co-cultured with HA and 0.03 mg/mL COL I (mean rank of 39.77 for Capan-2 cells near the core and 86.32 for Capan-2 cells near the edge, $p < 0.001$), indicating the amount of COL I in the spheroids could affect YAP signalling.

Next, we also test the hypothesis that HA and the concentration of COL I could affect the subcellular localisation of YAP. Both the ratios of nuclear YAP intensity to total YAP intensity of the whole cell near the edge of the spheroids were significantly higher than the ones of cytoplasmic YAP intensity, regardless whether the spheroids were cultured with HA or without HA ($p < 0.001$).

There was no significant difference in the ratios of nuclear YAP intensity to total YAP intensity of the whole cell and the ratios of cytoplasmic YAP intensity to total YAP intensity of the whole cell near the

core of the spheroid co-cultured with PSCs without HA (p = 0.16) whereas the ratios of nuclear YAP intensity to total YAP intensity of the whole cell decreased significantly compared to the ratios of cytoplasmic YAP intensity to total YAP intensity of the whole cell near the core of the spheroid co-cultured with PSCs in presence of HA (p < 0.001). Nevertheless, there was a significant increase in the ratios of nuclear YAP intensity to total YAP intensity of the whole cell compared to the ratios of cytoplasmic YAP intensity to total YAP intensity of the whole cell in Capan-2 cells near the core of the spheroids cultured with HSCs in presence of HA (p = 0.005). Meanwhile, there was no significant difference in the ratios of nuclear YAP intensity to total YAP intensity of the whole cell and the ratios of cytoplasmic YAP intensity to total YAP intensity of the whole cell near the edge of the spheroid co-cultured with HSCs and HA (p = 0.217). It may be possible that different cell type of stellate cells can affect the overall outcomes of interaction between stellate cells and cancer cells on YAP signalling.

Opposing to the data in 0.1 mg/mL COL I in the presence of HSCs and HA, there was a significant decrease in the ratios of nuclear YAP intensity to total YAP intensity of the whole cell compared to the ratios of cytoplasmic YAP intensity to total YAP intensity of the whole cell in Capan-2 cells near the core of the spheroids cultured with 0.03 mg/mL and 0.05 mg/mL COL I in the presence of HSCs and HA (p < 0.001), indicating higher amount of COL I can induce YAP nuclear translocation near the core of the spheroids.

Compared to the data in Figure 47 where a 3D mono-culture spheroid of Capan-2 was measured, the overall level of cytoplasmic YAP dropped while the level of nuclear YAP increased, suggesting a shift in the subcellular localisation of YAP in the current models. Consistent with the data in Figure 59 when Capan-2 cells were cultured with HA, inclusion of ECM in the 3D co-culture models can cause increased nuclear localisation of YAP.

To summarize, spheroids grown in 0.1 mg/mL COL I exhibited a greater fraction of cancer cells with nuclear YAP localisation than spheroids grown in 0.05 mg/mL and 0.03 mg/mL COL I. More nuclear accumulation of YAP could be found in the core of spheroids cultured in 0.1 mg/mL COL I. The addition of 3.5 mg/mL HA induced YAP expression in the core of spheroids co-cultured with PSCs. However, more independent experiments are needed to validate this observation. Cytoplasmic YAP could also be detected in those cells with nuclear YAP expression, suggesting accumulation of both nuclear and cytoplasmic YAP, consistent with the dynamic YAP signalling in section 5.4. Cells with cytoplasmic accumulation of YAP were more often detected near the core of the spheroids than near the edge of the spheroids grown in 0.05 and 0.03 mg/mL COL I.

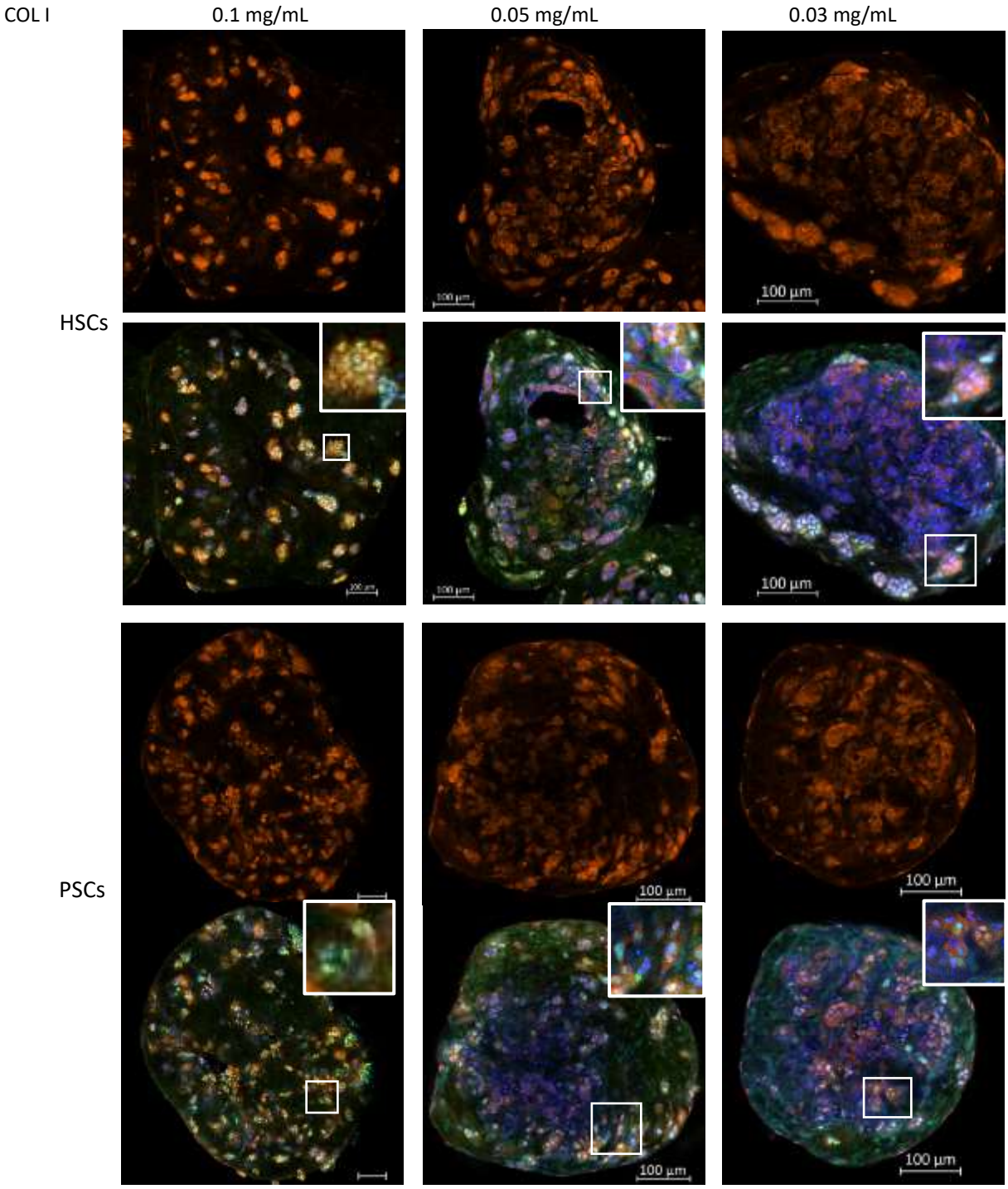

Figure 96. YAP expression and subcellular localisation in intact spheroids co-cultured with Capan-2 cells and stellate cells.

Spheroids prepared from 500 Capan-2 cells and 1,000 hepatic stellate cells (HSCs) or pancreatic stellate cells (PSCs) in 50 µL of 0.1 mg/mL, 0.05 mg/mL, 0.03 mg/mL of collagen I (COL I) and 3.5 mg/mL hyaluronic acid were grown for 4 days, fixed with PFA and then stained with DAPI (blue) and for p53 (green) and YAP (orange). Images were acquired by CLSM using Zeiss LSM880 and image analysis was done in Zen 2.3 (blue edition). Representative images from two spheroids in one independent experiment were shown. Scale bar, 100 µm.

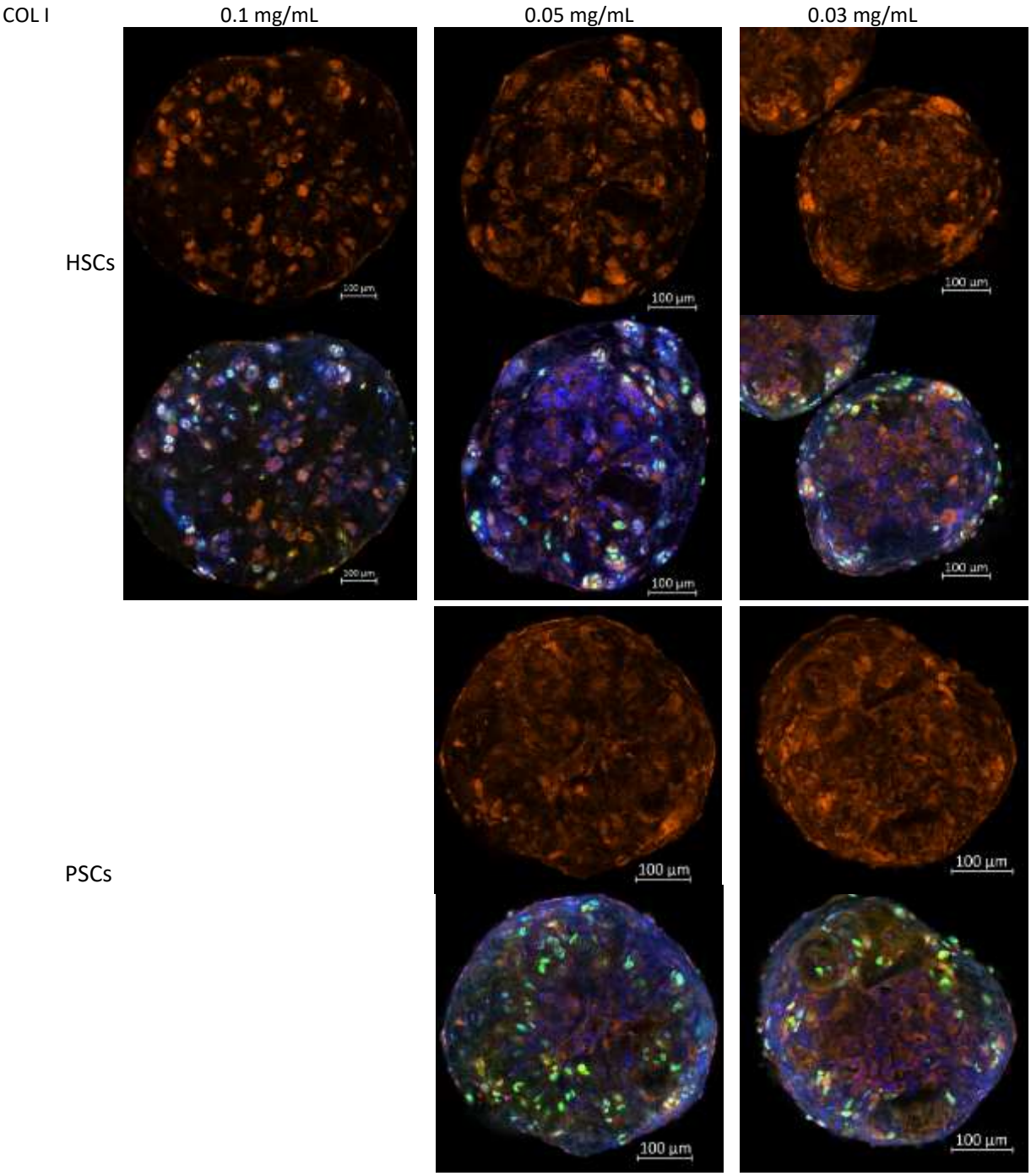

Figure 97. YAP expression and subcellular localisation in intact spheroids co-cultured with PANC1 cells and stellate cells.

Spheroids prepared from 500 PANC-1 cells and 1,000 hepatic stellate cells (HSCs) or pancreatic stellate cells (PSCs) in 50 µL of 0.1 mg/mL, 0.05 mg/mL, 0.03 mg/mL of collagen I (COL I) and 3.5 mg/mL hyaluronic acid were grown for 4 days, fixed with PFA and then stained with DAPI (blue) and for p53 (green) and YAP (orange). Images were acquired by CLSM using Zeiss LSM880 and image analysis was done in Zen 2.3 (blue edition). Representative images from two spheroids in one independent experiment were shown. Scale bar, 100 µm.

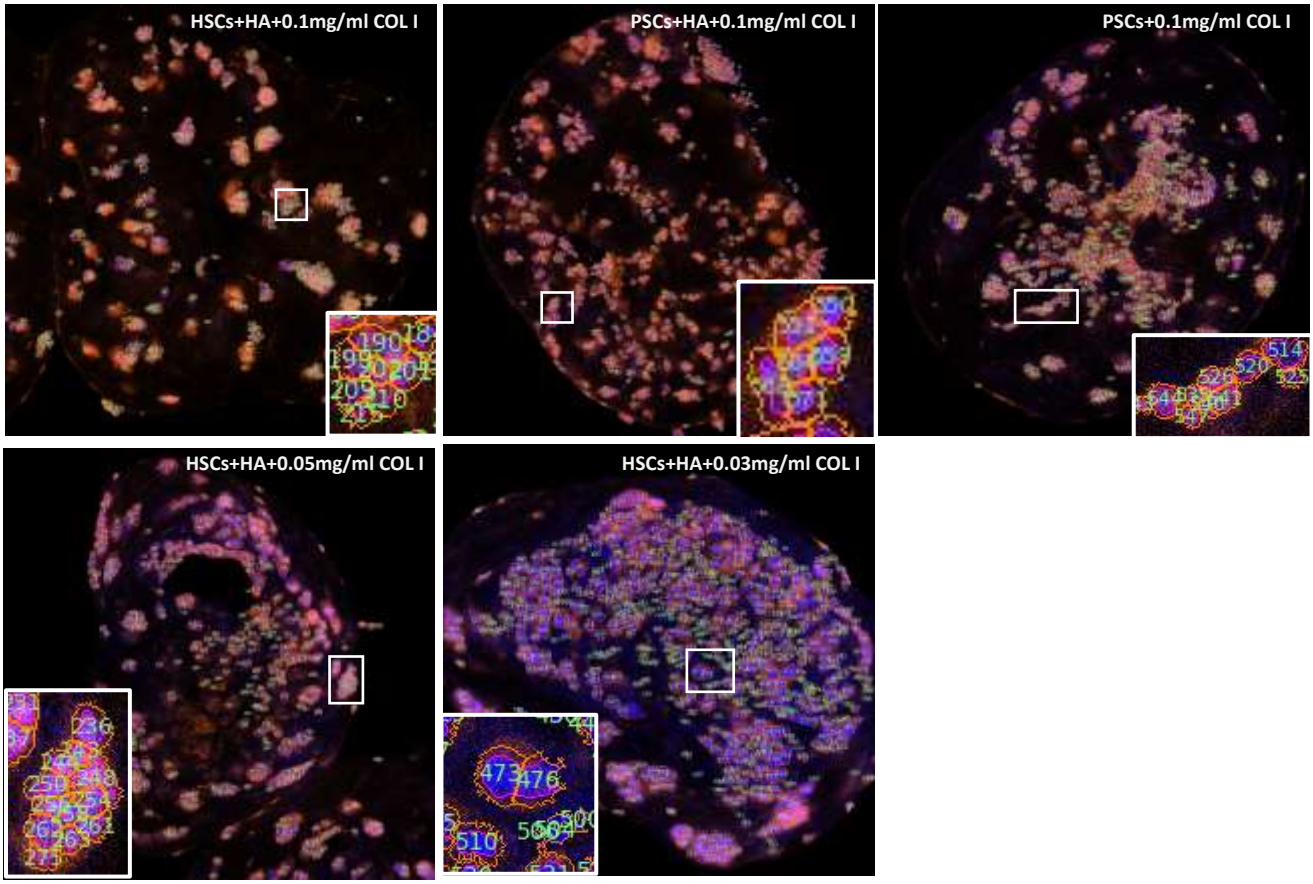

Figure 98. Identification of YAP localisation in image processing by CellProfiler.

Spheroids prepared from 500 Capan-2 cells and 1,000 hepatic stellate cells (HSCs) or pancreatic stellate cells (PSCs) in 50 µL of 0.1 mg/mL, 0.05 mg/mL, 0.03 mg/mL of collagen I (COL I) with or without 3.5 mg/mL hyaluronic acid as indicated were grown for 4 days, fixed with PFA and then stained with DAPI (blue) and for p53 (green) and YAP (orange). Images were acquired by CLSM using Zeiss LSM880 and image analysis was done in Zen 2.3 (blue edition). Representative images from two spheroids in one independent experiment were shown. Representative images processed by CellProfiler was shown, depicting the outlined nuclear areas and the cytoplasmic areas labelled with numbers.

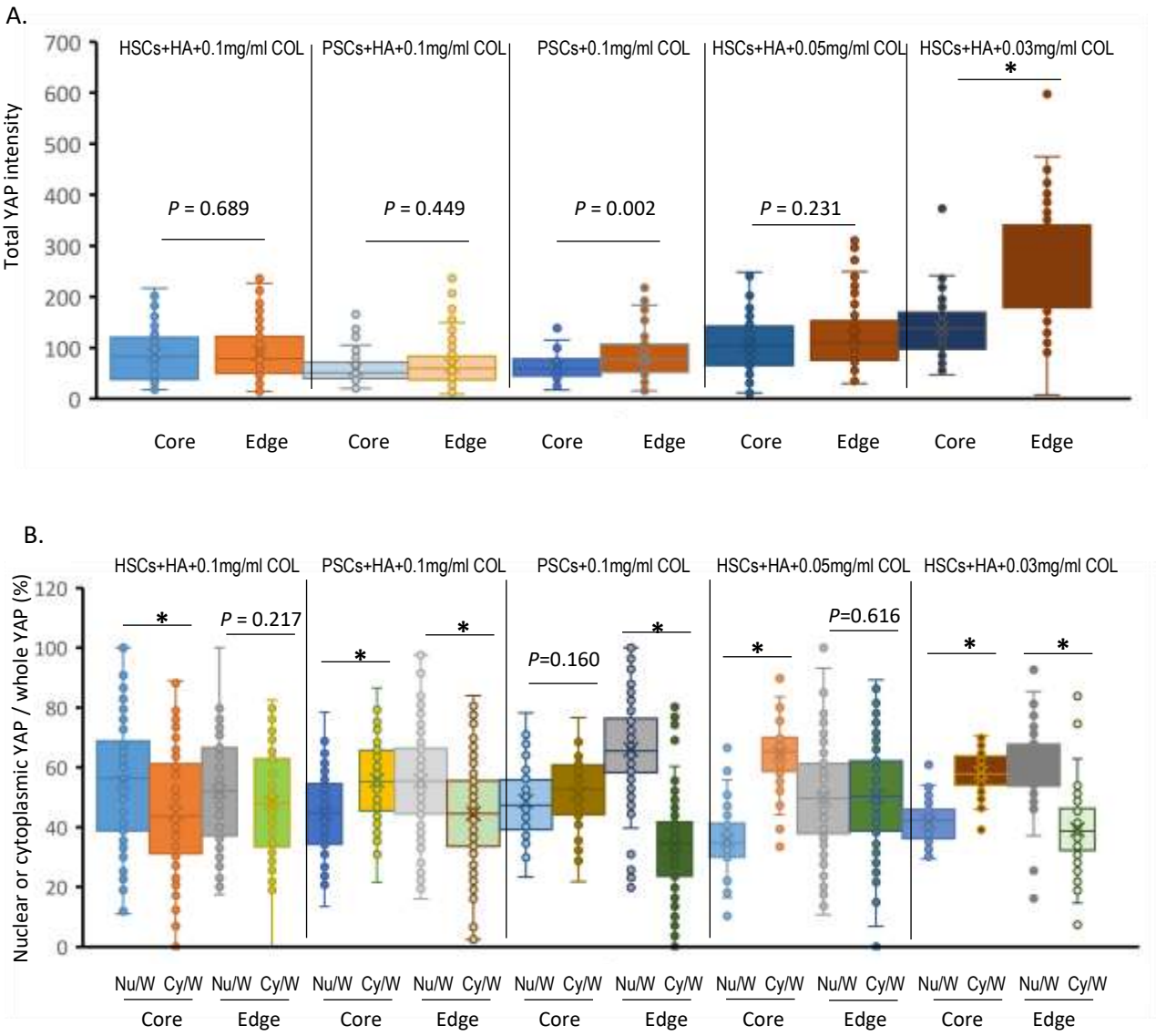

Figure 99. Semi-quantification of YAP subcellular expression near the edge and the core of 3D co-culture spheroids.

Spheroids prepared from 500 Capan-2 cells and 1,000 hepatic stellate cells (HSCs) or pancreatic stellate cells (PSCs) in 50 µL of 0.1 mg/mL, 0.05 mg/mL, 0.03 mg/mL of collagen I and 3.5 mg/mL HA were grown for 4 days and then stained with DAPI (blue) and for YAP (orange). Images were acquired by CLSM using Zeiss LSM880 and image analysis was done in Zen 2.3 (blue edition). Representative images from 2 spheroids in one independent experiment were shown. Intensities of YAP in single cell on one optical slide were generated by CellProfiler. Whisker box graph was made from all the values of total YAP intensity in the whole cells (A) or the intensity ratios of nuclear YAP intensity to total YAP intensity in the whole cell or cytoplasmic YAP intensity to total YAP intensity in the whole cell (B) from around 50-150 cells near the core of the spheroid and the edge of the spheroid, using Excel. Mean markers were shown. Median was exclusive from quartile calculation. Dots indicated the values in cells automatically generated by Excel. Non-parametric Mann-Whitney U test was used to calculate the *p* values, using SPSS. *: $p < 0.05$. Nu: nucleus, Cy: cytoplasm, W: whole cell.

5.6 Discussion

There are three major strengths and merits of this chapter. Firstly, imaging methods combining optical clearing with ethanol and BABB, Z-stack and Airyscan using the Zeiss LSM880 with a 10x objective lens are validated to be robust for future phenotypic analysis in thick cancer models with approximately 500 µm diameter without disturbing the samples, leading to higher efficiency comparing with the traditional histology methods such as tissue processing using paraffin. This is the vital step to characterize the 3D co-culture models in order to get a clear and defined cell distribution in larger volume and more cell layers than single-layered 2D culture. Secondly, compared with commonly used of PDAC models using 1-2 mg/mL collagen I concentration [Coleman *et al*, 2014a; Froeling *et al*, 2009; Kadaba *et al*, 2013], our study provides evidence of building PDAC models with reduced concentration of collagen I. YAP nuclear translocation could be seen in the 3D co-culture models with 0.1 mg/mL collagen I, a phenomenon relevant to the PDAC microenvironment in patients. Thirdly, compounds PsA-D and Tylophorinine derived from natural products are able to reduce p53, Ki67 and YAP expression in the 3D co-culture models with HSCs and PSCs, indicating the potentials of the two compounds to inhibit pancreatic cancer growth in the pancreas and the liver.

Initially, we attempted to develop a 3D co-culture model with PDAC cells and stellate cells without animal-derived materials to reduce the cost and the variability of PDAC models. However, the approach with PDAC spheroids in stellate cells suspension with pure HA was not able to form a single spheroid. One possible reason could be that the distances between stellate cells are too large for them to migrate towards the centre of the well. Also, stellate cells might need a scaffold to form a single spheroid in the well. As collagen I was added in the model, a single spheroid was formed within 24 hour. The main reason for the failure of dropping the spheroid into HA with collagen I to form a models with multilayers of stellate cells surrounding the cancer cells core was probably because cancer cells did not communicate with stellate cells sufficiently through chemoattractant and stellate cells were prone to attach to the same cell type in 3D conditions.

When we analysed the protein expression in the 3D co-culture models, we have the following questions in mind: why is p53 expression reduced at the core of the spheroids/at high cell density? Does p53 reduction happen before or after cytoplasmic retention of YAP?

As seen in chapter 3 when studying 3D mono-culture models of PDAC cells without ECM, p53 expression was high but YAP still mainly retained in the cytoplasm of the majorities of cancer cells. However, reduction of p53 expression correlates with YAP cytoplasmic localisation in the 3D co-culture models of PDAC in this chapter. Unfortunately, 3D mono-culture of PDAC cells with ECM failed to form spheroids within the same period of time as the 3D co-culture models. Even when we attempted to perform the immunofluorescence on the fractions of 3D mono-culture of PDAC cells with collagen I collected from the wells, they disappeared during the process and thus this experiments were stopped. Based on the data from other research groups and the data from section 4.2 where HA was shown to induce YAP nuclear translocation, the role of ECM has been considered mainly to facilitate YAP entering the nucleus [Miroshnikova *et al*, 2017; Rice *et al*, 2017]. Wild-type p53 is a tumour suppressor as a pro-apoptotic inducer whereas mutant p53 has anti-apoptotic and tumour-promoting function, contributing to cancer progression [Muller *et al*, 2014; Ozaki *et al*, 2011]. The YAP localisation pattern was the same in Capan-2 cells that express a wild-type p53 and in PANC-1 cells that express a mutant p53 [Deer *et al*, 2010]. In the case of mutant p53, this protein could bind to YAP and promote its nuclear

accumulation, as suggested by Ferraiuolo *et al* [Ferraiuolo *et al*, 2017]. However, some PANC-1 cells presented with mutant p53 expression and cytoplasmic YAP expression, indicating other mechanisms may need to be explored to link p53 signalling with YAP signalling in these 3D co-culture spheroids. In the beginning, we were convinced by the reported data on the existence of wild-type p53 in Capan-2 cell lines [Deer *et al*, 2010] and confused by our data indicating the possible binding of wild-type p53 with YAP which is inconsistent with the proposed crosstalk between p53 signalling and YAP signalling [Ferraiuolo *et al*, 2017]. Thus, more efforts were used to investigate the p53 status in Capan-2 cell lines. A review was found and more papers were read carefully. As reviewed by Berglind *et al*., three different p53 statuses in Capan-2 cell line have been reported: wild-type, mutated at p.R273H or p53 gene deletion [Berglind *et al*, 2008]. In 1992, sequence analysis of exons 5-8 of the *p53* gene in Capan-2 cells revealed point mutation at Arg273His [Ruggeri *et al*, 1992]. In 1994, Japanese researchers reported that Capan-2 cells showed a 200-bp deletion of the 3' side of exon 4 and a frame shift using PCR, a G-T base pair substitution at the third nucleotide of codon 125 using direct sequencing and were weakly positive for p53 using anti-p53 antibody (DO7) that recognized both wild-type and mutant p53 in immunocytochemistry [Suwa *et al*, 1994], concluding that Capan-2 cells expressed mutant p53. However, in the same year, mutant p53 protein was reported to be undetectable in Capan-2 cells by immunocytochemistry and immunoblotting using both anti-p53 antibodies (pAB421) that bind to wild-type and mutant p53 and anti-p53 antibodies (pAB240) that bind to mutant p53 while mutant *p53* gene was also not detected using PCR for amplification of exons 5-9 of the *p53* gene by German researchers [Simon *et al*, 1994], leading to the opposite conclusion as the one in 1992 and drawn by the Japanese research group. Two research groups reported mutant *p53* in exon 4 while one group could not detect the amplification of exons 5-9 of the *p53* gene. We wonder if using the same PCR protocol would have produced the same result. In the same group, mutant *p53* gene was detected but weak staining of mutant p53 protein was found. We wonder if using another antibodies against mutant p53 would have detected p53 expression. Since our data indicated possible binding of p53 to YAP in Capan-2 cells, we postulated that the Capan-2 cell lines in our lab express mutant p53, which needs further verification using other antibodies specific for mutant p53. Therefore, reduction of mutant p53 in Capan-2 cells and PANC-1 cells could cause the disassociation of YAP with mutant p53, leading to the lack of binding partner of YAP in the nucleus that could retain nuclear localisation of YAP.

Alternatively, hypoxia and depletion of nutrients such as glucose occurring at the core of the spheroids may cause the imbalance of mechanisms to promote YAP nuclear accumulation and the ones to promote YAP cytoplasmic accumulation, independent of p53 signalling. Immunoprecipitation to study the binding of p53 to endogenous YAP is necessary to elucidate the interaction of YAP signalling and P53 signalling. More specific antibodies against wild-type p53 and mutant p53 or other gene sequencing methods were helpful to distinguish the isoforms of p53 in the current co-culture models.

Factors that affect YAP localisation include:

- The stellate cells can be in close contact with a portion of cancer cells, as seen in section 5.3 where stellate cells attached to certain regions of the edge of cancer spheroids. However, some stellate cells are not in a close cell-cell contact with cancer cells, as noted in section 5.4 and 5.5, so the influence of stellate cells on YAP signalling based on the cell-cell contact which associated with nuclear exclusion of YAP [Gumbiner *et al*, 2014] may be minimal.
- Spheroid volume increased in relation to higher amounts of collagen I which associated with nuclear accumulation of YAP [Rice *et al*, 2017].

- The distance of cancer cells to the spheroid surface determine the oxygen level and nutrient level which related to cytoplasmic retention of YAP [Mo *et al*, 2015; Wang *et al*, 2015].
- Higher amounts of collagen may affect the density and the tension sensed by cancer cells which could change from the edge to the core [Aragona *et al*, 2013; Butcher *et al*, 2009; Dupont *et al*, 2011].
- High cancer cell-cell contact at the core could lead to nuclear exclusion of YAP [Gumbiner *et al*, 2014].

Quantification of YAP expression and the location of cancer cells in the spheroids will need to be delineated in order to get a better understanding of how different factors affecting YAP signalling in the current 3D co-culture PDAC models, which will contribute to untangling the similar complex networks also expected for cancer cells to encounter in PDAC.

The strengths and limitations of the 2:1 ratio of stellate cells to cancer cells is that the cancer model closely resembled the pathophysiological barriers as ECM organization, where a few stellate cells scattered, wrapping around cancer cell clusters; however, the insufficient number of stellate cells shown in the Figure 79, 80, and 93-85 comparing to clinical biopsies reported [Coleman *et al*, 2014b; Erkan *et al*, 2007; Gopinathan *et al*, 2015; Hwang *et al*, 2016; Logsdon *et al*, 2015; Whatcott *et al*, 2015; Yen *et al*, 2002] made the models less ideal to recapitulate the intense interaction between stellate cells and cancer cells found in patients with late-stage PDAC. Nevertheless, based on the data presented in this chapter, future work could easily be built on choosing the highe ratio of stellate cells to cancer cells such as 5:1 or 10:1 to carry on refining the 3D co-culture models.

Another major drawback of the models described in this chapter is the lack of immune cells that are abundant in the PDAC tumour environment. At present, it is unclear which receptors and cytokines that might be provided by immune cells are needed to recapitulate the complex networks affecting YAP signalling in PDAC tumours.

Chapter 6. Conclusion and future direction

6.1 Conclusion

In the current studies, direct mixture of cancer cells and stellate cells co-cultured in a scaffold-free environment recreates a model with cancer cells wrapping around a sphere of stellate-cells. Thus, this format fails to establish a model emulating the organization observed in PDAC tumours where clusters of cancer cells are surrounded by and intermingle with multiple layers of stellate cells. Higher level of endogenous YAP is found in the cytoplasm than in the nucleus of the majority of cancer cells in the direct mixture of cancer cells and stellate cells co-cultured in a scaffold-free environment, indicating that a small amount of YAP might be sufficient to drive pancreatic cancer growth.

Collagen I, collagen IV, fibronectin and laminin can be detected in Myogel. Myogel may be biocompatible with certain subtypes of pancreatic cancer cells. Unmodified hyaluronic acid (HA) derived from *Streptococcus equi* is biocompatible with pancreatic cancer cells and promotes nuclear accumulation of YAP.

Dropping of PDAC mono-culture spheroids into a stellate cells suspension in HA or HA with collagen I is able to establish a 3D co-culture model where only fractions of the cancer cells have contacted with stellate cells without the multi-layered stellate cells barrier around the cancer cells core.

Mixing PDAC cells and stellate cells in a collagen I matrix with or without HA can result in the formation of multiple cancer cells cores inside the 3D co-culture models that resemble the fibrotic cancer microenvironment in patients with advanced and metastatic PDAC. Dynamic YAP subcellular localisation is found in these 3D co-culture models of PDAC cells and stellate cells. Reduction of p53 expression correlates with YAP cytoplasmic localisation in these 3D co-culture models of PDAC cells and stellate cells. Potential anti-cancer compounds Pseudopterosin A-D and Tylophorinine, derived from natural products, can reduce p53, Ki67 and YAP expression in these 3D co-culture models of PDAC cells and stellate cells.

Imaging methods combining optical clearing with ethanol and BABB, Z-stack and Airyscan using the Zeiss LSM880 with a 10x objective lens are validated to be robust for future phenotypic analysis in thick cancer models with approximately 500 µm diameter without disturbing the samples, leading to higher efficiency comparing with the traditional histology methods such as tissue processing using paraffin.

6.2 Future direction for developing biomaterials from porcine species for modelling pancreatic cancer

Porcine species has been regarded to share a number of similarities such as physiology and metabolic profile with humans [Gutierrez *et al*, 2015], thereby positioning themselves as better models than rodents in some research areas. Recently, pancreata from mice [Goh *et al*, 2013], rats [Yu *et al*, 2018] and pigs [Elebring *et al*, 2017; Mirmalek-Sani *et al*, 2013] have been attempted be developed into a novel extracellular matrix scaffold for pancreas bioengineering. For modelling pancreatic cancer

microenvironment, one of the research themes is finding a cost-effective way to recapitulate an environment for tumour cells and stromal cells grown *in vitro* to preserve their phenotypes and genotypes as close as the ones in patients with PDAC [Baker *et al*, 2016]. Conventional biomaterials such as rat tail collagen I and Matrigel® derived from rodents have been a standard of components in building 3D culture models using cancer cell lines and organoids from patients. It is still debatable to what degree that the rodents-derived materials could affect the biological properties of cancer cells. Meanwhile, experts in the research field have also raised the question of whether the cost of modelling PDAC could be reduced by novel biomaterials [Baker *et al*, 2016]. The main reason to choose rat tail collagen I and Matrigel® derived from rodents is that they contain the major components in ECM that are abundant in PDAC microenvironment. If a biomaterial could facilitate the cancer models achieve the similar levels of ECM in PDAC, initial attempts could be made to test its feasibility for modelling pancreatic cancer.

For the purpose of reducing animal use for addressing public sensitivities and moral obligations [Brown *et al*, 2018], porcine pancreas will be better than the ones from mice and rats due to the difference in weight. The mean weight of the whole porcine pancreas was 347±103 g, with a range from 190 to 698 g per pig [Ferrer *et al*, 2008]. The wet weight of pancreas in 3, 12 and 18 months old rats was reported to be 0.8-1 g per rat [Jiang *et al*, 2013]. The total weight of the dry pancreas in 11-week-old and 12-month-old male and female rats was reported to be around 0.3 – 0.5 g per rat [Reaven *et al*, 1987]. Among rodent species and porcine species, the size of mice is the smallest, making the weight of the pancreas less than the one in rats. Complying with the same principle, the amount of porcine skeletal muscle (PSM) per pig is higher than that of pancreas. Besides, collagens content of the muscle extract is reported to be higher than the one in pancreas. The collagens content was 486.7 ± 133 μg per mg of the skeletal muscle extract [Abberton *et al*, 2008]. The collagens content in porcine pancreas was reported to be 0.029 μg per mg [Mirmalek-Sani *et al*, 2013] and 40 μg collagens per mg wet tissue was detected by another research group [Elebring *et al*, 2017]. Those three research groups all used Sirius Red dye to measure the collagens content. Beside, fibronectin and laminins are also found in extract from skeletal muscle [Abberton *et al*, 2008; Wolf *et al*, 2012]. Although the high ECM content was not found in the current study, the lack of purification and the detection methods could affect the reproducibility. Also, the strain of pigs may also be important to keep a record of in term of the ECM content. Therefore, further exploration to refine the protocols for extracting ECM from PSM in the future is needed.

Indeed, maintaining the biological properties of cancer cells should be the priority in choosing the right biomaterial so that effective treatments could be developed using the novel *in vitro* cancer models [Baker *et al*, 2016]. More studies will need to be undertaken to compare genotypes and phenotypes of tumour cells and stromal cells grown in the extract from porcine muscle and porcine pancreas with the ones in patients. If no significant difference of genotypes and phenotypes of tumour cells and stromal cells could be found when they culture in the extract from porcine muscle and porcine pancreas, together with accuracy in matching clinical samples, then the porcine muscle would worth being developed further for wider use.

6.3 Future direction for refinement of the current 3D co-culture models

In order to develop an *in vitro* biological model mimicking PDAC in patients, it is imperative to delineate the components as the building blocks with the accurate ratios and distribution. It is well-known that around 10% of cells within PDAC microenvironment are pancreatic cancer cells [Neesse *et al*, 2011]. Compared to primary tumours in the pancreas site, more cancer cells are detected at metastatic site in the liver of patients with PDAC [Whatcott *et al*, 2015]; however, the exact percentage of cancer cell regions in the liver has not yet been confirmed in large cohort of patients with metastatic PDAC. The animal models of human PDAC have not been able to recreate the highly fibrotic microenvironment [Logsdon *et al*, 2015]. The 3D co-culture models with human cancer cell lines, patient-derived stellate cells and ECM possess the potential to be manipulated *in vitro* to create a more realistic model with cell ratios and distribution resembling the situation in patients with PDAC than the animal models. Although the current 3D co-culture models of stellate cells to cancer cells at a 2:1 cell ratio have recreated a microenvironment where cancer cells located near the core of the models, surrounded by collagen I and stellate cells, there are a few improvements could be made.

Firstly, the area of stellate cells within the models shown in Figure 79, 80, and 93-95 was not the same as the one detected by histology and immunochemistry [Coleman *et al*, 2014b; Erkan *et al*, 2007; Gopinathan *et al*, 2015; Hwang *et al*, 2016; Logsdon *et al*, 2015; Whatcott *et al*, 2015; Yen *et al*, 2002], making them less ideal to recapitulate the intense interaction between cancer cells and stellate cells. The areas of stellate cells within the models of stellate cells to cancer cells at a 10:1 cell ratio illustrated in Figure 68 represented a closer situation to the ones in patients compared to the models with a 2:1 cell ratio of stellate cells to cancer cells. Although the 2:1 ratio of stellate cells to cancer cells were used commonly [Coleman *et al*, 2014b; Fujiwara *et al*, 2016; Lee *et al*, 2018a; Ware *et al*, 2016], higher ratios of stellate cells to cancer cells, which is feasible based on data presented in the current section 5.3, could have the potential to make the cancer models recapitulate the realistic ratio of 10% cancer cells in the microenvironment as found in PDAC patients.

Secondly, the current 3D co-culture models lack the characterisation of ECM. The phase-contrast images shown in the Figure 75-78 and 89-92 suggested the strong likelihood of collagen I present in the models; however, the solid evidence should be obtained by specific detection using antibodies against collagen I. Likewise, detection of fibronectin, hyaluronic acid and laminins using antibodies is also required to provide as parameters to adjust the initial ECM concentrations.

Thirdly, inclusion of immune cells is also critical for modelling PDAC. Tumour-infiltrating immune cells in PDAC tumours are commonly detected [Bailey *et al*, 2016; Seo *et al*, 2017]. Immunotherapeutic strategies have provided novel approaches to treat PDAC [Neoptolemos *et al*, 2018], which required realistic models to test their efficacy and effectiveness. Recently, immune cells have been successfully incorporated into an organoid model of PDAC [Tsai *et al*, 2018]. Therefore, further exploration adding immune cells into *in vitro* PDAC models will be achievable.

Fourthly, more specific and stable markers for cancer cells are needed in the current models. In the Figure 27-28 and 93-95, cancer cells presented with negative staining for p53 were found. While it may create an opportunity to study the p53 signalling in the models, p53 expression level might not be a good indicator for cell growth in terms of testing the therapeutic agents to inhibit cancer cell proliferation. Alternatively, construction of pancreatic cancer cell lines with fluorescent proteins has

been successfully established [Hiroshima *et al*, 2014; Katz *et al*, 2003; Park *et al*, 2015]. For instance, green fluorescent protein expressing PANC-1 cell lines and MIA-PaCa-2 cell lines have been used in xenograft models [Hiroshima *et al*, 2014; Park *et al*, 2015]; red fluorescent protein expressing MIA-PaCa-2 cells have been visualized to study tumour growth and metastasis *in vivo* [Katz *et al*, 2003]. Thus, the feasibility of using genetic modified cancer cell lines with fluorescent protein could be tested in the 3D co-culture models with the protocol developed in the current study.

6.4 Future direction for application of the current 3D co-culture models in screening anti-cancer agents

In 1980s, the US National Cancer Institute (NCI) 60 tumour cell line anticancer drug screen was established, using 96-well plates to culture leukaemia, colon, lung, CNS, renal, melanoma, ovarian, breast and prostate cancer cell lines as 2D cancer models and screen for cytotoxic compounds [Shoemaker, 2006]. This kind of screening contributes to the translational examples such as eribulin mesylate to treat late-stage breast cancer and bortezomib to treat myeloma [Shoemaker, 2006]. 2D culture has the advantages for scalable high-throughput screening such as low cost and fast establishment. However, the unrealistic cell-cell spatial organization, cell proliferation and growth, cell polarity and tumour progression, migration and response to therapies have been acknowledged to be the limitations of 2D culture [Hoarau-Vechot *et al*, 2018; Yamada *et al*, 2007]. In recent year, 3D co-culture models have been refined to be more easy-to-use than before. The protocol of the current study is based on other established protocols with minor modification such as reduction of use of centrifugation [Friedrich *et al*, 2009; Kota *et al*, 2018], which provides evidence that 3D co-culture models are suitable to use in a 96-well plate for screening of anti-cancer agents. It is predicted to be applicable in 384-well plates, both of which will fit the automatic drug screening equipment currently developed for conventional 2D culture in the future.

With the development of bio-printing, 3D co-culture models can be built in an accurate, defined, consistent, fast and precise manner. Cancer cells, fibroblasts, immune cells and ECM can be mixed with various approaches and spatially dispensed in a microscale within seconds, aided by state-of-art equipment [Zhang *et al*, 2016]. This kind of automation will also increase the efficiency of establishing the models and reduce the unavoidable human error during manual handling large numbers of samples.

However, it is also imperative to compare the accuracy and effectiveness of the 3D co-culture models with the conventional animal models and biopsies from patients. Researchers have been gathering data on the accuracy of organoids to mimic cancer microenvironment in patients by comparing with clinical specimen and xenografts [Boj *et al*, 2015; Gao *et al*, 2014]. Clinical trials may need to be conducted to compare the outcomes of drug treatment among animal models, 3D co-culture models and patients with informed consent, which require the collaboration among academics, industry and healthcare system.

6.4 Future direction for semi-quantification of YAP expression

In the current study, semi-quantification of YAP expression with image processing software CellProfiler has been conducted on one optical section. Measurement of YAP intensities in hundreds of cells was aided by machine learning, reducing the burden of manual identification. However, there are a few modifications should be made in the future.

Firstly, more evidence for efficient antibody penetration in the whole spheroids processed using the current protocol should be collected. The experiment on p53 quantification was only performed once, which is insufficient for testing the reproducibility. Conventional methods for detecting cancer markers should also be conducted on the same batch of 3D co-culture spheroids to produce histology slides, which should be analysed with the similar immunofluorescence protocol in the current study. If there is no statically significant difference in certain protein expression patterns and protein intensities between the cells near the edge and the core of the spheroids, or the differential expression patterns and protein intensities are statically comparable between the detection on staining the whole spheroid and the histology slide, then concrete evidence on efficient antibody penetration in whole spheroids will be attained.

Secondly, there is a need for membrane markers on PDAC cells to aid the identification of cell borders. In the current study, the borders used to separate individual cells were processed using the images with YAP staining. However, YAP distributes homogenously in the nucleus and the cytoplasm in the 3D models without a defined membrane localisation. Therefore, after verification of the accuracy of the module 'IdentifySecondaryObjects', there were a number of cells with inaccurate identification of the cytoplasmic YAP, which were excluded from the final calculation. It is uncertain that to what degree this elimination of data will affect the outcomes of the measurements. Undoubtedly, counting as many cells as possible should be one of the effective strategies to get the accurate overview of the protein expression in the 3D models. There are a few membrane proteins in the PDAC cell lines could be tested in the future, such as EGFR, E-cadherin and TGF-β type I receptors in both Capan-2 cells and PANC-1 cells [Kimple *et al*, 2010; Subramanian *et al*, 2004; Toyoda *et al*, 2005] and CD44 in PANC-1 cells [Zhao *et al*, 2016b].

Thirdly, in order to increase the efficiency to a greater extent, high-content microscope with programming is required to acquire and process a large number of optical sections from 3D co-culture models. 3D voxel measurement of Ki67 and YAP could be conducted in CellProfile. However, the immense workload requires more than one researcher to draw the conclusion quickly and accurately. Artificial intelligent will certainly speed up the process.

6.5 Future direction for studying the crosstalk between p53 signalling and YAP signalling

In the current study, p53 expression was high but YAP still mainly retained in the cytoplasm of the majorities of cancer cells in the 3D mono-cultures of PDAC cells without ECM. However, reduction of p53 expression correlated with YAP cytoplasmic localisation in the 3D co-culture models of PDAC. Based on the data from other research groups and the data from section 4.2 where HA is shown to

induce YAP nuclear translocation, the role of ECM is considered mainly to facilitate YAP entering the nucleus [Miroshnikova *et al*, 2017; Rice *et al*, 2017]. However, in the presence of HA and collagen I, a group of cells still presented with cytoplasmic accumulation of YAP and negative staining of p53. We postulated that disassociation with p53 may cause translocation of YAP from the nucleus to the cytoplasm. Consistent with the proposed role of mutant p53 in YAP signalling, mutant p53 could bind to YAP and promote its nuclear accumulation, as suggested by Ferraiuolo *et al* [Ferraiuolo *et al*, 2017]. This could be the case for PANC-1 cells in the current co-culture models. As for the Capan-2 cells, the first step should be the validation of p53 status using specific antibodies against mutant p53, which are available as commercial ones and self-produced ones [Hwang *et al*, 2018]. Meanwhile, advanced sequencing analysis should be used together with PANC-1 cells as positive controls. Correlation of p53 expression and nuclear YAP expression needs to be quantified using CellProfiler to measure the p53 intensity. Immunoprecipitation to study the p53 binding to endogenous YAP is necessary to elucidate the interaction of YAP and p53. However, immunoprecipitation may disrupt the binding of p53 to YAP during the experimental procedure, leading to false findings indicating p53 may not bind to YAP. Long-term searching for the suitable antibodies to perform the immunoprecipitation may be required. Development of Förster resonance energy transfer and fluorescence lifetime imaging microscopy to detect protein interaction in intact spheroids may be helpful in the future without disturbing the 3D structure [Margineanu *et al*, 2016].

6.6 Future direction for Pseudopterosin A-D and Tylophorinine

The current studies have shown the potential of Pseudopterosin A-D (PsA-D) and Tylophorinine to inhibit PDAC growth in the liver and the pancreas, using a 3D co-culture PDAC model. There is still a long way to go for PsA-D and Tylophorinine from bench to bedside in terms of cancer treatment. Two successful natural products, irinotecan (camptothecin analogue) and paclitaxel that have been translated from discovery to clinic, provide excellent examples for the development of PsA-D and Tylophorinine [Wall *et al*, 1996]. Irinotecan and paclitaxel have been used in as parts of combinatory treatments for several cancers including PDAC [Neoptolemos *et al*, 2018; Wall *et al*, 1996].

Similar to paclitaxel [Cragg, 1998], the issue of the limited supply of the two compounds needs to be addressed [Berrue *et al*, 2011; Gantait *et al*, 2017]. PsA-D are originally derived from the gorgonian coral *Pseudopterogorgia elisabethae* [Mydlarz *et al*, 2003]. Tylophorinine is extracted from a perennial vine called *Tylophora indica* (Burm. f.) Merrill [Gantait *et al*, 2017]. Currently, researchers are optimising the synthesis of PsA-D and Tylophorinine for sustainable supplies due to environmental concerns [Gantait *et al*, 2017; Mydlarz *et al*, 2003]. Once the synthesis protocols are standardized, the residues from chemical reaction will be controllable to prevent potential harm to the patients.

Both of irinotecan and paclitaxel first exhibited anti-tumour activity against human tumour xenograft models and then were further investigated to uncover mechanism of actions during early years [Wall *et al*, 1996]. This kind of phenotypic screening has been considered with insufficient knowledge of the molecular mechanisms of disease, thereby being used less than the screening approach based on molecular mechanism of action [Swinney *et al*, 2011]. Therefore, mechanism of actions of PsA-D and Tylophorinine are being investigated across labs. The mechanism of PsA-D has been elicited to block the glucocorticoid receptor alpha signalling and NF-κB Signalling in breast cancer cell lines grown as 2D

and 3D [Sperlich *et al*, 2017; Sperlich *et al*, 2018]. A tylophorine analogue, DCB-3503, can inhibit pancreatic cancer cell growth by reducing cell cycle regulatory proteins and inhibiting NF-κB signalling in pancreatic cancer cell lines [Shiah *et al*, 2006]. The current study demonstrated PsA-D and Tylophorinine can attenuate expression of p53, Ki67 and YAP in a 3D co-culture PDAC models. However, whether targeting p53 and YAP is a direct or indirect effect of PsA-D and Tylophorinine in pancreatic cancer cells needs further exploration. Incubation of normal cells without mutant p53 expression or nuclear accumulation of YAP in 3D with the same concentration of PsA-D and Tylophorinine may be also able to test the specificity of those compounds.

Another issue that needs to be addressed is related to drug-like properties, such as solubility. The poor solubility of paclitaxel in water and its relatively high dose requirements led to a surfactant formulation with Cremophor EL, causing serious allergic reactions including anaphylaxis in patients [Cragg, 1998]. PsA-D and Tylophorinine require DMSO to be dissolved. In particular, the IC50 of PsA-D is high, indicating the possible high dose to be used in clinic. How to increase solubility of PsA-D and Tylophorinine without affecting potency may needs exploration.

After addressing the aforementioned issues, attention should be drawn to the safety-related issue. The adverse effects of drugs have led to high attrition rate in the drug discovery and development process [Bowes *et al*, 2012]. Therefore, a panel of targets that cause potential hazard in human body have been proposed, such as the GPCRs, ion channels, neurotransmitter transporters, two nuclear hormone receptors, to guide the assessments of the safety of compounds [Bowes *et al*, 2012]. Toxicology based on those targets will need to be assessed on PsA-D and Tylophorinine to come up with preventative strategies to minimize the side effects when given to patients.

Appendix

Poster presentation

6 Dec 2018, YAP signalling in 3D co-cultures of pancreatic cancer cells, stellate cells and ECM-like materials (abstract and poster), GW4 3Rs Symposium, National Centre for the Replacement, Reduction and Refinement of animals in Research, https://www.nc3rs.org.uk/

20-21 Apr 2017, The YAP signalling in pancreatic cancer assessed in a humanized model, 1st Cancer Research @ Bath Symposium (abstract and poster), http://50years.bath.ac.uk/story/event/15th-cancer-research-symposium/

11 Jul 2016, Yes-associated protein signalling in pancreatic cancer microenvironment (abstract and poster), 24TH Biennial Congress of the European Association for Cancer Research, https://www.ecco-org.eu/EACR

10-11 Jun 2016, YAP signalling in 2D and 3D pancreatic cancer culture systems (abstract and poster), International Symposium on Pancreatic Cancer, http://www.internationalpancreatology.org/events.php/26/pancreas-2016-international-symposium-on-pancreatic-cancer

2 Nov 2015, Actions of dobutamine in 3D multicellular pancreatic cancer spheroid models (abstract and poster), NCRI Cancer Conference, http://www.ncri.org.uk/events/ncri-cancer-conference/

27 Jul 2015, Effect of Dobutamine on Pancreatic Cancer in 3D Tumour Spheroid Model (abstract and poster), 42nd Annual Meeting & Exposition of the Controlled Release Society

https://www.controlledreleasesociety.org/meetings/Archives/2015AnnualMeeting/Pages/default.aspx

17 Jun 2015, Effect of Dobutamine on Pancreatic Cancer in 3D Spheroids (poster), University of Bath and Royal United Hospitals Bath NHS Foundation Trust Health Research Showcase, https://www.eventbrite.co.uk/e/health-research-showcase-tickets-16201928404#

Oral presentation

6 June 2016, YAP signalling in the context of cancer, Faculty of Science Graduate School Research Afternoon

Public engagement activities

11 Mar 2017, Reducing animal use in cancer research, St. Mary's Primary School (Bath Taps into Science)

6 May 2017, Understanding pancreatic cancer, University of Bath's 50th Anniversary Festival

http://blogs.bath.ac.uk/publicengagement/2017/07/24/reducing-animal-use-in-cancer-research/

Awards

May 2017, Foundation Main Grant, Funds for Women Graduates (FFWG), http://www.ffwg.org.uk/our-grants.html

Dec 2016, EACR Travel Fellowship, European Association for Cancer Research (EACR), https://www.eacr.org/travel-fellowships

Nov 2016, Chinese Student Awards, Great Britain-China Educational Trust (Han Suyin Trust), http://www.gbcc.org.uk/educational-grants

Nov 2016, Public Engagement Tier 1 Initiator Awards, The Widening participation Office, Public Engagement Unit, University of Bath, http://blogs.bath.ac.uk/publicengagement/2017/07/24/reducing-animal-use-in-cancer-research/

Copyright permission

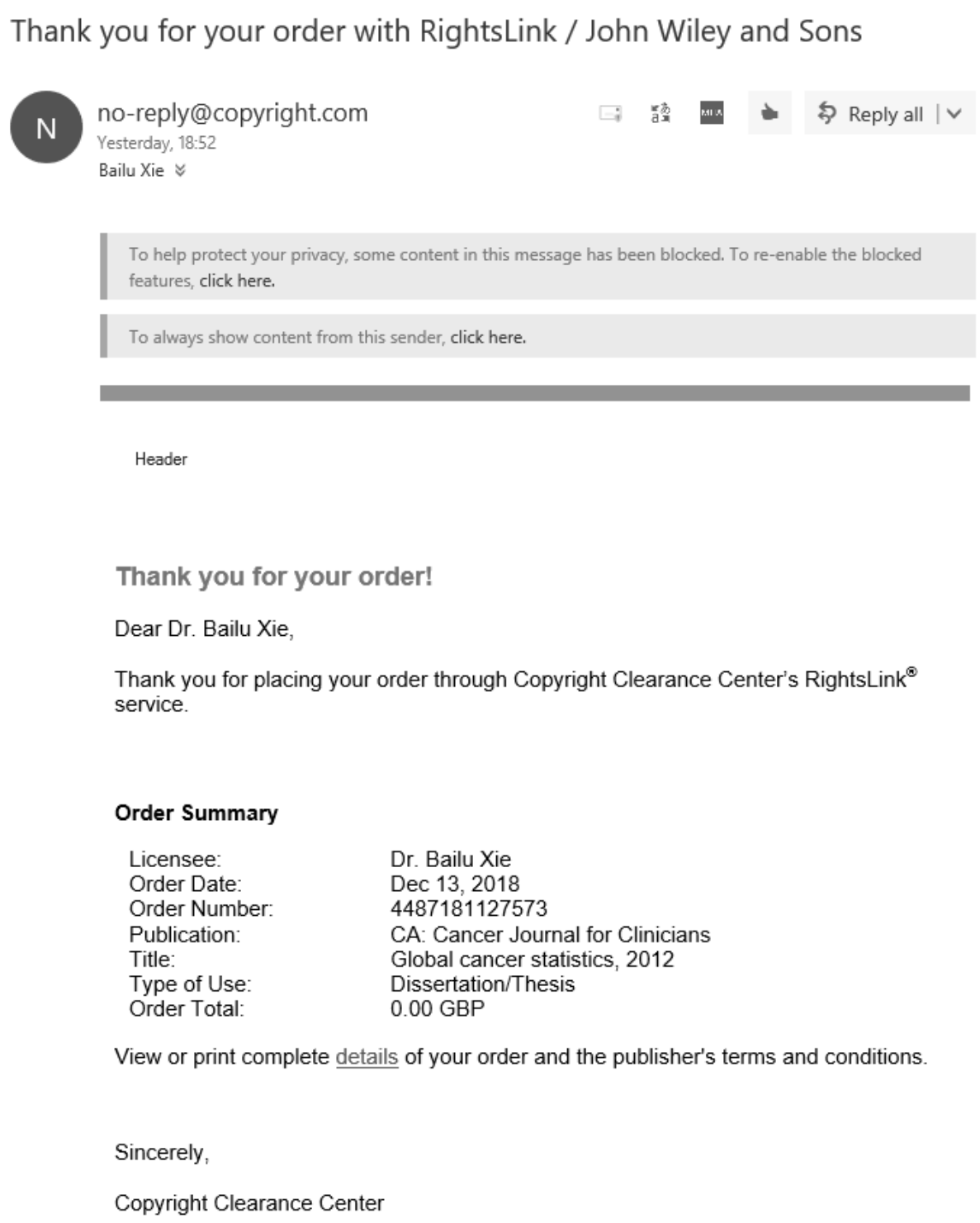

Thank you for your order with RightsLink / John Wiley and Sons

N no-reply@copyright.com
Yesterday, 18:52
Bailu Xie

Reply all

To help protect your privacy, some content in this message has been blocked. To re-enable the blocked features, click here.

To always show content from this sender, click here.

Header

Thank you for your order!

Dear Dr. Bailu Xie,

Thank you for placing your order through Copyright Clearance Center's RightsLink® service.

Order Summary

Licensee:	Dr. Bailu Xie
Order Date:	Dec 13, 2018
Order Number:	4487181127573
Publication:	CA: Cancer Journal for Clinicians
Title:	Global cancer statistics, 2012
Type of Use:	Dissertation/Thesis
Order Total:	0.00 GBP

View or print complete details of your order and the publisher's terms and conditions.

Sincerely,

Copyright Clearance Center

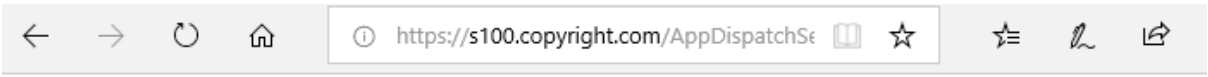

Copyright Clearance Center RightsLink®

Home | Account Info | Help

informa healthcare

Title:	Experimental anti-tumor therapy in 3-D: Spheroids – old hat or new challenge?
Author:	Juergen Friedrich, Reinhard Ebner, Leoni A. Kunz-Schughart
Publication:	INTERNATIONAL JOURNAL OF RADIATION BIOLOGY
Publisher:	Taylor & Francis
Date:	Jan 1, 2007

Rights managed by Taylor & Francis

Logged in as:
Bailu Xie
LOGOUT

Thesis/Dissertation Reuse Request

Taylor & Francis is pleased to offer reuses of its content for a thesis or dissertation free of charge contingent on resubmission of permission request if work is published.

BACK | CLOSE WINDOW

Thank you for your order with RightsLink / Elsevier

N

no-reply@copyright.com

Yesterday, 19:08

Bailu Xie

Reply all

To help protect your privacy, some content in this message has been blocked. To re-enable the blocked features, click here.

To always show content from this sender, click here.

Header

Thank you for your order!

Dear Dr. Bailu Xie,

Thank you for placing your order through Copyright Clearance Center's RightsLink® service.

Order Summary

Licensee:	Dr. Bailu Xie
Order Date:	Dec 13, 2018
Order Number:	4487190578784
Publication:	Journal of Biotechnology
Title:	Multicellular tumor spheroids: An underestimated tool is catching up again
Type of Use:	reuse in a thesis/dissertation
Order Total:	0.00 USD

View or print complete details of your order and the publisher's terms and conditions.

Sincerely,

Copyright Clearance Center

Thank you for your order with RightsLink / Springer Nature

N

no-reply@copyright.com

Yesterday, 19:14

Bailu Xie

Reply all

To help protect your privacy, some content in this message has been blocked. To re-enable the blocked features, click here.

To always show content from this sender, click here.

Header

Thank you for your order!

Dear Dr. Bailu Xie,

Thank you for placing your order through Copyright Clearance Center's RightsLink® service.

Order Summary

Licensee:	Dr. Bailu Xie
Order Date:	Dec 13, 2018
Order Number:	4487190906006
Publication:	Springer eBook
Title:	3D In Vitro Model for Breast Cancer Research Using Magnetic Levitation and Bioprinting Method
Type of Use:	Thesis/Dissertation
Order Total:	0.00 USD

View or print complete details of your order and the publisher's terms and conditions.

Sincerely,

Copyright Clearance Center

Thank you for your order with RightsLink / Elsevier

N

no-reply@copyright.com

Yesterday, 19:20

Bailu Xie

Reply all

To help protect your privacy, some content in this message has been blocked. To re-enable the blocked features, click here.

To always show content from this sender, click here.

Header

Thank you for your order!

Dear Dr. Bailu Xie,

Thank you for placing your order through Copyright Clearance Center's RightsLink® service.

Order Summary

Licensee:	Dr. Bailu Xie
Order Date:	Dec 13, 2018
Order Number:	4487191282017
Publication:	Cancer Cell
Title:	YAP/TAZ at the Roots of Cancer
Type of Use:	reuse in a thesis/dissertation
Order Total:	0.00 USD

View or print complete details of your order and the publisher's terms and conditions.

Sincerely,

Copyright Clearance Center

Thank you for your order with RightsLink / Elsevier

N

no-reply@copyright.com

Yesterday, 19:24

Bailu Xie

Reply all

To help protect your privacy, some content in this message has been blocked. To re-enable the blocked features, click here.

To always show content from this sender, click here.

Header

Thank you for your order!

Dear Dr. Bailu Xie,

Thank you for placing your order through Copyright Clearance Center's RightsLink® service.

Order Summary

Licensee:	Dr. Bailu Xie
Order Date:	Dec 13, 2018
Order Number:	4487200044121
Publication:	Cell
Title:	Hippo Pathway in Organ Size Control, Tissue Homeostasis, and Cancer
Type of Use:	reuse in a thesis/dissertation
Order Total:	0.00 USD

View or print complete details of your order and the publisher's terms and conditions.

Sincerely,

Copyright Clearance Center

References

Abberton, K.M., Bortolotto, S.K., Woods, A.A., Findlay, M., Morrison, W.A., Thompson, E.W., and Messina, A. (2008). Myogel, a novel, basement membrane-rich, extracellular matrix derived from skeletal muscle, is highly adipogenic in vivo and in vitro. **Cells Tissues Organs** *188*, 347-358.

Abylkassov, R., and Xie, Y. (2016). Role of Yes-associated protein in cancer: An update. **Oncol Lett** *12*, 2277-2282.

Akladios, B., Mendoza Reinoso, V., Cain, J.E., Wang, T., Lambie, D.L., Watkins, D.N., and Beverdam, A. (2017). Positive regulatory interactions between YAP and Hedgehog signalling in skin homeostasis and BCC development in mouse skin in vivo. **PLoS One** *12*, e0183178.

Ansari, D., Tingstedt, B., Andersson, B., Holmquist, F., Sturesson, C., Williamsson, C., Sasor, A., Borg, D., Bauden, M., and Andersson, R. (2016). Pancreatic cancer: yesterday, today and tomorrow. **Future Oncol** *12*, 1929-1946.

Aragona, M., Panciera, T., Manfrin, A., Giulitti, S., Michielin, F., Elvassore, N., Dupont, S., and Piccolo, S. (2013). A mechanical checkpoint controls multicellular growth through YAP/TAZ regulation by actin-processing factors. **Cell** *154*, 1047-1059.

Bailey, P., Chang, D.K., Nones, K., Johns, A.L., Patch, A.M., Gingras, M.C., Miller, D.K., Christ, A.N., Bruxner, T.J., Quinn, M.C., Nourse, C., Murtaugh, L.C., Harliwong, I., Idrisoglu, S., Manning, S., Nourbakhsh, E., Wani, S., Fink, L., Holmes, O., Chin, V., Anderson, M.J., Kazakoff, S., Leonard, C., Newell, F., Waddell, N., Wood, S., Xu, Q., Wilson, P.J., Cloonan, N., Kassahn, K.S., Taylor, D., Quek, K., Robertson, A., Pantano, L., Mincarelli, L., Sanchez, L.N., Evers, L., Wu, J., Pinese, M., Cowley, M.J., Jones, M.D., Colvin, E.K., Nagrial, A.M., Humphrey, E.S., Chantrill, L.A., Mawson, A., Humphris, J., Chou, A., Pajic, M., Scarlett, C.J., Pinho, A.V., Giry-Laterriere, M., Rooman, I., Samra, J.S., Kench, J.G., Lovell, J.A., Merrett, N.D., Toon, C.W., Epari, K., Nguyen, N.Q., Barbour, A., Zeps, N., Moran-Jones, K., Jamieson, N.B., Graham, J.S., Duthie, F., Oien, K., Hair, J., Grutzmann, R., Maitra, A., Iacobuzio-Donahue, C.A., Wolfgang, C.L., Morgan, R.A., Lawlor, R.T., Corbo, V., Bassi, C., Rusev, B., Capelli, P., Salvia, R., Tortora, G., Mukhopadhyay, D., Petersen, G.M., Australian Pancreatic Cancer Genome, I., Munzy, D.M., Fisher, W.E., Karim, S.A., Eshleman, J.R., Hruban, R.H., Pilarsky, C., Morton, J.P., Sansom, O.J., Scarpa, A., Musgrove, E.A., Bailey, U.M., Hofmann, O., Sutherland, R.L., Wheeler, D.A., Gill, A.J., Gibbs, R.A., Pearson, J.V., Waddell, N., Biankin, A.V., and Grimmond, S.M. (2016). Genomic analyses identify molecular subtypes of pancreatic cancer. **Nature** *531*, 47-52.

Baker, L.A., Tiriac, H., Clevers, H., and Tuveson, D.A. (2016). Modeling pancreatic cancer with organoids. **Trends Cancer** *2*, 176-190.

Basu, S., Totty, N.F., Irwin, M.S., Sudol, M., and Downward, J. (2003). Akt phosphorylates the Yes-associated protein, YAP, to induce interaction with 14-3-3 and attenuation of p73-mediated apoptosis. **Mol Cell** *11*, 11-23.

Beer, M., Kuppalu, N., Stefanini, M., Becker, H., Schulz, I., Manoli, S., Schuette, J., Schmees, C., Casazza, A., Stelzle, M., and Arcangeli, A. (2017). A novel microfluidic 3D platform for culturing pancreatic ductal adenocarcinoma cells: comparison with in vitro cultures and in vivo xenografts. **Sci Rep** *7*, 1325.

Berglind, H., Pawitan, Y., Kato, S., Ishioka, C., and Soussi, T. (2008). Analysis of p53 mutation status in human cancer cell lines: a paradigm for cell line cross-contamination. **Cancer Biol Ther** *7*, 699-708.

Berrue, F., McCulloch, M.W., and Kerr, R.G. (2011). Marine diterpene glycosides. **Bioorg Med Chem** *19*, 6702-6719.

Boj, S.F., Hwang, C.I., Baker, L.A., Chio, II, Engle, D.D., Corbo, V., Jager, M., Ponz-Sarvise, M., Tiriac, H., Spector, M.S., Gracanin, A., Oni, T., Yu, K.H., van Boxtel, R., Huch, M., Rivera, K.D., Wilson, J.P., Feigin, M.E., Ohlund, D., Handly-Santana, A., Ardito-Abraham, C.M., Ludwig, M., Elyada, E., Alagesan, B., Biffi, G., Yordanov, G.N., Delcuze, B., Creighton, B., Wright, K., Park, Y., Morsink, F.H., Molenaar, I.Q., Borel Rinkes, I.H., Cuppen, E., Hao, Y., Jin, Y., Nijman, I.J., Iacobuzio-Donahue, C., Leach, S.D., Pappin, D.J., Hammell, M., Klimstra, D.S., Basturk, O., Hruban, R.H., Offerhaus, G.J., Vries, R.G., Clevers, H., and Tuveson, D.A. (2015). Organoid models of human and mouse ductal pancreatic cancer. **Cell** *160*, 324-338.

Bolm, L., Cigolla, S., Wittel, U.A., Hopt, U.T., Keck, T., Rades, D., Bronsert, P., and Wellner, U.F. (2017). The Role of Fibroblasts in Pancreatic Cancer: Extracellular Matrix Versus Paracrine Factors. **Transl Oncol** *10*, 578-588.
Boreddy, S.R., and Srivastava, S.K. (2013). Pancreatic cancer chemoprevention by phytochemicals. **Cancer Lett** *334*, 86-94.
Bowes, J., Brown, A.J., Hamon, J., Jarolimek, W., Sridhar, A., Waldron, G., and Whitebread, S. (2012). Reducing safety-related drug attrition: the use of in vitro pharmacological profiling. **Nat Rev Drug Discov** *11*, 909-922.
Bramhall, S.R., Rosemurgy, A., Brown, P.D., Bowry, C., Buckels, J.A., and Marimastat Pancreatic Cancer Study, G. (2001). Marimastat as first-line therapy for patients with unresectable pancreatic cancer: a randomized trial. **J Clin Oncol** *19*, 3447-3455.
Bramhall, S.R., Schulz, J., Nemunaitis, J., Brown, P.D., Baillet, M., and Buckels, J.A. (2002). A double-blind placebo-controlled, randomised study comparing gemcitabine and marimastat with gemcitabine and placebo as first line therapy in patients with advanced pancreatic cancer. **Br J Cancer** *87*, 161-167.
Brennen, W.N., Isaacs, J.T., and Denmeade, S.R. (2012). Rationale behind targeting fibroblast activation protein-expressing carcinoma-associated fibroblasts as a novel chemotherapeutic strategy. **Mol Cancer Ther** *11*, 257-266.
Brown, M.J., Symonowicz, C., Medina, L.V., Bratcher, N.A., Buckmaster, C.A., Klein, H., and Anderson, L.C. (2018). Culture of Care: Organizational Responsibilities. In Management of Animal Care and Use Programs in Research, Education, and Testing, nd, R.H. Weichbrod, G.A.H. Thompson, and J.N. Norton, eds. (Boca Raton (FL)), pp. 11-26.
Buchholz, M., Kestler, H.A., Holzmann, K., Ellenrieder, V., Schneiderhan, W., Siech, M., Adler, G., Bachem, M.G., and Gress, T.M. (2005). Transcriptome analysis of human hepatic and pancreatic stellate cells: organ-specific variations of a common transcriptional phenotype. **J Mol Med (Berl)** *83*, 795-805.
Bumpers, H.L., Janagama, D.G., Manne, U., Basson, M.D., and Katkoori, V. (2015). Nanomagnetic levitation three-dimensional cultures of breast and colorectal cancers. **J Surg Res** *194*, 319-326.
Burdick, J.A., and Prestwich, G.D. (2011). Hyaluronic acid hydrogels for biomedical applications. **Adv Mater** *23*, H41-56.
Butcher, D.T., Alliston, T., and Weaver, V.M. (2009). A tense situation: forcing tumour progression. **Nat Rev Cancer** *9*, 108-122.
Cacemiro, M.C., Berzoti-Coelho, M.G., Cominal, J.G., Burin, S.M., and Castro, F.A. (2017). Hippo pathway deregulation: implications in the pathogenesis of haematological malignancies. **J Clin Pathol** *70*, 9-14.
Caliari, S.R., and Burdick, J.A. (2016). A practical guide to hydrogels for cell culture. **Nat Methods** *13*, 405-414.
Carrel, A., and Burrows, M.T. (1911). Cultivation of Tissues in Vitro and Its Technique. **J Exp Med** *13*, 387-396.
Chan, L.H., Wang, W., Yeung, W., Deng, Y., Yuan, P., and Mak, K.K. (2014). Hedgehog signaling induces osteosarcoma development through Yap1 and H19 overexpression. **Oncogene** *33*, 4857-4866.
Cheema, U., and Brown, R.A. (2013). Rapid Fabrication of Living Tissue Models by Collagen Plastic Compression: Understanding Three-Dimensional Cell Matrix Repair In Vitro. **Adv Wound Care (New Rochelle)** *2*, 176-184.
Chen, C., Zhao, S., Karnad, A., and Freeman, J.W. (2018a). The biology and role of CD44 in cancer progression: therapeutic implications. **J Hematol Oncol** *11*, 64.
Chen, C., Zhu, D., Zhang, H., Han, C., Xue, G., Zhu, T., Luo, J., and Kong, L. (2018b). YAP-dependent ubiquitination and degradation of beta-catenin mediates inhibition of Wnt signalling induced by Physalin F in colorectal cancer. **Cell Death Dis** *9*, 591.
Cicenas, J., Kvederaviciute, K., Meskinyte, I., Meskinyte-Kausiliene, E., Skeberdyte, A., and Cicenas, J. (2017). KRAS, TP53, CDKN2A, SMAD4, BRCA1, and BRCA2 Mutations in Pancreatic Cancer. **Cancers (Basel)** *9*.

Coleman, S.J., Chioni, A.M., Ghallab, M., Anderson, R.K., Lemoine, N.R., Kocher, H.M., and Grose, R.P. (2014a). Nuclear translocation of FGFR1 and FGF2 in pancreatic stellate cells facilitates pancreatic cancer cell invasion. **EMBO Mol Med** *6*, 467-481.
Coleman, S.J., Watt, J., Arumugam, P., Solaini, L., Carapuca, E., Ghallab, M., Grose, R.P., and Kocher, H.M. (2014b). Pancreatic cancer organotypics: High throughput, preclinical models for pharmacological agent evaluation. **World J Gastroenterol** *20*, 8471-8481.
Cottini, F., Hideshima, T., Xu, C., Sattler, M., Dori, M., Agnelli, L., ten Hacken, E., Bertilaccio, M.T., Antonini, E., Neri, A., Ponzoni, M., Marcatti, M., Richardson, P.G., Carrasco, R., Kimmelman, A.C., Wong, K.K., Caligaris-Cappio, F., Blandino, G., Kuehl, W.M., Anderson, K.C., and Tonon, G. (2014). Rescue of Hippo coactivator YAP1 triggers DNA damage-induced apoptosis in hematological cancers. **Nat Med** *20*, 599-606.
Cragg, G.M. (1998). Paclitaxel (Taxol): a success story with valuable lessons for natural product drug discovery and development. **Med Res Rev** *18*, 315-331.
Cravo, A.S., Carter, E., Erkan, M., Harvey, E., Furutani-Seiki, M., and Mrsny, R. (2015). Hippo pathway elements Co-localize with Occludin: A possible sensor system in pancreatic epithelial cells. **Tissue Barriers** *3*, e1037948.
Deer, E.L., Gonzalez-Hernandez, J., Coursen, J.D., Shea, J.E., Ngatia, J., Scaife, C.L., Firpo, M.A., and Mulvihill, S.J. (2010). Phenotype and genotype of pancreatic cancer cell lines. **Pancreas** *39*, 425-435.
DeQuach, J.A., Lin, J.E., Cam, C., Hu, D., Salvatore, M.A., Sheikh, F., and Christman, K.L. (2012). Injectable skeletal muscle matrix hydrogel promotes neovascularization and muscle cell infiltration in a hindlimb ischemia model. **Eur Cell Mater** *23*, 400-412; discussion 412.
Di Agostino, S., Sorrentino, G., Ingallina, E., Valenti, F., Ferraiuolo, M., Bicciato, S., Piazza, S., Strano, S., Del Sal, G., and Blandino, G. (2016). YAP enhances the pro-proliferative transcriptional activity of mutant p53 proteins. **EMBO Rep** *17*, 188-201.
Diep, C.H., Zucker, K.M., Hostetter, G., Watanabe, A., Hu, C., Munoz, R.M., Von Hoff, D.D., and Han, H. (2012). Down-regulation of Yes Associated Protein 1 expression reduces cell proliferation and clonogenicity of pancreatic cancer cells. **PLoS One** *7*, e32783.
Diwakarla, C., Hannan, K., Hein, N., and Yip, D. (2017). Advanced pancreatic ductal adenocarcinoma - Complexities of treatment and emerging therapeutic options. **World J Gastroenterol** *23*, 2276-2285.
Djurec, M., Grana, O., Lee, A., Troule, K., Espinet, E., Cabras, L., Navas, C., Blasco, M.T., Martin-Diaz, L., Burdiel, M., Li, J., Liu, Z., Vallespinos, M., Sanchez-Bueno, F., Sprick, M.R., Trumpp, A., Sainz, B., Jr., Al-Shahrour, F., Rabadan, R., Guerra, C., and Barbacid, M. (2018). Saa3 is a key mediator of the protumorigenic properties of cancer-associated fibroblasts in pancreatic tumors. **Proc Natl Acad Sci U S A** *115*, E1147-E1156.
Dobrokhotov, O., Samsonov, M., Sokabe, M., and Hirata, H. (2018). Mechanoregulation and pathology of YAP/TAZ via Hippo and non-Hippo mechanisms. **Clin Transl Med** *7*, 23.
Doherty, G.J., Tempero, M., and Corrie, P.G. (2018). HALO-109-301: a Phase III trial of PEGPH20 (with gemcitabine and nab-paclitaxel) in hyaluronic acid-high stage IV pancreatic cancer. **Future Oncol** *14*, 13-22.
Dong, M., Nio, Y., Tamura, K., Song, M.M., Guo, K.J., Guo, R.X., and Dong, Y.T. (2000). Ki-ras point mutation and p53 expression in human pancreatic cancer: a comparative study among Chinese, Japanese, and Western patients. **Cancer Epidemiol Biomarkers Prev** *9*, 279-284.
Dorfel, M.J., and Huber, O. (2012). Modulation of tight junction structure and function by kinases and phosphatases targeting occludin. **J Biomed Biotechnol** *2012*, 807356.
Dupont, S., Morsut, L., Aragona, M., Enzo, E., Giulitti, S., Cordenonsi, M., Zanconato, F., Le Digabel, J., Forcato, M., Bicciato, S., Elvassore, N., and Piccolo, S. (2011). Role of YAP/TAZ in mechanotransduction. **Nature** *474*, 179-183.
Elebring, E., Kuna, V.K., Kvarnstrom, N., and Sumitran-Holgersson, S. (2017). Cold-perfusion decellularization of whole-organ porcine pancreas supports human fetal pancreatic cell attachment and expression of endocrine and exocrine markers. **J Tissue Eng** *8*, 2041731417738145.

Enzo, E., Santinon, G., Pocaterra, A., Aragona, M., Bresolin, S., Forcato, M., Grifoni, D., Pession, A., Zanconato, F., Guzzo, G., Bicciato, S., and Dupont, S. (2015). Aerobic glycolysis tunes YAP/TAZ transcriptional activity. **EMBO J** *34*, 1349-1370.
Erkan, M. (2013). The role of pancreatic stellate cells in pancreatic cancer. **Pancreatology** *13*, 106-109.
Erkan, M., Adler, G., Apte, M.V., Bachem, M.G., Buchholz, M., Detlefsen, S., Esposito, I., Friess, H., Gress, T.M., Habisch, H.J., Hwang, R.F., Jaster, R., Kleeff, J., Kloppel, G., Kordes, C., Logsdon, C.D., Masamune, A., Michalski, C.W., Oh, J., Phillips, P.A., Pinzani, M., Reiser-Erkan, C., Tsukamoto, H., and Wilson, J. (2012). StellaTUM: current consensus and discussion on pancreatic stellate cell research. **Gut** *61*, 172-178.
Erkan, M., Kleeff, J., Gorbachevski, A., Reiser, C., Mitkus, T., Esposito, I., Giese, T., Buchler, M.W., Giese, N.A., and Friess, H. (2007). Periostin creates a tumor-supportive microenvironment in the pancreas by sustaining fibrogenic stellate cell activity. **Gastroenterology** *132*, 1447-1464.
Erkan, M., Michalski, C.W., Rieder, S., Reiser-Erkan, C., Abiatari, I., Kolb, A., Giese, N.A., Esposito, I., Friess, H., and Kleeff, J. (2008). The activated stroma index is a novel and independent prognostic marker in pancreatic ductal adenocarcinoma. **Clin Gastroenterol Hepatol** *6*, 1155-1161.
Espanel, X., and Sudol, M. (2001). Yes-associated protein and p53-binding protein-2 interact through their WW and SH3 domains. **J Biol Chem** *276*, 14514-14523.
Fan, R., Kim, N.G., and Gumbiner, B.M. (2013). Regulation of Hippo pathway by mitogenic growth factors via phosphoinositide 3-kinase and phosphoinositide-dependent kinase-1. **Proc Natl Acad Sci U S A** *110*, 2569-2574.
Feigin, M.E., and Tuveson, D.A. (2016). Challenges and Opportunities in Modeling Pancreatic Cancer. **Cold Spring Harb Symp Quant Biol** *81*, 231-235.
Ferlay, J., Colombet, M., Soerjomataram, I., Dyba, T., Randi, G., Bettio, M., Gavin, A., Visser, O., and Bray, F. (2018). Cancer incidence and mortality patterns in Europe: Estimates for 40 countries and 25 major cancers in 2018. **Eur J Cancer**.
Ferraiuolo, M., Verduci, L., Blandino, G., and Strano, S. (2017). Mutant p53 Protein and the Hippo Transducers YAP and TAZ: A Critical Oncogenic Node in Human Cancers. **Int J Mol Sci** *18*.
Ferrer, J., Scott, W.E., 3rd, Weegman, B.P., Suszynski, T.M., Sutherland, D.E., Hering, B.J., and Papas, K.K. (2008). Pig pancreas anatomy: implications for pancreas procurement, preservation, and islet isolation. **Transplantation** *86*, 1503-1510.
Francis, D., Abberton, K., Thompson, E., and Daniell, M. (2009). Myogel supports the ex-vivo amplification of corneal epithelial cells. **Exp Eye Res** *88*, 339-346.
Friedrich, J., Ebner, R., and Kunz-Schughart, L.A. (2007). Experimental anti-tumor therapy in 3-D: spheroids--old hat or new challenge? **Int J Radiat Biol** *83*, 849-871.
Friedrich, J., Seidel, C., Ebner, R., and Kunz-Schughart, L.A. (2009). Spheroid-based drug screen: considerations and practical approach. **Nat Protoc** *4*, 309-324.
Froeling, F.E., Mirza, T.A., Feakins, R.M., Seedhar, A., Elia, G., Hart, I.R., and Kocher, H.M. (2009). Organotypic culture model of pancreatic cancer demonstrates that stromal cells modulate E-cadherin, beta-catenin, and Ezrin expression in tumor cells. **Am J Pathol** *175*, 636-648.
Fujii, M., Toyoda, T., Nakanishi, H., Yatabe, Y., Sato, A., Matsudaira, Y., Ito, H., Murakami, H., Kondo, Y., Kondo, E., Hida, T., Tsujimura, T., Osada, H., and Sekido, Y. (2012). TGF-beta synergizes with defects in the Hippo pathway to stimulate human malignant mesothelioma growth. **J Exp Med** *209*, 479-494.
Fujita, H., Ohuchida, K., Mizumoto, K., Egami, T., Miyoshi, K., Moriyama, T., Cui, L., Yu, J., Zhao, M., Manabe, T., and Tanaka, M. (2009). Tumor-stromal interactions with direct cell contacts enhance proliferation of human pancreatic carcinoma cells. **Cancer Sci** *100*, 2309-2317.
Fujiwara, M., Kanayama, K., Hirokawa, Y.S., and Shiraishi, T. (2016). ASF-4-1 fibroblast-rich culture increases chemoresistance and mTOR expression of pancreatic cancer BxPC-3 cells at the invasive front in vitro, and promotes tumor growth and invasion in vivo. **Oncol Lett** *11*, 2773-2779.
Gantait, S., and Kundu, S. (2017). Neoteric trends in tissue culture-mediated biotechnology of Indian ipecac [Tylophora indica (Burm. f.) Merrill]. **3 Biotech** *7*, 231.
Gao, D., Vela, I., Sboner, A., Iaquinta, P.J., Karthaus, W.R., Gopalan, A., Dowling, C., Wanjala, J.N., Undvall, E.A., Arora, V.K., Wongvipat, J., Kossai, M., Ramazanoglu, S., Barboza, L.P., Di, W., Cao, Z.,

Zhang, Q.F., Sirota, I., Ran, L., MacDonald, T.Y., Beltran, H., Mosquera, J.M., Touijer, K.A., Scardino, P.T., Laudone, V.P., Curtis, K.R., Rathkopf, D.E., Morris, M.J., Danila, D.C., Slovin, S.F., Solomon, S.B., Eastham, J.A., Chi, P., Carver, B., Rubin, M.A., Scher, H.I., Clevers, H., Sawyers, C.L., and Chen, Y. (2014). Organoid cultures derived from patients with advanced prostate cancer. **Cell** *159*, 176-187.
Garrido-Laguna, I., and Hidalgo, M. (2015). Pancreatic cancer: from state-of-the-art treatments to promising novel therapies. **Nat Rev Clin Oncol** *12*, 319-334.
Gillies, A.R., and Lieber, R.L. (2011a). Structure and function of the skeletal muscle extracellular matrix. **Muscle Nerve** *44*, 318-331.
Gillies, A.R., Smith, L.R., Lieber, R.L., and Varghese, S. (2011b). Method for decellularizing skeletal muscle without detergents or proteolytic enzymes. **Tissue Eng Part C Methods** *17*, 383-389.
GM, O.K., and Knox, J.J. (2018). Locally advanced pancreatic cancer: An emerging entity. **Curr Probl Cancer** *42*, 12-25.
Goh, S.K., Bertera, S., Olsen, P., Candiello, J.E., Halfter, W., Uechi, G., Balasubramani, M., Johnson, S.A., Sicari, B.M., Kollar, E., Badylak, S.F., and Banerjee, I. (2013). Perfusion-decellularized pancreas as a natural 3D scaffold for pancreatic tissue and whole organ engineering. **Biomaterials** *34*, 6760-6772.
Gopinathan, A., Morton, J.P., Jodrell, D.I., and Sansom, O.J. (2015). GEMMs as preclinical models for testing pancreatic cancer therapies. **Dis Model Mech** *8*, 1185-1200.
Gopinathan, J., and Noh, I. (2018). Recent trends in bioinks for 3D printing. **Biomater Res** *22*, 11.
Goulitquer, S., Croyal, M., Lalande, J., Royer, A.L., Guitton, Y., Arzur, D., Durand, S., Le Jossic-Corcos, C., Bouchereau, A., Potin, P., Akoka, S., Antignac, J.P., Krempf, M., Ferchaud-Roucher, V., Giraudeau, P., and Corcos, L. (2018). Consequences of blunting the mevalonate pathway in cancer identified by a pluri-omics approach. **Cell Death Dis** *9*, 745.
Govindachari, T.R., Pai, B.R., Prabhakar, S., and Savitri, T.S. (1965). Synthesis of (+ -) tylophorinine. **Tetrahedron** *21*, 2573-2578.
Greer, J.B., and Whitcomb, D.C. (2007). Role of BRCA1 and BRCA2 mutations in pancreatic cancer. **Gut** *56*, 601-605.
Gumbiner, B.M., and Kim, N.G. (2014). The Hippo-YAP signaling pathway and contact inhibition of growth. **J Cell Sci** *127*, 709-717.
Gutierrez, K., Dicks, N., Glanzner, W.G., Agellon, L.B., and Bordignon, V. (2015). Efficacy of the porcine species in biomedical research. **Front Genet** *6*, 293.
Hagmeyer, B., Zechnall, F., and Stelzle, M. (2014). Towards plug and play filling of microfluidic devices by utilizing networks of capillary stop valves. **Biomicrofluidics** *8*, 056501.
Haisler, W.L., Timm, D.M., Gage, J.A., Tseng, H., Killian, T.C., and Souza, G.R. (2013). Three-dimensional cell culturing by magnetic levitation. **Nat Protoc** *8*, 1940-1949.
Hariharan, D., Saied, A., and Kocher, H.M. (2008). Analysis of mortality rates for pancreatic cancer across the world. **HPB (Oxford)** *10*, 58-62.
Harvey, K.F., Zhang, X., and Thomas, D.M. (2013). The Hippo pathway and human cancer. **Nat Rev Cancer** *13*, 246-257.
He, C., Lv, X., Hua, G., Lele, S.M., Remmenga, S., Dong, J., Davis, J.S., and Wang, C. (2015). YAP forms autocrine loops with the ERBB pathway to regulate ovarian cancer initiation and progression. **Oncogene** *34*, 6040-6054.
Highley, C.B., Prestwich, G.D., and Burdick, J.A. (2016). Recent advances in hyaluronic acid hydrogels for biomedical applications. **Curr Opin Biotechnol** *40*, 35-40.
Hill, B.S., Pelagalli, A., Passaro, N., and Zannetti, A. (2017). Tumor-educated mesenchymal stem cells promote pro-metastatic phenotype. **Oncotarget** *8*, 73296-73311.
Hiroshima, Y., Maawy, A., Zhang, Y., Sato, S., Murakami, T., Yamamoto, M., Uehara, F., Miwa, S., Yano, S., Momiyama, M., Chishima, T., Tanaka, K., Bouvet, M., Endo, I., and Hoffman, R.M. (2014). Fluorescence-guided surgery in combination with UVC irradiation cures metastatic human pancreatic cancer in orthotopic mouse models. **PLoS One** *9*, e99977.
Hirschhaeuser, F., Menne, H., Dittfeld, C., West, J., Mueller-Klieser, W., and Kunz-Schughart, L.A. (2010). Multicellular tumor spheroids: an underestimated tool is catching up again. **J Biotechnol** *148*, 3-15.

Hoarau-Vechot, J., Rafii, A., Touboul, C., and Pasquier, J. (2018). Halfway between 2D and Animal Models: Are 3D Cultures the Ideal Tool to Study Cancer-Microenvironment Interactions? **Int J Mol Sci** *19*.
Huang, Y.H., Chen, M.H., Guo, Q.L., Chen, Y.X., Zhang, L.J., Chen, Z.X., and Wang, X.Z. (2018). Interleukin10 promotes primary rat hepatic stellate cell senescence by upregulating the expression levels of p53 and p21. **Mol Med Rep** *17*, 5700-5707.
Hwang, C.I., Boj, S.F., Clevers, H., and Tuveson, D.A. (2016). Preclinical models of pancreatic ductal adenocarcinoma. **J Pathol** *238*, 197-204.
Hwang, L.A., Phang, B.H., Liew, O.W., Iqbal, J., Koh, X.H., Koh, X.Y., Othman, R., Xue, Y., Richards, A.M., Lane, D.P., and Sabapathy, K. (2018). Monoclonal Antibodies against Specific p53 Hotspot Mutants as Potential Tools for Precision Medicine. **Cell Rep** *22*, 299-312.
Hwang, R.F., Moore, T., Arumugam, T., Ramachandran, V., Amos, K.D., Rivera, A., Ji, B., Evans, D.B., and Logsdon, C.D. (2008). Cancer-associated stromal fibroblasts promote pancreatic tumor progression. **Cancer Res** *68*, 918-926.
Inch, W.R., McCredie, J.A., and Sutherland, R.M. (1970). Growth of nodular carcinomas in rodents compared with multi-cell spheroids in tissue culture. **Growth** *34*, 271-282.
Ivascu, A., and Kubbies, M. (2006). Rapid generation of single-tumor spheroids for high-throughput cell function and toxicity analysis. **J Biomol Screen** *11*, 922-932.
Iwamura, T., Katsuki, T., and Ide, K. (1987). Establishment and characterization of a human pancreatic cancer cell line (SUIT-2) producing carcinoembryonic antigen and carbohydrate antigen 19-9. **Jpn J Cancer Res** *78*, 54-62.
Jaganathan, H., Gage, J., Leonard, F., Srinivasan, S., Souza, G.R., Dave, B., and Godin, B. (2014). Three-dimensional in vitro co-culture model of breast tumor using magnetic levitation. **Sci Rep** *4*, 6468.
Jansson, L., and Larsson, J. (2012). Normal hematopoietic stem cell function in mice with enforced expression of the Hippo signaling effector YAP1. **PLoS One** *7*, e32013.
Jeong, J., Park, Y.N., Park, J.S., Yoon, D.S., Chi, H.S., and Kim, B.R. (2005). Clinical significance of p16 protein expression loss and aberrant p53 protein expression in pancreatic cancer. **Yonsei Med J** *46*, 519-525.
Jeric, I., Maurer, G., Cavallo, A.L., Raguz, J., Desideri, E., Tarkowski, B., Parrini, M., Fischer, I., Zatloukal, K., and Baccarini, M. (2016). A cell-autonomous tumour suppressor role of RAF1 in hepatocarcinogenesis. **Nat Commun** *7*, 13781.
Jiang, X., Abiatari, I., Kong, B., Erkan, M., De Oliveira, T., Giese, N.A., Michalski, C.W., Friess, H., and Kleeff, J. (2009). Pancreatic islet and stellate cells are the main sources of endocrine gland-derived vascular endothelial growth factor/prokineticin-1 in pancreatic cancer. **Pancreatology** *9*, 165-172.
Jiang, Z., Zhou, C., Cheng, L., Yan, B., Chen, K., Chen, X., Zong, L., Lei, J., Duan, W., Xu, Q., Li, X., Wang, Z., Ma, Q., and Ma, J. (2018). Inhibiting YAP expression suppresses pancreatic cancer progression by disrupting tumor-stromal interactions. **J Exp Clin Cancer Res** *37*, 69.
Jiang, Z.E., Jiang, C., Chen, B., Koh, C.S., Yong, J.H., Park, D.H., Won, M.H., and Lee, Y.L. (2013). Age-associated changes in pancreatic exocrine secretion of the isolated perfused rat pancreas. **Lab Anim Res** *29*, 19-26.
Kadaba, R., Birke, H., Wang, J., Hooper, S., Andl, C.D., Di Maggio, F., Soylu, E., Ghallab, M., Bor, D., Froeling, F.E., Bhattacharya, S., Rustgi, A.K., Sahai, E., Chelala, C., Sasieni, P., and Kocher, H.M. (2013). Imbalance of desmoplastic stromal cell numbers drives aggressive cancer processes. **J Pathol** *230*, 107-117.
Kapalczynska, M., Kolenda, T., Przybyla, W., Zajaczkowska, M., Teresiak, A., Filas, V., Ibbs, M., Blizniak, R., Luczewski, L., and Lamperska, K. (2018). 2D and 3D cell cultures - a comparison of different types of cancer cell cultures. **Arch Med Sci** *14*, 910-919.
Kapoor, A., Yao, W., Ying, H., Hua, S., Liewen, A., Wang, Q., Zhong, Y., Wu, C.J., Sadanandam, A., Hu, B., Chang, Q., Chu, G.C., Al-Khalil, R., Jiang, S., Xia, H., Fletcher-Sananikone, E., Lim, C., Horwitz, G.I., Viale, A., Pettazzoni, P., Sanchez, N., Wang, H., Protopopov, A., Zhang, J., Heffernan, T., Johnson, R.L., Chin, L., Wang, Y.A., Draetta, G., and DePinho, R.A. (2014). Yap1 activation enables bypass of oncogenic Kras addiction in pancreatic cancer. **Cell** *158*, 185-197.

Katz, M.H., Takimoto, S., Spivack, D., Moossa, A.R., Hoffman, R.M., and Bouvet, M. (2003). A novel red fluorescent protein orthotopic pancreatic cancer model for the preclinical evaluation of chemotherapeutics. **J Surg Res** *113*, 151-160.
Khan, M.A., Azim, S., Zubair, H., Bhardwaj, A., Patel, G.K., Khushman, M., Singh, S., and Singh, A.P. (2017). Molecular Drivers of Pancreatic Cancer Pathogenesis: Looking Inward to Move Forward. **Int J Mol Sci** *18*.
Kim, E.J., Sahai, V., Abel, E.V., Griffith, K.A., Greenson, J.K., Takebe, N., Khan, G.N., Blau, J.L., Craig, R., Balis, U.G., Zalupski, M.M., and Simeone, D.M. (2014). Pilot clinical trial of hedgehog pathway inhibitor GDC-0449 (vismodegib) in combination with gemcitabine in patients with metastatic pancreatic adenocarcinoma. **Clin Cancer Res** *20*, 5937-5945.
Kimple, R.J., Vaseva, A.V., Cox, A.D., Baerman, K.M., Calvo, B.F., Tepper, J.E., Shields, J.M., and Sartor, C.I. (2010). Radiosensitization of epidermal growth factor receptor/HER2-positive pancreatic cancer is mediated by inhibition of Akt independent of ras mutational status. **Clin Cancer Res** *16*, 912-923.
Knowlton, S., Onal, S., Yu, C.H., Zhao, J.J., and Tasoglu, S. (2015). Bioprinting for cancer research. **Trends Biotechnol** *33*, 504-513.
Koikawa, K., Ohuchida, K., Ando, Y., Kibe, S., Nakayama, H., Takesue, S., Endo, S., Abe, T., Okumura, T., Iwamoto, C., Moriyama, T., Nakata, K., Miyasaka, Y., Ohtsuka, T., Nagai, E., Mizumoto, K., Hashizume, M., and Nakamura, M. (2018). Basement membrane destruction by pancreatic stellate cells leads to local invasion in pancreatic ductal adenocarcinoma. **Cancer Lett** *425*, 65-77.
Konsavage, W.M., Jr., Kyler, S.L., Rennoll, S.A., Jin, G., and Yochum, G.S. (2012). Wnt/beta-catenin signaling regulates Yes-associated protein (YAP) gene expression in colorectal carcinoma cells. **J Biol Chem** *287*, 11730-11739.
Kopecky, B.J., Duncan, J.S., Elliott, K.L., and Fritzsch, B. (2012). Three-dimensional reconstructions from optical sections of thick mouse inner ears using confocal microscopy. **J Microsc** *248*, 292-298.
Kota, S., Hou, S., Guerrant, W., Madoux, F., Troutman, S., Fernandez-Vega, V., Alekseeva, N., Madala, N., Scampavia, L., Kissil, J., and Spicer, T.P. (2018). A novel three-dimensional high-throughput screening approach identifies inducers of a mutant KRAS selective lethal phenotype. **Oncogene** *37*, 4372-4384.
Kultti, A., Li, X., Jiang, P., Thompson, C.B., Frost, G.I., and Shepard, H.M. (2012). Therapeutic targeting of hyaluronan in the tumor stroma. **Cancers (Basel)** *4*, 873-903.
LaBarbera, D.V., Reid, B.G., and Yoo, B.H. (2012). The multicellular tumor spheroid model for high-throughput cancer drug discovery. **Expert Opin Drug Discov** *7*, 819-830.
Laklai, H., Miroshnikova, Y.A., Pickup, M.W., Collisson, E.A., Kim, G.E., Barrett, A.S., Hill, R.C., Lakins, J.N., Schlaepfer, D.D., Mouw, J.K., LeBleu, V.S., Roy, N., Novitskiy, S.V., Johansen, J.S., Poli, V., Kalluri, R., Iacobuzio-Donahue, C.A., Wood, L.D., Hebrok, M., Hansen, K., Moses, H.L., and Weaver, V.M. (2016). Genotype tunes pancreatic ductal adenocarcinoma tissue tension to induce matricellular fibrosis and tumor progression. **Nat Med** *22*, 497-505.
Lau, S.C., and Cheung, W.Y. (2017). Evolving treatment landscape for early and advanced pancreatic cancer. **World J Gastrointest Oncol** *9*, 281-292.
Lee, J.H., Kim, S.K., Khawar, I.A., Jeong, S.Y., Chung, S., and Kuh, H.J. (2018a). Microfluidic co-culture of pancreatic tumor spheroids with stellate cells as a novel 3D model for investigation of stroma-mediated cell motility and drug resistance. **J Exp Clin Cancer Res** *37*, 4.
Lee, S.S., Bindokas, V.P., and Kron, S.J. (2017). Multiplex three-dimensional optical mapping of tumor immune microenvironment. **Sci Rep** *7*, 17031.
Lee, Y., Kim, N.H., Cho, E.S., Yang, J.H., Cha, Y.H., Kang, H.E., Yun, J.S., Cho, S.B., Lee, S.H., Paclikova, P., Radaszkiewicz, T.W., Bryja, V., Kang, C.G., Yuk, Y.S., Cha, S.Y., Kim, S.Y., Kim, H.S., and Yook, J.I. (2018b). Dishevelled has a YAP nuclear export function in a tumor suppressor context-dependent manner. **Nat Commun** *9*, 2301.
Leonard, F., and Godin, B. (2016). 3D In Vitro Model for Breast Cancer Research Using Magnetic Levitation and Bioprinting Method. **Methods Mol Biol** *1406*, 239-251.

Li, Q., Chen, C., Kapadia, A., Zhou, Q., Harper, M.K., Schaack, J., and LaBarbera, D.V. (2011). 3D models of epithelial-mesenchymal transition in breast cancer metastasis: high-throughput screening assay development, validation, and pilot screen. **J Biomol Screen** *16*, 141-154.
Li, X., Wang, Z., Ma, Q., Xu, Q., Liu, H., Duan, W., Lei, J., Ma, J., Wang, X., Lv, S., Han, L., Li, W., Guo, J., Guo, K., Zhang, D., Wu, E., and Xie, K. (2014). Sonic hedgehog paracrine signaling activates stromal cells to promote perineural invasion in pancreatic cancer. **Clin Cancer Res** *20*, 4326-4338.
Lin, C.H., Yang, J.R., Chiang, N.J., Ma, H., and Tsay, R.Y. (2014). Evaluation of decellularized extracellular matrix of skeletal muscle for tissue engineering. **Int J Artif Organs** *37*, 546-555.
Lo, A., Li, C.P., Buza, E.L., Blomberg, R., Govindaraju, P., Avery, D., Monslow, J., Hsiao, M., and Pure, E. (2017). Fibroblast activation protein augments progression and metastasis of pancreatic ductal adenocarcinoma. **JCI Insight** *2*.
Logsdon, C.D., Arumugam, T., and Ramachandran, V. (2015). Animal Models of Gastrointestinal and Liver Diseases. The difficulty of animal modeling of pancreatic cancer for preclinical evaluation of therapeutics. **Am J Physiol Gastrointest Liver Physiol** *309*, G283-291.
Longati, P., Jia, X., Eimer, J., Wagman, A., Witt, M.R., Rehnmark, S., Verbeke, C., Toftgard, R., Lohr, M., and Heuchel, R.L. (2013). 3D pancreatic carcinoma spheroids induce a matrix-rich, chemoresistant phenotype offering a better model for drug testing. **BMC Cancer** *13*, 95.
Longxi, P., Buwu, F., Yuan, W., and Sinan, G. (2011). Expression of p53 in the effects of artesunate on induction of apoptosis and inhibition of proliferation in rat primary hepatic stellate cells. **PLoS One** *6*, e26500.
Luk, J.M., and Guan, K.L. (2014). An alternative DNA damage pathway to apoptosis in hematological cancers. **Nat Med** *20*, 587-588.
Madihally, S.V., Flake, A.W., and Matthew, H.W. (1999). Maintenance of CD34 expression during proliferation of CD34+ cord blood cells on glycosaminoglycan surfaces. **Stem Cells** *17*, 295-305.
Mahlbacher, V., Sewing, A., Elsasser, H.P., and Kern, H.F. (1992). Hyaluronan is a secretory product of human pancreatic adenocarcinoma cells. **Eur J Cell Biol** *58*, 28-34.
Margineanu, A., Chan, J.J., Kelly, D.J., Warren, S.C., Flatters, D., Kumar, S., Katan, M., Dunsby, C.W., and French, P.M. (2016). Screening for protein-protein interactions using Forster resonance energy transfer (FRET) and fluorescence lifetime imaging microscopy (FLIM). **Sci Rep** *6*, 28186.
Maritan, S.M., Lian, E.Y., and Mulligan, L.M. (2017). An Efficient and Flexible Cell Aggregation Method for 3D Spheroid Production. **J Vis Exp**.
Matsudaira, T., Mukai, K., Noguchi, T., Hasegawa, J., Hatta, T., Iemura, S.I., Natsume, T., Miyamura, N., Nishina, H., Nakayama, J., Semba, K., Tomita, T., Murata, S., Arai, H., and Taguchi, T. (2017). Endosomal phosphatidylserine is critical for the YAP signalling pathway in proliferating cells. **Nat Commun** *8*, 1246.
Millet, L.J., and Gillette, M.U. (2012). Over a century of neuron culture: from the hanging drop to microfluidic devices. **Yale J Biol Med** *85*, 501-521.
Mirmalek-Sani, S.H., Orlando, G., McQuilling, J.P., Pareta, R., Mack, D.L., Salvatori, M., Farney, A.C., Stratta, R.J., Atala, A., Opara, E.C., and Soker, S. (2013). Porcine pancreas extracellular matrix as a platform for endocrine pancreas bioengineering. **Biomaterials** *34*, 5488-5495.
Miroshnikova, Y.A., Rozenberg, G.I., Cassereau, L., Pickup, M., Mouw, J.K., Ou, G., Templeman, K.L., Hannachi, E.I., Gooch, K.J., Sarang-Sieminski, A.L., Garcia, A.J., and Weaver, V.M. (2017). alpha5beta1-Integrin promotes tension-dependent mammary epithelial cell invasion by engaging the fibronectin synergy site. **Mol Biol Cell** *28*, 2958-2977.
Missiaglia, E., Blaveri, E., Terris, B., Wang, Y.H., Costello, E., Neoptolemos, J.P., Crnogorac-Jurcevic, T., and Lemoine, N.R. (2004). Analysis of gene expression in cancer cell lines identifies candidate markers for pancreatic tumorigenesis and metastasis. **Int J Cancer** *112*, 100-112.
Mo, J.S., Meng, Z., Kim, Y.C., Park, H.W., Hansen, C.G., Kim, S., Lim, D.S., and Guan, K.L. (2015). Cellular energy stress induces AMPK-mediated regulation of YAP and the Hippo pathway. **Nat Cell Biol** *17*, 500-510.
Moore, M.J., Hamm, J., Dancey, J., Eisenberg, P.D., Dagenais, M., Fields, A., Hagan, K., Greenberg, B., Colwell, B., Zee, B., Tu, D., Ottaway, J., Humphrey, R., Seymour, L., and National Cancer Institute of Canada Clinical Trials, G. (2003). Comparison of gemcitabine versus the matrix metalloproteinase

inhibitor BAY 12-9566 in patients with advanced or metastatic adenocarcinoma of the pancreas: a phase III trial of the National Cancer Institute of Canada Clinical Trials Group. **J Clin Oncol** *21*, 3296-3302.
Morvaridi, S., Dhall, D., Greene, M.I., Pandol, S.J., and Wang, Q. (2015). Role of YAP and TAZ in pancreatic ductal adenocarcinoma and in stellate cells associated with cancer and chronic pancreatitis. **Sci Rep** *5*, 16759.
Muller, P.A., and Vousden, K.H. (2014). Mutant p53 in cancer: new functions and therapeutic opportunities. **Cancer Cell** *25*, 304-317.
Murakami, S., Shahbazian, D., Surana, R., Zhang, W., Chen, H., Graham, G.T., White, S.M., Weiner, L.M., and Yi, C. (2017). Yes-associated protein mediates immune reprogramming in pancreatic ductal adenocarcinoma. **Oncogene** *36*, 1232-1244.
Mydlarz, L.D., Jacobs, R.S., Boehnlein, J., and Kerr, R.G. (2003). Pseudopterosin biosynthesis in Symbiodinium sp., the dinoflagellate symbiont of Pseudopterogorgia elisabethae. **Chem Biol** *10*, 1051-1056.
Neesse, A., Michl, P., Frese, K.K., Feig, C., Cook, N., Jacobetz, M.A., Lolkema, M.P., Buchholz, M., Olive, K.P., Gress, T.M., and Tuveson, D.A. (2011). Stromal biology and therapy in pancreatic cancer. **Gut** *60*, 861-868.
Neoptolemos, J.P., Kleeff, J., Michl, P., Costello, E., Greenhalf, W., and Palmer, D.H. (2018). Therapeutic developments in pancreatic cancer: current and future perspectives. **Nat Rev Gastroenterol Hepatol** *15*, 333-348.
Nichols, J., Silva, J., Roode, M., and Smith, A. (2009). Suppression of Erk signalling promotes ground state pluripotency in the mouse embryo. **Development** *136*, 3215-3222.
Nishio, M., Sugimachi, K., Goto, H., Wang, J., Morikawa, T., Miyachi, Y., Takano, Y., Hikasa, H., Itoh, T., Suzuki, S.O., Kurihara, H., Aishima, S., Leask, A., Sasaki, T., Nakano, T., Nishina, H., Nishikawa, Y., Sekido, Y., Nakao, K., Shin-Ya, K., Mimori, K., and Suzuki, A. (2016). Dysregulated YAP1/TAZ and TGF-beta signaling mediate hepatocarcinogenesis in Mob1a/1b-deficient mice. **Proc Natl Acad Sci U S A** *113*, E71-80.
Nishizawa, H., Iguchi, G., Fukuoka, H., Takahashi, M., Suda, K., Bando, H., Matsumoto, R., Yoshida, K., Odake, Y., Ogawa, W., and Takahashi, Y. (2016). IGF-I induces senescence of hepatic stellate cells and limits fibrosis in a p53-dependent manner. **Sci Rep** *6*, 34605.
Nyga, A., Loizidou, M., Emberton, M., and Cheema, U. (2013). A novel tissue engineered three-dimensional in vitro colorectal cancer model. **Acta Biomater** *9*, 7917-7926.
Ohlund, D., Handly-Santana, A., Biffi, G., Elyada, E., Almeida, A.S., Ponz-Sarvise, M., Corbo, V., Oni, T.E., Hearn, S.A., Lee, E.J., Chio, II, Hwang, C.I., Tiriac, H., Baker, L.A., Engle, D.D., Feig, C., Kultti, A., Egeblad, M., Fearon, D.T., Crawford, J.M., Clevers, H., Park, Y., and Tuveson, D.A. (2017). Distinct populations of inflammatory fibroblasts and myofibroblasts in pancreatic cancer. **J Exp Med** *214*, 579-596.
Ohlund, D., Lundin, C., Ardnor, B., Oman, M., Naredi, P., and Sund, M. (2009). Type IV collagen is a tumour stroma-derived biomarker for pancreas cancer. **Br J Cancer** *101*, 91-97.
Ohuchida, K., Mizumoto, K., Murakami, M., Qian, L.W., Sato, N., Nagai, E., Matsumoto, K., Nakamura, T., and Tanaka, M. (2004). Radiation to stromal fibroblasts increases invasiveness of pancreatic cancer cells through tumor-stromal interactions. **Cancer Res** *64*, 3215-3222.
Oren, R., Fellus-Alyagor, L., Addadi, Y., Bochner, F., Gutman, H., Blumenreich, S., Dafni, H., Dekel, N., Neeman, M., and Lazar, S. (2018). Whole Organ Blood and Lymphatic Vessels Imaging (WOBLI). **Sci Rep** *8*, 1412.
Overholtzer, M., Zhang, J., Smolen, G.A., Muir, B., Li, W., Sgroi, D.C., Deng, C.X., Brugge, J.S., and Haber, D.A. (2006). Transforming properties of YAP, a candidate oncogene on the chromosome 11q22 amplicon. **Proc Natl Acad Sci U S A** *103*, 12405-12410.
Ozaki, T., and Nakagawara, A. (2011). Role of p53 in Cell Death and Human Cancers. **Cancers (Basel)** *3*, 994-1013.
Ozcelikkale, A., Moon, H.R., Linnes, M., and Han, B. (2017). In vitro microfluidic models of tumor microenvironment to screen transport of drugs and nanoparticles. **Wiley Interdiscip Rev Nanomed Nanobiotechnol** *9*.

Ozdemir, B.C., Pentcheva-Hoang, T., Carstens, J.L., Zheng, X., Wu, C.C., Simpson, T.R., Laklai, H., Sugimoto, H., Kahlert, C., Novitskiy, S.V., De Jesus-Acosta, A., Sharma, P., Heidari, P., Mahmood, U., Chin, L., Moses, H.L., Weaver, V.M., Maitra, A., Allison, J.P., LeBleu, V.S., and Kalluri, R. (2014). Depletion of carcinoma-associated fibroblasts and fibrosis induces immunosuppression and accelerates pancreas cancer with reduced survival. **Cancer Cell** *25*, 719-734.
Pang, W., Su, J., Wang, Y., Feng, H., Dai, X., Yuan, Y., Chen, X., and Yao, W. (2015). Pancreatic cancer-secreted miR-155 implicates in the conversion from normal fibroblasts to cancer-associated fibroblasts. **Cancer Sci** *106*, 1362-1369.
Park, J.Y., Hiroshima, Y., Lee, J.Y., Maawy, A.A., Hoffman, R.M., and Bouvet, M. (2015). MUC1 selectively targets human pancreatic cancer in orthotopic nude mouse models. **PLoS One** *10*, e0122100.
Patra, B., Peng, C.C., Liao, W.H., Lee, C.H., and Tung, Y.C. (2016). Drug testing and flow cytometry analysis on a large number of uniform sized tumor spheroids using a microfluidic device. **Sci Rep** *6*, 21061.
Phung, Y.T., Barbone, D., Broaddus, V.C., and Ho, M. (2011). Rapid generation of in vitro multicellular spheroids for the study of monoclonal antibody therapy. **J Cancer** *2*, 507-514.
Quaresma, M., Coleman, M.P., and Rachet, B. (2015). 40-year trends in an index of survival for all cancers combined and survival adjusted for age and sex for each cancer in England and Wales, 1971-2011: a population-based study. **Lancet** *385*, 1206-1218.
Reaven, E.P., Curry, D.L., and Reaven, G.M. (1987). Effect of age and sex on rat endocrine pancreas. **Diabetes** *36*, 1397-1400.
Reddy, B.V., and Irvine, K.D. (2013). Regulation of Hippo signaling by EGFR-MAPK signaling through Ajuba family proteins. **Dev Cell** *24*, 459-471.
Rhim, A.D., Oberstein, P.E., Thomas, D.H., Mirek, E.T., Palermo, C.F., Sastra, S.A., Dekleva, E.N., Saunders, T., Becerra, C.P., Tattersall, I.W., Westphalen, C.B., Kitajewski, J., Fernandez-Barrena, M.G., Fernandez-Zapico, M.E., Iacobuzio-Donahue, C., Olive, K.P., and Stanger, B.Z. (2014). Stromal elements act to restrain, rather than support, pancreatic ductal adenocarcinoma. **Cancer Cell** *25*, 735-747.
Rice, A.J., Cortes, E., Lachowski, D., Cheung, B.C.H., Karim, S.A., Morton, J.P., and Del Rio Hernandez, A. (2017). Matrix stiffness induces epithelial-mesenchymal transition and promotes chemoresistance in pancreatic cancer cells. **Oncogenesis** *6*, e352.
Rosenbluh, J., Nijhawan, D., Cox, A.G., Li, X., Neal, J.T., Schafer, E.J., Zack, T.I., Wang, X., Tsherniak, A., Schinzel, A.C., Shao, D.D., Schumacher, S.E., Weir, B.A., Vazquez, F., Cowley, G.S., Root, D.E., Mesirov, J.P., Beroukhim, R., Kuo, C.J., Goessling, W., and Hahn, W.C. (2012). beta-Catenin-driven cancers require a YAP1 transcriptional complex for survival and tumorigenesis. **Cell** *151*, 1457-1473.
Rozengurt, E., Sinnett-Smith, J., and Eibl, G. (2018). Yes-associated protein (YAP) in pancreatic cancer: at the epicenter of a targetable signaling network associated with patient survival. **Signal Transduct Target Ther** *3*, 11.
Ruess, D.A., Gorgulu, K., Wormann, S.M., and Algul, H. (2017). Pharmacotherapeutic Management of Pancreatic Ductal Adenocarcinoma: Current and Emerging Concepts. **Drugs Aging** *34*, 331-357.
Ruggeri, B., Zhang, S.Y., Caamano, J., DiRado, M., Flynn, S.D., and Klein-Szanto, A.J. (1992). Human pancreatic carcinomas and cell lines reveal frequent and multiple alterations in the p53 and Rb-1 tumor-suppressor genes. **Oncogene** *7*, 1503-1511.
Salgado, M., Arevalo, S., Hernando, O., Martinez, A., Yaya, R., and Hidalgo, M. (2018). Management of unresectable, locally advanced pancreatic adenocarcinoma. **Clin Transl Oncol** *20*, 113-118.
Sato, N., Cheng, X.B., Kohi, S., Koga, A., and Hirata, K. (2016a). Targeting hyaluronan for the treatment of pancreatic ductal adenocarcinoma. **Acta Pharm Sin B** *6*, 101-105.
Sato, N., Kohi, S., Hirata, K., and Goggins, M. (2016b). Role of hyaluronan in pancreatic cancer biology and therapy: Once again in the spotlight. **Cancer Sci** *107*, 569-575.
Schlegelmilch, K., Mohseni, M., Kirak, O., Pruszak, J., Rodriguez, J.R., Zhou, D., Kreger, B.T., Vasioukhin, V., Avruch, J., Brummelkamp, T.R., and Camargo, F.D. (2011). Yap1 acts downstream of alpha-catenin to control epidermal proliferation. **Cell** *144*, 782-795.
Seino, T., Kawasaki, S., Shimokawa, M., Tamagawa, H., Toshimitsu, K., Fujii, M., Ohta, Y., Matano, M., Nanki, K., Kawasaki, K., Takahashi, S., Sugimoto, S., Iwasaki, E., Takagi, J., Itoi, T., Kitago, M., Kitagawa,

Y., Kanai, T., and Sato, T. (2018). Human Pancreatic Tumor Organoids Reveal Loss of Stem Cell Niche Factor Dependence during Disease Progression. **Cell Stem Cell** *22*, 454-467 e456.
Seo, Y.D., and Pillarisetty, V.G. (2017). T-cell programming in pancreatic adenocarcinoma: a review. **Cancer Gene Ther** *24*, 106-113.
Sherman, M.H., Yu, R.T., Tseng, T.W., Sousa, C.M., Liu, S., Truitt, M.L., He, N., Ding, N., Liddle, C., Atkins, A.R., Leblanc, M., Collisson, E.A., Asara, J.M., Kimmelman, A.C., Downes, M., and Evans, R.M. (2017). Stromal cues regulate the pancreatic cancer epigenome and metabolome. **Proc Natl Acad Sci U S A** *114*, 1129-1134.
Shiah, H.S., Gao, W., Baker, D.C., and Cheng, Y.C. (2006). Inhibition of cell growth and nuclear factor-kappaB activity in pancreatic cancer cell lines by a tylophorine analogue, DCB-3503. **Mol Cancer Ther** *5*, 2484-2493.
Shoemaker, R.H. (2006). The NCI60 human tumour cell line anticancer drug screen. **Nat Rev Cancer** *6*, 813-823.
Siegel, R.L., Miller, K.D., and Jemal, A. (2015). Cancer statistics, 2015. **CA Cancer J Clin** *65*, 5-29.
Simon, B., Weinel, R., Hohne, M., Watz, J., Schmidt, J., Kortner, G., and Arnold, R. (1994). Frequent alterations of the tumor suppressor genes p53 and DCC in human pancreatic carcinoma. **Gastroenterology** *106*, 1645-1651.
Sorrentino, G., Ruggeri, N., Specchia, V., Cordenonsi, M., Mano, M., Dupont, S., Manfrin, A., Ingallina, E., Sommaggio, R., Piazza, S., Rosato, A., Piccolo, S., and Del Sal, G. (2014). Metabolic control of YAP and TAZ by the mevalonate pathway. **Nat Cell Biol** *16*, 357-366.
Souza, G.R., Molina, J.R., Raphael, R.M., Ozawa, M.G., Stark, D.J., Levin, C.S., Bronk, L.F., Ananta, J.S., Mandelin, J., Georgescu, M.M., Bankson, J.A., Gelovani, J.G., Killian, T.C., Arap, W., and Pasqualini, R. (2010). Three-dimensional tissue culture based on magnetic cell levitation. **Nat Nanotechnol** *5*, 291-296.
Sperlich, J., Kerr, R., and Teusch, N. (2017). The Marine Natural Product Pseudopterosin Blocks Cytokine Release of Triple-Negative Breast Cancer and Monocytic Leukemia Cells by Inhibiting NF-kappaB Signaling. **Mar Drugs** *15*.
Sperlich, J., and Teusch, N. (2018). Pseudopterosin Inhibits Proliferation and 3D Invasion in Triple-Negative Breast Cancer by Agonizing Glucocorticoid Receptor Alpha. **Molecules** *23*.
Stern, M.M., Myers, R.L., Hammam, N., Stern, K.A., Eberli, D., Kritchevsky, S.B., Soker, S., and Van Dyke, M. (2009). The influence of extracellular matrix derived from skeletal muscle tissue on the proliferation and differentiation of myogenic progenitor cells ex vivo. **Biomaterials** *30*, 2393-2399.
Storm, M.P., Sorrell, I., Shipley, R., Regan, S., Luetchford, K.A., Sathish, J., Webb, S., and Ellis, M.J. (2016). Hollow Fiber Bioreactors for In Vivo-like Mammalian Tissue Culture. **J Vis Exp**.
Subramanian, G., Schwarz, R.E., Higgins, L., McEnroe, G., Chakravarty, S., Dugar, S., and Reiss, M. (2004). Targeting endogenous transforming growth factor beta receptor signaling in SMAD4-deficient human pancreatic carcinoma cells inhibits their invasive phenotype1. **Cancer Res** *64*, 5200-5211.
Sudol, M. (1994). Yes-associated protein (YAP65) is a proline-rich phosphoprotein that binds to the SH3 domain of the Yes proto-oncogene product. **Oncogene** *9*, 2145-2152.
Sullivan, A., and Lu, X. (2007). ASPP: a new family of oncogenes and tumour suppressor genes. **Br J Cancer** *96*, 196-200.
Suwa, H., Yoshimura, T., Yamaguchi, N., Kanehira, K., Manabe, T., Imamura, M., Hiai, H., and Fukumoto, M. (1994). K-ras and p53 alterations in genomic DNA and transcripts of human pancreatic adenocarcinoma cell lines. **Jpn J Cancer Res** *85*, 1005-1014.
Swinney, D.C., and Anthony, J. (2011). How were new medicines discovered? **Nature Reviews Drug Discovery** *10*, 507-519.
Tai, J., Cheung, S.S., Ou, D., Warnock, G.L., and Hasman, D. (2014). Antiproliferation activity of Devil's club (Oplopanax horridus) and anticancer agents on human pancreatic cancer multicellular spheroids. **Phytomedicine** *21*, 506-514.
Tannenbaum, J., and Bennett, B.T. (2015). Russell and Burch's 3Rs then and now: the need for clarity in definition and purpose. **J Am Assoc Lab Anim Sci** *54*, 120-132.

Tauer, U. (2002). Advantages and risks of multiphoton microscopy in physiology. **Exp Physiol** *87*, 709-714.
Tibbitt, M.W., and Anseth, K.S. (2009). Hydrogels as extracellular matrix mimics for 3D cell culture. **Biotechnol Bioeng** *103*, 655-663.
Tiriac, H., Belleau, P., Engle, D.D., Plenker, D., Deschenes, A., Somerville, T.D.D., Froeling, F.E.M., Burkhart, R.A., Denroche, R.E., Jang, G.H., Miyabayashi, K., Young, C.M., Patel, H., Ma, M., LaComb, J.F., Palmaira, R.L.D., Javed, A.A., Huynh, J.C., Johnson, M., Arora, K., Robine, N., Shah, M., Sanghvi, R., Goetz, A.B., Lowder, C.Y., Martello, L., Driehuis, E., LeComte, N., Askan, G., Iacobuzio-Donahue, C.A., Clevers, H., Wood, L.D., Hruban, R.H., Thompson, E., Aguirre, A.J., Wolpin, B.M., Sasson, A., Kim, J., Wu, M., Bucobo, J.C., Allen, P., Sejpal, D.V., Nealon, W., Sullivan, J.D., Winter, J.M., Gimotty, P.A., Grem, J.L., DiMaio, D.J., Buscaglia, J.M., Grandgenett, P.M., Brody, J.R., Hollingsworth, M.A., O'Kane, G.M., Notta, F., Kim, E., Crawford, J.M., Devoe, C., Ocean, A., Wolfgang, C.L., Yu, K.H., Li, E., Vakoc, C.R., Hubert, B., Fischer, S.E., Wilson, J.M., Moffitt, R., Knox, J., Krasnitz, A., Gallinger, S., and Tuveson, D.A. (2018). Organoid Profiling Identifies Common Responders to Chemotherapy in Pancreatic Cancer. **Cancer Discov** *8*, 1112-1129.
Tomlinson, V., Gudmundsdottir, K., Luong, P., Leung, K.Y., Knebel, A., and Basu, S. (2010). JNK phosphorylates Yes-associated protein (YAP) to regulate apoptosis. **Cell Death Dis** *1*, e29.
Topalovski, M., and Brekken, R.A. (2016). Matrix control of pancreatic cancer: New insights into fibronectin signaling. **Cancer Lett** *381*, 252-258.
Torre, L.A., Bray, F., Siegel, R.L., Ferlay, J., Lortet-Tieulent, J., and Jemal, A. (2015). Global cancer statistics, 2012. **CA Cancer J Clin** *65*, 87-108.
Toyoda, E., Doi, R., Koizumi, M., Kami, K., Ito, D., Mori, T., Fujimoto, K., Nakajima, S., Wada, M., and Imamura, M. (2005). Analysis of E-, N-cadherin, alpha-, beta-, and gamma-catenin expression in human pancreatic carcinoma cell lines. **Pancreas** *30*, 168-173.
Tsai, S., McOlash, L., Palen, K., Johnson, B., Duris, C., Yang, Q., Dwinell, M.B., Hunt, B., Evans, D.B., Gershan, J., and James, M.A. (2018). Development of primary human pancreatic cancer organoids, matched stromal and immune cells and 3D tumor microenvironment models. **BMC Cancer** *18*, 335.
Tung, Y.C., Hsiao, A.Y., Allen, S.G., Torisawa, Y.S., Ho, M., and Takayama, S. (2011). High-throughput 3D spheroid culture and drug testing using a 384 hanging drop array. **Analyst** *136*, 473-478.
Turker, E., Demircak, N., and Arslan-Yildiz, A. (2018). Scaffold-free three-dimensional cell culturing using magnetic levitation. **Biomater Sci** *6*, 1745-1753.
Uccello, M., Moschetta, M., Mak, G., Alam, T., Henriquez, C.M., and Arkenau, H.T. (2018). Towards an optimal treatment algorithm for metastatic pancreatic ductal adenocarcinoma (PDA). **Curr Oncol** *25*, e90-e94.
Uquillas, J.A., and Akkus, O. (2012). Modeling the electromobility of type-I collagen molecules in the electrochemical fabrication of dense and aligned tissue constructs. **Ann Biomed Eng** *40*, 1641-1653.
Veenstra, V.L., Garcia-Garijo, A., van Laarhoven, H.W., and Bijlsma, M.F. (2018). Extracellular Influences: Molecular Subclasses and the Microenvironment in Pancreatic Cancer. **Cancers (Basel)** *10*.
von Ahrens, D., Bhagat, T.D., Nagrath, D., Maitra, A., and Verma, A. (2017). The role of stromal cancer-associated fibroblasts in pancreatic cancer. **J Hematol Oncol** *10*, 76.
Waddell, N., Pajic, M., Patch, A.M., Chang, D.K., Kassahn, K.S., Bailey, P., Johns, A.L., Miller, D., Nones, K., Quek, K., Quinn, M.C., Robertson, A.J., Fadlullah, M.Z., Bruxner, T.J., Christ, A.N., Harliwong, I., Idrisoglu, S., Manning, S., Nourse, C., Nourbakhsh, E., Wani, S., Wilson, P.J., Markham, E., Cloonan, N., Anderson, M.J., Fink, J.L., Holmes, O., Kazakoff, S.H., Leonard, C., Newell, F., Poudel, B., Song, S., Taylor, D., Waddell, N., Wood, S., Xu, Q., Wu, J., Pinese, M., Cowley, M.J., Lee, H.C., Jones, M.D., Nagrial, A.M., Humphris, J., Chantrill, L.A., Chin, V., Steinmann, A.M., Mawson, A., Humphrey, E.S., Colvin, E.K., Chou, A., Scarlett, C.J., Pinho, A.V., Giry-Laterriere, M., Rooman, I., Samra, J.S., Kench, J.G., Pettitt, J.A., Merrett, N.D., Toon, C., Epari, K., Nguyen, N.Q., Barbour, A., Zeps, N., Jamieson, N.B., Graham, J.S., Niclou, S.P., Bjerkvig, R., Grutzmann, R., Aust, D., Hruban, R.H., Maitra, A., Iacobuzio-Donahue, C.A., Wolfgang, C.L., Morgan, R.A., Lawlor, R.T., Corbo, V., Bassi, C., Falconi, M., Zamboni, G., Tortora, G., Tempero, M.A., Australian Pancreatic Cancer Genome, I., Gill, A.J., Eshleman, J.R., Pilarsky, C., Scarpa,

A., Musgrove, E.A., Pearson, J.V., Biankin, A.V., and Grimmond, S.M. (2015). Whole genomes redefine the mutational landscape of pancreatic cancer. **Nature** *518*, 495-501.
Wall, M.E., and Wani, M.C. (1996). Camptothecin and taxol: from discovery to clinic. **J Ethnopharmacol** *51*, 239-253; discussion 253-234.
Walsh, A.J., Castellanos, J.A., Nagathihalli, N.S., Merchant, N.B., and Skala, M.C. (2016). Optical Imaging of Drug-Induced Metabolism Changes in Murine and Human Pancreatic Cancer Organoids Reveals Heterogeneous Drug Response. **Pancreas** *45*, 863-869.
Wang, W., Xiao, Z.D., Li, X., Aziz, K.E., Gan, B., Johnson, R.L., and Chen, J. (2015). AMPK modulates Hippo pathway activity to regulate energy homeostasis. **Nat Cell Biol** *17*, 490-499.
Ware, M.J., Keshishian, V., Law, J.J., Ho, J.C., Favela, C.A., Rees, P., Smith, B., Mohammad, S., Hwang, R.F., Rajapakshe, K., Coarfa, C., Huang, S., Edwards, D.P., Corr, S.J., Godin, B., and Curley, S.A. (2016). Generation of an in vitro 3D PDAC stroma rich spheroid model. **Biomaterials** *108*, 129-142.
Wei, H., Wang, F., Wang, Y., Li, T., Xiu, P., Zhong, J., Sun, X., and Li, J. (2017). Verteporfin suppresses cell survival, angiogenesis and vasculogenic mimicry of pancreatic ductal adenocarcinoma via disrupting the YAP-TEAD complex. **Cancer Sci** *108*, 478-487.
Weinberg, B.A., Yabar, C.S., Brody, J.R., and Pishvaian, M.J. (2015). Current Standards and Novel Treatment Options for Metastatic Pancreatic Adenocarcinoma. **Oncology (Williston Park)** *29*, 809-820, 886.
Wen, Z., Liao, Q., Hu, Y., You, L., Zhou, L., and Zhao, Y. (2013). A spheroid-based 3-D culture model for pancreatic cancer drug testing, using the acid phosphatase assay. **Braz J Med Biol Res** *46*, 634-642.
Whatcott, C.J., Diep, C.H., Jiang, P., Watanabe, A., LoBello, J., Sima, C., Hostetter, G., Shepard, H.M., Von Hoff, D.D., and Han, H. (2015). Desmoplasia in Primary Tumors and Metastatic Lesions of Pancreatic Cancer. **Clin Cancer Res** *21*, 3561-3568.
Wolf, M.T., Daly, K.A., Reing, J.E., and Badylak, S.F. (2012). Biologic scaffold composed of skeletal muscle extracellular matrix. **Biomaterials** *33*, 2916-2925.
Wormann, S.M., Song, L., Ai, J., Diakopoulos, K.N., Kurkowski, M.U., Gorgulu, K., Ruess, D., Campbell, A., Doglioni, C., Jodrell, D., Neesse, A., Demir, I.E., Karpathaki, A.P., Barenboim, M., Hagemann, T., Rose-John, S., Sansom, O., Schmid, R.M., Protti, M.P., Lesina, M., and Algul, H. (2016). Loss of P53 Function Activates JAK2-STAT3 Signaling to Promote Pancreatic Tumor Growth, Stroma Modification, and Gemcitabine Resistance in Mice and Is Associated With Patient Survival. **Gastroenterology** *151*, 180-193 e112.
Xu, F., Celli, J., Rizvi, I., Moon, S., Hasan, T., and Demirci, U. (2011). A three-dimensional in vitro ovarian cancer coculture model using a high-throughput cell patterning platform. **Biotechnol J** *6*, 204-212.
Yamada, K.M., and Cukierman, E. (2007). Modeling tissue morphogenesis and cancer in 3D. **Cell** *130*, 601-610.
Yang, S., Zhang, L., Purohit, V., Shukla, S.K., Chen, X., Yu, F., Fu, K., Chen, Y., Solheim, J., Singh, P.K., Song, W., and Dong, J. (2015). Active YAP promotes pancreatic cancer cell motility, invasion and tumorigenesis in a mitotic phosphorylation-dependent manner through LPAR3. **Oncotarget** *6*, 36019-36031.
Yen, T.N.F., Aardal, N.P., Bronner, M.P., Thorning, D.R., Savard, C.E., Lee, S.P., and Bell, R.H. (2002). Myofibroblasts are responsible for the desmoplastic reaction surrounding human pancreatic carcinomas. **Surgery** *131*, 129-134.
Yeon, S.E., No da, Y., Lee, S.H., Nam, S.W., Oh, I.H., Lee, J., and Kuh, H.J. (2013). Application of concave microwells to pancreatic tumor spheroids enabling anticancer drug evaluation in a clinically relevant drug resistance model. **PLoS One** *8*, e73345.
Yu, F.X., Zhao, B., and Guan, K.L. (2015). Hippo Pathway in Organ Size Control, Tissue Homeostasis, and Cancer. **Cell** *163*, 811-828.
Yu, F.X., Zhao, B., Panupinthu, N., Jewell, J.L., Lian, I., Wang, L.H., Zhao, J., Yuan, H., Tumaneng, K., Li, H., Fu, X.D., Mills, G.B., and Guan, K.L. (2012). Regulation of the Hippo-YAP pathway by G-protein-coupled receptor signaling. **Cell** *150*, 780-791.

Yu, H., Chen, Y., Kong, H., He, Q., Sun, H., Bhugul, P.A., Zhang, Q., Chen, B., and Zhou, M. (2018). The rat pancreatic body tail as a source of a novel extracellular matrix scaffold for endocrine pancreas bioengineering. **J Biol Eng** *12*, 6.
Yuan, Y., Li, D., Li, H., Wang, L., Tian, G., and Dong, Y. (2016). YAP overexpression promotes the epithelial-mesenchymal transition and chemoresistance in pancreatic cancer cells. **Mol Med Rep** *13*, 237-242.
Yuhas, J.M., Li, A.P., Martinez, A.O., and Ladman, A.J. (1977). A simplified method for production and growth of multicellular tumor spheroids. **Cancer Res** *37*, 3639-3643.
Zanconato, F., Battilana, G., Cordenonsi, M., and Piccolo, S. (2016a). YAP/TAZ as therapeutic targets in cancer. **Curr Opin Pharmacol** *29*, 26-33.
Zanconato, F., Cordenonsi, M., and Piccolo, S. (2016b). YAP/TAZ at the Roots of Cancer. **Cancer Cell** *29*, 783-803.
Zhang, K., Qi, H.X., Hu, Z.M., Chang, Y.N., Shi, Z.M., Han, X.H., Han, Y.W., Zhang, R.X., Zhang, Z., Chen, T., and Hong, W. (2015). YAP and TAZ Take Center Stage in Cancer. **Biochemistry** *54*, 6555-6566.
Zhang, W., Erkan, M., Abiatari, I., Giese, N.A., Felix, K., Kayed, H., Buchler, M.W., Friess, H., and Kleeff, J. (2007). Expression of extracellular matrix metalloproteinase inducer (EMMPRIN/CD147) in pancreatic neoplasm and pancreatic stellate cells. **Cancer Biol Ther** *6*, 218-227.
Zhang, Y.S., Duchamp, M., Oklu, R., Ellisen, L.W., Langer, R., and Khademhosseini, A. (2016). Bioprinting the Cancer Microenvironment. **ACS Biomater Sci Eng** *2*, 1710-1721.
Zhao, B., Ye, X., Yu, J., Li, L., Li, W., Li, S., Yu, J., Lin, J.D., Wang, C.Y., Chinnaiyan, A.M., Lai, Z.C., and Guan, K.L. (2008). TEAD mediates YAP-dependent gene induction and growth control. **Genes Dev** *22*, 1962-1971.
Zhao, H., Wang, Q., Wang, X., Zhu, H., Zhang, S., Wang, W., Wang, Z., and Huang, J. (2016a). Correlation Between RAB27B and p53 Expression and Overall Survival in Pancreatic Cancer. **Pancreas** *45*, 204-210.
Zhao, S., Chen, C., Chang, K., Karnad, A., Jagirdar, J., Kumar, A.P., and Freeman, J.W. (2016b). CD44 Expression Level and Isoform Contributes to Pancreatic Cancer Cell Plasticity, Invasiveness, and Response to Therapy. **Clin Cancer Res** *22*, 5592-5604.
Zhao, X., Wang, X., Fang, L., Lan, C., Zheng, X., Wang, Y., Zhang, Y., Han, X., Liu, S., Cheng, K., Zhao, Y., Shi, J., Guo, J., Hao, J., Ren, H., and Nie, G. (2017). A combinatorial strategy using YAP and pan-RAF inhibitors for treating KRAS-mutant pancreatic cancer. **Cancer Lett** *402*, 61-70.